ATTOSECOND SPECTROSCOPY OF AUTOIONIZING STATES

ÁLVARO JIMÉNEZ-GALÁN

A Thesis submitted for the degree of Doctor

Departamento de Química
Facultad de Ciencias
Universidad Autónoma de Madrid

Supervisors:
Luca Argenti & Fernando Martín

Madrid,December 2015

A todos los que han estado ahí

ABSTRACT

In this PhD Thesis we report a theoretical time-resolved study of the effects of electron correlation in the single photoionization spectrum of atomic systems, with particular focus on multi-photon transitions occurring in the presence of autoionizing states. For this task, we take two complementary approaches. On the one hand, we solve *ab initio* the time dependent Schrödinger equation in a virtually exact way for the helium atom. Helium is a hallmark system for electron correlation studies, and will be our target in the majority of this work. The results obtained, however, are general and apply to many-electron systems. On the other hand, we derive simplified models, which allow to gain physical insight on the phenomenology observed and to extend our theoretical predictions on helium to larger systems. The models are benchmarked against the *ab initio* solution yielding results in excellent agreement.

We explore electron dynamics by means of two novel attosecond pump-probe techniques: reconstruction of attosecond beating by interference of two-photon transitions and attosecond transient absorption spectroscopy.

First, by using a weak probe field, we study two-photon transitions resonant with the doubly-excited autoionizing states embedded in the single-channel single-ionization continuum of helium. Using the reconstruction of attosecond beating by interference of two-photon transitions technique, we access both the amplitude and phase of the transitions, which permits us to extract the dynamical properties of the doubly-excited wave packet. Excellent agreement is found by comparing an experimentally reconstructed meta-stable wave packet with that reconstructed from theory. The predictions of our model are then applied to experiments performed in the multi-channel continuum of the argon atom, confirming that the extension of the model to larger systems works.

Second, we investigate the effects of varying the probe field intensity on the phases and positions of doubly-excited states in helium. By looking at the intensity-dependent phase of doubly-excited states in the attosecond transient absorption spectrum, we show that the ac-Stark shift higher terms in the doubly-excited series exceeds the ponderomotive energy. This circumstance indicates that the concurrent motion of the two correlated electrons plays a crucial role in the response of the electron wave packet to the driving laser field at relatively high intensities. By photoionizing selected doubly-excited states, we see that the shift of the photoelectron signal depends on both the final ionization channel and the series to which the doubly-excited state belongs.

Finally, in the non-resonant region, we explore angularly-resolved two-photon transitions. We discuss quantitatively that, when measuring photo-ejection time delays, the measurement process induces a universal anisotropy. At variance

with hydrogen, in helium the polarizable parent ion has a noticeable effect on the observed time delay anisotropy, which points out the potential of angularly-resolved time delay measurements to investigate multi-electron effects.

RESUMEN

En esta Tesis presentamos un estudio teórico de los efectos de correlación electrónica resueltos temporalmente en el espectro de ionización simple de sistemas atómicos, con particular atención a las transiciones multifotónicas que ocurren en presencia de estados autoionizantes. Para ello, hemos tomado dos enfoques complementarios. Por un lado, resolvemos de manera *ab initio* la ecuación de Schrödinger dependiente del tiempo de manera virtualmente exacta para el átomo de helio. El átomo de helio es un candidato perfecto para estudios de correlación electrónica, y lo usaremos como principal objeto de nuestro estudio. Los resultados obtenidos, no obstante, son generales y aplicables a átomos de más electrones. Por otro lado, hemos derivado modelos analíticos, que permiten obtener una comprensión más profunda de la fenomenología observada y extender las predicciones teóricas para el átomo de helio a sistemas más grandes. Los modelos son comparados con la solución *ab initio* obteniéndose un acuerdo excelente.

Exploramos la dinámica electrónica por medio de dos técnicas *pump-probe*: reconstrucción de la oscilación de attosegundos por medio de la interferencia de transiciones a dos fotones (RABITT , por sus siglas en inglés) y espectroscopía de absorción transitoria de attosegundos (ATAS, por sus siglas en inglés).

Primero, usando un láser de intensidad débil, estudiamos transiciones de dos fotones resonantes con los estados doblemente excitados que se encuentran contenidos en el continuo de ionización simple del helio. Usando la técnica de RABITT , accedemos a las amplitudes y las fases de las transiciones, lo que nos permite extraer las propiedades dinámicas del paquete de ondas doblemente excitado. Comparando el paquete de ondas metaestable reconstruido experimentalmente con el predicho por la teoría, encontramos un acuerdo excelente. Posteriormente aplicamos las predicciones de nuestro modelo a experimentos realizados en el continuo multi-canal del átomo de argon, confirmando que la extensión de nuestro modelo a sistemas más grandes funciona.

Segundo, investigamos los efectos que produce la variación de la intensidad del láser en las fases y posiciones de los estados doblemente excitados del helio. Mirando a la fase de los estados doblemente excitados en el espectro de ATAS, mostramos que el desplazamiento ac-Stark para los órdenes más altos de la serie de estados doblemente excitados excede la energía ponderomotriz. Esta circunstancia indica que el movimiento correlacionado de dos electrones juega un papel crucial en la respuesta del paquete de ondas electrónico al campo láser para intensidades relativamente altas. Mediante la fotoionización a partir estados doblemente excitados, encontramos que el desplazamiento de la señal fotoelectrónica depende tanto del canal del continuo final de ionización como de la serie autoionizante a la que el estado doblemente excitado pertenece.

Por último, en la región no resonante, exploramos transiciones a dos fotones resueltas angularmente. Mostramos de manera cuantitativa que en el proceso de medición de los tiempos de fotoemisión, se induce una anisotropía universal. A diferencia del átomo de hidrógeno, en el helio la polarizabilidad del ión padre tiene un efecto notable en la anisotropía observada, lo que pone de manifiesto el potencial de usar mediciones del tiempo de fotoemisión resueltas angularmente para investigar efectos multi-electrónicos.

PUBLICATIONS

This thesis is based on the following papers:

1. **The soft-photon approximation in infrared laser-assisted atomic ionization by extreme-ultraviolet attosecond-pulse trains**. A. Jiménez-Galán, L. Argenti, F. Martín. *New Journal of Physics* **15**, 113009 (2013).

2. **Modulation of Attosecond Beating in Resonant Two-Photon Ionization**. A. Jiménez-Galán, L. Argenti, F. Martín.*Phys.Rev.Lett.* **113**, 263001 (2014).

3. **Dressing effects in the attosecond transient absorption spectra of doubly excited states in helium**. L. Argenti, A. Jiménez-Galán, C. Marante, C. Ott, T. Pfeifer, F. Martín. *Phys.Rev.A **91**, 061403(R) (2015).*

4. **Modulation of Attosecond Beating by Resonant Two-Photon Transition**. A. Jiménez-Galán, L. Argenti, F. Martín. *In press. Journal of Physics: Conference Series*.

5. **Two-photon finite-pulse model for resonant transitions in attosecond experiments**. A. Jiménez-Galán, F. Martín, L. Argenti. *Accepted. Phys. Rev. A* (arXiv:1509.05814).

6. **Time delay anisotropy in photoelectron emission from the isotropic ground state of helium**. S. Heuser, A. Jiménez-Galán, C. Cirelli, M. Sabbar, R. Boge, M. Lucchini, L. Gallmann, I. Ivanov, A. S. Kheifets, J. M. Dahlström, E. Lindroth, L. Argenti, F. Martín, U. Keller. *Submitted (arXiv:1503.08966)*.

7. **Phase measurement of a Fano window resonance using tunable attosecond pulses**. M. Kotur, D. Guenot, A. Jiménez-Galán, D. Kroon, E. W. Larsen, M. Louisy, S. Bengtsson, M. Miranda, J. Mauritsson, C. L. Arnold, S. E.Canton, M. Gisselbrecht, T. Carette, J. M. Dahlström, E. Lindroth, A. Maquet, L. Argenti, F. Martín, A. L'Huillier. *Submitted* (arXiv:1505.02024).

8. **Watching the birth of an electron wavepacket generated by resonant photo-ionization**. V. Gruson, L. Barreau, A. Jiménez-Galán, F. Risoud, J. Caillat, A. Maquet, B. Carré, F. Lepetit, J. F. Hergott, T. Ruchon, L. Argenti, R. Taïeb, F.Martín, P. Salières. *In preparation*.

9. **Photoemission time delay in two-photon resonant transitions**. A. Jiménez-Galán, L. Argenti, R. Taïeb, A. Maquet, F.Martín. *In preparation*.

10. **On the angular dependence of the photoemission time delay in helium**. I. A. Ivanov, J. M. Dahlström, E. Lindroth, A. Jiménez-Galán, L. Argenti, F.Martín, A .S. Kheifets. *In preparation*.

AGRADECIMIENTOS / ACKNOWLEDGEMENTS

There are times when you know you have landed in the right place, at the right time and with the right person. Luca, all of this work would never have been possible without your passion, support, enthusiasm and knowledge. Thank you for building me up from scratch, for your patience, for being always accessible and kind, and, most of all, thank you for showing me to love this. The devotion and enthusiasm you transmit has been the backbone of this work.

Quiero agradecer especialmente al jefe, a Fernando, por haber depositado su confianza en mí desde el primer momento y por haberme dado la oportunidad de trabajar en este maravilloso grupo y en este proyecto. La claridad en sus explicaciones y sus ideas han sido una enorme inspiración para mi.

I want to thank all the wonderful people I met at my stay in Paris. In particular, Alfred Maquet, Richard Taïeb and Jeremie Caillat for their kind hospitality and for giving me the chance to share my work with them. The friendly and innovative atmosphere at UPMC made me feel very welcome and made my stay really enjoyable.

I want to thank our experimental collaborators. In particular: Sebastian Heuser, Claudio Cirelli, Ursula Keller and the group at ETH Zurich, Marija Kotur, Anne L'Huillier and the whole group in Lund, and Vincent Gruson, Lou Barreau, Pascal Salières and the atto group at CEA Saclay. It was a real pleasure to work with all of you, and I hope these collaborations are just the beginning of many more to come!

A la gente del trabajo, por hacer que no sea sólo un trabajo. Al muchacho, por estar ahí delante, por todos esos cafés que se pagan solos, porque nos podemos permitir ir a comer al sitio bueno...en fin, por lo que ha habido y lo que habrá. Lara, gracias por tu apoyo, por estar siempre dispuesta a ayudar y por tus consejos (sobre todo el de Fausto, el más valioso). Gracias a la gente de la tercera planta ¡y al polaco en la sexta! Gracias a toda la gente que ha pasado por el departamento, desde que llegué hasta hoy, por haberme ayudado en todo lo que he necesitado.

A la gente de físicas. Luis (primero, y no creo que nadie proteste), Javi, Yuste, Sara, Cuerpo, Robert, Gema, Emiliano, Manuela, Yago...y muchos más. Gracias por hacer de la carrera una experiencia inolvidable.

A Oriana. Por todos los momentos contigo. Por tu infinita paciencia. Gracias por estar en los momentos más duros con el apoyo más grande. Gracias por hacerme feliz.

Por último, a mis padres. Porque siempre están ahí. Por haberme apoyado en todas mis decisiones. Por haberme ayudado a crecer.

CONTENTS

ACRONYMS

APT Attosecond Pulse Train

ATAS Attosecond Transient Absorption Spectroscopy

CAP Complex Absorption Potential

CEP Carrier Envelope Phase

COLTRIMS Cold-Target-Recoil-Momentum-Spectroscopy

DES Doubly Excited States

ECS Exterior Complex Scaling

EWP Electron wave packet

FEL Free Electron Laser

FROG Frequency Resolved Optical Gating

FT Fourier Transform

FWHM Full Width at Half Maximum

HHG High Harmonic Generation

IP Ionization Potential

IR Infra-red

LC Localized Channel

LOPT Lowest Order Perturbation Theory

PWC Partial Wave Channel

RABITT Reconstruction of Attosecond Beating by Interference of Two-photon Transitions

SAE Single Active Electron

SAP Single Attosecond Pulse

SFA Strong Field Approximation

SPA Soft Photon Approximation

TDSE Time Dependent Schrödinger Equation

TOF Time Of Flight

VIS Visible

VMI Velocity Map Imaging

XUV Extreme-ultraviolet

Part I

INTRODUCTION

1

INTRODUCTION

Electron dynamics is a process of fundamental importance in nature. It forms the basis of the molecular bonds and is responsible for changes in the chemical composition and function of biological systems. To understand how electronic processes unfold, is to understand the foundations of chemistry. This is why control and time-resolved imaging of electron dynamics in atoms and molecules has become a central focus in today's science. The multidisciplinary character of this topic is shown in a large number of existing applications to physics, chemistry and biology [1, 2]. Yet, how is monitoring and controlling of electrons possible? A simple calculation shows that the characteristic beating period of the ground state (1s) and first excited state (2p) of hydrogen is $T = 2\pi/\omega_{2p-1s} = 24$ attoseconds. Seven attoseconds are to one second what one second is to the age of the Earth. In our time scale, it is impossible to have a deep knowledge of how electrons move, they are just too fast. We still can affect the electron motion by perturbing it at uncontrolled stages of its evolution. In this case, we will be able to see a final effect induced by such incoherent perturbation, but we will be unable to monitor or alter any given intermediate passage selectively. It is the information in these intermediate steps that has only recently started to be revealed with the advent of attosecond physics [3]. A deep knowledge of these dynamics will be essential to achieve control over electrons in atoms, molecules and nanodevices.

Ever since its theoretical explanation in 1905 [4], the photoelectric effect has been a major tool to study the structure and properties of atoms and molecules. Ordinary spectroscopic techniques in the stationary regime have been able to provide many information on electron dynamics interacting with light at an unprecedented level of detail thanks to high resolution x-ray sources [5] used in conjunction with advanced photofragment detection techniques such as velocity map imaging (VMI) [6] , COLTRIMS [7], time of flight detectors (TOF) [8] or magnetic bottle coincidence spectrometers [9]. Part of the electron dynamics can be understood with single particle approximation methods. However, a lot is governed by electron correlation, which occurs in the timescale of attoseconds. One of the most dramatic evidence of such correlation is autoionization, the process in which electron interaction leads to the spontaneous emission of one electron from a transiently bound state.

Autoionizing states have been the subject of extensive investigation since Madden and Codling reported the asymmetric profile of helium doubly excited states in the first energy-resolved x-ray photoabsorpion spectrum recorded using synchrotron radiation, a pioneering experiment which signed the birth of modern photoelectron spectroscopy [10]. Synchrotron radiation gave access to the study of one-electron processes with exquisite detail; the width and energy of several

autoionizing states have been firmly established. Due to the characteristic properties of synchrotron radiation (incoherent highly monochromatized pulses with a duration of several picoseconds), the majority of available studies involving doubly excited states are based on one-photon stationary processes.

Despite all their value, however, methods that rely solely on one-photon absorption processes, cannot give a complete picture of the electron dynamics initiated by light. This is because the full quantum mechanical information of a particle's dynamics is encoded in the complex coefficients of all the states that are populated, i.e., in their absolute value as well as in their relative phase, while the energy distribution of the photo-fragments measured in traditional photoelectron spectroscopies are insensitive to the relative phase of transition amplitudes to states with different final energies; hence, any information on coherent dynamics is lost. To recover this information, therefore, it is necessary to go beyond the absorption of a single photon and consider multiphoton or even non-perturbative processes instead. With the advent of the highly intense laser technology [11, 12], some authors addressed the problem of multiphoton transitions involving autoionizing states when in the presence of such strong laser fields [13]. These studies, however, are mostly based on formalisms appropriate to long and/or incoherent laser fields. To extract any meaningful information on the phases of the system, the spectral and phase properties of the electromagnetic radiation used to induce the radiative transitions need to be fully characterized to start with. In addition, these multiphoton transitions must occur on a time scale comparable to that of the electronic movement they are meant to highlight. All of these requisites are realized by novel attosecond pump-probe techniques [3].

1.1 OVERVIEW OF ATTOSECOND PHYSICS

Electromagnetic pulses with the aforementioned characteristics have become accessible with the advent of mode-locked pulsed lasers like Ti:Sapphire [14]. These lasers are able to produce coherent light pulses at intensities of the order of $I = 10^{16}$ W/cm^2. When an atom or molecule interacts with electromagnetic fields that reach intensities comparable to the Coulomb force that binds the electron in the atom ($I \approx 1\text{a.u.} = 3.509 \cdot 10^{16}\text{W/cm}^2$), a series of short and energetic electromagnetic pulses are created, the so-called attosecond pulse train (APT). This process is known as high harmonic generation (HHG) [15], and it can be described classically with the three-step model (see Fig. 1) [16]. In the HHG process, the generated pulses are separated by half the period of the electromagnetic field, thus forming a train of pulses, each with a duration that is a small fraction of the field period. Due to the even spacing and alternating sign of the pulses in the train, only odd harmonics of the initial electromagnetic frequency are created. The intensity of the high harmonic spectrum reaches a plateau up to a maximum energy of $E = 3.17U_p + I_p$, where U_p is the ponderomotive energy of the field and I_P is the ionization potential of the atom or molecule. After the plateau, the spectrum drops off exponentially.

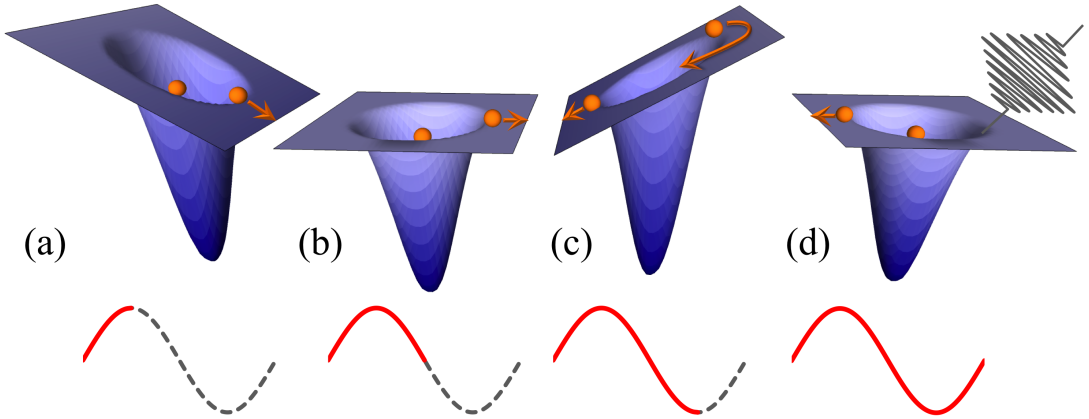

Figure 1: The three step model. (a) In the first step, the intense electromagnetic field distorts the Coulomb attractive potential, creating a barrier through which the electron can tunnel to the continuum. (b) In the second step, the free electron is driven apart from the ion by the external field; (c) as the field changes sign, the electron can invert its trajectory and be driven back to the ion, gaining a large kinetic energy. (d) Lastly, the electron recollides with the initial parent ion, liberating the acquired energy in the form of a short electromagnetic pulse. This process is repeated every half period of the field, so that a coherent series of pulses are created.

The access to infrared pulsed lasers with intensities on focus as high as 10^{15} W/cm^2 and a duration of 5 to 30 fs [17] permitted to generate short trains or even isolated extreme-ultraviolet (XUV) pulses with a duration of the order of 100 as [18, 19]. Such characteristics make HHG an ideal candidate to study electronic excitation and ionization in atoms and molecules (XUV range) at their intrinsic timesecale (attoseconds). This is generally done with pump-probe techniques, in which both the generating infra-red (IR) laser and the XUV pulse (or pulse train) are used in conjunction. In these techniques, after the generation process, the XUV field is separated from the IR laser field, while a replica of the latter travels through an alternative optical path with a controllable time delay with respect to the path followed by the high harmonic light. In this way, it is possible to subsequently collimate the XUV and the IR pulses with any desired time delay within an accuracy of few attoseconds (see Fig. 2).

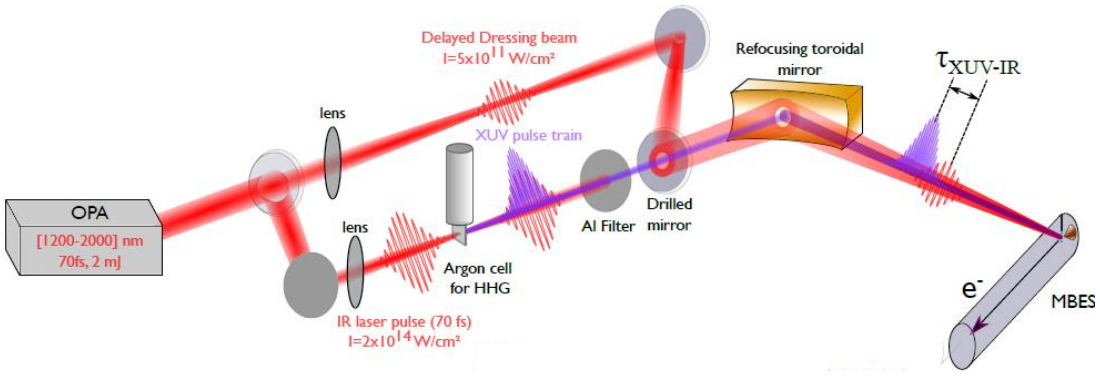

Figure 2: Experimental setup for a typical pump-probe scheme. The output from an optical parametric amplifier (OPA) providing tunable mid-IR pulses is split into two beams: the most intense beam is focused in an argon gas cell to produce a comb of mutually coherent high harmonics, and is then filtered out with an Al foil. The mid-IR weak beam enters a delay line with piezoelectric translation (not shown) and is then recombined with the harmonic beam using a drilled mirror. Both beams are refocused using a toroidal mirror into a jet of the target atoms placed in the source volume of a magnetic bottle electron spectrometer. The photoelectron time of flight, reflecting the energy spectrum, is measured as a function of the delay between the harmonic and mid-IR dressing fields. Credits for this figure: Vincent Gruson.

High harmonic generation is not an easily reproducible process. In particular, it is not granted that the high harmonics generated in the recollision combine to form an APT. For this to occur, the individual harmonics of the pulses must be in phase at some point in space and time (see Fig. 3), and this circumstance cannot be ascertained by looking at the one-photon ionization spectrum alone, which only provides a measure of the intensity of the harmonics. Even if by virtue of the recollision mechanism, the harmonics are initially generated in phase, when the radiation passes through the filter in order to cut the lower frequency components and isolate the XUV frequency, the harmonics can lose their synchronization. To characterize the coherent pulse-train nature of the radiation, techniques such as frequency resolved optical gating (FROG) [20] and reconstruction of attosecond beating by interference of two photon transitions (RABITT) [21, 22] were proposed. This latter technique proved useful not only to characterize high harmonic radiation, but also to study the electron dynamics. In the past years, attention has shifted from the creation of novel ways to obtain and characterize attosecond pulses towards the use of these pulses to monitor and control electron dynamics, following the path of what was done with reaction dynamics in molecules with femtosecond lasers [23, 24, 25].

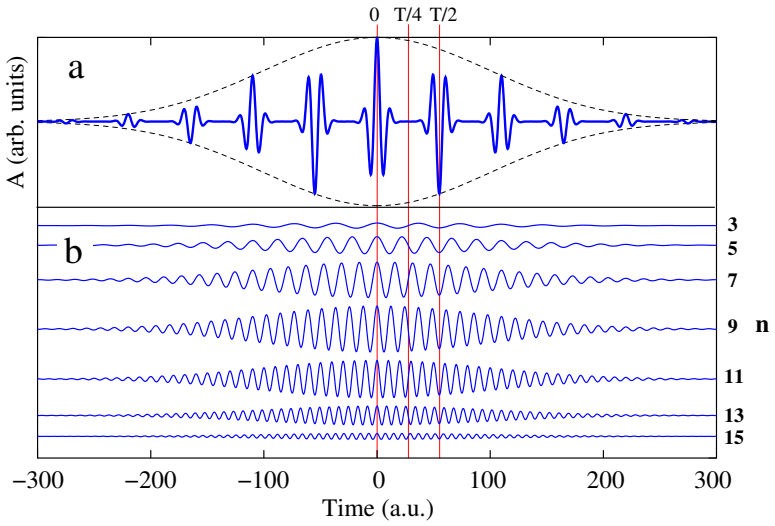

Figure 3: Schematic representation of an APT (a) and of its harmonic composition (b).

1.2 ATTOSECOND PULSE METROLOGY

Several techniques have been proposed so far for the study of electron dynamics. In the following we highlight the most relevant ones, with a particular emphasis on the RABITT technique, which forms the basis of the interferometric photoelectron techniques we devised in this thesis to investigate the ultrafast response of correlated electron dynamics to external pulses. We can make a distinction between those techniques whose observable is the matter fragments and those whose observable is the transmitted radiation.

1.2.1 *Measuring the photoelectron spectrum*

ATTOSECOND PULSE TRAINS. THE RABITT TECHNIQUE. In RABITT spectroscopy a target atom or molecule is ionized by an APT, acting as a pump, in association with a weak long IR probe pulse, with a controllable time delay τ between APT and probe. The spectrum of the APT is formed by odd harmonics ω_{2n+1} of the fundamental IR frequency, $\omega_{2n+1} = (2n+1)\omega_{\mathrm{IR}}$, while the IR probe is a weak replica of the IR pulse used to generate the train. When the APT pump and the IR probe overlap, therefore, the target can either absorb one XUV photon from harmonic $2n-1$ plus one IR photon, or absorb one XUV photon from harmonic $2n+1$ and emit, in a stimulated way, one IR photon. These two processes interfere, giving rise to a sideband photoelectron signal SB_{2n} which, in stationary conditions, oscillates as a function of the time delay as $I_{\mathrm{SB}_{2n}} = I_0 \cos(2\omega_{\mathrm{IR}}\tau + \Delta\phi_{\mathrm{H}} + \Delta\varphi_{\mathrm{at}})$ [26], where $\Delta\phi_{\mathrm{H}}$ is the phase difference between two consecutive harmonics in the APT spectrum, while $\Delta\varphi_{\mathrm{at}}$, the so-called atomic phase, is the relative argument of the two-photon transition matrix elements for the IR absorption and the IR emission quantum paths. In Fig. 4 we show the principle of the measurement and the resulting photoelectron spectrum.

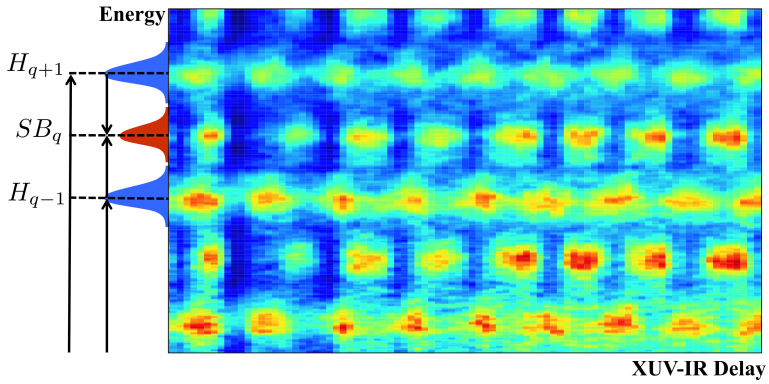

Figure 4: The RABITT principle. An XUV APT ionizes the target and populates a coherent superposition of continuum states ($H_{q-1}, H_{q+1}, \ldots$)centered at odd multiples of the IR frequency ω_{IR} used to generate the APT. In presence of a weak replica of the IR pulse, a further exchange of one IR photon occurs, thus populating states ($SB_{q-2}, SB_q, \ldots$)at even multiples of the IR frequency. Different paths lead to the same sideband energy and their interference is reflected in the photoelectron spectrum as characteristic oscillations with respect to the XUV APT pump-IR probe time delay, with periodicity $2\omega_{\mathrm{IR}}$.

If $\Delta\varphi_{\mathrm{at}}$ is a known slowly varying function of photoelectron energy, from the beating of the RABITT sidebands one can recover the relative phase between the harmonics in the train. Use of the RABITT technique with this approach has been instrumental to demonstrate that the harmonics from HHG [27] came in the form of trains of pulses [21], to understand the generation of attosecond light bursts [28] and to develop phase-compensation techniques that minimize the duration of individual pulses within the train [29, 30]. Conversely, if the harmonic phases are known, from the sideband beatings it is possible to reconstruct the atomic phases [31]. This latter approach permits one to measure both phase and amplitude of the dipole transition matrix element from the ground to the intermediate continuum states and, in turn, to reconstruct the dynamics of the pho-

toemission event. This procedure has been followed, for example, to determine the relative delay between photoemission from the $3s$ and the $3p$ sub-shells of argon [32, 33], the phase difference between photoemission from the outermost s shell in different rare gases [34, 35], the energy-sharing resolved double ionization of Xenon [36], and the nuclear dynamics in H_2 [37]. Therefore, the RABITT technique lends itself naturally to the study of radiative transitions within the ionization continuum which are not easily accessible with standard stationary photoelectron spectroscopies.

SINGLE ATTOSECOND PULSES. THE STREAKING TECHNIQUE. With the most recent experimental advances in laser technology, it is now possible to generate isolated single attosecond pulses (SAP) [19, 18, 38]. SAP provide access to a method to study atomic and/or molecular ionization dynamics called *streaking*, which consists in the photoionization of atoms or molecules by a single attosecond pulse in the presence of an intense IR field. As opposed to the perturbative regime in which RABITT works, streaking techniques are in the so-called strong field regime. Interpretation of the results now comes from a purely classical picture, or from non-perturbative quantum models such as the strong field or soft photon approximations. The idea of the technique is the following: a single attosecond XUV pulse ionizes the sample, populating a wide energy spectrum. When the IR is present, the photoelectrons will receive a momentum shear proportional to the vector field of the IR, according to the classical formula $\Delta\vec{p} = -\alpha\vec{A}_{IR}(t)$. Depending on the time delay between the two pulses, the momentum shift will have different values. In this way, one can achieve control over photoelectron ejection processes [39, 40].

XUV-PUMP XUV-PROBE SCHEME. Recently, XUV-pump XUV-probe schemes have also been proposed [41]. Such schemes are particularly indicated for molecular interferometry since the lower intensity and shorter wavelength of the XUV as compared to the IR pulses used in the previous techniques, ensures that the ponderomotive energy is negligible in comparison with the electron-electron and electron-nucleus interactions, and thus effects due to the perturbation of the molecular potential by the probing field are eliminated. Also, the duration of the XUV pulses are generally much shorter than that of the IR pulses, which translates into a much higher temporal resolution, in detriment of spectral resolution, though. The major drawback of this technique comes from the experimental side, since generating and controlling two coherent attosecond XUV pulses still represents a very hard task.

1.2.2 *Measuring the transmitted light*

An approach complementary to the ones considered so far, where the only observable is the distribution of the photofragments at the end of the ionization event, is to monitor the change in the state of the light transmitted through the sample. Two major experimental techniques based on this idea have acquired

considerable importance in attosecond time-resolved studies: high harmonic generation spectroscopy and attosecond transient absorption spectroscopy.

HIGH HARMONIC SPECTROSCOPY. The HHG process described in the previous section is at the basis of the generation of attosecond pulses, but its application is not restricted to this. Indeed, the coherent high harmonic spectrum generated contains information on the nonlinear response of the target atom or molecule, which can be extracted [42, 43, 44, 45]. Theoretical description of the three-step process generally comes from single active electron pictures, where the ionization is described as a pure one-electron process in which all the remaining electrons act as frozen spectators, although the effects of ionizing from and recombination to different orbitals has also been studied [46, 47].

ATTOSECOND TRANSIENT ABSORPTION SPECTROSCOPY. In contrast to HHG, attosecond transient absorption spectroscopy (ATAS) is based on the assumption that only pre-existing XUV light can be altered by means of stimulated emission/absorption induced by the interaction with a dressing field. Therefore, ATAS manifests itself already in perturbative conditions. This technique is a combination of the novel attosecond technology and the method of transient absorption spectroscopy, widely used in time-resolved molecular dynamics [48, 49]. ATAS has been used, for example, to observe the motion of valence electrons in Krypton ions [50] or to reconstruct the two-electron wave packet in helium [51].

1.3 MONITOR AND CONTROL OF ELECTRON DYNAMICS

So far, most of the investigations on continuum-continuum transitions have concentrated on energy regions where metastable states did not appear. However, transiently bound states are an important aspect of ionization dynamics and their influence on two-photon transitions is still widely unexplored. Indeed, while in stationary conditions, one-photon resonant transitions are well-accounted for by Fano's model of autoionization [52], which has found enormous number of applications in fields that range from atomic to condensed-matter physics [10, 53], a theoretical framework for time-resolved resonant multi-photon transitions, required by modern attosecond techniques, is still missing. In fact, how an autoionizing state evolves in time is a task particularly suited for pump-probe techniques, since its evolution is mapped in a timescale smaller than its lifetime. The reconstruction of an autoionizing wave packet is a challenging goal of current time-resolved attosecond spectroscopy. Theory has predicted the feasibility of observing the evolution of a Fano resonance in the time domain with the attosecond streaking technique[54, 55]. This method led to the direct determination of the lifetime of the sp_2^+ autoionizing state in helium [40]. Still, the presence of the strong IR field makes the photoelectron spectra very complicated [54], and can even drastically affect the spectral lineshapes [56]. Almost all studies have concentrated on these distortions and couplings between autoionizing states [51],

and a direct measurement of the unperturbed autoionizing EWP still remains unreported.

Linked to the phase of photoionization transition amplitudes, is an important aspect that so far can only be studied with time resolved spectroscopy: photo-ejection time delays, i.e., the time it takes an electron to be ejected from a given localized state of the atom after absorbing a photon [57]. Photo-ejection time delay has gained much prominence lately due to its connection with electronic correlation. Schultze *et al.* conducted an attosecond streaking pump-probe experiment in which they measured the difference in the ejection time delay between the $2s$ and $2p$ shells of neon, finding that when the electron is released from the latter, the process takes 20 as longer [58]. Part of this delay is associated to the effective potentials the electron feels, and can be accounted for already in the independent particle approximation. Part is induced by the measurement itself, which uses a strong infrared field that perturbs the electron dynamics. Even when these effects are taken into account, though, a considerable residual delay remains. One possible cause of the time delay not explained by the single particle approximation is the relaxation process that the non-ejected electrons undergo when one of the electrons is removed. This relaxation consists on a fast rearrangement of the electrons in the atom (normally of the order of few tens of attoseconds) [59]. When the ejection of the photoelectron takes place on a timescale comparable to the relaxation time, the two processes can influence each other: in figurative terms, the rearranging electrons *kick out* the photoelectron. This dynamical correlation can be measured as a time delay in the photoelectron emission. The angular dependence of photo-ejection time delays or the influence of autoionizing states on the atomic phases of continuum-continuum transitions still remains unexplored. Furthermore, occasional discrepancies between existing experimental data and state-of-the-art theories for poly-electronic atoms [60, 33, 61] indicate that deeper investigation of smaller systems is still required to shed light on the influence of electronic correlation in transitions in the continuum. In fact, a few works in these directions have already made their appearance in the literature [62, 63, 64].

Information on all of the above can be provided by pump-probe schemes that use weak IR fields as a tool for monitoring the electron dynamics, such as RABITT . In addition, streaking, HHG or ATAS permit to control the electronic dynamics by varying the intensity of the IR field, from a weak- to a strong-field regime. Recently, several authors have addressed the problem of the control of the dynamics of autoionizing states [56, 51, 65]. Yet, the full description of such highly correlated states presents a challenge to theory and, thus, many aspects of this promising field are still to be investigated.

1.4 MOTIVATION AND OUTLINE OF THE THESIS

This thesis is aimed at explaining the coherent and time-resolved correlated electron dynamics in atoms that are triggered, monitored and controlled with modern attosecond laser technologies. In particular, we propose the validity of two attosecond techniques previously described, RABITT and ATAS, to analyze the

role of autoionizing states in multi-photon transitions in the continuum. We do so in two ways: with *ab initio* calculations that come out from the exact numerical solution of the Time Dependent Schrödinger Equation [66], and with simplified models.

To isolate the background single-particle effects from those with many-body character, we extended the soft photon model [67], which is based on a single particle approximation, to treat realistic pulses both for streaking and RABITT techniques. With this tool, we studied in detail several effects of these techniques that could possibly lead to unexpected results, such as the pulse duration or the intensity of the fields. In this way, when the model is compared to the full ab-initio result or experimental spectrum, we can fully isolate the effects due uniquely to electronic correlation.

We then propose the RABITT technique as a valid candidate to give insight on the role of autoionizing states in continuum-continuum transitions by extracting information from the sideband phases in the photoelectron spectrum. We develop a resonant two-photon model that permits us to quantitatively reproduce and understand recent experimental observations in RABITT experiments. In this way, we are able to give theoretical support to two important experiments: one, performed by the group of Anne L'Huillier, which demonstrates the distortion of the continuum phase induced by an autoionizing state embedded in a multichannel continuum, and another, performed by the group of Pascal Salières, which is able to reconstruct the "unperturbed" metastable electronic wave packet, i.e., with a negligible influence of the IR probing field.

With the full solution of the TDSE for helium, we investigate the angular dependence on the photoemission time delay from isotropic systems. In collaboration with the experimental group lead by Ursula Keller, we demonstrate and interpret a measurable difference in the delay of electrons ejected at different angles with respect to the polarization axis of the impinging light.

Motivated by the work in [56, 51], we use ATAS for the study of the effects of laser intensity on the profiles and phases of the doubly-excited sp_n^+ series of helium. We theoretically demonstrate that, as the intensity is increased, the Fano profile undergoes several inversions and the AC-Stark shift exceeds by more than twice the theoretical SAE limit. In the same context, we shed light on a current discrepancy between the theoretical predictions [51] and the observations of the experiment in [68], which measured a depletion of the population of the DES in helium above $I = 4$ TW/cm^2, not present in the theoretical simulations. With the use of the *ab initio* solution of the TDSE, we explore the photoionization process from DES in helium, investigating the tunneling probability from the innermost orbital of the DES and showing that the AC-Stark shifts of DES vary across final ionization channels and series.

This thesis is structured as follows. In Chapter 2, we give an overview of the radiation-matter interaction. We introduce the minimal coupling Hamiltonian and give the formal solutions of the TDSE, with particular emphasis on the perturbative expansion. Chapter 3 focuses on the field-free Hamiltonian. Since we

will particularize the study to multiphoton single-ionization processes, we introduce the close-coupling *ansatz*, on which the *ab initio* code we used is based. We will describe the main spectroscopic features of the helium atom, which stands as a perfect candidate for correlation studies and was thus chosen as the main target of this thesis. In Chapter 4, we discuss the three different theoretical approaches used throughout this thesis: the *ab initio* close-coupling full solution of the TDSE for the helium atom [66], the finite-pulse soft photon approximation [69], and a novel lowest order perturbative resonant model [70]. In Chapter 5, we apply the theoretical methods outlined in Chapter 4 to study, in real systems, the effects of resonances and correlation on electron dynamics in the continuum, within the RABITT pump-probe scheme. Making use of the *ab initio* method for helium, in Chapter 6 we investigate the effects of the dressing laser intensity on the dynamics of doubly excited states. Finally, in Chapter 7 we draw conclusions and future prospects of this work.

Part II

THEORETICAL METHODS

2

RADIATION-MATTER INTERACTION

Throughout this thesis, we will be interested in the processes triggered by the interaction between an atom and a coherent external pulse of electromagnetic radiation, such as those observed by attosecond table-top laser setups or seeded free electron laser (FEL) facilities. We will focus in particular on processes that liberate one electron in the continuum (single ionization), leaving behind a parent ion, possibly in an excited state. Modern detection apparatus such as magnetic bottles [9], velocity-map imaging detectors [6] and reaction microscopes [7] are able to record with high accuracy the asymptotic energy and angular distribution of the photoelectron. Furthermore, as the atom responds to the external field, it develops a dipole moment that acts as a source in the equation of motion of the external field thus progressively altering the spectrum of the impinging radiation as it propagates through the sample. In this way, the variation of the spectrum of the impinging light also encodes information on the electronic processes that unfolds in the atom, and complements the one obtained from photoelectron distributions. Today, high resolution spectrometers can be used to record such variation [51].

To replicate theoretically these processes, we need a description of both the initial bound and final single-ionization scattering states of the field-free atom, as well as an expression for the radiation-matter interaction Hamiltonian and for the macroscopic propagation of light through the sample. To describe the interaction between matter and radiation we will take a semiclassical approach, in which the electromagnetic field is treated classically while the atom-laser interaction is quantized [1]. For sufficiently weak fields, the interaction between atom and laser can nevertheless be expressed in terms of the exchange of a finite number of energy quanta. Even in absence of the explicit quantization of the field, therefore, we can consider one-, two-, and multiple-photon processes.

We shall consider the process in which n photons γ of, in principle, different frequencies ω_n interact with an atom $\mathrm{A}(g)$ in the initial ground state $|g\rangle$ with energy E_g, to produce an electron of energy ε and an ion $\mathrm{A}^+(f)$ in state $|f\rangle$ with final total energy E_f. This process is known as single ionization and can be written as the reaction

$$\sum_n \nu_n \gamma_n + \mathrm{A}(g) \to \mathrm{A}^+(f) + e^-, \quad \nu_n \in \mathcal{Z}. \tag{2.1}$$

1 This is not justified in the case of spontaneous emission, but the characteristic timescale of these processes is much larger than those we are interested in, and they lie beyond the scope of this work.

Neglecting the recoil effects of the parent ion, from energy conservation we have

$$\sum_n \nu_n \omega_n + E_g = \varepsilon + E_f. \tag{2.2}$$

In the so-called low frequency regime ($\omega < 1$ keV), the processes described above accounts for nearly all the processes associated to single photoionization, which is the objective of the present work. In this regime, the most relevant observables are the total photoabsorption cross section and the photoionization cross section. The effects of the laser-matter interaction process can thus be observed by looking at either the ejected photoelectron or the absorbed light using photoionization or transient absorption experiments, respectively. We will explore both of these techniques in this work.

2.1 CLASSICAL DESCRIPTION OF A LASER FIELD

Classically, the external electric $\vec{\mathcal{E}}$ and magnetic fields $\vec{\mathcal{B}}$ are well-defined functions of space and time that can be written in terms of the external vector and scalar potentials $\vec{A}$ and Φ as [71]

$$\vec{\mathcal{E}} = -\nabla\Phi - \frac{1}{c}\frac{\partial \vec{A}}{\partial t}, \qquad \vec{\mathcal{B}} = \vec{\nabla} \times \vec{A}. \tag{2.3}$$

The potentials Φ and $\vec{A}$ are not uniquely defined, since the gauge transformation

$$\vec{A} \to \vec{A}' = \vec{A} + \vec{\nabla} f, \qquad \phi \to \phi' = \phi - \frac{\partial f}{\partial t}, \tag{2.4}$$

leaves the fields $\vec{\mathcal{E}}$ and $\vec{\mathcal{B}}$ unchanged. We will exploit this arbitrariness in the following by adopting the Coulomb gauge, which is defined by the condition

$$\vec{\nabla} \cdot \vec{A} = 0, \quad \Phi = 0. \tag{2.5}$$

A pulse of plane-wave radiation can be represented by a superposition of monochromatic plane waves around a certain frequency, ω_0, each with the same direction of propagation $\hat{k}$ and polarization $\hat{\epsilon}$,

$$\vec{A}(\vec{r}, t) = \int A_0(\omega)\hat{\epsilon}\cos(\vec{k}\cdot\vec{r} - \omega t + \delta_\omega)d\omega, \tag{2.6}$$

where $A_0(\omega)$ is the peak value of the vector potential of the field, δ_ω represents a real phase. In this thesis, we will consider linear polarizations only, $\hat{\epsilon} = \hat{z}$.

2.1.1 *The minimal coupling Hamiltonian*

The classical interaction between a particle with charge q moving with velocity $\vec{v}$ and an electromagnetic field is described by the Lorentz force, $\vec{F} = q\left(\vec{\mathcal{E}} + \frac{\vec{v}}{c} \times \vec{\mathcal{B}}\right)$, which stems from the minimal coupling Hamiltonian [72]

$$H_{mc} = \frac{1}{2m}\left[\vec{p} - \frac{q}{c}\vec{A}(\vec{r}, t)\right]^2, \tag{2.7}$$

where c is the speed of light, $\vec{p}$ is the canonical momentum of the particle and m its mass. Let us consider the particle to be an electron, for which $q = -1$ and $m = 1$. By replacing $\vec{p}$ with its quantized counterpart, $\vec{p} \to \hat{\vec{p}} = -i\vec{\nabla}$, we arrive to the semiclassical equivalent of Equation (2.7)

$$H_{mc} = \frac{p^2}{2} + \alpha\, \vec{A}(\vec{r}, t) \cdot \vec{p} + \frac{\alpha^2}{2} A^2(\vec{r}, t), \tag{2.8}$$

where we introduced the fine-structure constant $\alpha = 1/c \simeq 1/137$. The motion of the electron in this case is dictated by the time-dependent Schrödinger equation (TDSE):

$$i\partial_t \Psi(\vec{r}, t) = H_{mc} \Psi(\vec{r}, t). \tag{2.9}$$

The generalization to the interaction of an electromagnetic field with an N-electron atom is straightforward. The Hamiltonian in this case is composed of a field-free (atomic) and an interaction term,

$$H = H_a + H_{int}. \tag{2.10}$$

Let us focus on the interaction Hamiltonian, which for an N-electron system reads

$$H_{int} = \alpha \sum_{i=1}^{N} \vec{A}(\vec{r}_i, t) \cdot \vec{p}_i + \frac{\alpha^2}{2} \sum_{i=1}^{N} A^2(\vec{r}_i, t). \tag{2.11}$$

When the wavelength of the radiation is much larger than the distance over which the interaction with the atom takes place, it is common to use the *dipole approximation*, in which the spatial dependence of the vector potential $\vec{A}$ [see Equation (2.6)] is neglected, i.e., $\vec{A}$ is assumed to be uniform across all space. This is our case, since the wavelengths we will be considering are typically of several hundreds of atomic units, while the characteristic size of an atom is of the order of 1 a.u. Under such assumption, the interaction Hamiltonian takes a particularly simple form,

$$H_{int} = \alpha\, A(t) \cdot \vec{P} + \alpha^2 \frac{N}{2} A^2(t), \tag{2.12}$$

where $\vec{P} = \sum_{i=1}^{N} \vec{p}_i$. We can obtain equivalent descriptions of the radiation-matter interaction by means of unitary transformations of the wave function: $|\Psi\rangle \to U|\Psi\rangle$, which satisfies the TDSE where the Hamiltonian is replaced by

$$H \to UHU^\dagger - iU\dot{U}^\dagger. \tag{2.13}$$

Since in the dipole approximation the A^2 term in the interaction Hamiltonian only depends on the time parameter, we can eliminate it by extracting from the wave function a time-dependent phase factor

$$\Psi^V(\vec{r}, t) = \exp\left[i\alpha^2 \frac{N}{2} \int_{-\infty}^{t} A^2(t')dt' \right] \Psi(\vec{r}, t), \tag{2.14}$$

which transforms the interaction Hamiltonian [Equation (2.12)] into the so-called *velocity* gauge

$$H_{int}^V(t) = \alpha\, \vec{A}(t) \cdot \vec{P}. \tag{2.15}$$

Similarly, the Göppert-Mayer unitary transformation

$$\Psi^L(\vec{r},t) = \exp\left[i\alpha\,\vec{A}(t)\cdot\vec{R}\right]\Psi(\vec{r},t), \tag{2.16}$$

where $\vec{R} = \sum_{i=1}^{N}\vec{r}_i$, leads to the interaction Hamiltonian in *length* gauge,

$$H_{int}^L = \alpha\,\vec{E}(t)\cdot\vec{R}. \tag{2.17}$$

We can connect the transition matrix elements of the interaction Hamiltonians in velocity and length gauges between eigenstates of H_a, $H_a\Psi_n = E_n\Psi_n$, by using the relation $[\,H_a,\hat{\vec{R}}\,] = -i\hat{\vec{P}}$:

$$\langle\Psi_m|\vec{P}|\Psi_n\rangle = i(E_n - E_m)\,\langle\Psi_m|\vec{R}|\Psi_n\rangle\,. \tag{2.18}$$

It is worth noticing that, when the length and velocity matrix elements are evaluated numerically, Equation (2.18) is only satisfied if the eigenstates that are used are sufficiently accurate. Conversely, the gauge invariance of the results of a calculation is a useful cross-check of the accuracy with which the eigenstate is represented.

2.2 FORMAL SOLUTIONS OF THE TIME-DEPENDENT SCHRÖDINGER EQUATION

2.2.1 *Dyson series*

Equations (2.10) and (2.11) give the explicit form of the Hamiltonian that describes an atom in an electromagnetic field. To obtain the time-evolution of the atom under the action of the external field, one must solve the time-dependent Schrödinger equation. In the interaction picture [73] and in integral form, this equation reads

$$\Psi_I(t) = \Psi_I(t_0) - i\int_{t_0}^{t} dt_1 H_{int}^I(t_1)\Psi_I(t_1), \tag{2.19}$$

where $\Psi(t_0)$ is an arbitrary state of the system, for example, the ground state. The connection to the Schrödinger picture is given by

$$\begin{aligned} |\Psi_I(t)\rangle &= e^{iH_at}|\Psi(t)\rangle, \\ H_{int}^I(t) &= e^{iH_at}\,H_{int}(t)\,e^{-iH_at}. \end{aligned} \tag{2.20}$$

It is convenient to cast Equation (2.19) in the form of the Dyson series,

$$\begin{aligned} |\Psi_I(t)\rangle &= \sum_{n=0}^{\infty} U^{(n)}(t,t_0)\,|\Psi_I(t_0)\rangle = U(t,t_0)\,|\Psi_I(t_0)\rangle\,, \\ U^{(n)} &= (-i)^n\int_{t_0}^{t} dt_1\int_{t_0}^{t_1} dt_2\cdots\int_{t_0}^{t_{n-1}} dt_n H_{int}^I(t_1)H_{int}^I(t_2)\cdots H_{int}^I(t_n). \end{aligned} \tag{2.21}$$

Equation (2.21) is at the basis of the perturbative expansion of the transition amplitude from an initial state $|i\rangle$ to a final state $|f\rangle$.

$$\mathcal{A}_{f\leftarrow i} = \mathcal{A}^{(0)}_{f\leftarrow i} + \mathcal{A}^{(1)}_{f\leftarrow i} + \mathcal{A}^{(2)}_{f\leftarrow i} + \cdots, \qquad \text{where} \qquad \mathcal{A}^{(n)}_{f\leftarrow i} = \langle f|U^{(n)}(t,t_0)|i\rangle. \tag{2.22}$$

The perturbative expressions [Equations (2.21) and (2.22)] can be interpreted in a simple way. At t_0, the system is evolving under the influence of the field-free Hamiltonian. At $t = t_n$, the atom interacts with the laser field, and then this new states evolves freely until the next time step, where it interacts again with the field, and so on. Overall, the atom interacts n times with the laser field. In the dipole approximation and in either length or velocity gauge, each of this laser-atom interactions can be interpreted as the absorption or stimulated emission of a photon by the atom. These processes are commonly represented by Feynman diagrams (see Fig. 5).

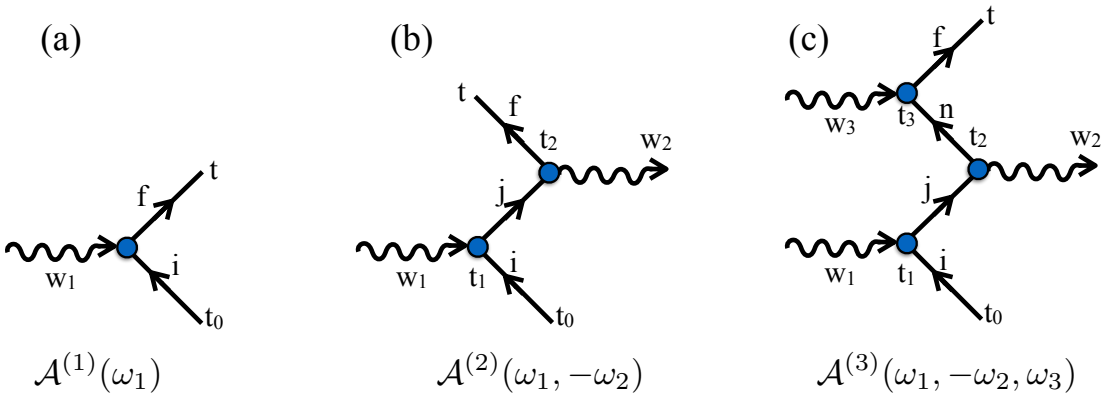

Figure 5: Feynman diagrams corresponding to one-, two- and three-order processes, respectively: (a) one photon absorption, (b) one photon absorption followed by one photon emission, (c) one photon absorption followed by one emission followed by one photon absorption.

The Dyson series can be expressed in compact form with the T-exponential operator,

$$U(t,t_0) = \hat{T}\exp\left[-i\int_{t_0}^{t} d\tau H^I_{int}(\tau)\right], \tag{2.23}$$

where $\hat{T}$ is the time ordering operator which ensures that the operators in the time integrals of the series expansion of the exponential act in chronological order since, in general, the operators $H^I_{int}(t_i)$ and $H^I_{int}(t_j)$ do not commute when $t_i \neq t_j$.

Except in the special case of a single free electron, for which H_a and H_{int} do commute, generally it is not possible to compute infinite terms of the Dyson series. For weak external potentials, however, the perturbative expansion converges rapidly and we may find a solution by truncating the series after a few terms. Notice that, when the Dyson series is truncated, the resulting propagator

$$\sum_{n=0}^{N} U^{(n)}(t,t_0), \quad N < \infty$$

is not unitary and, therefore, the norm of the wave function is not rigorously conserved.

The question arises as to whether a truncated version of the expansion in Equation (2.22) can adequately describe photoionization experiments. The answer depends on the intensity of the laser, its duration and the coupling strength between all the states involved. In attosecond pump-probe experiments, with the strong VIS and IR dressing pulses available today, the contribution of terms beyond lowest order may indeed become important [13, 74, 75, 55, 76, 65, 51, 77]. Rabi oscillations, for example, require the summation of the perturbative series to sufficiently high order to be reproduced across any given finite time interval. If both pump and probe ultrashort pulses are weak, however, the lowest-order approximation can be used to make accurate predictions. This is certainly the case, for example, of the RABITT technique, in which the probe intensity is deliberately kept small to permit a perturbative expansion. In this technique, the lowest perturbative transition amplitude $\mathcal{A}_{fg}^{(n)} = \langle f|\psi^{(n)}(\infty)\rangle$, from the initial ground state $|g\rangle$ to a final state $|f\rangle$, $H_a|f\rangle = |f\rangle E_f$, featuring both pump and probe contributions, appears at second order. Let us, therefore, derive the first two orders of the perturbative expansion. In dipole approximation, the interaction Hamiltonian $H_{int}^I(t)$ is given by the product of a time-dependent field-factor $\vec{F}(t) = F(t)\hat{z}$, and of a time-independent operator $\hat{\mathcal{O}} = \vec{\mathcal{O}} \cdot \hat{z} \equiv \mathcal{O}$,

$$H_{int}^I(t) = F(t)\, e^{i H_a t}\, \mathcal{O}\, e^{-i H_a t}. \tag{2.24}$$

For example, in velocity gauge $\vec{F}(t)$ is the vector potential $\vec{A}(t)$ and $\vec{\mathcal{O}}$ is proportional to the total canonical electron momentum [Equation (2.15)], while in length gauge $\vec{F}(t)$ is the light electric field and $\vec{\mathcal{O}}$ is minus the dipole moment of the system [Equation (2.17)].

2.2.2 *First order perturbation theory. Dipole selection rules*

The first order transition amplitude between two eigenstates of the field-free hamiltonian H_a, $|g\rangle$ and $|f\rangle$, is linear with the perturbation $H_{int}^I(t)$,

$$\mathcal{A}_{f\leftarrow g}^{(1)} = \frac{1}{i}\int_{t_0}^{t} \langle f|H_{int}^I(t_1)|g\rangle\, dt_1 = -i\mathcal{O}_{fg}\int_{-\infty}^{\infty} e^{iE_{fg}t_1} F(t_1)\, dt_1 \tag{2.25}$$

where $E_{fg} = E_f - E_g = \omega_{fg}$ and $\mathcal{O}_{fg} = \langle f|\mathcal{O}|g\rangle$. The amplitude $\mathcal{A}_{f\leftarrow g}^{(1)}$, therefore, is proportional to the Fourier transform of the field,

$$\mathcal{A}_{f\leftarrow g}^{(1)} = -i\sqrt{2\pi}\,\mathcal{O}_{fg}\tilde{F}(\omega_{fg}), \quad \text{where} \quad \tilde{F}(\omega) = \frac{1}{\sqrt{2\pi}}\int dt e^{i\omega t} F(t). \tag{2.26}$$

Thus, the transition probability for the first order perturbative expansion is given by

$$P_{f\leftarrow g}^{(1)} = 2\pi\,|\mathcal{O}_{fg}|^2\,|\tilde{F}(\omega_{fg})|^2. \tag{2.27}$$

DIPOLE SELECTION RULES. One-photon electric dipole (E1) matrix elements $\mathcal{O}_{fg}$ between states with well-defined angular momenta can be factorized, using the Wigner-Eckart theorem, in the product between a reduced transition matrix element that does not depend on any magnetic quantum numbers, and a Clebsch-Gordan coefficient,

$$\langle E_f L_f M_f | T_{L\mu} | E_g L_g M_g \rangle = C^{L_f\, M_f}_{L_g\, M_g,\, L\, \mu} \langle E_f L_f || T_L || E_g L_g \rangle \,, \tag{2.28}$$

where E represents the energy, L the orbital angular momentum, M the magnetic quantum number and $T_{L\mu}$ is the μ-th component of a spherical tensor of rank L [78]. Since the dipole operator in either length or velocity gauge is a spherical tensor of rank one, the properties of the Clebsch-Gordan coefficients [78] impose the following selection rules on the matrix element:

$$\Delta L = L_f - L_g = 0, \pm 1 \qquad \Delta M = 0, \pm 1, \tag{2.29}$$

which are known as the dipole selection rules. For linear polarization ($\lambda = 1$), along a common direction $\hat{z}$ (μ=0), and starting from a spherically symmetric system ($L_g = 0$), as it is usually the case, the problem preserves its cylindrical symmetry and the total z-projection of the angular momentum, M, will not change ($\Delta M = 0$). In these conditions, due to the symmetry $C^{c\,\gamma}_{a\,\alpha,\,b\beta} = (-1)^{a+b+c}\, C^{c\,-\gamma}_{a\,-\alpha,\,b\,-\beta}$ and hence $C^{c\,0}_{a\,0,\,b\,0} = 0$ if $a+b+c$ is an odd number, $\Delta L = 0$ transitions are prohibited.

2.2.3 *Second order perturbation theory: ac-Stark shift &* RABITT *technique*

Let us continue with the following term in the perturbative expansion. The second order expression reads

$$\mathcal{A}^{(2)}_{f\leftarrow g} = -\int_{-\infty}^{\infty} dt_1 \int_{-\infty}^{t_1} dt_2 e^{i\omega_f t_1} F(t_1) F(t_2) \, \langle f | \mathcal{O} e^{-iH_a(t_1-t_2)} \mathcal{O} | g \rangle \, e^{-i\omega_g t_2} \tag{2.30}$$

where we have taken $t_0 = -\infty$ and $t = \infty$ since we are in the interaction representation, where there are no temporal changes in the transition amplitude associated to the time propagation before the external pulse impinges on the system. Equation (2.30) has a well known equivalent frequency counterpart,

$$\mathcal{A}^{(2)}_{fg} = -i \int_{-\infty}^{\infty} d\omega \tilde{F}(\omega_{fg} - \omega) \tilde{F}(\omega) \mathcal{M}^{(2)}_{fg}(\omega), \tag{2.31}$$

where $\mathcal{M}^{(2)}_{fg}(\omega)$ is a two-photon transition matrix element,

$$\mathcal{M}^{(2)}_{fg}(\omega) = \langle f | \mathcal{O} G^{+}_{a}(\omega_g + \omega) \mathcal{O} | g \rangle. \tag{2.32}$$

In the above, we have introduced the important resolvent operator, defined as

$$G^{\pm}_{\alpha}(E) = \frac{1}{E - H_\alpha \pm i0^+}. \tag{2.33}$$

From equation (2.31), it is easy to derive the familiar formula for stationary transition rates [79]. To do so, let us suppose that the field comprises a set of overlapping square pulses $F_\alpha(t)$, with different frequencies ω_α and amplitudes $F_{\alpha,0}$, but all linearly polarized along the z axis and having the same duration T,

$$\begin{aligned} F(t) =& \sum_\alpha F_\alpha(t), \\ F_\alpha(t) =& F_{\alpha,0} \cos(\omega_\alpha t + \varphi_\alpha)\, \theta(T/2 - |t|). \end{aligned} \tag{2.34}$$

The FT of the individual pulses can be decomposed in the sum of an absorption $(+)$ and an emission $(-)$ component,

$$\tilde{F}_\alpha(\omega) = \tilde{F}^+_\alpha(\omega) + \tilde{F}^-_\alpha(\omega), \tag{2.35}$$

$$\tilde{F}^\pm_\alpha(\omega) = \sqrt{\frac{\pi}{2}}\, F_{\alpha,0}\, e^{\mp i\varphi_\alpha} \delta_T(\omega \mp \omega_\alpha), \tag{2.36}$$

where the function $\delta_T(\omega)$, proportional to the FT of the characteristic function of the $[-T/2, T/2]$ time interval,

$$\delta_T(\omega) = \frac{1}{\sqrt{2\pi}} \mathcal{F}\left[\theta(T/2 - |t|)\right](\omega) = \frac{\sin(\omega T/2)}{\pi\omega}, \tag{2.37}$$

is a representation of the Dirac delta function. When replacing expressions (2.34-2.37) in (2.31), there are a limited number of contributions for which the frequency components from the two convoluted field FT overlap and which thus need to be considered,

$$\begin{aligned} \mathcal{A}^{(2)}_{fi} =& \frac{\pi}{2i} \sum_{\alpha\sigma} F_{\alpha,0}\, e^{i\sigma\varphi_\alpha} \sum_{\beta\sigma'} F_{\beta,0}\, e^{i\sigma'\varphi_\beta} \;\times \\ \times& \int_{-\infty}^{\infty} d\omega\, \delta_T(\omega_{fi} + \sigma'\omega_\beta - \omega)\, \delta_T(\omega + \sigma\omega_\alpha)\, \mathcal{M}_{fi}(\omega), \end{aligned} \tag{2.38}$$

where $\sigma = \mp 1$ stands for photon absorption and emission, respectively. The last integral becomes negligible as soon as the energy-preserving condition is not satisfied, $|\omega_{fi} + \sigma\omega_\alpha + \sigma'\omega_\beta| \gg 1/T$. If the two-photon matrix element $\mathcal{M}_{fi}(\omega)$ is almost constant for $|\omega + \sigma\omega_\alpha| \leq 1/T$, then we can replace it with the constant term $\mathcal{M}_{fi}(-\sigma\omega_\alpha)$ and move it out of the integral. Using the convolution theorem, $\int \tilde{f}(x-\omega)\tilde{g}(\omega)d\omega = \sqrt{2\pi}\,\widetilde{fg}(x)$, together with Equation (2.37), the remaining integral can be evaluated as

$$\int d\omega\, \delta_T(\Delta - \omega)\, \delta_T(\omega) = \delta_T(\Delta). \tag{2.39}$$

The second order transition amplitudes, therefore, becomes

$$\begin{aligned} \mathcal{A}^{(2)}_{fi} \simeq& \frac{\pi}{2i} \sum_{\alpha\sigma} F_{\alpha,0}\, e^{i\sigma\varphi_\alpha} \sum_{\beta\sigma'} F_{\beta,0}\, e^{i\sigma'\varphi_\beta}\, \mathcal{M}_{fi}(-\sigma\omega_\alpha) \;\times \\ \times& \;\delta_T(\omega_{fi} + \sigma\omega_\alpha + \sigma'\omega_\beta), \end{aligned} \tag{2.40}$$

Equation (2.40) is the familiar stationary formula expressing the transition amplitude as a coherent sum of contributions from individual time-ordered Feynman diagrams. When Equation (2.40) is valid, it is possible to define a transition rate $\mathcal{W}_{fi} = \lim_{T\to\infty} |\mathcal{A}^{(2)}_{fi}|^2/T$ on account of being $\lim_{T\to\infty} 2\pi\, \delta^2_T(\omega)/T \to \delta(\omega)$.

AC-STARK SHIFT Let us consider the process of stimulated single-mode Rayleigh scattering, i.e., a process where the system absorbs and re-emits or, conversely, emits and then absorbs a photon from a single-mode field, returning to the same initial state. This is a second order process described by Equation (2.40) for the case in which $\sigma' \neq \sigma$. These two terms are non-vanishing only when $\omega_f = \omega_g$ and give rise to a shift in the energy level E_g called the dynamic or ac-Stark shift. Indeed, in length gauge and by taking into account $\delta_T(0) = (2\pi)^{-1}T$, the state vector $|g(t)\rangle$ is modified to second order in $\mathcal{E}_0$ to read

$$\begin{aligned} |g(t)\rangle &= |g(t_0)\rangle \exp\left(-i\,E_g\,t\right) \\ &\times \left\{1 - iT\frac{\mathcal{E}_0^2}{4}\left[\langle g|DG_0^+(E_g+\omega)D|g\rangle + \langle g|DG_0^+(E_g-\omega)D|g\rangle\right]\right\} \\ &\approx |g(t_0)\rangle \exp\left[-i\,(E_g + \Delta E_g^{(2)})t\right], \end{aligned} \tag{2.41}$$

where

$$\Delta E_g^{(2)} = \frac{\mathcal{E}_0^2}{4}\left[\langle g|DG_0^+(E_g+\omega)D|g\rangle + \langle g|DG_0^+(E_g-\omega)D|g\rangle\right]. \tag{2.42}$$

THE RABITT TECHNIQUE Let us consider an isolated attosecond pulse train superposed, with a controlled time delay, to a weak replica of the IR pulse used to generate it, and employed to ionize a rare gas. If the intensities of both the XUV train and the IR pulse are kept weak, the ionization process can be described at the level of the second order perturbation theory. This is the pump-probe scheme at the basis of the RABITT technique.

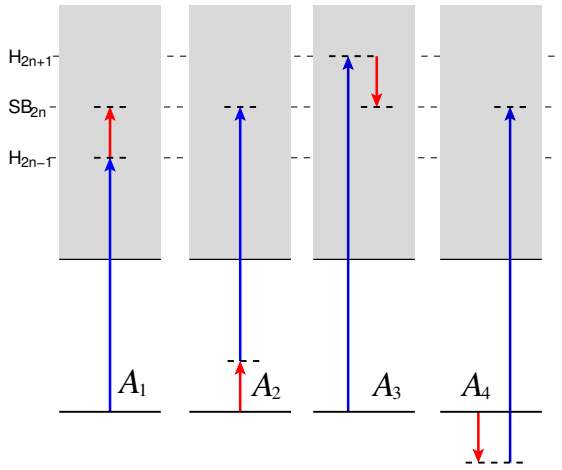

Figure 6: Quantum paths contributing to a sideband signal in RABITT spectroscopy. The amplitudes of both paths 1 and 2, in which one IR photon is absorbed, are modulated by a phase factor $e^{i\omega_{IR}\tau}$, while those of paths 3 and 4 are modulated by a phase factor $e^{-i\omega_{IR}\tau}$. As a result of the interference between the four amplitudes, therefore, the sideband signal beats with angular frequency $2\omega_{IR}$.

In absence of the IR, the XUV train alone will create a series of odd harmonic peaks at the photoelectron kinetic energies $(2n+1)\omega_{IR}$ - IP. This is a one-photon process and can be accounted for with a first order perturbative approach. When the IR is present, two photon transitions corresponding to the absorption of one XUV photon and to the exchange of one IR photon take place. As a consequence,

photoelectron signals at energies $2n\omega_{IR}$ minus the ionization potential, the so-called sidebands, also appear. These sidebands are related to both the relative phase of the harmonics in the XUV train and to the intrinsic phases of electronic transitions involved.

The total two-photon transition amplitude $\mathcal{A}_{2n}^{(2)}$ giving rise to the sideband $2n$ in the RABITT pump-probe scheme is the sum of the amplitudes for the four diagrams depicted in Figure 6. Using (2.40), $\mathcal{A}_{2n}^{(2)}$ can be readily written as

$$\begin{aligned}\mathcal{A}_{2n}^{(2)} &= \mathcal{A}_1 + \mathcal{A}_2 + \mathcal{A}_3 + \mathcal{A}_4 = \\ &= \frac{\pi}{2i}\,\left(\,F_{2n-1}F_{\mathrm{IR}}\,\mathcal{M}_{2n-1} + F_{2n+1}F_{\mathrm{IR}}^{*}\,\mathcal{M}_{2n+1}\right)\;\delta_T(E-\omega_{\mathrm{g}}-2n\omega).\end{aligned} \tag{2.43}$$

The subscripts in the two-photon transition matrix elements $\mathcal{M}_{2n\pm1}$ indicate the paths containing the $2n\pm1$ harmonics,

$$\mathcal{M}_{2n\pm1} = \langle f|\mathcal{O}\left[G_a^{+}(\omega_{\mathrm{g}}\mp\omega) + G_a^{+}(\omega_{\mathrm{g}}+\omega_{2n\pm1})\right]\mathcal{O}|i\rangle. \tag{2.44}$$

The argument of the two-photon matrix element is known as *atomic phase*, $\varphi_n^{\mathrm{At}} = \arg\mathcal{M}_n$. The factors F_{IR} and $F_{2n\pm1}$ are the peak amplitude of the vector potential of the IR and of the two harmonics, respectively. The transition rate to a given sideband $2n$, therefore, is given by

$$\mathcal{W}_{2n}^{(2)} = \int dE\,\left|\mathcal{A}_{2n}^{(2)}(E)\right|^2 = \frac{\pi}{8}\,\left|F_{2n-1}F_{\mathrm{IR}}\,\mathcal{M}_{2n-1} + F_{2n+1}F_{\mathrm{IR}}^{*}\,\mathcal{M}_{2n+1}\right|^2. \tag{2.45}$$

If we use the attosecond pulse train as a reference to define the temporal scale, and thus keep it fixed with respect to the time delay, then the phases of the harmonics field amplitudes do not change with the time delay, while the phase of the IR, which we can here assume to be very long, is linear with the time delay:

$$F_{2n\pm1} = |F_{2n\pm1}|e^{-i\phi_{2n\pm1}}, \qquad F_{\mathrm{IR}} = |F_{\mathrm{IR}}|e^{-i(\varphi_{\mathrm{IR},0}+\omega\tau)}. \tag{2.46}$$

Inserting these latter parametrization in the expression (2.45) for the transition rate to the sideband, and expressing the module of the vector potential amplitude in terms of the photon flux Φ

$$|A| = \frac{\sqrt{8\pi\Phi c}}{\omega}, \tag{2.47}$$

we finally get

$$\begin{aligned}\mathcal{W}_{2n\omega}^{(2)} \;&=\; \frac{8\pi^3}{\omega_{\mathrm{IR}}}\Phi_{\mathrm{IR}}\Big\{\Phi_{2n-1}\,|\,\mathcal{M}_{2n-1}|^2 + \Phi_{2n+1}\,|\mathcal{M}_{2n+1}|^2 + \\ &+\; 2\sqrt{\Phi_{2n-1}\Phi_{2n+1}}\,|\mathcal{M}_{2n-1}\,\mathcal{M}_{2n+1}|\,\cos\left[\,\Delta\phi_{2n} + \Delta\varphi_{2n}^{\mathrm{At}} - 2\,(\varphi_{\mathrm{IR},0}+\omega_{\mathrm{IR}}\,\tau)\,\right]\Big\},\end{aligned} \tag{2.48}$$

where $\Delta\phi_{2n} \equiv \phi_{2n+1} - \phi_{2n-1}$ and $\Delta\varphi_{2n}^{\mathrm{At}} = \varphi_{2n+1}^{\mathrm{At}} - \varphi_{2n-1}^{\mathrm{At}}$. If the properties of the ionization continuum do not change much across the energy span of few ω's, as it is generally the case for rare gases in the energy region far from the ionization threshold, on the one side, and far from autoionizing states, on the other side, then the two integrals $\mathcal{M}_{2n+1}$ and $\mathcal{M}_{2n-1}$ are similar both in absolute value and

in phase. In particular, the atomic phase can be accurately linearized across the energy separation of two consecutive harmonics: $\varphi^{\mathrm{At}}_{2n+1} - \varphi^{\mathrm{At}}_{2n-1} \simeq 2\omega_{\mathrm{IR}}\partial_E\varphi^{\mathrm{At}}_E$. As a result, the phase of the sideband can be written as

$$\Phi_{2n} = \phi_{2n+1} - \phi_{2n-1} - 2\varphi_{\mathrm{IR},0} + 2\omega_{\mathrm{IR}}\partial\varphi^{\mathrm{At}}_E/\partial E. \tag{2.49}$$

Both the absolute value of the IR phase and the (typically small) value of the atomic phase change are a single unknown constant. If these constants are known, then the individual differences $\phi_{2n+1} - \phi_{2n-1}$ can be determined and, from these, by means of an inverse discrete Fourier transform, the envelope of the whole train can be obtained in absolute terms. If one is not particularly interested in knowing exactly where the pulse train is located within the IR pulse, the absolute value of the IR phase or the energy derivative of the atomic phase are not particularly relevant. Even without knowing the value of $\varphi_{\mathrm{IR},0}$ and $\partial_E\varphi^{\mathrm{At}}_E$, from all the values of $\Phi_{2n} - \Phi_{2n-2}$, it is still possible to determine the average shape of the envelope of an attosecond pulse in the train, and in particular its duration. Conversely, if the phase difference between consecutive harmonics is known, from the sideband phase one can extract the variation of the atomic phase. We will be using this latter approach to study resonant continuum-continuum transitions in Chapter 5.

In energy regions where the two-photon matrix elements display sharp energy changes, for instance in the presence of intermediate resonant states, Equation (2.49) is not valid. Moreover, while either Equation (2.30) or (2.31) are applicable in the presence of intermediate resonant states, the stationary expression (2.40) generally is not. The reason is that, the closer one gets to the resonance, the longer the exposure time required to legitimately factor out the two-photon matrix element from the integral in Equation (2.38). Thus, for pulses comparable to or shorter than the characteristic lifetime of the resonance, Equation (2.40) is not applicable as such, even if the truncated perturbative expression is valid. In this latter case, despite the transition being second order, a stationary regime is never achieved and a transition rate cannot consequently even be defined. Furthermore, for long exposures the second-order transition amplitude may become so large that higher-order terms, possibly infinitely many of them, are required to achieve a physically meaningful result. In § 4.4, we will derive the expression for the second-order finite-pulse transition amplitude necessary to interpret current pump-probe experiments with ultrashort pulses and in the presence of autoionizing states.

2.2.4 *N-th order perturbation theory*

Equation (2.40) can be easily generalized to the case of multi-photon transitions in the stationary regime. Once all the diagrams γ that contribute to a given transition are known, the corresponding amplitude is obtained as

$$\begin{aligned}\mathcal{A}_{f\leftarrow g} = &-2i\pi\,\delta_T(\omega_{fg} - \Delta\Omega_n) \\ &\times \sum_\gamma \frac{F^\gamma_n}{2}\cdots\frac{F^\gamma_1}{2}\,\langle f|\mathcal{O}G^+_0(\omega_g + \Delta\Omega^\gamma_{n-1})\mathcal{O}\cdots G^+_0(\omega_g + \Delta\Omega^\gamma_1)\mathcal{O}|g\rangle\,,\end{aligned} \tag{2.50}$$

where $F_i^\gamma = F_i^\gamma e^{-i\varphi_i^\gamma}$ if the i-th photon is absorbed, $F_i^\gamma = F_i^\gamma e^{+i\varphi_i^\gamma}$ if the i-th photon is emitted, and $\Delta\Omega_i^\gamma$ is the sum of the frequencies (positive if absorbed, negative if emitted) of the exchanged photons. In the case of the exchange of $n \geq 2$ photons, the transition rate is proportional to the n-th power of the photon flux. Therefore, for multi-photon processes, it is no longer possible to define a cross section with units of area that depends only on the properties of the system. At best, we can define a so-called generalized cross section

$$\tilde{\sigma}_{fi}^{(n)} = \Phi^{-n}\, \mathcal{W}_{fi}^{(n)}, \tag{2.51}$$

which has dimensions of (time)$^{n-1}\times$ (area)^n.

Finally, we note that other approximate methods exist to obtain the photoionization transition probabilities which are not based on a truncated perturbative expansion. In particular, the strong-field approximation, which neglects the interaction of a photoelectron with the parent ion, is well suited for the cases in which the intensity of the fields is so high to be the dominant term in the Hamiltonian. In § 4.3, we will discuss the soft-photon model, which is a particular case of this approximation.

2.3 OBSERVABLES

2.3.1 *Photoionization probabilities*

Direct information about the photoionization process is obtained by detecting the photoelectron emerging from the interaction region with a certain energy ε about the direction $\Omega \equiv (\theta, \phi)$. This is given by the transition probability from an initial state $|g\rangle$ to a collection of final (out) scattering states $\psi^-_{\alpha\varepsilon\hat{\Omega}}$:

$$\frac{dP^{(\alpha)}_{\varepsilon\hat{\Omega}\leftarrow g}}{d\Omega d\varepsilon} = \left|\mathcal{A}_{\alpha\varepsilon\hat{\Omega}\leftarrow g}\right|^2 = \left|\langle\psi^-_{\alpha\varepsilon\hat{\Omega}}|U(t_f,t_0)|g\rangle\right|^2, \tag{2.52}$$

where at time t_f the interaction has ended, and the index α denotes the collection of quantum numbers, other than the energy and the photoemission angle, sufficient to identify any given scattering state (channel index). The scattering states deserve more attention. They are eigenfunctions of the field-free Hamiltonian H_a. This Hamiltonian can be divided into two time-independent terms: an asymptotic (channel) Hamiltonian H_0, and a perturbation V, so that $H_a = H_0 + V$. The scattering states are then defined to satisfy either incoming (ψ^-_α) or outgoing (ψ^+_α) boundary conditions,

$$\psi^\pm_\alpha = \lim_{t\to\mp\infty} e^{-iH_0t}e^{iH_at}\Phi_\alpha, \tag{2.53}$$

where Φ_α are solutions of the channel Hamiltonian H_0. In other words, what in ψ^- (ψ^+) differs asymptotically from Φ_α has incoming (outgoing) character and, in the convolution with an $\mathcal{L}^2$ test function, will thus manifest itself only in the

past (future). The scattering states are the solutions of the Lippman-Schwinger equation [80],

$$|\psi^{\pm}_{\alpha E}\rangle = |\Phi_{\alpha E}\rangle + G^{\pm}_0(E)V|\psi^{-}_{\alpha E}\rangle, \tag{2.54}$$

where G_0 is the resolvent operator, defined in Equation (2.33), of the channel Hamiltonian H_0. In photoionization experiments, one measures the detection probability, at large times, along definite asymptotes $\Phi_{\alpha E}$:

$$\begin{aligned} P_{\alpha E} &= \lim_{t\to\infty} |\langle\Phi_{\alpha E}|\Psi(t)\rangle|^2 = \left|\lim_{t\to\infty}\langle\Phi_{\alpha E}(t)|\Psi(t)\rangle\right|^2 \\ &= \left|\lim_{t\to\infty}\langle\Phi_{\alpha E}(t_f)|e^{iH_0(t-t_f)}e^{-iH_a(t-t_f)}|\Psi(t_f)\rangle\right|^2 \\ &= \left|\langle\psi^{-}_{\alpha E}(t_f)|\Psi(t_f)\rangle\right|^2 = \left|\langle\psi^{-}_{\alpha E}|\Psi(t_f)\rangle\right|^2. \end{aligned} \tag{2.55}$$

The transition amplitude, therefore, is given by the projection on the scattering states fulfilling incoming boundary conditions. The calculation of these states will be the subject of § 3.6.2.

2.3.2 *Transient absorption cross section*

So far we have considered the interaction between light and matter only by looking at the observables of the latter, e.g., excitation and ionization probabilities. Alternatively, we can ask what happens to the light after this interaction. To do so, we must introduce the equations of motion for the field under the influence of a time dependent charge distribution. To remain within the semi-classical approximation we use the macroscopic Maxwell's equations in absence of free charges or currents and neglecting magnetization,

$$\begin{aligned} &\vec{\nabla}\cdot D = 0, \qquad \vec{\nabla}\cdot\vec{\mathcal{B}} = 0, \\ &\vec{\nabla}\times\vec{\mathcal{B}} = \frac{1}{c}\frac{\partial\vec{D}}{\partial t}, \qquad \vec{\nabla}\times\vec{\mathcal{E}} = -\frac{1}{c}\frac{\partial\vec{B}}{\partial t}, \end{aligned} \tag{2.56}$$

where the electric displacement $\vec{D}$ is related to the electric field through the relation $\vec{D} = \vec{\mathcal{E}} + 4\pi\vec{P}$. To simplify our treatment, we further assume that the laser fields are plane waves propagating in the x direction and linearly polarized along z, $\vec{\mathcal{E}}(\vec{r},t) = \hat{z}\mathcal{E}(x,t)$, and that the system is isotropic at $t = -\infty$. By doing so, the sample will remain invariant with respect to translations in either the y or z directions at any time, and the polarization of any vector quantity along z will be preserved, $\vec{P}(\vec{r},t) = \hat{z}P(x,t)$. Under these hypothesis, from Equation (2.56) we may derive the following equation for the wave-propagation:

$$\left(\frac{\partial^2}{\partial x^2} - 2i\frac{\omega}{c}\frac{\partial}{\partial x}\right)\tilde{\mathcal{E}}(x,\omega) = -4\pi\frac{\omega^2}{c^2}\tilde{P}(x,\omega), \tag{2.57}$$

where we have used the Fourier representations

$$\begin{aligned} \mathcal{E}(x,t) &= \int_0^\infty \frac{d\omega}{2\pi}\tilde{\mathcal{E}}(x,\omega)e^{-i\omega(t-x/c)} + C.C., \\ P(x,t) &= \int_0^\infty \frac{d\omega}{2\pi}\tilde{P}(x,\omega)e^{-i\omega(t-x/c)} + C.C., \end{aligned} \tag{2.58}$$

where $C.C$ represents the complex conjugate. If the medium is diluted, the electric field amplitude does not change appreciably across one wavelength, so the second derivative on the left hand side of Equation (2.57) can be safely neglected,

$$\frac{\partial}{\partial x}\tilde{\mathcal{E}}(x,\omega) = -2i\pi\frac{\omega}{c}\tilde{P}(x,\omega). \tag{2.59}$$

In the limit of a thin sample, neither the spectral components of the electric field, $\tilde{\mathcal{E}}(x,\omega)$, nor those of the polarization density, $\tilde{P}(x,\omega)$, change much. To a first approximation, therefore, we can estimate the variation of $\tilde{\mathcal{E}}(x,\omega)$ across a sample of thickness L by assuming that the polarization density is uniform, $\tilde{P}(x,\omega) \simeq \tilde{P}(\omega)$:

$$\tilde{\mathcal{E}}(L,\omega) \simeq \tilde{\mathcal{E}}(0,\omega) - 2i\pi\frac{\omega}{c}\,L\,\tilde{P}(\omega). \tag{2.60}$$

In actual experiments, one generally measures the relative variation of the spectral density of the field,

$$S(\omega) = \frac{|\tilde{\mathcal{E}}(0,\omega)|^2 - |\tilde{\mathcal{E}}(L,\omega)|^2}{|\tilde{\mathcal{E}}(0,\omega)|^2} \simeq 4\pi\frac{\omega}{c}\,L\,\Im\left[\frac{\tilde{P}(\omega)}{\tilde{\mathcal{E}}(\omega)}\right]. \tag{2.61}$$

Since the polarization density is given by the density of atoms, n, times the atomic dipole moment, d, we can derive an expression for $S(\omega)$ in terms of an effective transient absorption cross section,

$$\sigma(\omega;\tilde{\mathcal{E}}) = \frac{S}{nL} = 4\pi\alpha\omega\,\Im\left[\frac{\tilde{d}(\omega)}{\tilde{\mathcal{E}}(\omega)}\right]. \tag{2.62}$$

A velocity gauge analogue of this expression can be found via the Ehrenfest theorem [81],

$$\sigma(\omega;\tilde{A}) = 4\pi\alpha\omega^{-1}\,\Im\left[\frac{\tilde{p}(\omega)}{\tilde{A}(\omega)}\right]. \tag{2.63}$$

To compute the above equation, one needs to compute the dipolar response $\tilde{d}(\omega)$ of the system. We leave this for § 4.2.3.

3

FIELD-FREE ATOMIC STATES

3.1 FIELD-FREE HAMILTONIAN

In the previous section we encountered the field-free time-independent Hamiltonian H_a, whose stationary solutions we assumed to be known. In this chapter we illustrate how to obtain these solutions. For light systems, either in isolation or in the dynamical regimes triggered by currently available attosecond light sources, relativistic and QED terms give rise to very small corrections (of the order of α^2), which are beyond the scope of the current investigation and which can be safely neglected [82]. By doing so, the field-free electrostatic hamiltonian for an N-electron system, neglecting mass polarization terms, reads

$$H_a = \frac{1}{2\mu}\sum_{i=1}^{N}\left(p_i^2 - \frac{Ze^2}{r_i}\right) + \sum_{i>j=1}^{N}\frac{e^2}{r_{ij}}, \quad \mu = \frac{m_{e^-}\cdot m_{A^+}}{m_A} \tag{3.1}$$

where Z is the nuclear charge, $\vec{p}_i$ and $\vec{r}_i$ are the momentum and position operators of the individual particles, $r_{ij} = |\vec{r}_i - \vec{r}_j|$ is the interelectronic distance, and μ is the reduced mass of the electron - parent-ion binary system.

The electron-electron interaction term r_{ij}^{-1}, makes Equation (3.1) non-integrable; nonetheless, one still has conserved quantities. The electrostatic Hamiltonian (3.1) is independent on spin and it is spherically symmetric. Therefore, the total orbital angular momentum and the spin are independently conserved,

$$[H, L_i] = 0, \quad [H, L^2] = 0, \quad [H, S_i] = 0, \quad [H, S^2] = 0, \tag{3.2}$$

and transitions between states of different spin are prohibited. Since in this work our initial states will always be singlet states, we need to consider only singlet intermediate and final states. Due to inversion symmetry of H_a, the total parity (Π) must also be conserved,

$$[H, \Pi] = 0, \qquad \Pi = \pi_1 + \pi_2, \qquad \pi\vec{r} = -\vec{r}. \tag{3.3}$$

Energy, parity, angular momentum and spin are thus constants of motion. Therefore, all eigenstates of the Hamiltonian in Equation (3.1) can be labeled according to their quantum numbers S, L, Π, traditionally gathered in the spectral term

$$^{2S+1}L^{\pi}, \tag{3.4}$$

where $2S+1$ is the spin multiplicity, $L = S, P, D, \ldots$ is the total angular momentum and $\pi = e/o$, defines the even (e) or odd (o) parity of the state. If the parity of L is the same as Π, then the state is said to be a *natural* state, e.g., $^{1,3}S^e$, $^{1,3}P^o$,

$^{1,3}D^e$, etc. If, on the contrary, the parity is not the same, then it is an *unnatural* state, e.g. $^{1,3}S^o$, $^{1,3}P^e$, $^{1,3}D^o$, etc. Notice, however, that there are no odd S states for two-electron systems. It is also common to identify the eigenstates by their dominant configuration, i.e., by individual occupancy and coupling of the orbitals with n_i, ℓ_i quantum numbers. For example, for the ground state of Argon we may write

$$\mathrm{Ar} : 1s^2\, 2s^2\, 2p^6\, 3s^2\, 3p^6. \tag{3.5}$$

However, this notation does not account for electron correlation. In general, the real states will be a mixture of several configurations. Only in those cases in which one of them is largely dominant is this nomenclature meaningful.

The Pauli principle dictates that the total wavefunction of a quantum system must be anti-symmetric with respect to arbitrary permutation of identical particles with half integer spin (as are the electrons)

$$\forall \wp \in \mathcal{S}_N, \quad \wp\psi(x_1, x_2, ..., x_N) = \psi(x_{\wp_1}, x_{\wp_2}, ..., x_{\wp_N}) = (-1)^{\wp}\psi(x_1, x_2, ..., x_N). \tag{3.6}$$

The permutational symmetry is preserved since the hamiltonian is totally symmetric with respect to permutations of identical particles

$$H_a = \sum_i h(\vec{r}_i) + \frac{1}{2}\sum_{i,j\neq i} g(\vec{r}_i, \vec{r}_j) \Rightarrow \forall \wp \in \mathcal{S}_N, \quad [\wp, H_a] = 0. \tag{3.7}$$

In the case of two-electron systems, e.g. helium, the antisymmetry property can be enforced in a particularly simple way. This is because the symmetric group for two particles has just two irreducible representations: the symmetric one and the antisymmetric one, both monodimensional. Furthermore, the total spin operator is also totally symmetric. As a consequence, the spin functions with well defined total spin also have a well defined symmetry: singlet (S=0) and triplet (S=1) functions are anti-symmetric and symmetric, respectively

$$^1\Theta_0 = \frac{1}{\sqrt{2}}(\alpha\beta - \beta\alpha); \quad ^3\Theta_\mu = \begin{cases} \alpha\alpha, & \mu = +1 \\ \frac{1}{\sqrt{2}}(\alpha\beta + \beta\alpha), & \mu = 0 \\ \beta\beta, & \mu = -1 \end{cases} \tag{3.8}$$

$$\wp_{12}\, ^1\Theta_0 = -^1\Theta_0; \quad \wp_{12}\, ^3\Theta_\mu = ^3\Theta_\mu$$

This means that the total wave function for a state with well-defined spin can be exactly factorized in a spin and a spatial component, both with well defined and opposite parity

$$\begin{cases} ^1\psi(x_1, x_2) = ^1F(\vec{r}_1, \vec{r}_2)\, ^1\Theta_0(\zeta_1, \zeta_2), \quad ^{2S+1}F(\vec{r}_2, \vec{r}_1) = (-1)^S\, ^{2S+1}F(\vec{r}_1, \vec{r}_2) \\ ^3\psi(x_1, x_2) = ^3F(\vec{r}_1, \vec{r}_2)\, ^3\Theta_0(\zeta_1, \zeta_2), \end{cases} \tag{3.9}$$

The totally symmetric spatial wave function is normally called para, and the totally anti-symmetric is called ortho.

For more than two electrons, factorization of the wave function in a spatial and a spin factor is possible only for the states of highest multiplicity, $2S+1 = N+1$, in which case the spin function is totally symmetric [e.g., $\alpha(\zeta_1), \alpha(\zeta_2), \ldots, \alpha(\zeta_N)$] and the spatial function is fully antisymmetric. In all the other cases, spatial and spin components are irreducibly intertwined. A full description of the properties of spin-adapted antisymmetric wave functions is beyond the scope of this thesis. It is nevertheless worth mentioning how a spin-adapted antisymmetric wave function can be constructed from an $(N-1)$ antisymmetric wave function with well-defined spin ${}^{2S+1}\Phi_{\alpha\Sigma_\alpha}(x_1, \ldots, x_N)$ and a spin orbital ${}^{2}\varphi(x_N)$ as

$$ {}^{2S+1}\psi_\Sigma = \mathcal{A}^{(N)} \sum_{\sigma\Sigma_\alpha} C^{S\Sigma}_{S_\alpha\Sigma_\alpha\frac{1}{2}\sigma}\, {}^{2S_\alpha+1}\Phi_{\alpha,\Sigma_\alpha}(x_1, \ldots, x_{N-1})\, {}^{2}\varphi(x_N) \tag{3.10} $$

where $\mathcal{A}^{(N)} = \frac{1}{N!}\sum_{\wp\in S_N}(-1)^\wp \hat{\wp}$ is the antisymmetrizer. It is easy to verify that

$$ \mathcal{A}^{(N)} = \frac{1}{N}(1 - \sum_{i=1}^{N-1} \wp_{iN})\mathcal{A}^{(N-1)}. \tag{3.11} $$

Furthermore, since ${}^{2S+1}\Phi_{\alpha\Sigma_\alpha}$ is already antisymmetric,

$$ \mathcal{A}^{(N-1)}\ {}^{2S+1}\Phi_{\alpha\Sigma_\alpha} = {}^{2S+1}\Phi_{\alpha\Sigma_\alpha}, \tag{3.12} $$

and Equation (3.10) can be written as

$$ {}^{2S+1}\psi_\Sigma = \frac{1}{N}(1 - \sum_{i=1}^{N-1} \wp_{iN}) \sum_{\sigma\Sigma_\alpha} C^{S\Sigma}_{S_\alpha\Sigma_\alpha\frac{1}{2}\sigma}\, {}^{2S+1}\Phi_{\alpha\Sigma_\alpha}(x_1, \ldots, x_{N-1})\, {}^{2}\varphi_\sigma(x_N). \tag{3.13} $$

In § 5.3.2 we will use this expression to justify the estimate of dipole matrix elements between continuum states of the argon atom.

3.2 CLOSE-COUPLING EXPANSION

Let us now seek a formal solution to the time-independent Schrödinger equation

$$ H_a\Psi = E\Psi, \tag{3.14} $$

for H_a in Equation (3.1). In the case of single ionization, the generalized eigenfunctions of an N-electron system can be conveniently formulated by means of the close-coupling expansion [72]. The parent-ion eigenstates ϕ_i and the corresponding eigenenergies E_i satisfy the equation

$$ \langle\phi_i|H_a^{(N-1)}|\phi_j\rangle = E_i\delta_{ij}, \tag{3.15} $$

where $H_a^{(N-1)}$ is the field-free Hamiltonian for $N-1$ electrons, and δ_{ij} is the Kronecker delta. Depending on the energy of the N-electron system, E, considered, we can distinguish between closed channels ($E < E_i$) and open channels ($E > E_j$). In closed channels, the motion of the N-th electron is bound and its wave functions vanish asymptotically. In open channels, the motion of the N-th electron

is unbound and its wave functions oscillate asymptotically. Each of the (infinite) number of eigenenergies, E_i, of Equation (3.15) thus defines a channel threshold, above which the wave function of the outer coupled electron in the respective channel is in the continuum.

Asymptotically the N-electron wave function must be a linear combination of the parent ion in one of the permissible energy levels ($E_i \leq E$) times an electron in the field of the ion with residual asymptotic energy $\varepsilon = E - E_n$

$$\Phi(\vec{x}_1, \ldots, \vec{x}_N) = \mathcal{A}^{(N)} \sum_{\alpha=1}^{n} \bar{\phi}_\alpha(\vec{x}_1, \ldots, \vec{x}_{N-1}; \hat{r}_N \sigma_N) \frac{F_\alpha(r_N)}{r_N}, \tag{3.16}$$

where $\vec{x}_i = \vec{r}_i \sigma_i$ represents the space and spin coordinates of the i-th electron. The functions $\bar{\phi}_\alpha$ are obtained by coupling the orbital and spin angular momenta of the parent-ion eigenstates ϕ_i with those of the outer electron to give rise to well-defined total angular momentum and spin quantum numbers

$$\Gamma \equiv L M_L S M_S \pi, \tag{3.17}$$

which are conserved in the electron collision with the parent ion. Finally, F_α are the radial wave functions associated asymptotically to the N-th electron.

Additionally, one can include in the close-coupling expansion (3.16) a finite set of square integrable functions χ_k^Γ, generally known as pseudo-channel or correlation functions, that allow for additional correlation effects that come from the coupling between the states included in the truncated close-coupling expression (3.16) and the highly-localized virtual excitations of those closed channels that are not included in the close-coupling *ansatz*,

$$\begin{aligned} \Phi(\vec{x}_1, \ldots, \vec{x}_N) = \mathcal{A}^{(N)} \sum_{\alpha=1}^{n} \bar{\phi}_\alpha(\vec{x}_1, \ldots, \vec{x}_{N-1}; \hat{r}_N \sigma_N) \frac{F_\alpha(r_N)}{r_N} \\ + \sum_{k}^{m} \chi_k(\vec{x}_1, \ldots, \vec{x}_N) b_k, \end{aligned} \tag{3.18}$$

By substituting Equation (3.18) into the time-independent Schrödinger equation, projecting onto the channel functions $\bar{\phi}_\alpha$ and onto the square integrable functions χ_k and eliminating the coefficients b_k, we obtain n coupled integrodifferential equations satisfied by the radial wave function F_α, which represents the motion of the outer electron, given by [82]

$$\left(\frac{d^2}{dr^2} - \frac{\ell_\alpha(\ell_\alpha + 1)}{r^2} + \frac{2(Z-N)}{r} + k_\alpha^2 \right) F_\alpha(r) = 2 \sum_k \left(V_{\alpha k} + W_{\alpha k} + X_{\alpha k} \right) F_k, \tag{3.19}$$

where $k_\alpha = \sqrt{2(E - I_p^\alpha)}$ (I_p^α is the ionization potential of channel α) and ℓ are the linear and angular momentum, respectively, of the outer electron, and the potentials $V_{\alpha\ell}$, $W_{\alpha\ell}$ and $X_{\alpha E}$ are the direct, exchange and correlation potentials, respectively [72]. It is worth noting that the close-coupling expansion is dominated in

neutral atoms by the direct potential which, to first order in the r^{-1} expansion, is responsible for the long range Coulomb potential describing the attraction of the outer electron by the net charge of the nucleus plus core electrons. The exchange and correlation potentials, unlike the direct potential, are both nonlocal. Due to the exponential decay of the bound state wave functions of the parent-ion, the nonlocal exchange potential vanishes exponentially for large r.

3.2.1 *Scattering states. Phase shifts*

The scattering states of the system can be found by solving Equation (3.19) for a given set of good quantum numbers Γ subject to the following boundary conditions. For closed channels ($E < E_i$), the radial wave function is localized and should vanish at long distances,

$$\lim_{r\to\infty} F_{\alpha\beta}(r) = 0. \tag{3.20}$$

For open channels, the photoelectrons are subject to the long-range Coulomb potential of the remaining ion plus a multipolar potential due to electron-electron interaction. If the channels are decoupled for large values of r, the wave function $F_{\alpha\beta}$ in Equation (3.19) is given by a linear combination of the regular and irregular Coulomb functions [73]:

$$F_{\alpha\beta}(r) = F_\alpha(r)A^{\text{reg}}_{\alpha\beta} + G_\alpha(r)A^{\text{irr}}_{\alpha\beta} = \mathcal{W}^+_\alpha(r)A^+_{\alpha\beta} + \mathcal{W}^-_\alpha(r)A^-_{\alpha\beta} \tag{3.21}$$

where $\mathcal{W}^\pm_\alpha = G_\alpha \pm iF_\alpha$. As we have seen in § 2.3.1, of particular interest are those functions which fulfill incoming ($A^+_{\alpha\beta} = \delta_{\alpha\beta}$) or outgoing ($A^-_{\alpha\beta} = \delta_{\alpha\beta}$) boundary conditions. From any independent set of scattering solutions, either the incoming or the outgoing set can be obtained by the transformation

$$\psi^\pm_\alpha = \sum_\beta \psi_\beta (\mathbb{A}^\mp)^{-1}_{\beta\alpha}. \tag{3.22}$$

For scattering states with incoming wave normalization (ψ^-), i.e., states with outgoing spherical Coulomb functions only in channel α and incoming spherical Coulomb waves in all channels [83],

$$F_{\alpha\beta} \sim k_\alpha^{-1/2}\left(e^{i\theta_\alpha}\delta_{\alpha\beta} - e^{-i\theta_\alpha}S^\dagger_{\alpha\beta}\right). \tag{3.23}$$

The quantity θ_α is given by

$$\theta_\alpha = k_\alpha r - \ell_\alpha \pi/2 - (Z-N)/k_\alpha \log(2k_\alpha r) + \sigma_\alpha, \tag{3.24}$$

where $\sigma_\alpha = \arg\Gamma\left[\ell_\alpha + 1 + i(Z-N)/k_\alpha\right]$ is the Coulomb phase shift, while $S_{\alpha\beta}$ is the *on-shell* n-dimensional S-matrix [83], where n is the number of open channels. The *on-shell* S-matrix is related to the overlap between the scattering states satisfying incoming and outgoing boundary conditions (see Sec. 2.3.1), as

$$\langle \psi^-_{\beta E} | \psi^+_{\alpha E'} \rangle = S_{\alpha\beta}\,\delta(E - E'), \tag{3.25}$$

so that it contains all of the information on the scattering process, including the short-range correlation effects. Owing to the conservation of probability, the S-matrix is unitary and, in spherically symmetric systems, it commutes with the total angular momentum L. Due to unitarity, the S-matrix can be diagonalized as

$$\mathbb{S} = \mathbb{U}\mathbf{\Lambda}\mathbb{U}^\dagger, \quad \mathbf{\Lambda}_{\alpha\beta} = \lambda_\alpha \delta_{\alpha\beta}, \quad |\lambda_\alpha| = 1. \tag{3.26}$$

Its eigenvalues, which have module one, are generally written as

$$\lambda_\alpha = e^{2i\varphi_\alpha}, \tag{3.27}$$

where φ_α are the so-called eigenphases, while the solutions

$$\boldsymbol{\psi}^{\mathcal{P}} \equiv \boldsymbol{\psi}^{\pm}\, \mathbb{U}\, e^{\mp i\boldsymbol{\varphi}}, \tag{3.28}$$

where either the $+$ or $-$ can be indifferently taken, are real stationary scattering solutions, called eigenchannels. In an eigenchannel, each channel has equal incoming and outgoing flux, and the outgoing component of each channel is dephased by the same quantity $2\varphi_\alpha$ with respect to the corresponding incoming component. In the special case in which only one channel is open or, in the case of multiple open channels, if they are decoupled, the scattering matrix is already diagonal and the scattering event is thus entirely characterized by a single channel phase shift δ_α for each outgoing (or incoming) channel. The asymptotic form of the photoelectron [Equation (3.23)] can thus be rewritten as

$$\psi_\alpha^- \sim e^{-i\delta_\alpha} \sin\left[kr - \frac{1}{2}\ell_\alpha \pi + (Z-N)/k \log 2kr + \sigma_\alpha + \delta_\alpha\right]. \tag{3.29}$$

3.2.2 *Wigner time delay & photo-ejection time delay*

The definition of a temporal observable in quantum mechanics requires special care. Indeed, as recognized as early as 1926 by Pauli [84, 85], it is not possible to define a self-adjoint operator $\hat{t}$ with the property $[\hat{t}, H] = i\hbar$, because such relation would require the spectrum of H to be the whole $\Re$, while it is bounded from below [86, 87]. In the context of scattering by a short range potential, however, Wigner, Eisenbud and Smith [57, 88] showed that the energy derivative of the phase shift δ_E experienced by a scattered particle with respect to a free wave, can be interpreted as the group delay with which a spectrally narrow scattered wave packet arrives at the detector, compared with a free reference wave packet (see Fig. 7). This is known as the Eisenbud-Wigner-Smith (or Wigner, for short) time delay,

$$\tau_W = 2\frac{\partial \delta_E}{\partial E}. \tag{3.30}$$

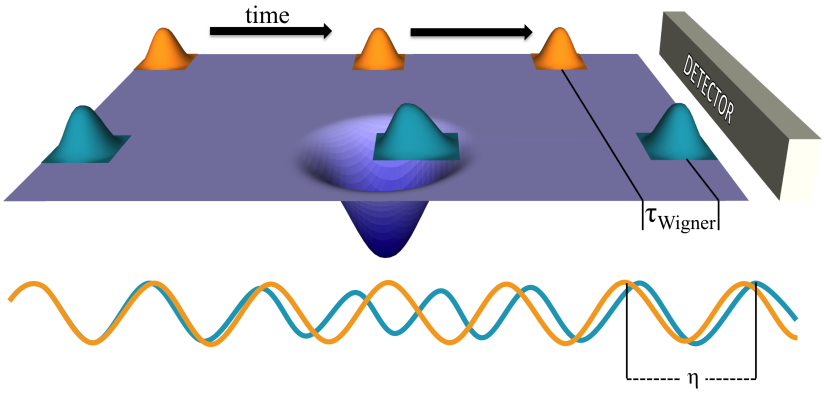

Figure 7: Sketch of the Wigner time delay. As the electron wave packet (green) scatters off the potential, it acquires a phase shift η as compared to a reference free electron (orange). This phase shift is related to the time lapsed between the detection of the scattered electronic wave packet and the detection of the unscattered free electron, called the Wigner time delay.

Let us now consider the process of photo-ionization. The concept of photo-ejection time delay is the subject of an ongoing debate in the attosecond physics community. For an in-depth treatment on this subject, we refer the reader to the reviews [89, 90]. Here, we will give a physical interpretation of time delay in relation to the measured phase in RABITT experiments.

We assume ionization from the ground state $|g\rangle$ is triggered by a single long XUV pulse $\mathcal{E}(t)$ centered at $t_{\text{XUV}} = 0$, and whose Fourier transform is sharply peaked around $\omega_0 = E_0 - E_g$ and real, $\mathcal{E}(\omega) \in \Re \ \forall \omega$. From first order perturbation theory in the interaction representation, the coefficients $\mathcal{A}^{(1)}$ of the resulting wave packet to a state in the continuum ψ_E^- are:

$$\mathcal{A}_{Eg}^{(1)} = -i\sqrt{2\pi}\,\langle\psi_E^-|\mathcal{O}|g\rangle\,\mathcal{F}[\mathcal{E}](\omega). \tag{3.31}$$

At any time after the radiation-matter interaction, the photoelectron wave packet $\Psi(t)$ is given by:

$$\Psi(t) = \int dE\,|\psi_E^-\rangle\,e^{-iEt}\mathcal{A}_E = \int dE\,|\psi_E^-\rangle\,e^{-iEt}(-i\sqrt{2\pi})\,\langle\psi_E^-|\mathcal{O}|g\rangle\,\mathcal{F}[\mathcal{E}](\omega_{Eg}). \tag{3.32}$$

At large times, the wave packet is purely outgoing and the expansion in terms of ψ_E^- can be replaced by an expression over the outgoing asymptotes of ψ_E^- which, by definition, are the eigenstates Φ_E of a reference Hamiltonian H_0,

$$\Psi(t) = \frac{\sqrt{2\pi}}{i}\int dE\,|\Phi_E\rangle\,e^{-iEt}\,\langle\psi_E^-|\mathcal{O}|g\rangle\,\mathcal{F}[\mathcal{E}](\omega_{Eg}). \tag{3.33}$$

Let us now make the following question: if we were to propagate back the wave packet with the dynamics of the unperturbed system, i.e., with the $U_0(t,t') = e^{-iH_0(t-t')}$ propagator, at what time t_0 would the wave packet be centered at the origin? In this case, we have,

$$e^{-iH_0(t_0-t)}\Psi(t) = \frac{\sqrt{2\pi}}{i}\int dE\,|\Phi_E\rangle\,e^{-iEt_0}\,\langle\psi_E^-|\mathcal{O}|g\rangle\,\mathcal{F}[\mathcal{E}](\omega_{Eg}). \tag{3.34}$$

In single-channel scattering, Φ_E can be chosen up to an arbitrary and immaterial phase factor. In particular, Φ_E can be chosen to be real on all space. We can therefore isolate the complex components of the wave packet back-propagated at t_0 as:

$$\begin{aligned} e^{-iH_0(t_0-t)}\Psi(t) &\simeq \frac{\sqrt{2\pi}}{i} e^{-iE_0 t_0} e^{i\varphi_{E_0}} \times \\ &\times \int dE\, |\Phi_E\rangle\, e^{-i(E-E_0)t_0} e^{i(E-E_0)\partial_E \varphi_E|_{E_0}} \left|\langle \psi_E^- | \mathcal{O} | g\rangle\right| \mathcal{F}[\mathcal{E}](\omega_{Eg}), \end{aligned} \tag{3.35}$$

where we defined $\varphi_E \equiv \arg\left(\langle \psi_E^- | \mathcal{O} | g\rangle\right)$ and approximated $\varphi_E \approx \varphi_{E_0} + (E - E_0)\partial_E \varphi_E|_{E_0}$, on account of being $\mathcal{F}[\mathcal{E}](\omega_{Eg})$ narrowly peaked around $E = E_0$. The global phase factors outside the integral do not affect the spatial distribution of the wave packet and can therefore be ignored in the search for an answer to our original question. The result of the integral will have equal incoming and outgoing components (i.e., the wave packet is centered at the origin) if the result is real. Except for the exponential phase factors, all the factors in the integrals are real. A sufficient solution for the wave packet to be centered at the origin, therefore, is that the two exponential phase factors cancel each other, which happens at:

$$t_0 = \partial_E \varphi_E|_{E_0}. \tag{3.36}$$

If the system under study were really an unperturbed system described by H_0, we would expect that this time t_0, where the wave packet is real, is the time at which the XUV pulse impinges on the target ($t_{\text{XUV}} = 0$). In general, however, $t_0 \neq 0$. If $t_0 > 0$, the wave packet seems to have waited a time t_0 after the XUV before being released, and then we talk about a positive time delay, $\tau = t_0 - t_{\text{XUV}} = t_0$. Conversely, we can say that, knowing the time at which the XUV has reached the target and estimating the travel time on the basis of the free propagation, we (in principle) detect the wave packet at an arrival time that is delayed by $\tau = t_0$.

How does this apparent delay compare with the scattering (Wigner) time delay? Remaining in the single channel case, we know that the *real* generalized eigenstate $\psi^{\mathcal{P}}$ of the full field-free Hamiltonian H_a differs asymptotically from the reference *real* asymptote Φ_E by a phase shift δ_E,

$$\Phi_E \sim \sin\theta_E(r), \quad \psi_E^{\mathcal{P}} \sim \sin(\theta_E(r) + \delta_E). \tag{3.37}$$

The above is true under the implicit assumption that H_0 is chosen in such a way that $H_a - H_0$ is short-range, e.g., in the case of Coulomb scattering, the reference Hamiltonian H_0 must contain the Coulomb phase due to its logarithmic divergence. The scattering states whose outgoing components coincide with those of the real asymptotes Φ_E are

$$\psi_E^- \equiv e^{-i\delta_E}\psi_E^{\mathcal{P}} \quad : \quad \text{out}\left[\psi_E^-\right] = e^{i\theta_E(r)} = \text{out}\left[\Phi_E\right]. \tag{3.38}$$

The argument of the transition amplitude $\langle \psi_E^- | \mathcal{O} | g\rangle$, therefore is

$$\varphi_E \equiv \arg\left(\langle \psi_E^- | \mathcal{O} | g\rangle\right) = \arg\left(e^{i\delta_E} \langle \psi_E^{\mathcal{P}} | \mathcal{O} | g\rangle\right) = \delta_E, \tag{3.39}$$

and using Equation 3.36,

$$\tau_{PI} = \partial_E \varphi_E|_{E_0} = \partial_E \delta_E|_{E_0}. \tag{3.40}$$

Apart for a factor of two, the time delay in a photoionization process coincides with the Wigner time delay (see Equation 3.30). Hence why photoionization is sometimes referred to as a *half-scattering* process.

From experiments relying on stationary one-photon absorption processes, however, the transition phases φ_E cannot be obtained. One-photon emission time delay, therefore, cannot be directly measured. However, two-photon techniques such as RABITT , do provide the access to the two-photon time delay. In the multiphoton case, the transition matrix elements can be complex even if all the states involved are real. In particular, even in the case of the ionization of a reference system H_0, the interaction representation expansion coefficients of a multiphoton wave packet have a phase modulation, i.e.,

$$\partial_E \arg\left\{\langle\Phi_E|\mathcal{O}\prod_i[G_0^+(\Omega_i)\mathcal{O}]|g\rangle\right\} \neq 0, \quad \text{even if } \langle\Phi_E|\mathcal{O}|g\rangle \text{ is real.} \tag{3.41}$$

This means that multiphoton wave packets are already intrinsically delayed with respect to the one-photon wave packet, even in absence of intermediate resonances. If, furthermore, the system is not the reference one, both the multiphoton delay and the short-range effects of the perturbative potential affect the total time delay.

In some cases, the multiphoton time delay is the same in the interacting and non-interacting ionization. This is expected if the photon exchanged after the first mostly interacts with a wave packet that is already asymptotic in character. Under these conditions, the problem of relating the one- and multi-photon time delays has been addressed by many authors [91, 64, 92]. In particular, Dahlström *et al* [93] showed that the two-photon atomic time delay recorded with the RABITT technique incorporates two contributions, $\tau_{at}^{(2)} = \tau_W + \tau_{CC}$, the Wigner time delay τ_W of the one-XUV-photon ionization and an additional continuum-continuum term τ_{CC}, which is a measurement-induced delay associated to the IR-probe photon exchange process, this is, to the probing of the electron by the IR field in a long-range potential with a Coulomb tail. In this context, in § 5.4.1 we will discuss the angular dependence of the atomic photoemission time delay for the ionization from an isotropic atomic state, which shows that this τ_{CC} contribution introduces anisotropy.

In general cases, however, the intermediate wave packet prior to the absorption of a second photon is not asymptotic in character. The most evident counterexample is if an intermediate resonant state, not contemplated by the H_0 Hamiltonian, is populated and subsequently undergoes a radiative transition to the final continuum.

3.2.3 *Metastable states*

The channel phase shifts δ_α are generally slowly varying functions of the energy. There are certain energies, however, at which these phase shifts, and the corresponding cross sections, vary pronouncedly. Let us consider two channels, whose thresholds, I_1 and I_2, are determined by the eigenenergies of the $N-1$ core electrons. At energies between I_1 and I_2, there can be states in channel 2 which would be bound if there were no coupling to the open channel 1. Following a single particle picture, the channel coupling makes it possible for the excited core electron in channel 2 to impart its excitation energy $E_2 - E_1$ to the outer electron, returning to the less excited state. The outer electron, in this way, gains sufficient energy to be ejected in a process known as autoionization, which is depicted in Fig. 8 (due to the indistinguishability of the two electrons, the process in which the outer electron fills an inner vacancy, while the inner excited electron is ejected is also possible). These states, known as Feshbach resonances [94], have a finite lifetime and have a dramatic effect on photoionization cross sections, where they manifest themselves as characteristically asymmetric peaks [10].

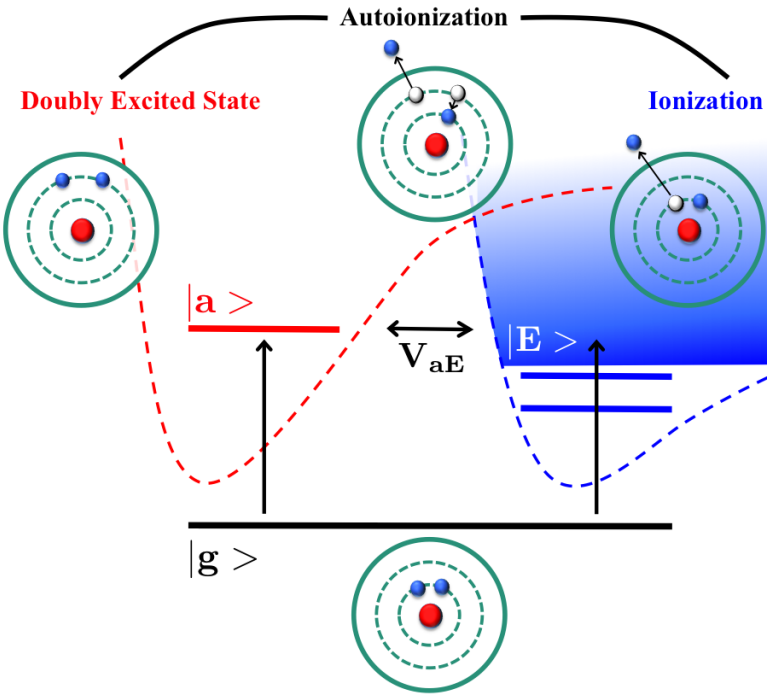

Figure 8: The process of autoionization. The coupling V_{aE} between the closed channel (red) and the open channel (blue) at the considered total energy, makes it possible for the bound doubly-excited configuration $|a\rangle$ in the closed channel to decay by autoionization to the continuum $|E\rangle$ of the open channel.

Ugo Fano developed more than 50 years ago [52] an effective formalism that describes the process of autoionization and provides an expression for the wave function of a bound state embedded in a continuum. This approach is at the basis of the theoretical model developed in § 4.4. In the following, we provide an outline of Fano's model.

3.3 FANO MODEL OF AUTOIONIZATION

In the simplest formulation of Fano's approach, the field-free Hamiltonian H_a is given by the sum of an unperturbed component H_0 and a "configuration interaction" component V, $H_a = H_0 + V$, where the eigenstates of H_0 comprise a featureless single-channel continuum $|\varepsilon\rangle$ and a bound state $|a\rangle$, $H_0|\varepsilon\rangle = |\varepsilon\rangle\varepsilon$, $H_0|a\rangle = |a\rangle E_a$, while the configuration interaction only couples the bound state to the continuum, $V_{a\epsilon} = \langle a|H_a - H_0|\epsilon\rangle$. For future convenience, we will not follow the original Fano's derivation in [52]. Instead, starting from the Lippmann-Schwinger equation

$$|\psi_E\rangle = |E\rangle + G_0^+(E)V|\psi_E\rangle \tag{3.42}$$

we guarantee at the outset that the interacting continuum $|\psi_E\rangle$ is normalized, $\langle\psi_E|\psi_{E'}\rangle = \delta(E - E')$. Notice that these states fulfill outgoing boundary conditions and so are formally ψ^+ states. Replacing the resolvent in the equation above with its spectral resolution,

$$G_0^+(E) = \frac{|a\rangle\langle a|}{E - E_a + i0^+} + \sum\!\!\!\!\!\!\int d\varepsilon \frac{|\varepsilon\rangle\langle\varepsilon|}{E - \epsilon + i0^+}, \tag{3.43}$$

we obtain the expression

$$|\psi_E\rangle = |E\rangle + \frac{|a\rangle\, T_{a,E}}{E - E_a + i0^+} + \sum\!\!\!\!\!\!\int \frac{d\varepsilon|\varepsilon\rangle\, T_{\varepsilon,E}}{E - \varepsilon + i0^+}, \tag{3.44}$$

where $T_{a,E} = \langle a|V|\psi_E\rangle$ and $T_{\varepsilon,E} = \langle\varepsilon|V|\psi_E\rangle$. We will refer to the first, second and third term in the RHS of Equation (3.44) as the homogeneous (H), discrete (D) and modified-continuum (M) components of the scattering wavefunction, respectively.

Under the assumption that $V_{\varepsilon\varepsilon'} = 0\ \forall\varepsilon, \varepsilon'$ and $V_{aa} = 0$, the T coefficients can be determined algebraically by requesting that $\langle a|E - H_a|\psi_E\rangle = 0$ and $\langle\varepsilon|E - H_a|\psi_E\rangle = 0\ \forall\varepsilon$. The result is

$$|\psi_E\rangle = |E\rangle + \left(|a\rangle + \sum\!\!\!\!\!\!\int \frac{d\varepsilon|\varepsilon\rangle\, V_{\varepsilon a}}{E - \varepsilon + i0^+}\right) \frac{V_{aE}}{E - \tilde{E}_a(E)}, \tag{3.45}$$

where $\tilde{E}_a(E) = E_a + \Delta_a(E) - i\Gamma_a(E)/2$ is a complex function of the energy, with the so-called energy shift $\Delta_a(E)$ and width $\Gamma_a(E)$ defined as $\Delta_a(E) = P\sum\!\!\!\!\!\!\int d\varepsilon|V_{\varepsilon a}|^2/(E - \varepsilon)$ and $\Gamma_a(E) = 2\pi^2|V_{Ea}|^2$. The pole of $E - \tilde{E}_a(E)$ in the negative complex plane is, by convention, the complex resonance energy. The energy shift $\Delta_a(E)$ and width $\Gamma_a(E)$ depend only weakly on the energy E, so that one can assume they are constant in the energy region of interest, $\Gamma_a(E) \simeq \Gamma_a(E_a) = \Gamma_a$, $\Delta_a(E) \simeq \Delta_a(E_a) = \Delta_a$. Within these assumptions, the complex resonance energy is thus well approximated as $\tilde{E}_a \simeq E_a + \Delta_a - i\Gamma_a/2$. For our convenience, we will indicate the real part of the resonance energy as $\bar{E}_a = \mathrm{Re}[\tilde{E}_a] = E_a + \Delta_a$. It is customary to define a reduced energy variable $\epsilon = 2(E - \bar{E}_a)/\Gamma_a$, and a distorted component $|\tilde{a}\rangle \equiv |a\rangle + P\sum\!\!\!\!\!\!\int d\varepsilon|\varepsilon\rangle V_{\varepsilon,a}/(E - \varepsilon)$ which incorporates the original bound state $|a\rangle$. Using this notation, Equation (3.45) can be reformulated as

$$|\psi_E\rangle = |E\rangle\frac{\epsilon}{\epsilon + i} + |\tilde{a}\rangle\frac{1}{\pi V_{Ea}}\frac{1}{\epsilon + i}. \tag{3.46}$$

Notice that for $\epsilon \to \pm\infty$, $|\psi_E\rangle$ converges (strongly) to $|E\rangle$. We also define a resonant phase shift ϕ_E as

$$\phi_E \equiv \pi/2 + \arctan\epsilon, \tag{3.47}$$

which is a *continuous, monotonically increasing* function of E, with $\phi_{-\infty} = 0$, $\phi_\infty = \pi$. Conversely, $\epsilon = -\cos\phi/\sin\phi$ (we will drop the energy suffix from ϕ_E, when E is clear from the context). Using ϕ we can write the $|\psi_E\rangle$ in yet a third form,

$$|\psi_E\rangle = |E\rangle\,\cos\phi\, e^{i\phi} - |\tilde{a}\rangle \frac{1}{\pi V_{Ea}}\,\sin\phi\, e^{i\phi}. \tag{3.48}$$

By virtue of it being a single ionization channel in an N-electron atom, for large values of one of the electronic radii, say, $r = r_N$, the state $|E\rangle$ can be expressed in the close-coupling spirit, as the product of two factors: i) a localized function of $N-1$ electronic coordinates and of the angular and spin coordinates of the N-th electron, which we indicate with the collective symbol $|X\rangle$, and ii) an oscillatory function of r [compare with Equation (3.29)],

$$\begin{aligned} \langle X; r|E\rangle &= N_E \sin[\theta(r) + \delta],\ kr \gg 1, \\ \theta(r) &= kr + k^{-1}\ln 2kr - \ell\pi/2 + \sigma_\ell, \end{aligned} \tag{3.49}$$

where N_E is a normalization factor, and δ is the channel phaseshift of the featureless continuum. From this result and the definition of $|\tilde{a}\rangle$, we have

$$\langle X; r|\tilde{a}\rangle = -\pi V_{Ea} N_E \cos[\theta(r) + \delta],\ kr \gg 1, \tag{3.50}$$

and hence ϕ enters the interacting continuum in two ways, as a phaseshift as well as a global phase factor

$$\langle X; r|\psi_E\rangle = N_E \sin[\theta(r) + \delta + \phi]\, e^{i\phi},\ kr \gg 1. \tag{3.51}$$

Using as reference asymptotes the $|E\rangle$ channel functions, the *on-shell* scattering matrix $s(E)$ associated to the collisional excitation of the resonance is

$$s(E) = e^{2i\phi} = (\epsilon - i)/(\epsilon + i). \tag{3.52}$$

The effect of the coupling between the bound state $|a\rangle$ and the continuum $|E\rangle$ on the scattering phase shifts is, therefore, to introduce an additional phase ϕ, which varies by π across the resonance as a function of energy. As an example, the *ab-initio* calculated total scattering phase shift, $\eta = \delta + \phi$, of the $1s\varepsilon_p(^1P^o)$ channel of helium, is shown in Fig. (9). Abrupt π jumps are observed in correspondence with each doubly-excited state of $^1P^o$ symmetry.

3.3.1 *Multiple open channels*

The results obtained in the previous section are valid only for the case of a single ionization channel. As long as the resonances are isolated, and that the matrix elements involving the continua are smooth and slowly varying functions of the energy, however, Fano's theory can be generalized to the case of an arbitrary

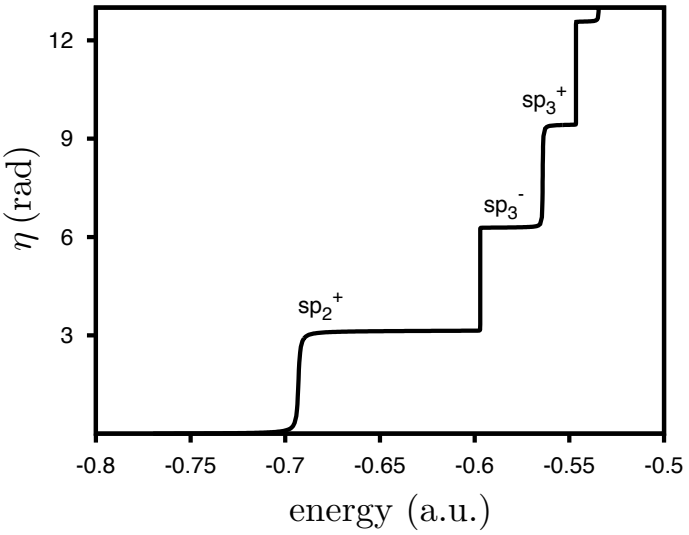

Figure 9: Scattering phase for the $^1P^o$ symmetry. π jumps are observed in correspondence to every doubly excited state with this symmetry.

number n of open channels. As shown in Section 4 of the original Fano paper [52], the case of a bound state $|a\rangle$ coupled to several unperturbed continua $|\alpha\varepsilon\rangle$, $V_{\alpha a} = \langle\alpha\varepsilon|H|a\rangle$, can be reduced to that of the bound state $|a\rangle$ coupled to a *single* interacting continuum $|R\,\varepsilon\rangle$, $V_{Ra} = \sqrt{\sum_\alpha |V_{\alpha a}|^2} = \langle R\,\varepsilon|H|a\rangle$, plus a set of fully decoupled residual featureless continua $|\alpha'\varepsilon\rangle$, $\langle\alpha'\varepsilon|H|a\rangle = 0$, by means of a unitary transformation of the degenerate unperturbed continua,

$$|R\,\varepsilon\rangle = \sum_\alpha |\alpha\varepsilon\rangle U_{\alpha R}, \quad |\alpha'\varepsilon\rangle = \sum_\alpha |\alpha\varepsilon\rangle U_{\alpha\alpha'}, \tag{3.53}$$

$$U_{\alpha R} = V_{\alpha a}/V_{Ra}, \quad V_{Ra} \equiv \sqrt{\sum_\alpha |V_{\alpha a}|^2}, \tag{3.54}$$

$$U^\dagger U = U U^\dagger = 1. \tag{3.55}$$

In this case, however, the interacting channel is generally not an eigenchannel of the Hamiltonian restricted to the unperturbed continuum states only. As a consequence, signatures of the resonance appear in all eigenphases and not just one of them. Still, the argument of the determinant of S does undergo an increase of 2π.

3.3.2 *Energy distribution and lifetime of a metastable state*

By projecting the resonant scattering wave function in Equation (3.46) onto the original unperturbed state $|a\rangle$, we find that the energy distribution of the latter is a Lorentzian peak at the shifted energy $\bar{E}_a$,

$$\frac{dP_a}{d\varepsilon} = |\langle\psi_E|a\rangle|^2 = \frac{1}{\pi}\frac{1}{\varepsilon^2+1}, \quad \int \frac{dP_a}{d\varepsilon} d\varepsilon = 1. \tag{3.56}$$

We can additionally calculate the probability of finding the system, originally in state $|a\rangle$, in that same state at time t. For a resonance sufficiently far from threshold and for large times, this gives

$$P_a(t) = \left| \int dE \langle a|\psi_E\rangle e^{-iEt} \langle \psi_E|a\rangle \right|^2 = e^{-\Gamma_a t}. \tag{3.57}$$

In other words, the state $|a\rangle$ decays exponentially with lifetime $\tau_a = 1/\Gamma_a$. From the natural width of the resonance recovered from the one-photon spectrum, therefore, one can infer the lifetime of the resonances. The timescale of autoionization decay is generally of the order of femtoseconds. For the case of the sp_2^+ doubly-excited state of helium, for example, the lifetime is $\tau_{sp_2^+} \sim 17.5$ fs.

3.3.3 *One-photon Fano transition amplitude*

The dipole transition matrix element between an initial ground state $|g\rangle$ and a final resonant continuum $|\psi_E\rangle$, solution of Fano's scattering problem (3.46), can be written as

$$\langle \psi_E|\mathcal{O}|g\rangle = \mathcal{O}_{Eg} \frac{\epsilon + q_{\tilde{a}g}}{\epsilon - i}, \qquad \mathcal{O}_{Ea} = \langle E|\mathcal{O}|g\rangle, \tag{3.58}$$

where $q_{\tilde{a}g}$ is a real parameter that measures the relative strength of the transition from the ground state to the autoionizing state, relative to that of the direct-ionization process,

$$q_{\tilde{a}g} = \frac{\mathcal{O}_{\tilde{a}g}}{\pi V_{aE} \mathcal{O}_{Eg}}. \tag{3.59}$$

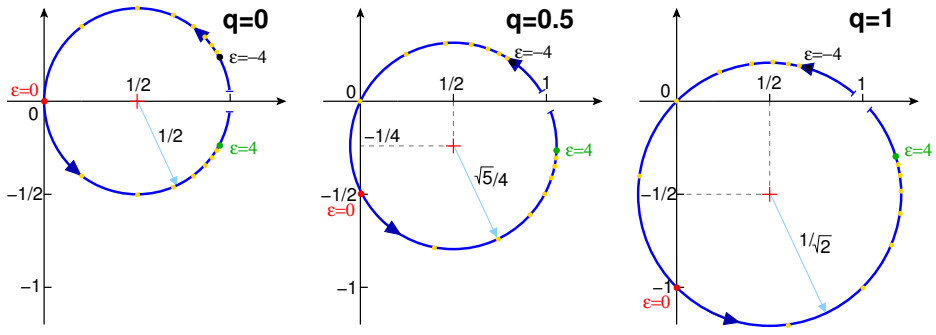

Figure 10: Trajectory in the complex plane of the $\mathcal{R}(\epsilon)$ resonant factor in Fano's dipole transition amplitude, as the reduced detuning ϵ varies from large negative to large positive values. The three panels correspond to different values of the q parameter. See text for more details.

The resonant factor $\mathcal{R}(\epsilon) = (\epsilon + q_{\tilde{a}g})/(\epsilon + i)$ in the dipole transition amplitude (3.58) can be written as the sum of a constant term plus a second term proportional to the unimodular function $(\epsilon - i)/(\epsilon + i)$,

$$\mathcal{R}(\epsilon) = \frac{\epsilon + q}{\epsilon + i} = \frac{1 - iq}{2} + \frac{1 + iq}{2} \frac{\epsilon - i}{\epsilon + i}. \tag{3.60}$$

This means that, as ϵ increases from $-\infty$ to $+\infty$, $\mathcal{R}(\epsilon)$ describes counterclockwise a circle in the complex plane. The circle is centered at $(1 - iq)/2$, it has radius $r = \sqrt{1+q^2}\,/\,2$, and it both starts and ends at 1, intercepting the origin at $\epsilon = -q$. Figure 10 illustrates the trajectory of $R(\epsilon)$, from large negative ($\epsilon \ll -1$) to large positive detunings ($\epsilon \gg 1$), for three representative values of q: 0, 0.5, and 1.

This geometrical interpretation can be visualized even more clearly by defining the angular variable $\varphi = \arctan(q) \in (-\pi/2, \pi/2)$, equivalent to the one introduced by Ott *et al.* [56] in the context of the dipolar response of a Fano resonance, with which $\mathcal{R}(\epsilon)$ becomes

$$\mathcal{R}(\epsilon) \;=\; r\,e^{-i\varphi} \;+\; r\,e^{i\varphi}\,e^{2i\phi}. \tag{3.61}$$

Notice that even if the resonant dipole transition amplitude (3.58) is a continuous function of ϵ, its phase is not. Indeed, the latter experiences a discontinuous jump of π in correspondence of $\epsilon = -q$, when the circle intercepts the origin,

$$\begin{aligned} \arg \mathcal{R}(\epsilon) \;&=\; \arg\left\{ e^{i\phi}\left[e^{i(\phi+\varphi)} + e^{-i(\phi+\varphi)} \right] \right\} = && (3.62)\\ &=\; \phi + \arg\left[\cos(\phi+\varphi)\right] = && (3.63)\\ &=\; \arctan(\epsilon) - \pi\theta(\epsilon+q). && (3.64) \end{aligned}$$

Far from reflecting a real discontinuity in the physical properties of the system, this circumstance simply reflects the fact that $\arg(z)$ is discontinuous at the origin.

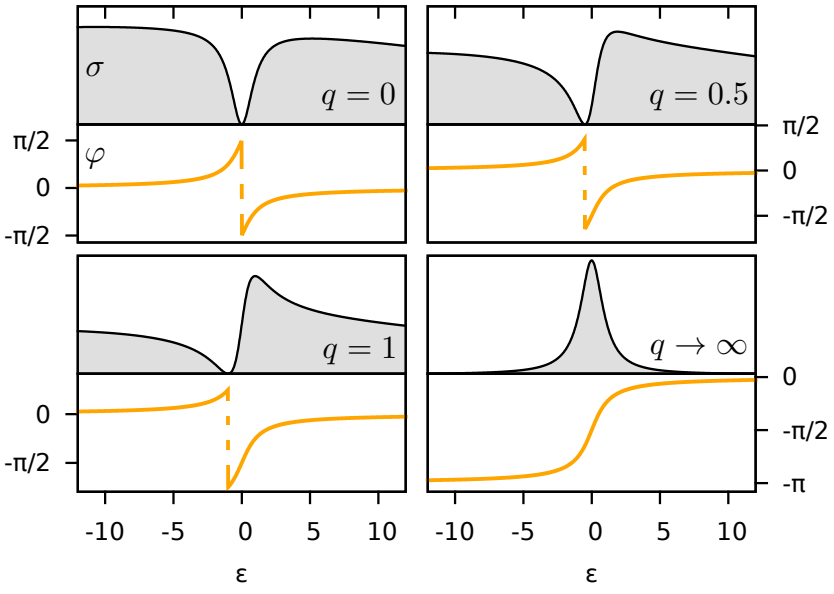

Figure 11: Photoionization cross section σ [Equation 3.65] and corresponding phase φ of the transition amplitude [Equation 3.61] as a function of the reduced energy for four values of the coupling parameter q. For $q = 0$, the resonant state $|a\rangle$ is not coupled radiatively to the ground, i.e., it is a "dark" state. For other finite values of q, the cross section displays the well-known asymmetric Fano profile due to the interference between the resonant and non-resonant paths. For an infinitely strong radiative coupling between the ground and the resonant state, $q \to \infty$, a Lorentzian peak is observed in the cross section [see Equation 3.56]. In all cases, the phase grows by π as the resonance is traversed, following an arctangent function, and jumps discontinuously by π at the value $\epsilon = -q$. For $q \to \infty$, such discontinuity has occurred at an infinitely negative value of the reduced energy, and is thus not observed (notice that in this case the phase starts at $-\pi$ instead of 0).

The photoionization cross section $\sigma(E)$, which is proportional to the square module of the dipole transition amplitude to the resonant continuum, therefore,

is the product between a background smooth cross section $\sigma_{\mathrm{bg}}(E)$, associated to direct photoionization, and the celebrated Fano profile,

$$\sigma(E) = \sigma_{\mathrm{bg}}(E)\frac{(\epsilon + q_{\tilde{a}g})^2}{\epsilon^2 + 1}. \tag{3.65}$$

In this latter expression, any information on the relative phase between different frequency components of the photoelectron wave packet generated by the interaction of the impinging ionizing light is lost. Therefore, while Equation (3.65) is sufficient to interpret one-photon ionization experiments such as those conducted at synchrotron facilities, when two or more photons are exchanged in a coherent transition, the relative phase of intermediate transition amplitudes becomes essential and we must go back to Eq. (3.58) instead.

3.4 THE SPECTRUM OF HELIUM

As an important example in this work, we highlight the main spectroscopic features of helium. It will be clear that all the concepts that we conveyed up to now for N-electron atoms (electron correlation, channel opening, autoionization) arise already in this system.

Helium is the second lightest element and the smallest neutral system featuring electronic correlation. Composed of two electrons and a nucleus, it has been a benchmark for correlation studies due to the fact that it is one of the few systems that can be solved numerically in a virtually exact way. Theoretical support can thus be used to explain the different features seen in spectroscopic measurements and which are characteristic of a many-body system, like autoionization and multiple-channel opening. Furthermore, helium is the quantum paradigm of a three body system, which is a non-integrable and, thus, classically chaotic system [95]. Numerical methods are hence necessary for a full solution of an interacting three-body-system helium.

If we neglect the interaction between the two electrons, the helium energy spectrum will be given by the sum of the two arbitrary energy levels. In particular, the bound part of the spectrum has the form of the He^+ parent ion

$$E_{N,n} = -\frac{Z^2}{2}\left(\frac{1}{N^2} + \frac{1}{n^2}\right). \tag{3.66}$$

where $N = 1, 2, \ldots$, and $n = N, N+1, \ldots$ are the principal quantum number of the two electrons, while the branches of the single-ionization continuum are

$$E_{N,\varepsilon} = -\frac{Z^2}{2}\frac{1}{N^2} + \varepsilon, \quad \varepsilon \geq 0. \tag{3.67}$$

The smallest quantum number N indicates the principal quantum number of the He^+ parent ion, while ε indicates the excitation level of the outer electron. The non-interacting bound states thus form Rydberg series converging to the ionization thresholds of the He^+ ion, in analogy with hydrogen. In Equation (3.66), the

energies below the $N = 1$ threshold in particular, correspond to the ground and to singly excited states, in which one electron remains in the $1s$ orbital while the other electron occupies any bound orbital. In absence of electronic repulsion, the $^1S^e$ ground-state energy is -4 a.u. This value is well below the Hartree-Fok energy of helium ground state $E_{HF} = -2.86168$ a.u., where the state is still restricted to the $1s^2$ configuration, but the orbital is optimized taking interelectronic repulsion into account. In the presence of electron interaction, singly excited states can be treated as hydrogenic states in which the excited electron feels an asymptotic effective charge of $Z_{eff} = 1$ due to the shielding effect of the core electron. To a first approximation, therefore,

$$E_n \approx -2 - \frac{1}{2n^2}. \tag{3.68}$$

However the electron can penetrate this shielding barrier. As a result of this short-range interaction, the principal quantum numbers of the excited states are collectively shifted by a quantity known as the quantum defect δ_ℓ,

$$E_n \simeq -2 - \frac{1}{2(n-\delta_\ell)}, \quad \lim_{n\to\infty} \delta_{\ell n} = \delta_\ell. \tag{3.69}$$

The quantum defect converges to a finite value for $n \to \infty$, but it becomes rapidly small as ℓ increases. It is intuitive to understand the dependence of the quantum defect on the angular momentum. For low values of the angular momentum, there is a higher probability of finding the excited electron near the nucleus, where the shielding effect of the other electron is lower. The inclusion of the interelectronic repulsion not only shifts the energy of the configurations, it also removes the degeneracies of the $(n\ell, n\ell')$ states. If no mean field approximations are made, the ground state energy drops to the electrostatic limit of -2.90372 a.u. [82]. The phenomenon responsible for the difference between the real energy and the Hartree-Fok energy is called electron correlation. In other words, electron correlation stems from the fact that the wave function cannot be expressed as a single determinant.

Let us consider now the so-called doubly excited states (DES) in the non-interacting electron model, i.e., the configurations in which both electrons are promoted out of the $1s$ orbital. These states form infinite sets of Rydberg series converging to the excited thresholds of the He atom. Due to the large value of the first excited energy of the parent ion, $E_{N=2} - E_{N=1} = 1.5$ a.u., all DES are located above the first ionization threshold and hence they are embedded in the ionization continuum of the atom. This circumstance remains true even when the energy of the DES configurations is corrected for the interelectronic repulsion. While in the non-interacting case the DES configurations do not interact either among themselves or with the continuum in which they are embedded, and are therefore rigorously bound, in the real system, interelectronic repulsion alters the picture in two major ways. If for truly bound states correlation manifests itself in the form of a real energy shift but a single configuration $1sn\ell$ still dominates, in the case of doubly excited states, it induces a strong mixing between doubly-excited configurations (that we call long-range correlation) as well as a mixing between DES and continuum (short-range correlation) which causes the states to become unstable and decay spontaneously by autoionization.

A second distinctive feature of multielectron atoms, if compared to hydrogenic atoms or single-active electron models, is channel-opening. Each energy N of the parent ion, which for helium corresponds to the energies of a hydrogenic atom of charge $Z = 2$, defines a channel threshold. Above N=2, for any given total symmetry, the asymptotically-free electron can be associated to several different states of the parent ion, e.g., $1s, 2s, 2p$. (see Fig. 12). As we go higher in energy and the value of the principal quantum number N increases, so do the number of open channels. For $N \to \infty$, we approach the double ionization threshold, where both electrons can be released into the continuum, leaving a bare He^{2+} nucleus behind.

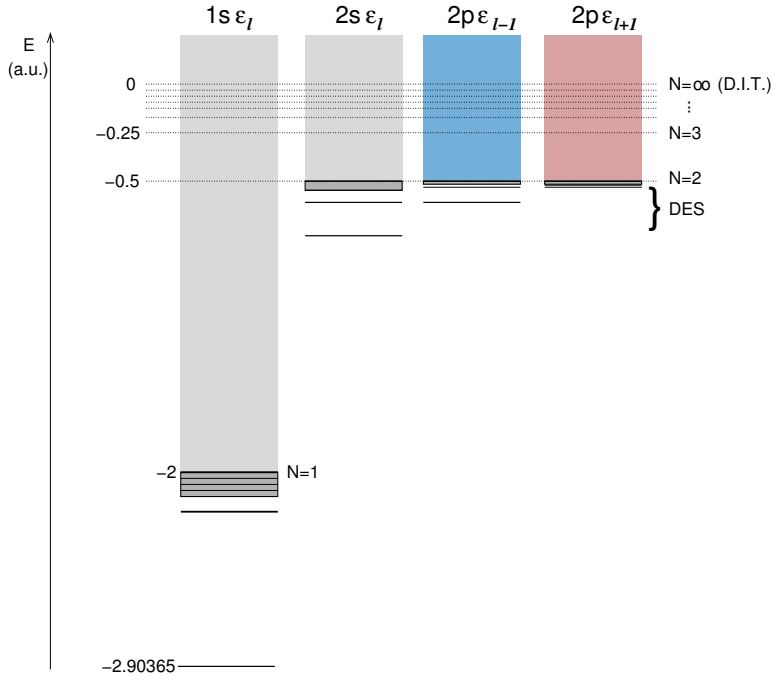

Figure 12: Helium energy scheme for a total angular momentum L=ℓ, showing the single ionization channels which open at the N=1 and N=2 thresholds. The states below N=1 are bound Rydberg states. The doubly-excited states associated to the N=2 excited parent ion give rise to autoionizing states as a result of the interaction with the $1s\epsilon_\ell$ continuum they are embedded in. Nℓ specifies the state of the parent ion, while ϵ_ℓ refers to the energy and orbital angular momentum of the asymptotically free electron.

3.5 ELECTRON CORRELATION IN DOUBLY-EXCITED STATES

Doubly excited states are not easily classified due to the strong *correlation* between the two particles. At the most basic level, two particles are said to be correlated when their pair probability distribution, $P_{12}(\vec{r}_1, \vec{r}_2)$, does not factorize in the product of individual particle distributions, i.e., $P_{12}(\vec{r}_1, \vec{r}_2) \neq P_1(\vec{r}_1) \cdot P_2(\vec{r}_2)$. Due to the antisymmetry requirement imposed by the Pauli principle on the wavefunction, however, it is convenient to distinguish between two kinds of correlation: Fermi correlation and Coulomb correlation. Fermi correlation is due to the fact that electrons are indistinguishable. For example, in the simplest case of a single configuration, in which the wavefunction is the antisymmetrized product of two orbitals, the pair distribution is already non-factorizable. This correlation is already

taken into account in a mean-field approximation. In this context, therefore, a correlated state will be one which needs more than a single pair of orbitals to be described and which is induced by the non-mean-field component of the $1/r_{12}$ electronic repulsion, i.e., the Coulomb correlation. In the case of the He doubly excited states, there is a special long-range correlation associated to the fact that the excited thresholds of He^+, a hydrogenic system, are degenerate. For example, below the N=2 threshold, the states $2snp$ and $2pns$ are degenerate. As a consequence, the state that results from even the slightest interaction between them cannot possibly be described by a single reference determinant. Cooper *et al.* [96] realized that the electron-electron interaction removes this degeneracy, replacing the independent-particle configurations $2snp$ and $2pns$ with the pair

$$\Phi_{sp_n^{\pm}} = 2snp \pm 2pns. \tag{3.70}$$

This first type of correlation thus leads to the classification of DES in terms of the $sp_n^{\pm}$ series. This kind of correlation does not lead by itself to Auger decay. The correlation which does lead to Auger decay is the one that couples these states to the open ionization channels. This term is negligible when the two electrons are far apart from each other, hence the alternative name short range correlation. A schematic diagram showing the two types of correlation is shown in Fig.(13).

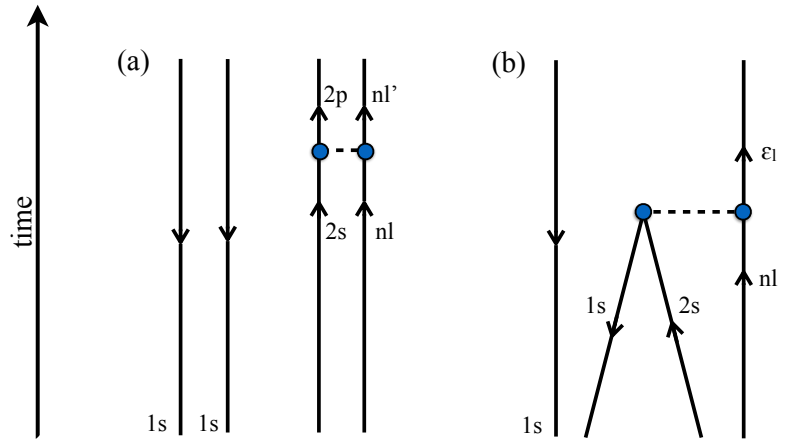

Figure 13: Diagram showing the two types of Coulomb correlation. (a). Long range correlation. Two holes in the 1S orbital and a doubly excited state with $N = 2$, $n = n$. Due to the degeneracy between the $2s$ and $2p$ states, the states of the outer electron are strongly coupled. To lowest order, this coupling results in a correlation that is independent on the excitation of the outer electron. Yet the holes and electrons do not mix. (b). Short range correlation. Starting from the same configuration as in the previous case, the collision between the two electrons can result in a large energy exchange, leading to autoionization.

The effects of long-range and short-range Coulomb correlation are thus particularly evident for doubly excited states. In Fig.(14) we show the isosurface of the conditional probability density $\rho^{(2)}(\vec{r}_1|\vec{r}_2)$ of a doubly-excited wave packet generated by the absorption, from the ground state, of one XUV photon from a single attosecond XUV pulse with 60 eV central energy. The conditional probability density is defined as the probability density of finding electron 1 at a given position in space, once the position of the other electron is fixed,

$$\rho^{(2)}(\vec{r}_1|\vec{r}_2) = \frac{\rho^{(2)}(\vec{r}_1, \vec{r}_2)}{\rho^{(1)}(\vec{r}_2)} \tag{3.71}$$

where $\rho^{(1)}(\vec{r})$ and $\rho^{(2)}(\vec{r}_1, \vec{r}_2)$ are the electron density and the pair density, respectively. In the case of helium:

$$\begin{aligned} \rho^{(2)}(\vec{r}_1, \vec{r}_2) &= \sum_{\xi_1, \xi_2} \Psi^*(\vec{x}_1, x_2)\Psi(x_1, x_2), \quad x_i = (\vec{r}_i, \xi_i), \quad \xi_i = -\frac{1}{2}, \frac{1}{2} \\ \rho^{(1)}(\vec{r}) &= 2 \int d^3r' \rho^{(2)}(\vec{r}, \vec{r}\,'). \end{aligned} \tag{3.72}$$

To illustrate the nodal structure of the wave function, the interior part of the volume delimited by the isosurface is coloured according to the value of the real part of the wave function itself. In the left column, the fixed electron is fixed at a constant distance R from the nucleus, while the polar angle changes from 0 to π. In this case, the distribution is governed by long range (static) correlation. If we write the wavefunction for the doubly excited state of the sp_n^+ series as

$$\Psi_{sp_n^+} = {}^1\Theta(\xi_1, \xi_2)\mathcal{S}\left[2s(\vec{r}_1)np(\vec{r}_2) + 2p(\vec{r}_1)ns(\vec{r}_2)\right] \tag{3.73}$$

where ${}^1\Theta(\xi_1, \xi_2)$ is the singlet spin function and $\mathcal{S}$ is the symmetrizer, and choose the position of the fixed electron such that the value of the parent-ion orbitals are negligible, $2s(\vec{r}_2) \approx 0$ and $2p(\vec{r}_2) \approx 0$, then

$$\Psi_{sp_n^+} \cong \frac{1}{2}{}^1\Theta(\xi_1, \xi_2)\left[2s(\vec{r}_1)np(\vec{r}_2) + 2p(\vec{r}_1)ns(\vec{r}_2)\right]. \tag{3.74}$$

This means that when $\theta_2 = 0$, the parent ion is strongly polarized upward, i.e., towards the outer electron, in a sp orbital; when $\theta_2 = \pi/2$, the parent ion is in a pure p state; finally, when $\theta_2 = \pi$, the parent ion is again strongly polarized towards the outer electron. In other terms, the polarization of the inner electron follows adiabatically the position of the outer electron like a sunflower does with the sun. At a closer inspection, one can see a clear asymmetry of the distribution of the parent ion with respect to the z-axis; and this is because (3.74) does not account for the short-range correlation which, due to electronic repulsion, polarizes the electronic charge. Indeed, configuration mixing is large for DES, and the individual quantum numbers n_1, n_2, ℓ_1, ℓ_2 that we used to identify the state in Equation (3.74) are, in general, not enough to identify a real DES [97].

The central and right columns illustrate the dramatic effect of short-range correlation, in which the distance between the fixed electron and the nucleus now varies.

In two electron atoms or ions, only DES are embedded in the single ionization continuum and, therefore, lead to autoionization. For multi-electron atoms, on the other hand, an electron can be excited to an outer orbital from an inner-valence or core orbital. The resulting singly-excited configurations, therefore, can have high energy and be above the ionization threshold. In poly-electronic atoms, therefore, singly-excited states can also decay by autoionization. For example, in Chapter 5 we will study the autoionization process of the $[\mathrm{Ne}]\,3s\,3p^6\,4p$ singly-excited state of Argon to the two $[\mathrm{Ne}]\,3s^2\,3p^5\,\varepsilon_{s/d}$ ionization continua.

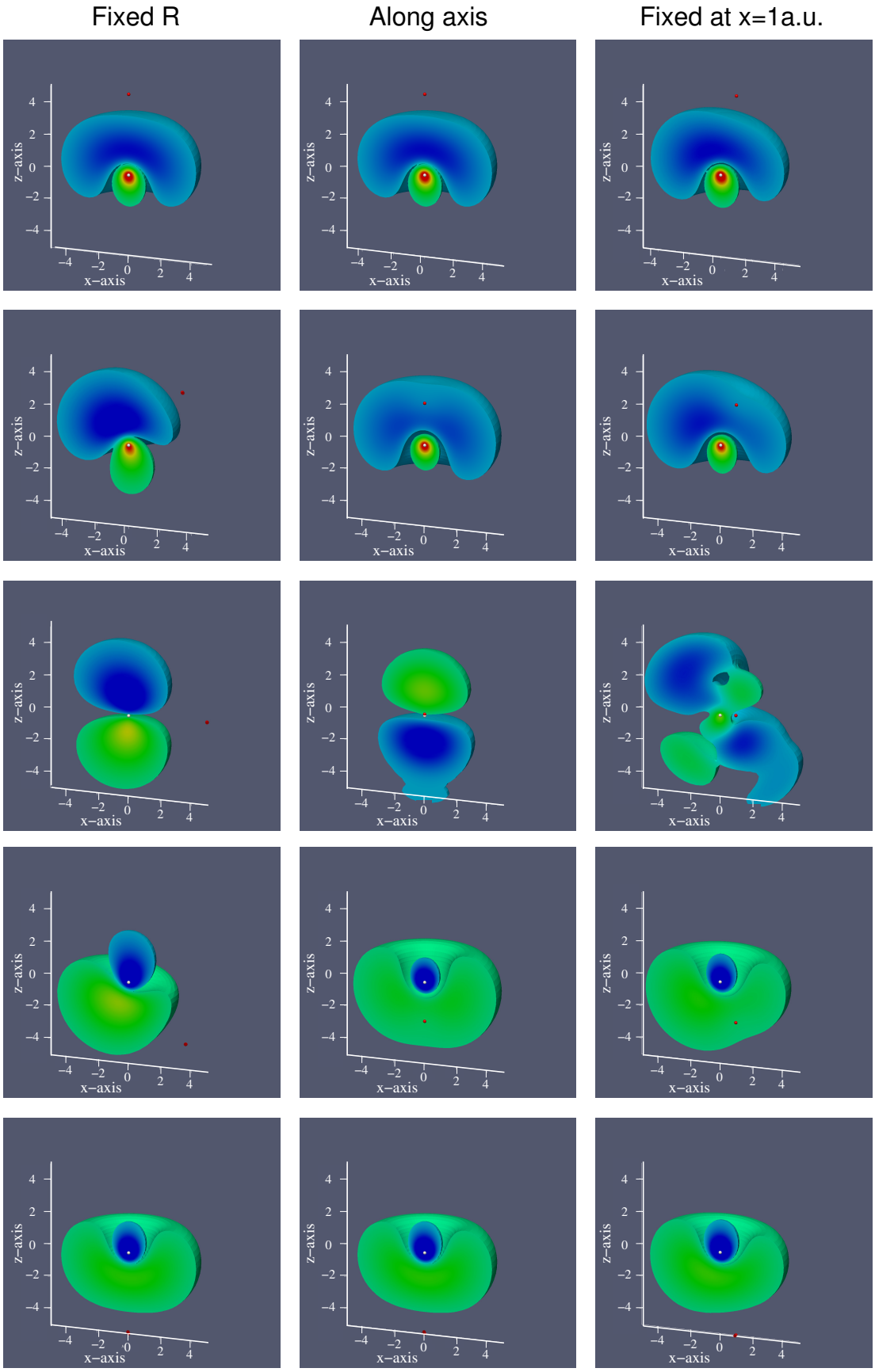

Figure 14: Conditional pair electron density for a superposition of doubly excited states in the $^1P^o$ sp_n^+ series with M=0 (z is the quantization axis). The position of the fixed electron is indicated by a red sphere. The nucleus, shown as a white sphere, is set at the origin. In the left column, the distance r_2 of the fixed electron from the nucleus is kept constant while the polar angle θ_2 is, from top to bottom, 0, $\pi/4$, $\pi/2$, $3\pi/4$, π. In the central column, we varied the position of the electron along the quantization axis. In the right column, the x-coordinate of the fixed electron is set at x=1 a.u. while z changes from 5 to -5.

3.6 *ab initio* DESCRIPTION OF THE HELIUM ATOM

The close-coupling approach described in § 3.2 enforces exact boundary conditions for the problem of single photoionization and hence it can be systematically improved by expanding the set of localized configurations. The practical implementation of this method including all electron-electron interaction effects to machine accuracy, however, is still intractable for atoms with more than few electrons. Helium is one case in which highly accurate numerical solution can be obtained. For this reason, helium is a common benchmark for any *ab initio* calculations. In this section we describe the procedure we used to calculate the eigenenergies and eigenstates of helium as well as the scattering states.

3.6.1 *Numerical basis*

To produce the two-electron basis, we use the close coupling *ansatz* (3.18). The basis is formed by various partial wave channels (PWC),

$$\Phi_{\alpha E} = \mathcal{N}\hat{\mathcal{A}}\,\Theta_{S\Sigma}\,\mathcal{Y}^{L0}_{L_\alpha \ell_\alpha}(\Omega_1,\Omega_2)\,R_{N_\alpha L_\alpha}(r_1)\,\frac{F_{\alpha E}(r_2)}{r_2}, \tag{3.75}$$

where α is an index that uniquely identifies the PWC, $\Theta_{S\Sigma}$ is a two-electron spin function with total spin S and spin projection Σ, which in our case is Θ_{00}. $R_{N_\alpha L_\alpha}$ is the radial part of the frozen He^+ parent ion state with principal quantum number N_α and angular momentum L_α. $F_{\alpha E}$ is the radial function of the second electron, associated to the orbital angular momentum ℓ_α but which is otherwise unconstrained. The function $\mathcal{Y}^{L0}_{L_\alpha \ell_\alpha}$ is a bipolar spherical harmonic [78] with total coupled angular momentum L and projection $M = 0$, defined as

$$\begin{aligned}\mathcal{Y}^{LM}_{L_\alpha \ell_\alpha}(\Omega_1,\Omega_2) &= \sum_{m_1,m_2} C^{LM}_{\ell_1,m_1,\ell_2,m_2} Y_{\ell_1,m_1}(\Omega_1) Y_{\ell_2,m_2}(\Omega_2) \\ &= \left(\langle\Omega_1| \otimes \langle\Omega_2|\right)|\ell_1\ell_2 LM\rangle\,.\end{aligned} \tag{3.76}$$

Finally, $\mathcal{A}$ is the two particle antisymmetrizer, and $\mathcal{N}$ is a normalization factor. The radial wave functions are expressed in terms of B-spline basis functions, which are capable of reproducing bound and continuum states of atomic and molecular wavefunctions with high accuracy [98]. The radial parts of the one particle orbitals $F_{\alpha E}$ are defined so that $\Phi_{\alpha E}$ diagonalize the channel Hamiltonian H_0,

$$\begin{aligned}\langle\Phi_{\alpha E+\varepsilon}|H_0|\Phi_{\alpha E_{\alpha+\varepsilon'}}\rangle &= (E_\alpha+\varepsilon)\delta(\varepsilon-\varepsilon'), \quad \varepsilon > 0, \\ \langle\Phi_{\alpha E+\varepsilon_i}|H_0|\Phi_{\alpha E_{\alpha+\varepsilon_j}}\rangle &= (E_\alpha+\varepsilon_i)\delta_{ij}, \quad \varepsilon_i,\varepsilon_j < 0.\end{aligned} \tag{3.77}$$

In numerical computation, the PWC expansion needs to be truncated and, thus, it is not possible to include all single ionization channels of helium. Moreover, the set of bound states of the parent ion is not complete in the first place. The closed channels of the channel Hamiltonian H_0 (both for single and double electron escape) that are excluded in the truncated close-coupling expansion contribute

STATE	E_{lit}	E_{code}
1s	-2.903 724 377	-2.903 602 759
2s	-2.145 974 046	-2.145 966 683
2p	-2.123 843 086	-2.123 832 661
3s	-2.061 271 989	-2.061 269 940
3p	-2.055 146 362	-2.055 142 999
3d	-2.055 620 732	-2.055 620 575
4s	-2.033 586 717	-2.033 585 860

Table 1: Eigenvalues of the first seven bound states in helium. Comparison between the values obtained from the literature [82], E_{lit}, and the values of our calculation, E_{code}.

to the short range correlation between the two electrons in the single-ionization states of the full Hamiltonian. Since all these channels are closed, however, their wave function at the energy of interest decays exponentially with the radius of any of the electrons. Therefore, to take their contribution into account, it is sufficient to include in the basis a *full-CI* pseudo-state localized channel (LC) composed of a large number of normalized two-electron functions built from localized orbitals. In this way, we effectively complete the functional space required to represent the eigenspace of the full time-independent hamiltonian in any given single-ionization spectral region, attaining both convergence and good accuracy. The final basis is thus built from linearly independent PWC and LC basis functions with well defined S, Σ, L and Π.

The field-free electrostatic hamiltonian H_a of the atom, is fully diagonalized in the ${}^1L^\pi$ basis, and the matrix elements of the dipole operators $\vec{P} = \vec{p}_1 + \vec{p}_2$ and $\vec{R} = \vec{r}_1 + \vec{r}_2$ are computed for both the PWC and the LC basis. This full diagonalization is appropriate to compute the bound states of the system. The use of partial wave channels permits to compute several Rydberg states at a comparatively little cost. The eigenstates of H_a thus obtained form the basis for the time propagation of the atomic state under the action of external fields. The good accuracy of the calculations is illustrated in Table (1) where we compare the first seven bound state energies with values from the literature. In this calculation, we limited the close coupling expansion to the PWCs with N $\leq$ 2: $1sE_L$, $2sE_L$, $2pE_{L+1}$ and $2pE_{L-1}$ (the latter being present only for non-zero total angular momentum L). Short-range correlation in the energy region of interest was found to be adequately taken into account by constructing the LC from orbitals with maximum radius $R_{loc} = 40$ a.u. and with a maximum orbital angular momentum $\ell_{max} = 5$. The number of linearly independent PWC and LC basis functions with well defined S, Σ, L , M and parity obtained with this choice of parameters is comprised between a minimum of 9064 for the ${}^1S^e$ symmetry and a maximum of 13498 for the ${}^1D^e$ symmetry.

3.6.2 *Computation of scattering states. The K-matrix method*

Several methods have been proposed to calculate scattering states; we follow the so-called K-matrix method. The scattering solutions can be expressed in terms of a linear combination of PWC and LC functions by means of the Lippman-Schwinger equation

$$\psi^{\pm}_{\alpha E} = \Phi_{\alpha E} + \sum_{\gamma} \int d\varepsilon \Phi_{\gamma\varepsilon} \frac{1}{E - \varepsilon \pm i0^{+}} \mathbf{T}^{\pm}_{\gamma\varepsilon,\alpha E}, \tag{3.78}$$

where

$$\mathbf{T}^{\pm}_{\gamma\varepsilon,\alpha E} = \langle \Phi_{\gamma\varepsilon} | H_a - H_0 | \psi^{\pm}_{\alpha E} \rangle \tag{3.79}$$

is the off-shell T-matrix [83]. The index γ runs over all open and closed channels, including the localized one. Since the system is invariant under time inversion, we can cast the problem in an alternative form. We look for stationary solutions as opposed to solutions that fulfill incoming and outgoing boundary conditions,

$$\psi^{\mathrm{P}}_{\alpha E} = \Phi_{\alpha E} + \sum_{\gamma} \int d\epsilon \, \Phi_{\gamma\epsilon} \, \mathrm{P} \frac{1}{E - \epsilon} \, \mathbf{K}_{\gamma\epsilon,\alpha E} \tag{3.80}$$

where P indicates the principal part and

$$\mathbf{K}_{\gamma\epsilon,\alpha E} = \langle \Phi_{\gamma\epsilon} | H_a - H_0 | \psi^{\mathrm{P}}_{\alpha E} \rangle \tag{3.81}$$

being $\psi^{\mathrm{P}}_{\alpha E}$ stationary solutions instead of the scattering functions. To find $\Psi^{\mathrm{P}}_{\alpha E}$ numerically, the expression (3.80) is required to fulfill the time independent Schrödinger equation,

$$H\psi^{\mathrm{P}}_{\alpha E} = E\psi^{\mathrm{P}}_{\alpha E}, \tag{3.82}$$

projected on the full numerical basis. The energy integrals in Equation (3.80) are discretized and the resulting linear system is solved for the unknown coefficients $\mathbf{K}_{\gamma\epsilon,\alpha E}$ by means of traditional numerical linear-algebra routines. The scattering states with definite spherical symmetry $\psi^{-}_{\alpha E}$ are then computed as [compare with (3.22)]

$$\psi^{\pm}_{\alpha E} = \sum_{\beta} \psi^{\mathrm{P}}_{\beta E} \left[\frac{1}{\mathbf{1} \pm i\pi \mathbf{K}(E)} \right]_{\beta\alpha} e^{\pm i(\sigma_{\ell_\alpha} + \delta_\alpha - \ell_\alpha \pi/2)}, \quad \langle \psi^{\pm}_{\alpha E} | \psi^{\pm}_{\beta E'} \rangle = \delta_{\alpha\beta} \delta(E - E'), \tag{3.83}$$

where $\mathbf{K}_{\alpha\beta}(E) \equiv \mathbf{K}_{\alpha E,\beta E}$ is the *on-shell* reactance matrix (§7.2.3 in [80]) which is hermitian, while σ_{ℓ_α} and δ_α are the phase shifts introduced in § 3.2.1. The stationary solutions $\psi^{\mathrm{P}}_{\alpha E}$ are not normalized, while $\psi^{\pm}_{\alpha E}$ are. Experimentally, one measures photoelectrons with asymptotically well-defined energy E, direction Ω and spin σ, and ions in well-defined states A. The scattering states $\psi^{-}_{A,E\Omega\sigma}$ required to reproduce the eigenstates of the detector, therefore, are obtained by uncoupling the ionic and electronic orbital spin angular momenta in the channel functions $\psi^{\pm}_{\alpha E}$ and projecting the photoelectron angular momentum states ℓ_α, m_α

onto the asymptotic photoelectron's direction Ω by means of the spherical harmonic $Y^*_{\ell_\alpha m_\alpha}(\Omega)$,

$$\psi^-_{A,E\Omega\sigma} = \sum_{\substack{\alpha \\ N_\alpha = N_A}}^{L_\alpha = L_A} C^{LM}_{L_A M_A, \ell m} C^{S\Sigma}_{(\frac{1}{2})\Sigma_A, (\frac{1}{2})\sigma} Y^*_{\ell m}(\Omega)\, \psi^-_{\alpha E}, \tag{3.84}$$

where L_A, M_A, and Σ_A indicate the angular momentum and spin of the parent ion, σ indicates the photoelectron's spin, and $C^{c\gamma}_{a\alpha,\, b\beta}$ are Clebsch-Gordan coefficients. The states $\psi^-_{A,E\Omega\sigma}$ are normalized according to

$$\langle \psi^-_{A,E\Omega\sigma} | \psi^-_{B,E'\Omega'\sigma'} \rangle = \delta_{AB}\delta_{\sigma\sigma'}\delta(E - E')\delta(\Omega - \Omega'). \tag{3.85}$$

4

THEORETICAL DESCRIPTION OF PUMP-PROBE EXPERIMENTS

In this Chapter, we detail the theoretical methods we employed to describe current attosecond pump-probe experiments. Due to the still comparatively low intensity of the sub-femtosecond XUV pulses [99] obtained with HHG [100], table-top experiments that investigate ultra-fast dynamics generally involve pump-probe schemes comprising a sequence of one or more XUV pulses in conjunction with a replica of the intense compressed Ti-Sapphire IR pulse used to create them [101, 58, 37]. As a result of the interaction with the field, an atomic or molecular target is ionized and the fragments emerging from the reaction centre are collected. The spectral and angular distribution of the photo fragments encode information about all steps of the process triggered by light: the initial excitation out of the original bound state, the field-free evolution of coherent superpositions of states in the continuum during the time gap between pump and probe pulse, the dressed-state dynamics within the IR field as well as further transitions between excited states induced by the probe. Disentangling the contribution of these steps from the experimental result is a hard task which often requires assistance by theory. Indeed, since non-stationary non-perturbative transitions between highly-excited states may be involved, direct solution of the TDSE is often needed to reproduce the experiment in all its aspects and in a quantitative way.

Freezing of selected degrees of freedom in the system, fine tuning of the laser parameters and wave-packet inspection can be used to characterize the underlying ionization mechanism. Yet, these are time-consuming procedures. The analysis of both experiments and theoretical simulations is thus greatly facilitated if major aspects of the results can be explained by simplified models. In the case of atomic photoionization, a most prominent example is the strong-field approximation (SFA) [102, 103, 104], a model which is able to reproduce well broad features of the photoelectron spectrum and which provided valuable insight into several non-perturbative processes triggered by radiation (see, e.g., [105, 106] and references therein). In this thesis, we will consider the soft-photon approximation (SPA) [67], a special case of the SFA. The SPA permits to compute non-resonant photoionization spectra in the presence of strong laser fields. At the basis of the SPA, however, there is the assumption that the photoelectron is essentially free once the atom is ionized, and that its dynamics is determined by its interaction with the external field alone. As a consequence, the SPA is not suited to describe ionization processes in which the structure of the electronic continuum, such as the one due to resonant states and threshold openings, play a major role.

In the opposite limit of weak external fields, for which a perturbative approach is applicable, the role of transiently bound states can be accounted for by the Fano model of autoionizing states presented in §3.3 [52]. Despite the extensive interest that autoionizing states in interaction with external fields has attracted across the last three decades, it is only recently that the characteristic manifestation of metastables states in attosecond experiments has started to be appreciated [54, 63]. On the light of the most recent developments in time-resolved study of Auger decay and of continuum-continuum coherent transitions, a generalization of existing models to current ultrafast time-resolved laser schemes is needed.

This Chapter is divided into the following sections. In §4.2 we describe the *ab intitio* method we used to extract the photoelectron and transient absorption spectra of helium. In §4.3 we discuss and extend the SPA to treat realistic effects in current attosecond experiments. In the last section, §4.4, we provide an analytical perturbative model to describe finite-pulse pump-probe schemes with intermediate and final autoionizing states.

4.1 THE PUMP-PROBE SCHEME

In pump-probe experiments, the total external field is the sum of a pump field $F_1(t)$, which can be assumed not to depend on the pump-probe time delay, thus defining the time reference, and of a probe field $F_2(t;\tau) \equiv F_2(t-\tau)$, delayed with respect to the pump by a time lapse τ (see Fig. 15a),

$$F(t) = F_1(t) + F_2(t-\tau). \tag{4.1}$$

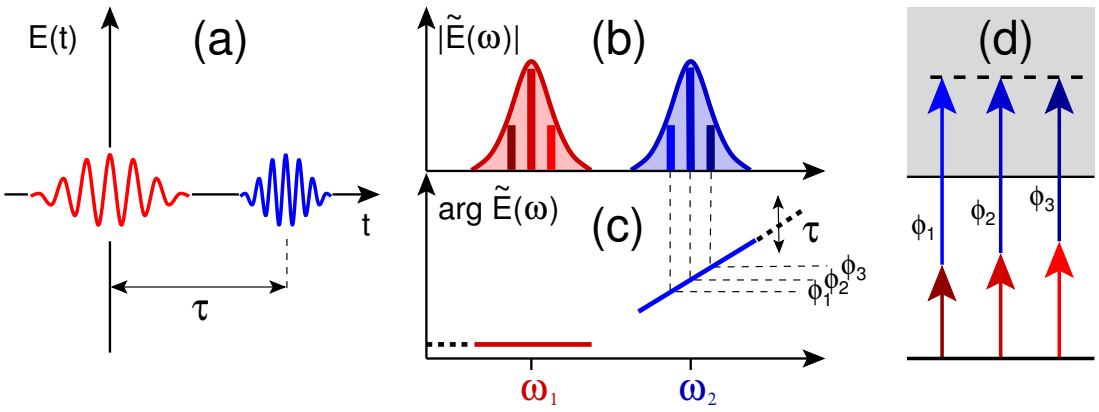

Figure 15: Pump-probe scheme. (a) Temporal perspective: the second pulse is centered at a time τ from the first pulse, which defines the time origin. (b) With non-overlapping pump and probe spectra, the photon distribution of the pump-probe sequence does not depend on the delay between the two pulses. (c) The relative phase between different frequency components of the field, however, does depend on the time delay. (d) Since the same final energy can be reached with different combinations of the energies contained in the two pulses, the corresponding amplitudes can interfere constructively or destructively depending on their mutual phases and, in turn, on the pump-probe time delay.

The FT of the total field has a simple parametrization in terms of the FT of the pump and non-delayed probe pulses (Fig. 15b,c),

$$\tilde{F}(\omega) = \tilde{F}_1(\omega) + \tilde{F}_2(\omega)e^{i\omega\tau}. \tag{4.2}$$

In attosecond experiments, the time lapse τ can be controlled with attosecond resolution. By recording the photoelectron or the transient absorption spectrum at several time delays, a picture of the evolution of the atomic or molecular system at the attosecond time scale emerges. In all of the cases considered in this thesis, the pump photon will have XUV frequency, while the laser probe (or laser-dressing) field will be either of IR or visible (VIS) frequency.

4.2 *ab initio* SOLUTION OF THE TDSE

We wish to find the solutions of the TDSE for the Hamiltonian

$$H = H_a + V_{abs} + H_{int}, \tag{4.3}$$

where H_a is the field-free Hamiltonian of helium,

$$H_a = \frac{p_1^2}{2} + \frac{p_2^2}{2} - \frac{2}{r_1} - \frac{2}{r_2} + \frac{1}{r_{12}}. \tag{4.4}$$

The properties and numerical ways of computing single-ionization eigenstates of (4.4) were already discussed in § 3.6.1. H_{int} is the interaction Hamiltonian (see § 2.1.1), which we calculate in both velocity (2.15) and length gauges (2.17), and V_{abs} is a symmetric complex absorption potential that prevents reflections from the boundary of the quantization box where the wave function is defined. The absorption potential is given by

$$V_{abs}(\vec{r_1}, \vec{r_2}) = v_{abs}(r_1) + v_{abs}(r_2), \quad v_{abs}(r) = -ic_{abs}\theta(r - R_{abs})(r - R_{abs})^2, \tag{4.5}$$

where $\theta(x)$ is the Heaviside step function. In our calculations, we used the values of $c_{abs} = 5 \cdot 10^{-5}$ a.u. and $R_{abs} = R_{box} - 100$ a.u.

4.2.1 *Time evolution of the wave function*

The temporal evolution of the wave function ψ is computed using a second-order midpoint exponential time-step propagator:

$$\psi(t + dt) = e^{-iV_{abs}dt}e^{-iH_a dt/2}e^{-iH_{int}(t+dt/2)dt}e^{-iH_a dt/2}\,\psi(t) + o(dt^3). \tag{4.6}$$

In the implementation we use, the propagator and the wave functions are projected on the eigenstates of the field-free hamiltonian within the numerical B-spline close coupling basis. Hence, the field-free Hamiltonian H_a and the corresponding half-time-step propagator are diagonal. The action of the exponential containing the interaction term, which depends on the external fields and

couples blocks with different symmetry, is evaluated with an iterative Krylov-space method. The starting point is the construction of a Krylov space, which is generated by the repeated action of $A \equiv H_{int}(t + dt/2)dt$ on the state $\phi_0 \equiv \psi$: $\phi_{i+1} = A\phi_i$. The set of vectors $\{\phi_i\}$ thus generated, which is not orthogonal, is orthonormalized by a Gram-Schmidt procedure

$$|\bar{\varphi}_i\rangle = |\phi_i\rangle - \sum_{j=0}^{i-1} |\varphi_i\rangle \langle\varphi_i|\phi_i\rangle, \quad |\varphi_i\rangle = |\bar{\varphi}_i\rangle / ||\bar{\varphi}_i||. \tag{4.7}$$

In this way, we get the orthonormalized Krylov basis $\{\varphi_i\}$. The Hamiltonian is then approximated as an $(N+1) \times (N+1)$ matrix in this basis,

$$A \sim A^{(N)} = \sum_{ij} |\varphi_i\rangle A_{ij}^{(N)} \langle\varphi_j|, \qquad A_{ij}^{(N)} = \langle\varphi_i|A|\varphi_j\rangle \tag{4.8}$$

In the limit $N \to \infty$, the eigenvalues and eigenvectors of the approximated Hamiltonian will converge to those represented in the real spectrum of ψ. A value of $N < 10$ is typically sufficient to represent the time evolution of ψ across an interval of the order of 1 as induced by moderately intense lasers, $I \simeq 10^{14}$ W/cm^2. A direct diagonalization of such matrices can then be easily performed,

$$A^{(N)} \simeq \sum_i |\chi_i^N\rangle \lambda_i^{(N)} \langle\chi_i^N|. \tag{4.9}$$

The exponential of $A^{(N)}$ is exactly known

$$e^{-iA^{(N)}} = \sum_i |\chi_i^N\rangle e^{-i\lambda_i^{(N)}} \langle\chi_i^N|. \tag{4.10}$$

The operator containing the interaction Hamiltonian in Equation (4.6) is then approximated with the Krylov operator [Equation (4.9)], yielding

$$\psi'(t + dt) = e^{-iH_{int}(t+dt/2)dt}\psi(t) \simeq \sum_i |\chi_i^N\rangle e^{-i\lambda_i^{(N)}} \langle\chi_l^N|\psi(t)\rangle. \tag{4.11}$$

The numerical algorithm described above (Arnoldi's) does not make any explicit use of the hermiticity of A and therefore it is also suited to deal with non-hermitian matrices. Even if this feature has not been used here, it leaves open the possibility of incorporating the absorption potential in the field-free Hamiltonian that defines the spectral basis in terms of which the time-dependent wave function is expressed.

Once the external field has vanished, the propagation is dictated by a time-independent quenched Hamilonian, $H_Q = H_a + V_{abs}$, whose complex eigenvalues E_i^Q have non-positive imaginary components

$$H_Q = \sum_i |\varphi_{R,i}\rangle E_i \langle\varphi_{L,i}|, \quad \langle\varphi_{L,i}|\varphi_{R,j}\rangle = \delta_{ij}, \quad \Im E_i \leq 0 \ \forall i. \tag{4.12}$$

The states $\varphi_{L/R}$ are the left and right eigenstates of H_Q. The wave function evolution then becomes trivial,

$$\psi(t) = \sum_i |\varphi_{R,i}\rangle e^{iE_i^Q(t-t')} c_i(t'), \quad c_i(t') = \langle\varphi_{L,i}|\psi(t')\rangle. \tag{4.13}$$

4.2.2 *Extraction of photoelectron distributions*

To obtain the photoelectron distributions, the most straightforward method is to project the calculated wave function onto the channel eigenstates $\Phi_{\alpha E}(t)$ at $t \to \infty$. In many cases, however, this procedure may not be practicable because the time needed to obtain such asymptotic states can be prohibitively long. This is the case, for example, if long-lived resonances are populated, or if the wave packet contains components close to ionization thresholds, with vanishingly small kinetic energy that take exceedingly long times to reach large distances. We can circumvent this limitations using scattering states of the field-free atomic Hamiltonian H_a, as we mentioned in § 2.3.1.

To extract channel resolved photoelectron distributions, the final wave function is projected on the complete set of multi-channel scattering states computed with the K-matrix method detailed in § 3.6.2,

$$\frac{dP^{(\alpha)}_{A,E\Omega\sigma}}{dEd\Omega} = |\langle \Psi^{-}_{A\alpha\Omega\sigma}|\Psi(t)\rangle|^2. \tag{4.14}$$

4.2.3 *Calculation of transient absorption spectra*

To calculate the transient absorption cross section (see derivation in § 2.3.2),

$$\sigma(\omega;\tilde{A}) = 4\pi\alpha\omega^{-1}\,\Im\left[\frac{\tilde{p}(\omega)}{\tilde{A}(\omega)}\right], \tag{4.15}$$

that depends on the Fourier transform of the canonical momentum $p(\omega)$, we need the expectation value of $p(t)$ at arbitrarily large times t. The canonical momentum can be conveniently split into two smooth components

$$\begin{aligned} p(t) &= p^{-}(t) + p^{+}(t), \quad p^{-}(t) = \left[1 - \phi\left(\frac{t-t_c}{\sigma_c}\right)\right] p(t), \\ p^{+}(t) &= \phi\left(\frac{t-t_c}{\sigma_c}\right) p(t); \quad \phi(t) = \int_{-\infty}^{t} \frac{e^{-x^2/2}}{\sqrt{2\pi}} dx, \end{aligned} \tag{4.16}$$

defined in such a way that $p^{-}(t)$ coincides with $p(t)$ until the external field is over, and it becomes negligible, across a short time interval, shortly after the external field has vanished. Conversely, $p^{+}(t) = p(t) - p^{-}(t)$ is zero while the external field is active. In absence of external fields, the time evolution of the simulated system is exactly expressed in terms of the eigenstates of the quenched Hamiltonian [Equation (4.13)]. Therefore, if we assume that the population of the atom is mostly in the ground state,

$$p^{+}(t) = \phi\left(\frac{t-t_c}{\sigma_c}\right)\left\{p_{g,R_i}\, c^{*}_{g}(t_c) c_i(t_c) e^{-i(E_i - E^{*}_{g})(t-t_c)} + \text{c.c.}\right\}, \tag{4.17}$$

where $p_{g,R_i} = \langle \varphi_{L,g} | \hat{p} | \varphi_{R,i} \rangle$ is the dipole matrix element between a right eigenstate i and the ground state. As a result of the separation in Equation (4.16), the Fourier transform of $p(t)$ splits in two terms,

$$\tilde{p}(\omega) = \tilde{p}^{-}(\omega) + \tilde{p}^{+}(\omega). \tag{4.18}$$

The first Fourier transform, $\tilde{p}^{-}(\omega)$, is evaluated numerically from tabulated values of $p(t)$ on a dense time grid. The second Fourier transform, on the other hand, can be evaluated analytically

$$p^{+}(\omega) = \frac{i}{\sqrt{2\pi}} \frac{e^{i\omega t_c}}{\omega - \omega_{ig} + i0^{+}} p_{g,R_i} e^{-\frac{1}{2}\sigma_c^2(\omega-\omega_0)^2} c_g^*(t_c) c_i(t_c) + \{\text{c.c.}(\omega \to -\omega)\}. \tag{4.19}$$

This way of proceeding provides the same results as an infinite time propagation.

4.3 THE SOFT-PHOTON APPROXIMATION

Let us now turn our attention to the process of laser-assisted photoionization within the SPA. The SPA is a special case of the strong field approximation in which the dressing field is not strong enough to ionize the atom, while the central frequency ω_{XUV} of the pump pulse is assumed to be sufficiently high to drive the photoelectron well above the ionization threshold, $\omega_{\text{XUV}} - IP >> U_p$, where IP is the ionization potential and U_p is the ponderomotive potential. In these conditions, the dressing field promotes multi-photon transitions between continuum states, but the final photoelectron spectrum still lies well above the ionization threshold and recollision is excluded. This is equivalent to considering the limit $n\omega_{\text{IR}} << E_{\text{XUV}}$, where n is the number of dressed photons exchanged, ω_{IR} is the dressing laser frequency and E_{XUV} is the photoelectron kinetic energy resulting from the interaction with the pump pulse alone.

We first consider the motion of a free electron in an electromagnetic field. The minimal coupling Hamiltonian in velocity gauge is given by $H_{mc}^{v} = \alpha \vec{p} \cdot \vec{A}(t)$ [Equation (2.15)], and the TDSE reads

$$i\partial_t \Psi(t) = [\frac{p^2}{2} + \alpha\, \vec{p} \cdot \vec{A}(t)]\, \Psi(t). \tag{4.20}$$

Since the Hamiltonian is a function of the linear momentum $\vec{p}$, its eigenfunctions are plane waves with the following time dependence,

$$\Psi_{\vec{k}}^{V}(t) = \chi_{\vec{k}}(\vec{r}) \exp\left[-i\frac{k^2}{2}t - i\Theta(t)\right], \quad \chi_{\vec{k}}(\vec{r}) = \langle \vec{r} | \vec{k} \rangle = \frac{e^{i\vec{k}\cdot\vec{r}}}{(2\pi)^{3/2}}, \tag{4.21}$$

where

$$\Theta(t) = \alpha\, \vec{k} \cdot \int_0^t d\tau\, \vec{A}_{IR}(\tau). \tag{4.22}$$

Equation (4.21) is known as a Volkov state.

Let us now consider an atom A in its ground state $|\phi_g\rangle$ subject to a strong IR pulse and a weak XUV pulse (or pulse train) triggering the ionization process

$$\mathrm{A} + \gamma_{\mathrm{XUV}} \pm n\gamma_{\mathrm{IR}} \rightarrow \mathrm{A}^+ + e^-_{\vec{k}}, \tag{4.23}$$

where $\vec{k}$ is the momentum of the ejected photoelectron. The evolution of the system is dictated by the time-dependent Hamiltonian, given by

$$H = H_a + \alpha \left[\vec{A}_{\mathrm{IR}}(t) + \vec{A}_{\mathrm{XUV}}(t)\right] \cdot \vec{P}, \tag{4.24}$$

where $\vec{A}_{\mathrm{XUV}}$ and $\vec{A}_{\mathrm{IR}}$ are the transverse vector potentials of the XUV and IR pulses, respectively. Since the XUV field is assumed to be weak, its effects can be treated at the level of the first-order time-dependent perturbation theory. If the intensity of the IR field is to take on large values, however, the interaction of the atom with it must be treated non-perturbatively. Therefore, the transition amplitude $\mathcal{A}_{\alpha\leftarrow g}$ from the initial state $|\psi_g\rangle$ to a final (out) scattering state $|\psi^-_\lambda\rangle$ in channel λ, is given by the generalized expression

$$\mathcal{A}_{\lambda\leftarrow g} = -i \int_{-\infty}^{+\infty} \langle \phi^-_\lambda(t)|\alpha\, \vec{A}_{\mathrm{XUV}}(t) \cdot \vec{P}|\phi^+_g(t)\rangle dt, \tag{4.25}$$

where $|\phi^+_g(t)\rangle$ and $|\phi^-_\lambda(t)\rangle$ are the dressed states of the time-dependent Hamiltonian

$$H_F = H_0 + \alpha \vec{A}_{\mathrm{IR}}(t) \cdot \vec{P}, \tag{4.26}$$

which fulfill assigned asymptotic conditions at $t \rightarrow \mp\infty$, respectively,

$$i\partial_t|\phi^+_g\rangle = H_F(t)|\phi^+_g\rangle, \quad \lim_{t\rightarrow-\infty} e^{iE_g t}|\phi^+_g(t)\rangle = |\psi_g\rangle, \tag{4.27}$$

$$i\partial_t|\phi^-_\lambda\rangle = H_F(t)|\phi^-_\lambda\rangle \quad \lim_{t\rightarrow+\infty} e^{iE_\lambda t}|\phi^-_\alpha(t)\rangle = |\psi^-_\lambda\rangle, \tag{4.28}$$

where E_g and E_λ are the initial and final energy, respectively.

To evaluate Equation (4.25) within the SPA, we make three approximations. First, that the ground state $|\psi_g\rangle$ is unaffected by the IR field, i.e., $|\phi^+_g(t)\rangle = e^{-iE_g t}|\psi_g(t)\rangle$ identically. Second, that the atom behaves as an hydrogenic system which is ionized from the $1s$ orbital. Third, the interaction of the emitted photoelectron with the parent ion is neglected altogether. Less severe approximations which account for the interaction of the bound state with the dressing field [67], and for the interaction of the continuum state with the parent ion [107, 108] at a perturbative level have been considered in the past. These investigations confirm that if the neutral atom has large excitation energies, as it is certainly the case for the helium atom, which is the system to which we will apply the SPA, and the final energy of the photoelectrons are sufficiently far from the ionization threshold, these are reasonable approximations in many realistic conditions such as $\omega_{\mathrm{XUV}} = 60$ eV, $I_{\mathrm{IR}} = 10^{14}$ W/cm^2, $\omega_{\mathrm{IR}} = 1.5$ eV. Under these assumptions, the final state $|\phi^-_\lambda(t)\rangle$ in Equation (4.25) can be approximated with a Volkov state [Equation (4.21)].

4.3.1 *Long pulse limit*

For a monochromatic IR field,

$$\vec{A}_{\mathrm{IR}}(t) = A_0 \cos(\omega_{\mathrm{IR}} t + \varphi_{\mathrm{IR}})\hat{\epsilon}, \tag{4.29}$$

where A_0, ω_{IR}, φ_{IR}, and $\hat{\epsilon}$ are the field amplitude, frequency, phase and polarization, respectively, the time-dependent phase $\Theta(t)$ reads

$$\Theta(t) = \vec{\alpha}_0 \cdot \vec{k} \sin(\omega_{\mathrm{IR}} t + \varphi_{\mathrm{IR}}) \; - \; \vec{\alpha}_0 \cdot \vec{k} \sin(\varphi_{\mathrm{IR}}), \tag{4.30}$$

where we introduced the free-electron excursion amplitude $\vec{\alpha}_0 = \alpha \omega_{\mathrm{IR}}^{-1} A_0 \hat{\epsilon}$. The second term on the RHS of Equation (4.30) results in a time-independent phase factor in the wave function, equivalent to an intensity-dependent phase convention for the plane wave basis, which disappears when taking the square module of the transition amplitudes to compute observable quantities. Therefore, in the following we will simply neglect it. We can apply, as usual [79], the Jacobi-Anger expansion [109] to obtain

$$|\Psi_{\vec{k}}(t;\vec{\alpha}_0)\rangle = |\vec{k}\rangle \sum_{n=-\infty}^{\infty} J_n(\vec{\alpha}_0 \cdot \vec{k}) \, \exp\left[-i\left(k^2/2 + n\omega_{\mathrm{IR}}\right) t - in\varphi_{\mathrm{IR}}\right] \tag{4.31}$$

where J_n are Bessel functions. If we substitute Equation (4.31) in Equation (4.25), we obtain

$$\mathcal{A}_{\vec{k}\leftarrow g} \cong -i\sqrt{2\pi}\,\alpha\,(\vec{k}\cdot\hat{\epsilon})\,\phi_{\mathrm{g}}(k) \sum_{n=-\infty}^{+\infty} J_n(\xi\, x)\, e^{in\varphi_{\mathrm{IR}}}\, \tilde{A}_{\mathrm{XUV}}\left(E_{\mathrm{g}} - k^2/2 - n\omega_{\mathrm{IR}}\right), \tag{4.32}$$

where $\phi_{\mathrm{g}}(k)$ is the momentum representation of a $1s$ orbital with effective charge Z [73],

$$\phi_{1s}(k) = \frac{2\sqrt{2}\, Z^{5/2}}{\pi[k^2 + Z^2]^2}, \tag{4.33}$$

x is the cosine of the angle formed by the photoelectron momentum and the laser polarization, and where we introduced the reduced field strengths $\xi = \alpha_0 k$. The reduced field strength, formulated in terms of the photoelectron energy E_{e} and of the IR intensity I_{IR} expressed in TW/cm^2,

$$\xi = \frac{4\sqrt{\pi\alpha}\; E_{\mathrm{e}}^{1/2}}{\omega_{\mathrm{IR}}^2} \sqrt{\frac{I_{\mathrm{IR}}(\mathrm{TW/cm^2})}{3.51 \cdot 10^4 \ \mathrm{TW/cm^2}}}, \tag{4.34}$$

is a very convenient quantity in the context of attosecond pump-probe experiments, since, $E_{\mathrm{e}} = 1$ a.u., an intensity $I_{\mathrm{IR}} = 1$ TW/cm^2, and a driving laser frequency $\omega_{\mathrm{IR}} = 0.05712$a.u. (a common order of magnitude for compressed Ti-Sapphire pulses), corresponds to $\xi \simeq 0.99$, i.e., it is essentially equivalent to one reduced field strength unit. Equation (4.32) can be directly used to compute the photoelectron distribution as

$$\frac{dP_{E\hat{\Omega}\leftarrow g}}{dE\, d\Omega} = k \left|\mathcal{A}_{\vec{k}\leftarrow g}\right|^2 \tag{4.35}$$

and applied to several cases of interest. In the § 5.1 we will examine a few. For monochromatic XUV pulses, further simplifications of Equation (4.35) are possible [104, 106, 67]. Here, however, we are more interested on broadband XUV pulses in general, and on APTs in particular.

4.3.2 *Finite pulses*

To the best of our knowledge, the SPA has only been used in the monochromatic IR version outlined in the previous paragraph. This approximation, however, is justified only if the envelope of the dressing pulse does not change significantly across the duration of the XUV field. This is certainly the case of single attosecond pulses (SAPs), where the full width at half-maximum (fwhm) of the XUV does not exceed a half period of the IR (streaking conditions). It is generally the case in the RABITT method as well, since common IR pulses have a duration of few tens of femtoseconds, which is longer than the common duration of an APT. Yet, compressed IR pulses with a duration of only a few femtoseconds are routinely produced [19, 18] and it is in principle possible to devise an experiment where an APT is aligned to a compressed replica of the IR pulse used to generate it and which could easily be as short as the APT itself. Furthermore, use of short IR pulses is common practice when solving the TDSE to limit the cost of computation, or even to render the simulation possible altogether. The IR modulation can be appropriately accounted for with a truncated cosine-square envelope:

$$\vec{A}_{\text{IR}}(t) \;=\; \begin{cases} A_0\,\hat{\epsilon}\,\cos^2[\Omega(t-\tau)]\,\cos[\omega_{\text{IR}}(t-\tau)+\varphi_{\text{IR}}], & \text{for} |t-\tau| < \frac{\pi}{2\Omega} \\ \vec{0}, & \text{otherwise}\ , \end{cases} \tag{4.36}$$

where τ is the time delay between the IR and XUV pulses (assumed to be located at the center of the IR pulse). Since in the SPA model we are dealing with a structureless continuum, the multi-photon transition amplitudes which involve the absorption of at least one photon from the XUV field, rapidly vanish as soon as the XUV and the IR pulses do not overlap. As a consequence, to examine the influence of a finite duration of the IR dressing field, one can replace the cosine-square single IR pulse in Equation (4.36) by a cosine-square periodic envelope,

$$\vec{A}_{\text{IR}}(t) \;=\; A_0\,\hat{\epsilon}\,\cos^2[\Omega(t-\tau)]\,\cos[\omega_{\text{IR}}(t-\tau)+\varphi_{\text{IR}}] \qquad \forall t, \tag{4.37}$$

which corresponds to a non-truncated trichromatic IR field with well defined phase and intensity relations between the three frequency components of the envelope. As long as all the XUV pulses lie well within the region $|t-\tau| < \frac{\pi}{2\Omega}$, the contributions to the signal that come from the other oscillations of the IR envelope can be safely neglected. This periodic configuration for the IR dressing field, therefore, is appropriate to simulate the case of a finite IR pulse. With this choice, the free photoelectron will be indefinitely driven by the IR field, with no consequences other than an irrelevant phase factor due to forward Compton scattering. The phase $\Theta(t)$ in Equation (4.21) for the Volkov state in the presence of a modulated IR is

$$\Theta(t) = \vec{\alpha}_0 \cdot \vec{k}\ \cos^2[\Omega(t-\tau)]\sin[\omega_{\text{IR}}(t-\tau)+\varphi_{\text{IR}}] + o(\Omega/\omega_{\text{IR}}) + const. \tag{4.38}$$

The time-independent term *const* can be ignored, as we did in the case of Equation (4.30). The higher-order correction $o(\Omega/\omega_{\text{IR}})$ alters slightly the proportions of the monochromatic components of the zeroth-order term. If needed, it can be

taken into account exactly; yet, it can generally be safely neglected. If we do so, the three frequency components of $\Theta(t)$ are

$$\Theta(t) \simeq \frac{\vec{\alpha}_0 \cdot \vec{k}}{4} \Big\{ 2\sin\left[\omega_{\mathrm{IR}}(t-\tau)+\varphi_{\mathrm{IR}}\right] + \sin\left[(\omega_{\mathrm{IR}}+2\Omega)(t-\tau)+\varphi_{\mathrm{IR}}\right] + \sin\left[(\omega_{\mathrm{IR}}-2\Omega)(t-\tau)+\varphi_{\mathrm{IR}}\right] \Big\}, \tag{4.39}$$

so the Volkov phase factor for such field is just the product of the Volkov factors for the three individual monochromatic field components [see (4.31)]

$$\Psi_{\vec{k}}(\vec{r},t) \cong |\vec{k}\rangle \exp\left(-i\frac{k^2}{2}t\right) \sum_{\{n_i\}} J_{n_1}\left(\frac{x\,\xi}{2}\right) J_{n_2}\left(\frac{x\,\xi}{4}\right) J_{n_3}\left(\frac{x\,\xi}{4}\right) \times \exp\{-i\,n_{\mathrm{tot}}[\omega_{\mathrm{IR}}(t-\tau)+\varphi_{\mathrm{IR}}]\} \exp[-4i(n_3-n_2)\Omega(t-\tau)] \tag{4.40}$$

where the sum runs over all positive and negative integer values of the three n_i indexes, $n_{\mathrm{tot}} = n_1 + n_2 + n_3$. The transition amplitude is finally

$$A_{\vec{k}\leftarrow 0} \cong -i\sqrt{2\pi}\,\alpha\,x\,k\,\phi_g(k) \sum_{\{n_i\}} J_{n_1}\left(\tfrac{x\,\xi}{2}\right) J_{n_2}\left(\tfrac{x\,\xi}{4}\right) J_{n_3}\left(\tfrac{x\,\xi}{4}\right) \times \times \exp\left[i n_{\mathrm{tot}}(\varphi_{\mathrm{IR}}+\omega_{\mathrm{IR}}\tau) - 2i(n_3-n_2)\Omega\,\tau\right] \times \times \tilde{A}_{\mathrm{XUV}}\left[E_g - \tfrac{k^2}{2} - n_{\mathrm{tot}}\omega_{\mathrm{IR}} + 2(n_2-n_3)\Omega\right]. \tag{4.41}$$

In the low intensity limit, we recover the two-photon transition amplitude from the lowest-order perturbative treatment in the plane-wave approximation. The integrated sideband signal is given by

$$I_{2n} = \int_{E-}^{E+} dE \int d\Omega\,\sqrt{2E}\,|\mathcal{A}_{\vec{k}\leftarrow g}|^2, \quad E_\pm = E_g + \frac{4n\pm 1}{2}\,\omega_{\mathrm{IR}} \tag{4.42}$$

4.3.3 RABITT *for high intense fields*

Key to the standard application of the RABITT technique is the perturbative approximation where only one IR photon is assumed to be exchanged with the atom. At intensities of the order of 1 TW/cm^2, however, additional paths that imply the exchange of two or more IR photons become important (see Fig. 16). As a consequence, several transition matrix elements contribute to give rise to the variation of the photoelectron sideband intensity as a function of the time delay. In particular, on the side to the fundamental RABITT frequency $2\omega_{\mathrm{IR}}$, several overtones $2n\omega_{\mathrm{IR}}$ appear, which have an involved relation with the phases of the harmonics in the train.

For this reason, high intensities are generally considered detrimental to the resolution with which the RABITT technique can reconstruct the average profile of an attosecond pulse within the train [110]. This does not have to be necessarily the case, however, if a reliable correspondence between the sideband signal and the underlying harmonics beyond the perturbative regime can be established.

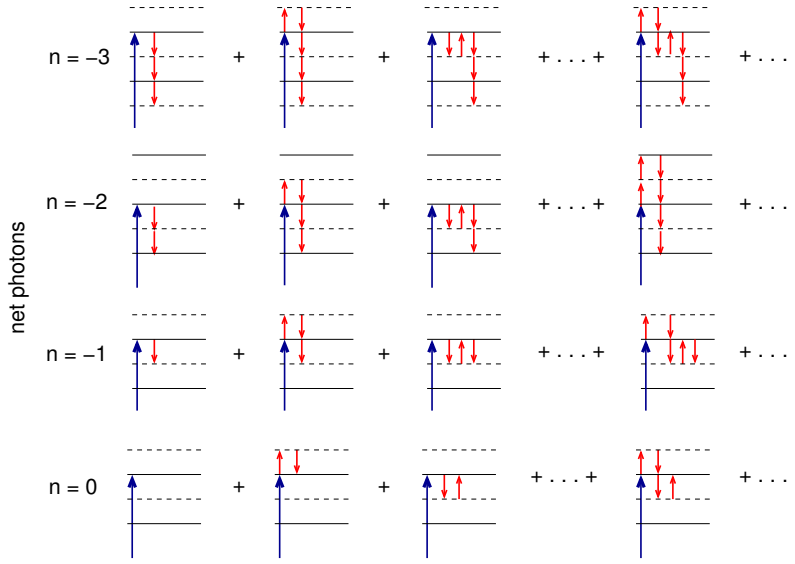

Figure 16: For intense dressing fields, several IR photons can be exchanged. For each amplitude that corresponds to a net number of IR photons absorbed or emitted, an infinite number of diagrams contribute. The soft-photon approximation adds up to infinite order the contribution of all the time-ordered diagram where the first absorbed photon is from the XUV field. The amplitude for a net exchange of n IR photons carries the phase $n\varphi_{\mathrm{IR}} = n\omega_{\mathrm{IR}} t_{\mathrm{d}} + \varphi_{\mathrm{IR},0}$. As a consequence, overtones at all even multiples $2m\omega_{\mathrm{IR}}$ of the dressing-laser fundamental frequency will appear in the time-delay dependence of the sideband intensity (only amplitudes with an odd net number of exchanged IR photons can contribute to sidebands).

To gain insight on the dependence of the sideband signal on the intensity of the dressing laser, let us consider the limiting case of a frequency comb [111], i.e., of a wide XUV spectrum formed by series of equally narrow peaks with similar height and in phase with each other. In this case, the XUV field comes in the form of a very long sequence of very short XUV pulses. We can extrapolate the SPA to this limit, and obtain an analytical expression for the intensity of all the discrete frequency components of the sidebands as a function of the time delay. Let us assume that the comb Fourier spectrum has the following expression (see Appendix A),

$$\tilde{\mathcal{A}}_{\mathrm{XUV}}(\omega) = A_0\,\omega_{\mathrm{IR}} \sum_{i=-\infty}^{+\infty} \tilde{g}\left[\omega - (2i+1)\omega_{\mathrm{IR}}\right], \tag{4.43}$$

where $\tilde{g}(\omega)$ is a sharp function centred in a small neighbourhood of $\omega = 0$. If we focus on the sideband $2m$, the photoelectron signal is negligible unless the electron final kinetic energy lies in the close vicinity of $E_{\mathrm{g}} + 2m\omega_{\mathrm{IR}}$, $k^2/2 = E_{\mathrm{g}} + 2m\omega_{\mathrm{IR}} + \varepsilon$. When inserted in Equation (4.32), therefore, Equation (4.43) gives rise to factors of the form

$$\tilde{g}[-(2m+n+2i+1)\omega_{\mathrm{IR}} + \varepsilon], \tag{4.44}$$

which are non-negligible only if $2m + n + 2i + 1 = 0$. As a consequence, only net exchanges of an odd number n of IR photons can contribute. The amplitude in Equation (4.32) is then,

$$\mathcal{A}_{\vec{k}\leftarrow 0} \cong -i\,A_0\,\omega_{\mathrm{IR}}\sqrt{2\pi}\,\alpha\,k_{2m}\,\phi_{\mathrm{g}}(k_{2m})\,\tilde{g}(\varepsilon) \sum_{n}^{\mathrm{odd}} x J_n(\xi\,x) e^{in\varphi_{\mathrm{IR}}}, \tag{4.45}$$

where x is the cosine of the angle formed by $\vec{\alpha}_0$ and $\vec{k}_{2m}$, and $k_{2m} = (4m\omega_{\mathrm{IR}} + 2E_g)^{1/2}$. Both the pre factor and the argument of the integral in Equation (4.45) are smooth functions of the electron energy: consecutive sidebands have almost identical qualitative behavior. In the following, therefore, for the sake of conciseness, we render the dependence on the final energy implicit, drop the sideband index and refer to a generic sideband instead. The integral of the sideband signal is thus

$$I_{\mathrm{SB}} = \beta \int_{-1}^{1} x^2 dx \left| \sum_{n}^{\mathrm{odd}} J_n(\xi x) e^{in\varphi_{\mathrm{IR}}} \right|^2 , \tag{4.46}$$

where β collects the fixed factors that depend on the details of the XUV spectrum but not on the IR intensity,

$$\beta = 2\pi \left| \alpha\, \omega_{\mathrm{IR}} A_0 k_{2m} \phi_g(k_{2m}) \right|^2 \int_0^{\infty} \sqrt{2\varepsilon}\; d\varepsilon\; |\tilde{g}(\varepsilon)|^2. \tag{4.47}$$

The integral in (4.46) determines the frequency composition of each and every sideband in the frequency-comb limit, due to the interference of the contributions arising from the net exchange of an arbitrary odd number of IR photons (see Figure 24). We can reformulate the expression (4.46) by factorizing the dependence on the IR phase $\varphi_{\mathrm{IR}} = \omega_{\mathrm{IR}}\tau$ (we assume a zero absolute IR phase $\varphi_{\mathrm{IR},0}$),

$$I_{\mathrm{SB}} = \beta \sum_{j=0}^{\infty} C_j(\xi) \cos(2j\,\omega_{\mathrm{IR}}\tau), \tag{4.48}$$

$$C_j(\xi) = \int_{-1}^{1} \frac{2x^2 dx}{1+\delta_{j0}} \sum_{n}^{\mathrm{odd}} J_n(\xi x) J_{n+2j}(\xi x) \tag{4.49}$$

where the index j designates the sideband harmonic component, namely: average (background) signal ($j = 0$); fundamental RABITT frequency ($j = 1$); first overtone ($j = 2$); second overtone ($j = 3$), etc. Equations (4.48) and (4.49) completely characterize the temporal profile of sideband intensities in the idealized case of a frequency comb pump sequence as a function of both the time delay and the IR intensity. The integral in Equation (4.49) could be expressed in closed form in terms of special functions. The result, however, is rather lengthy and does not seem to provide further insight. As will be discussed in more detail in § 5.1, a major feature of the $C_j(\xi)$ coefficients is that, for $j > 0$, they oscillate around zero as a function of ξ, crossing the axis for different values of the reduced field strength. This means that not only the relative proportion of the frequency-component amplitudes of the sideband changes with the intensity. In fact, the fundamental RABITT component periodically vanishes altogether, a condition in which overtones dominate.

4.4 MODEL FOR TIME-RESOLVED RESONANT TRANSITIONS

So far, we have outlined two powerful methods to describe pump-probe experiments, namely, a close-coupling *ab initio* method and the soft photon approximation. The former can give virtually exact solutions, but it is computationally

very expensive and its application has so far been limited to systems with only few electrons. Moreover, the computational cost increases dramatically with both the duration and intensity of the fields considered. Even if the time-consuming constraint that arises from using very long pulse durations can be somewhat kept under control by following a procedure similar to [112], the computational cost of describing intense fields still remains. Indeed, it is often impossible to apply *ab initio* approaches to faithfully reproduce real experimental conditions when long intense pulses are involved.

The soft photon approximation represents a valid alternative to *ab initio* methods. The SPA is applicable to many-electron systems in intense fields, whenever the single-active electron approximation (SAE) is justified, at a negligible computational cost. However, it completely fails in those energy regions where core electrons can be excited.

In this section we propose a third approach which is appropriate to study the role of autoionizing states in attosecond pump-probe experiments, thus going beyond the constraints imposed by the SAE approximation, while retaining the advantages of an analytical treatment of the finite character of radiation pulses, which circumvents the computational bottleneck entailed by the direct integration of the TDSE in the *ab initio* approach.

4.4.1 *Two photon non-resonant transitions*

Let us first examine how a finite-pulse formulation of the second-order transition amplitude [we repeat Eqs. (2.31) and (2.32) of § 2.3]

$$\begin{aligned} \mathcal{A}_{fg}^{(2)} &= -i \int_{-\infty}^{\infty} d\omega \tilde{F}(\omega_{fg} - \omega) \tilde{F}(\omega) \mathcal{M}_{fg}^{(2)}(\omega), \\ \mathcal{M}_{fg}^{(2)}(\omega) &= \langle f | \mathcal{O} G_a^+(\omega_g + \omega) \mathcal{O} | g \rangle, \end{aligned} \tag{4.50}$$

can be used to describe pump-probe experiments. In a two-photon transition with finite pulses, the energy preserving condition $\omega_1 + \omega_2 = \omega_{fg}$ is satisfied by several different pairs of frequency components (ω_1, ω_2), which result in separate contributions that interfere to give rise to the total transition amplitude (Fig. 15d). Changing the time delay between pump and probe pulses alters the relative phase between all these different contributions, thus affecting the total amplitude, which becomes a function of τ.

If we consider separately the positive and negative frequency components of the field (1 and $\bar{1}$, respectively, for the pump, 2 and $\bar{2}$ for the probe), replacement of Equation (4.2) in Equation (4.50) gives rise to sixteen terms associated to all possible time-ordered two-photon transitions: 21, absorption of a pump photon followed by the absorption of a probe photon; $\bar{2}1$, absorption of a pump photon followed by the emission of a probe photon; 12, absorption of a probe photon followed by the absorption of a pump photon, and so on. For example, the to-

tal transition amplitude for the absorption of one pump and one probe photon comprises two terms,

$$\mathcal{A}_{fg} = \mathcal{A}^{12}_{fg} + \mathcal{A}^{21}_{fg}, \tag{4.51}$$

$$\mathcal{A}^{21}_{fg} = -i \int_0^\infty d\omega\, \tilde{F}_2(\omega_{fg} - \omega; \tau) \tilde{F}_1(\omega) \mathcal{M}_{fg}(\omega), \tag{4.52}$$

$$\mathcal{A}^{12}_{fg} = -i \int_0^\infty d\omega\, \tilde{F}_1(\omega_{fg} - \omega) \tilde{F}_2(\omega; \tau) \mathcal{M}_{fg}(\omega), \tag{4.53}$$

which correspond to the time-ordered diagrams where the pump photon is absorbed first and last, respectively. Let us consider the first case in more detail. We can expand the resolvent $G_a^+(\omega_g + \omega)$ in the two-photon matrix element in terms of the generalized eigenstates $|\psi_{\alpha\varepsilon}\rangle$ of the field-free system, $H_a|\psi_{\alpha\varepsilon}\rangle = |\psi_{\alpha\varepsilon}\rangle\varepsilon$,

$$\mathcal{M}_{fg}(\omega) = \sum_\alpha \iint d\varepsilon\, \frac{\mathcal{O}_{f,\alpha\varepsilon}\mathcal{O}_{\alpha\varepsilon,g}}{\omega_g + \omega - \varepsilon + i0^+}. \tag{4.54}$$

If $|f\rangle$ is either a discrete state or a generalised state belonging to a featureless continuum (far from thresholds and from any resonant state), and the intermediate states contributing to Equation (4.54) are either similarly featureless continua or discrete states far from the resonance condition (virtual excitations), then $\mathcal{M}_{fg}(\omega)$ is a smooth function of ω. For sharply peaked field spectra, then, the same considerations with which Equation (2.40) was derived from Equation (2.38) in Chapter 2 apply here: $\mathcal{M}_{fg}(\omega)$ can be replaced with its value near the peak of the fields and moved out of the integral so that one recovers the familiar quasi-stationary expression for $\mathcal{A}^{(2)}_{fg}$ as a finite sum of weighted Feynmann diagrams. In the presence of intermediate resonant states with lifetime comparable to or longer than the duration of the light pulses involved, however, $\mathcal{M}_{fg}(\omega)$ has a sharp dependence on ω and the transition never achieves a stationary regime. In this latter case, the folding with the field in Equation (4.50) must be evaluated to the full.

THE *on-shell* APPROXIMATION. It is worth examining the special case for Equation (4.54) in which both the intermediate states $|\alpha\epsilon\rangle$ and the final state $|f\rangle = |\beta E\rangle$ are elastic-scattering featureless continuum states corresponding to a same parent ion. In this case, the largest contribution to the two-photon transition amplitude comes from the intermediate states that are degenerate or almost degenarate with the final state. This circumstance is evident if the continuum states are approximated with plane waves, which is a common assumption for energetic photoelectrons in multiphoton transitions (this approximation is employed in disguise, for example, in the strong-field [102, 103, 104] and in the soft-photon [67, 69] approximations, both of which, as we have seen in the previous section, work well sufficiently above threshold). Indeed, since plane waves are eigenstates of the dipole operator in velocity gauge, the only non-vanishing dipole transition matrix element is the one between two identical plane waves,

$$\langle \vec{k}|\, \hat{\vec{p}}\, |\vec{k}'\rangle = \vec{k}\, \delta^{(3)}(\vec{k} - \vec{k}') = \vec{k} \delta^{(2)}(\hat{k} - \hat{k}') \frac{\delta(E - E')}{\sqrt{2E}}. \tag{4.55}$$

Notice that such approximation applies when estimating the two-photon transition matrix element from a *bound state* $|g\rangle$ to the continuum,

$$\langle \vec{k}|p_z G^+(E_g+\omega)p_z|g\rangle \simeq \frac{k_z \langle \vec{k}|p_z|g\rangle}{E_g+\omega-k^2/2+i0^+}. \tag{4.56}$$

It does not imply, however, any net absorption or emission of photons between free-electron states, which is and remains a prohibited process. We will call *on-shell* approximation the assumption that the transition matrix element between unstructured continuum states is diagonal in the energy,

$$\langle \beta E'|\mathcal{O}|\alpha E\rangle \simeq \bar{O}_{\beta\alpha}(E)\delta(E-E'), \tag{4.57}$$

where $\bar{O}_{\alpha\beta}(E)$ is the integral of the actual transition amplitude $\mathcal{O}_{\beta E,\alpha\epsilon}$ in a narrow energy interval $\epsilon \in (E-\delta, E+\delta)$ to which significant values of $\bar{O}_{\alpha\beta}(E)$ are hopefully restricted,

$$\bar{O}_{\beta\alpha}(E) = \int_{E-\delta}^{E+\delta} \langle \beta E|\mathcal{O}|\alpha\varepsilon\rangle \, d\varepsilon. \tag{4.58}$$

The *on-shell* approximation is quite acceptable even when considering radiative transitions between the Coulomb or shifted Coulomb waves commonly encountered in atomic ionization, and it becomes increasingly more accurate as the electron energy increases. For example, Fig. 17 (see also [113]) shows the continuum-

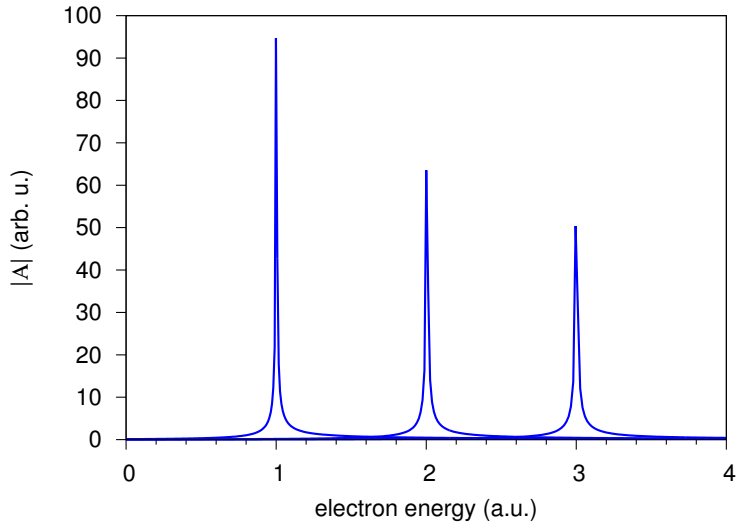

Figure 17: Absolute value, in atomic units, of the exact analytical reduced velocity-gauge dipole matrix element $\langle \psi_{E_p}\|\mathcal{O}_1^v\|\psi_{E_s}\rangle$ of the hydrogen atom, from three selected s scattering states ($E_s = 1, 2, 3$ a.u.), to several p states in the continuum. The sharp localisation of the amplitude at $E_p \simeq E_s$ underpins the validity of the *on-shell* approximation. For more details, see [113].

continuum transition matrix elements in the hydrogen atom from three selected initial scattering states with $\ell = 0$ and energies $E_s = 1, 2, 3$ a.u., to $\ell = 1$ scattering states as a function of the energy E_p of the final states. It is clear that the transition amplitudes are strongly peaked at $E_p = E_s$. In conclusion, using the *on-shell* approximation, the non-resonant two-photon transition matrix element from an

initial state $|g\rangle$ to a final continuum state $|\beta E\rangle$ through intermediate continuum states $|\alpha\varepsilon\rangle$, $\mathcal{M}^{(\alpha)}_{\beta E,g}(\omega) = \langle\beta E|\mathcal{O}G^+(E_g+\omega)Q_\alpha\mathcal{O}|g\rangle$, where Q_α is the projector on the intermediate continuum α, can be written as

$$\mathcal{M}^{(\alpha)}_{\beta E,g}(\omega) \simeq \frac{\bar{\mathcal{O}}_{\beta\alpha}(E)\mathcal{O}_{\alpha E,g}}{E_g+\omega-E+i0^+}. \tag{4.59}$$

The two-photon transition matrix element $\mathcal{M}_{fg}(\omega)$ has thus assumed the form of a rational function which, apart for a simple pole in the lower half of the complex plane, depends only weakly on the frequency ω. In the next section we will see that, with some additional approximations, $\mathcal{M}_{fg}(\omega)$ can be cast in a form similar to Equation (4.59) even in the presence of intermediate and final resonance states. When this is the case, folding with the field components, as in (4.52), can be computed analytically for certain shapes of the light pulses. In the following, we will examine the relevant case of Gaussian pulses. We will subsequently apply the formula to the case of the non-resonant RABITT transition and examine the effect of finite pulse duration on the RABITT beating frequency. The more general case of intermediate and final resonant states will be treated in § 4.4.2.

GAUSSIAN PULSES. The vector potential of an ultrashort laser pulse can be conveniently approximated with a linearly polarized Gaussian pulse $\vec{A}(t) = \hat{z}A(t)$ parametrized as

$$A(t) = A_0 \mathrm{e}^{-\frac{\sigma^2}{2}(t-t_0)^2}\cos[\omega_0(t-t_0)+\varphi], \tag{4.60}$$

where A_0, ω_0, t_0, σ and ϕ are the amplitude, carrier angular frequency, central time, spectral width and carrier-envelope phase of the pulse, respectively. Several Gaussian pulses can be combined to give rise to arbitrary pulse sequences, or to chirped pulses. The absorption and emission components in the FT of a single Gaussian pulse, $\tilde{A}(\omega) = \tilde{A}^+(\omega) + \tilde{A}^-(\omega)$, are

$$\tilde{A}^\pm(\omega) = \frac{A_0}{2\sigma}\mathrm{e}^{i(\omega t_0 \mp \varphi)}\mathrm{e}^{-\frac{(\omega\mp\omega_0)^2}{2\sigma^2}}. \tag{4.61}$$

As shown in App. B, in the case of Gaussian pulses, the folding of the field with a simple-pole function $(\omega - z_0)^{-1}$, as in Eq. (4.52), can be expressed in closed form,

$$\int_{-\infty}^{\infty} d\omega \, \frac{\tilde{F}_2(\omega_{\beta E,g}-\omega;\tau)\tilde{F}_1(\omega)}{E_g+\omega-E+i0^+} = i\mathcal{F}^{21}(\tau)\, e^{i\omega_2\tau}\, w(z_E^{21}), \tag{4.62}$$

where $\mathcal{F}^{21}(\tau)$ is a form factor of the pulse sequence

$$\mathcal{F}^{21}(\tau) = -\pi\frac{A_1A_2}{4\sigma_1\sigma_2}\mathrm{e}^{-i(\varphi_1+\varphi_2)}\exp\left[-\frac{1}{2}\left(\frac{\delta^2}{\sigma^2}+\frac{\tau^2}{\sigma_t^2}+2i\frac{\sigma_2}{\sigma_1}\frac{\delta}{\sigma}\frac{\tau}{\sigma_t}\right)\right], \tag{4.63}$$

with $\sigma = \sqrt{\sigma_1^2+\sigma_2^2}$, $\sigma_t = \sqrt{\sigma_1^{-2}+\sigma_2^{-2}}$, and $\delta = E_g+\omega_1+\omega_2-E$, while the complex parameter z_E^{21} is defined as

$$z_E^{21} = \frac{\sigma_t}{\sqrt{2}}\left[\left(\omega_1 - \frac{\sigma_1^2}{\sigma^2}\delta - i\frac{\tau}{\sigma_t^2}\right) - E + E_g\right], \tag{4.64}$$

with $w(z) = e^{-z^2}\mathrm{erfc}(-iz)$ being the Faddeeva special function. The transition amplitude $\mathcal{A}^{21}_{\beta E,g}$, therefore, takes on the form

$$\mathcal{A}^{21}_{\beta E,g} = \mathcal{F}^{21}(\tau)\, e^{i\omega_2 \tau} \sum_{\alpha} \bar{\mathcal{O}}_{\beta\alpha}(E)\mathcal{O}_{\alpha E,i}\, w(z^{21}_E). \tag{4.65}$$

This last equation is essentially equivalent to the one formulated by Ishikawa and Ueda in terms of the Dawson integral (compare with Eq. 2 in [114]).

In the region where the pulses do not overlap, the two-photon transition amplitude vanishes. How it gradually decays as a function of the pump-probe time delay is dictated by the product $\mathcal{F}^{21}(\tau)w(z^{21}_E)$, which falls off like a Gaussian for $|\tau| \gg \sigma_t$. The left panels of Figure 18 illustrate the photoelectron spectrum of

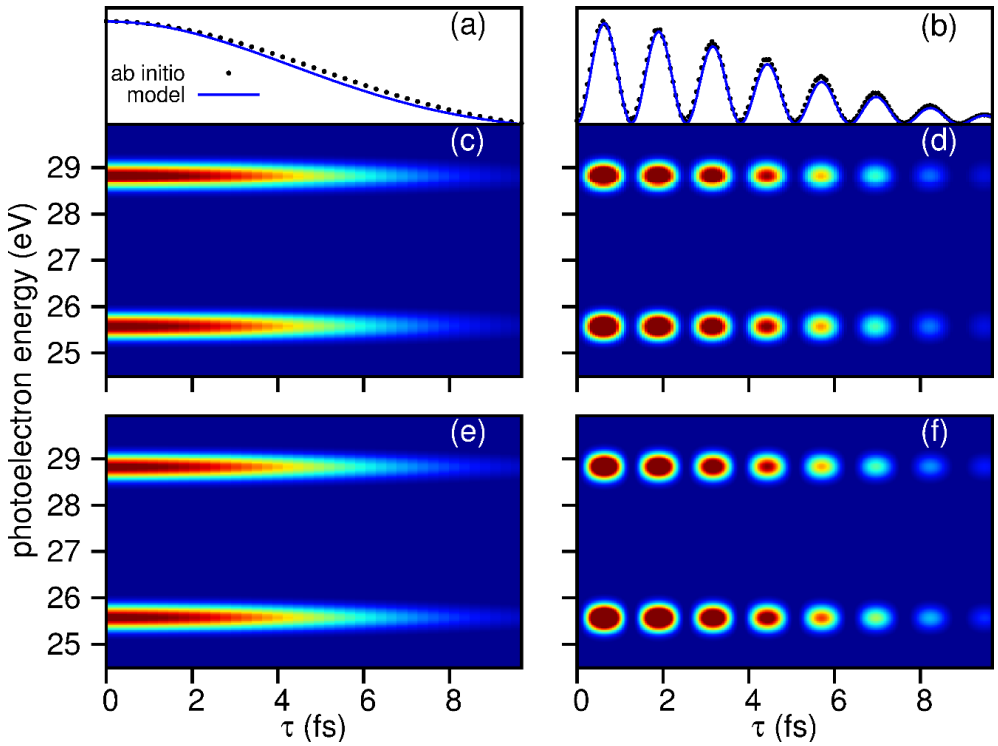

Figure 18: Spectrum for the two-photon ionization of the hydrogen atom from the ground state by means of a single (left panels) or a train (right panels) of XUV Gaussian pulses, in association with a 10 fs long IR probe pulse. Top panels (a,b): comparison between the energy integrated signal of the upper sideband, as a function the pump-probe time delay, computed *ab initio* (black dotted line) or with the model (blue solid line). Middle panels (c,d): energy and time-delay resolved spectra from the *ab initio* calculation (only states of even symmetry are shown). Bottom panels (e,f): energy and time-delay resolved spectra computed with the model.

the hydrogen atom ionized from the ground state with a single XUV Gaussian pulse with duration of 5 fs and central frequency 40.8 eV, in association with a 760 nm IR probe pulse 10 fs long, with an intensity of 10 GW/cm^2, as a function of the pump-probe time delay. The spectrum in the central panel is obtained *ab initio* by solving the TDSE for the atom in a numerical basis, while the bottom panel is computed using Eq. (4.65). The spectrum computed with the model, which includes all the terms proportional to the intensity of the probe laser, accurately reproduces all the features in the real energy-integrated (Fig. 18a) and energy-resolved (Fig. 18c) spectrum.

RED SHIFT OF RABITT BEATING WITH FINITE PULSES. As we saw in § 2.2.3, in RABITT spectroscopy the amplitude of each sideband SB_{2n} is given by the sum of four time-ordered two-photon amplitudes,

$$\mathcal{A}_{SB_{2n}} = \mathcal{A}_{SB_{2n}}^{H_{2n-1}IR} + \mathcal{A}_{SB_{2n}}^{IRH_{2n-1}} + \mathcal{A}_{SB_{2n}}^{H_{2n+1}\bar{I}R} + \mathcal{A}_{SB_{2n}}^{\bar{I}RH_{2n+1}}, \tag{4.66}$$

where $\bar{\text{IR}}$ indicates the emission component (negative frequency) of the IR pulse. In the limit of long pulses, the frequency of the RABITT beating is $2\omega_{IR}$ and the atomic phase shift in the standard expression for the sideband intensity, $I_{SB_{2n}} = I_0 \cos(2\omega_{IR}\tau + \Delta\phi_H + \Delta\varphi_{at})$ [26], is $\Delta\varphi_{at} = \arg[\mathcal{M}_{fi}(\omega_{2n-1}) + \mathcal{M}_{fi}(\omega_{IR})] - \arg[\mathcal{M}_{fi}(\omega_{2n+1}) + \mathcal{M}_{fi}(-\omega_{IR})]$. This is still the case if only one of either the APT or the IR has a long duration. Indeed, the RABITT frequency is given by the sum of the frequencies of the absorbed and of the emitted IR photons. If the XUV train comprises only multiples of the fundamental frequency ω_{IR} or if the probe pulse is monochromatic with frequency ω_{IR}, then the only possible outcome for the RABITT beating is $2\omega_{IR}$. On the other hand, when both the APT and the IR

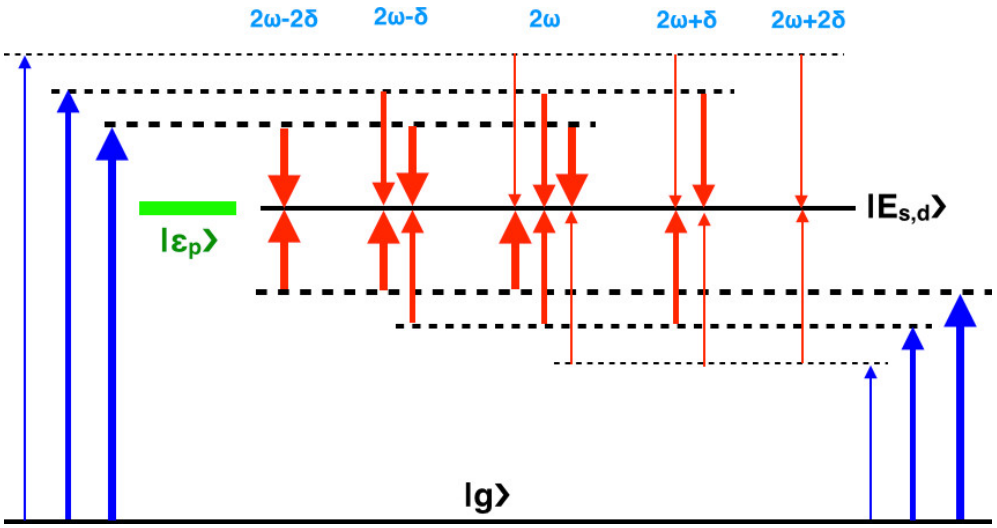

Figure 19: The XUV + IR above-threshold ionization amplitude is inversely proportional to the frequency of the IR photon. When both the XUV train and the IR pulse have finite duration, therefore, the signal is biased in favor of the low IR-frequency components. As a result, the spectrum of sideband beating in RABITT is red-shifted compared to the nominal $2\omega_{IR}$ value.

have finite duration, the RABITT beating is red-shifted with respect to the nominal $2\omega_{IR}$ value. This is because non-resonant two-photon matrix elements, which are dominated by contributions from virtual states at the same energy as the final state, are inversely proportional to the energy of the last-exchanged IR photon, $\mathcal{M}_{E,i} \propto (E_i + \omega_{2n\pm1} - E_{2n})^{-1} = \pm\omega_{IR}^{-1}$. Therefore, of the many IR wavelengths that contribute to the transition with finite pulses, long ones weigh more, thus biasing the RABITT beating towards the red (see Fig. 19). The right central and bottom panels of Figure 18 show the comparison between *ab initio* and model calculations in the case of the RABITT ionization of the hydrogen atom, where a 5 fs long (fwhm) Gaussian APT formed by Gaussian XUV pulses with central frequency of 40.8 eV and duration of 250 as is used in association with a 760 nm, 10 fs, 10 GW/cm^2 probe pulse. For these pulse parameters, the Fourier transform of the sideband oscillation in Figure 18b, reveals a beating frequency which is red-shifted with respect to the nominal RABITT frequency by an amount of 0.021

eV for the ab initio, in good agreement with the value of 0.017 eV predicted by the model. Part of the difference between these two values is explained by the use, in the *ab initio* calculation, of a probe pulse with cosine- squared instead of Gaussian envelope, which permits us to reduce the size of the quantization box.

4.4.2 *Two-photon resonant model*

In this section, we will use Fano formalism (see § 3.3) to compute two-photon transition amplitudes for the case in which the intermediate and/or final continuum states feature isolated resonances. After a short overview of the phase properties of the one-photon Fano transition matrix element, which will be relevant for the following of this section, we will consider two-photon transition amplitudes for the case of single-channel continuum states with at most one isolated resonance. The generalization to multiple single-channel isolated resonances will be straightforward and will be given at the end of this section. Finally, the model is not restricted to second order. At the end of the Chapter we outline the procedure required to compute higher order terms and illustrate it with a simple example. The extension of the resonant model to third order is provided in detail in Appendix D.

4.4.2.1 *Resonant two-photon transition matrix element.*

To derive the analytical formula for finite-pulse resonant two-photon transition amplitudes, we first need to obtain an approximated analytical expression for the two-photon ionization matrix element $\mathcal{M}_{\beta E,g}(\omega)$,

$$\mathcal{M}_{\beta E,g}(\omega) = \sum\!\!\!\!\!\!\int d\varepsilon \frac{\langle \psi_{\beta E}|\mathcal{O}|\psi_{\alpha\varepsilon}\rangle \langle \psi_{\alpha\varepsilon}|\mathcal{O}|g\rangle}{E_g + \omega - \varepsilon + i0^+}. \tag{4.67}$$

To do so, we assume that the continuum branches in both the intermediate states, $|\psi_{\alpha E}\rangle$, and final states, $|\psi_{\beta E}\rangle$, can be expressed, using Fano's formalism, in terms of known bound and continuum eigenstates of a reference hamiltonian H_0, $H_0|a\rangle = E_a|a\rangle$, $H_0|b\rangle = E_b|b\rangle$, $H_0|\gamma\varepsilon\rangle = \varepsilon|\gamma\varepsilon\rangle$,

$$|\psi_{\alpha E}\rangle = |\alpha E\rangle + \left(|a\rangle + \int \frac{d\varepsilon |\alpha\varepsilon\rangle\, V_{\alpha\varepsilon,a}}{E - \varepsilon + i0^+}\right) \frac{V_{a,\alpha E}}{E - \tilde{E}_a}, \tag{4.68}$$

$$|\psi_{\beta E}\rangle = |\beta E\rangle + \left(|b\rangle + \int \frac{d\varepsilon |\beta\varepsilon\rangle\, V_{\beta\varepsilon,b}}{E - \varepsilon + i0^+}\right) \frac{V_{b,\beta E}}{E - \tilde{E}_b}, \tag{4.69}$$

where V denotes the field-free electron-electron interaction not included in H_0, e.g., $V_{a,\alpha\varepsilon} = \langle a|H_a - H_0|\alpha\varepsilon\rangle$. The interacting-continuum wavefunctions in Eqns. (4.68) and (4.69) are normalized as $\langle \psi_{E'}|\psi_E\rangle = \delta(E' - E)$. The suffixes α and β identify the ionization channel in the intermediate and final states, respectively. Let us separate in $\mathcal{M}_{\beta E,g}(\omega)$ the contribution of the intermediate bound

states $\{|n\rangle\}$, $\mathcal{M}^{(b)}_{\beta E,g}(\omega)$, from that of the intermediate continuum states $|\psi_{\alpha E}\rangle$, $\mathcal{M}^{(c)}_{\beta E,g}(\omega)$,

$$\mathcal{M}_{\beta E,g}(\omega) = \mathcal{M}^{(b)}_{\beta E,g}(\omega) + \mathcal{M}^{(c)}_{\beta E,g}(\omega), \tag{4.70}$$

$$\mathcal{M}^{(b)}_{\beta E,g}(\omega) = \sum_n \frac{\langle\psi_{\beta E}|\mathcal{O}|n\rangle\,\mathcal{O}_{ng}}{\omega-\omega_{ng}+i0^+} \tag{4.71}$$

$$\mathcal{M}^{(c)}_{\beta E,g}(\omega) = \int d\varepsilon \frac{\langle\psi_{\beta E}|\mathcal{O}|\psi_{\alpha\varepsilon}\rangle\,\langle\psi_{\alpha\varepsilon}|\mathcal{O}|g\rangle}{E_g+\omega-\varepsilon+i0^+}. \tag{4.72}$$

The transition matrix elements between a localized state and a Fano continuum can be accurately parametrized with Fano's formula,

$$\langle\psi_{\alpha\varepsilon}|\mathcal{O}|g\rangle = \frac{\epsilon_{\varepsilon a}+q_{\tilde{a}g}}{\epsilon_{\varepsilon a}-i}\mathcal{O}_{\alpha\varepsilon,g}, \tag{4.73}$$

$$\langle\psi_{\beta E}|\mathcal{O}|n\rangle = \frac{\epsilon_{Eb}+q_{\tilde{b}n}}{\epsilon_{Eb}-i}\mathcal{O}_{\beta E,n}. \tag{4.74}$$

The contribution from bound intermediate states, therefore, is readily written as

$$\mathcal{M}^{(b)}_{\beta E,g}(\omega) = \sum_n \frac{\epsilon_{Eb}+q_{\tilde{b}n}}{\epsilon_{Eb}-i}\frac{\mathcal{O}_{\beta E,n}\mathcal{O}_{ng}}{\omega-\omega_{ng}+i0^+}. \tag{4.75}$$

In practical cases, this expression can often be restricted to the contribution from a limited set of intermediate bound states, or even from just one of them. For example, in the excitation of helium from the $1s^2$ ground state to the doubly excited states with $N=2$, the biggest role in (4.75) is played by the intermediate $1s2p$ state, for which the oscillator strength with the $N=2$ states is very large and the background ionization amplitude is very small ($q_{\tilde{b}n} \gg 1$. The $2p^2 \leftarrow 1s2p \leftarrow 1s^2$ is a characteristic example). In this case, if the intermediate bound state is non resonant, one can use the simplified expression

$$\mathcal{M}^{(b)}_{\beta E,g}(\omega) \approx \frac{q_{\tilde{b}n_0}}{\epsilon_{Eb}-i}\frac{\mathcal{O}_{\beta E,n_0}\mathcal{O}_{n_0,g}}{\omega-\omega_{n_0 g}}. \tag{4.76}$$

The latter expression is applicable even in the case of multiple intermediate states that contribute to the transition amplitude by means of virtual excitations and which are clustered in an energy region that is small if compared with the detuning $\omega-\omega_{n_0 g}$ from the absorption of the first photon. Let us now consider the contribution from the intermediate continuum states. Replacing (4.73) in (4.72) we find

$$\mathcal{M}^{(c)}_{\beta E,g}(\omega) = \int \frac{d\varepsilon\langle\psi_{\beta E}|\mathcal{O}|\psi_{\alpha\varepsilon}\rangle}{E_g+\omega-\varepsilon+i0^+}\frac{\epsilon_{\varepsilon a}+q_{\tilde{a}g}}{\epsilon_{\varepsilon a}-i}\mathcal{O}_{\alpha\varepsilon,g}. \tag{4.77}$$

To advance further, we must find an expression for the continuum-continuum resonant transition amplitude $\langle\psi_{\beta E}|\mathcal{O}|\psi_{\alpha\varepsilon}\rangle$ in terms of a limited number of almost-constant parameters. In analogy with the Fano formula for the dipole transition from bound states, we first take out from this matrix element the term that in-

volves only transition matrix elements between states in the unperturbed continuum,

$$\begin{aligned}\langle\psi_{\beta E}|\mathcal{O}|\psi_{\alpha\varepsilon}\rangle &= \langle\bar{\psi}_{\beta E}|\mathcal{O}|\bar{\psi}_{\alpha\varepsilon}\rangle - \\ &- \frac{V_{\beta E,b}}{E-\tilde{E}_b^*}\mathcal{O}_{ba}\frac{V_{a,\alpha\varepsilon}}{\varepsilon-\tilde{E}_a} + \frac{V_{\beta E,b}}{E-\tilde{E}_b^*}\langle b|\mathcal{O}|\psi_{\alpha\varepsilon}\rangle + \langle\psi_{\beta E}|\mathcal{O}|a\rangle\frac{V_{a,\alpha\varepsilon}}{\varepsilon-\tilde{E}_a} = \\ &= \langle\bar{\psi}_{\beta E}|\mathcal{O}|\bar{\psi}_{\alpha\varepsilon}\rangle + \frac{1}{\pi}\frac{1}{\epsilon_{Eb}-i}\frac{1}{\epsilon_{\varepsilon a}+i}\times \\ &\times\Big[-\frac{\mathcal{O}_{ba}}{\pi V_{b,\beta E}V_{\alpha\varepsilon,a}} + \frac{\mathcal{O}_{b,\alpha\varepsilon}}{V_{b,\beta E}}(\epsilon_{\varepsilon a}+q_{\tilde{a}b}) + \frac{\mathcal{O}_{\beta E,a}}{V_{\alpha\varepsilon,a}}(\epsilon_{Eb}+q_{\tilde{b}a})\Big],\end{aligned} \tag{4.78}$$

where the barred states represent the Fano continuum without the bound component, i.e.,

$$|\bar{\psi}_{\beta E}\rangle = |\beta E\rangle + \int\frac{d\varepsilon|\beta\varepsilon\rangle\, V_{\beta\varepsilon,b}}{E-\varepsilon+i0^+}\frac{V_{b,\beta E}}{E-\tilde{E}_b}, \tag{4.79}$$

and we used the relation $\Gamma_a = 2\pi|V_{a,\alpha E}|^2$. By applying the *on-shell* approximation, and assuming that $\bar{\mathcal{O}}_{\alpha\beta}\equiv\bar{\mathcal{O}}_{\alpha\beta}(E)$, $V_{a,\alpha E}$, and $V_{b,\beta E}$ are sufficiently slowly varying functions of E, it is easy to show that

$$\langle\bar{\psi}_{\beta E}|\mathcal{O}|\bar{\psi}_{\alpha\varepsilon}\rangle = \bar{\mathcal{O}}_{\beta\alpha}\delta(E-\varepsilon) + \frac{1}{\pi}\frac{\bar{\mathcal{O}}_{\beta\alpha}}{\varepsilon-E+i0^+}\frac{\epsilon_{Eb}-\epsilon_{\varepsilon a}}{(\epsilon_{\varepsilon a}+i)(\epsilon_{Eb}-i)}. \tag{4.80}$$

Indeed, to compute the transition matrix element between the two modified continua, it is sufficient to close the integration path with a semi-circular path in either the upper or the lower half complex plane, where the argument of the integral decreases quadratically with respect to the integration variable, and apply Cauchy residual theorem. By combining Eqs. (4.78) and (4.80), the dipole transition amplitudes between the two Fano resonant continua can be approximated as

$$\begin{aligned}\langle\psi_{\beta E}|\mathcal{O}|\psi_{\alpha\varepsilon}\rangle = \bar{\mathcal{O}}_{\beta\alpha}\delta(E-\varepsilon) + \frac{\bar{\mathcal{O}}_{\beta\alpha}}{\varepsilon-E+i0^+}\frac{\epsilon_{Eb}-\epsilon_{\varepsilon a}}{\pi(\epsilon_{\varepsilon a}+i)(\epsilon_{Eb}-i)} + \\ + \frac{\frac{\mathcal{O}_{b,\alpha\varepsilon}(\epsilon_{\varepsilon a}+q_{\tilde{a}b})}{V_{b,\beta E}} + \frac{\mathcal{O}_{\beta E,a}(\epsilon_{Eb}+q_{\tilde{b}a})}{V_{\alpha\varepsilon,a}} - \frac{\mathcal{O}_{ba}}{\pi V_{\alpha\varepsilon,a}V_{b,\beta E}}}{\pi(\epsilon_{\varepsilon a}+i)(\epsilon_{Eb}-i)}.\end{aligned} \tag{4.81}$$

We can now insert this expression in the continuum contribution (4.77) to the two-photon matrix element. The integral of the argument proportional to a Dirac delta function is evaluated immediately, while the other two terms require a more careful discussion,

$$\mathcal{M}^{(c)}_{\beta E,g}(\omega) = \frac{\bar{\mathcal{O}}_{\beta\alpha}\mathcal{O}_{\alpha E,g}}{E_g+\omega-E+i0^+}\frac{\epsilon_{Ea}+q_{\tilde{a}g}}{\epsilon_{Ea}-i} + I_2 + I_3, \tag{4.82}$$

where

$$I_2 = \frac{1/\pi}{\epsilon_{Eb}-i}\int\frac{\epsilon_{\varepsilon a}+q_{\tilde{a}g}}{\epsilon_{\varepsilon a}^2+1}\frac{\epsilon_{\varepsilon a}-\epsilon_{Eb}}{\varepsilon-E+i0^+}\frac{\bar{\mathcal{O}}_{\beta\alpha}\mathcal{O}_{\alpha\varepsilon,g}d\varepsilon}{\varepsilon-E_g-\omega-i0^+}$$

and

$$I_3 = \int \frac{\mathcal{O}_{\alpha\varepsilon,g}d\varepsilon}{E_g+\omega-\varepsilon+i0^+}\frac{\epsilon_{\varepsilon a}+q_{\tilde{a}g}}{\epsilon_{\varepsilon a}-i}\frac{\frac{\mathcal{O}_{b,\alpha\varepsilon}(\epsilon_{\varepsilon a}+q_{\tilde{a}b})}{V_{b,\beta E}}+\frac{\mathcal{O}_{\beta E,a}(\epsilon_{Eb}+q_{\tilde{b}a})}{V_{\alpha\varepsilon,a}}-\frac{\mathcal{O}_{ba}}{\pi V_{b,\beta E}V_{\alpha\varepsilon,a}}}{\pi(\epsilon_{\varepsilon a}+i)(\epsilon_{Eb}-i)}. \quad (4.83)$$

For large values of ε, the argument of the integral in I_2 is inversely proportional to ε^2. Therefore, this integral can be conveniently computed by closing the integration circuit with a semi-circular arc in the lower half of the complex plane, provided that the transition matrix elements are only weakly varying on the additional arc, for large enough arc radii. The result is

$$\begin{aligned} I_2 &= \frac{\epsilon_{Ea}-\epsilon_{Eb}}{(\epsilon_{Ea}-i)(\epsilon_{Eb}-i)}\frac{\epsilon_{Ea}+q_{\tilde{a}g}}{\epsilon_{Ea}+i}\frac{2i\bar{\mathcal{O}}_{\beta\alpha}\mathcal{O}_{\alpha E,g}}{\omega-E+E_g+i0^+}- \\ &\quad -\frac{\epsilon_{Eb}+i}{\epsilon_{Eb}-i}\frac{q_{\tilde{a}g}-i}{\epsilon_{Ea}+i}\frac{\bar{\mathcal{O}}_{\beta\alpha}\mathcal{O}_{\alpha E,g}}{\omega-\omega_{\tilde{a}g}}. \end{aligned} \quad (4.84)$$

The last integral, I_3, has only one simple pole in the lower complex plane and hence it also would be conveniently computed by closing the integration circuit in the lower half of the complex plane with the arc $\Gamma_R = \{Re^{-i\varphi}, \varphi \in [0,\pi]\}$,

$$I_3 = \lim_{R\to\infty}\left[\int_{[-R,R]\cup\Gamma_R}\mathcal{I}_3(z)dz - \int_{\Gamma_R}\mathcal{I}_3(z)dz\right], \quad (4.85)$$

where $\mathcal{I}_3(\varepsilon)$ indicates the argument of the integral in (4.83). In contrast to the previous case, however, the absolute value of $\mathcal{I}_3(\varepsilon)$ decays only as $|\varepsilon|^{-1}$. Instead of vanishing as $R\to\infty$, therefore, the contribution of the arc converges to a finite value that must be taken into account, and which is easily computed (as usual, we assume that all the matrix elements are constant in a region of the complex plane sufficiently large to attain reasonable convergence of the circuit integral),

$$\lim_{R\to\infty}\int_{\Gamma_R}\mathcal{I}_3(z)dz = \frac{i\mathcal{O}_{b,\alpha E}\mathcal{O}_{\alpha E,g}}{V_{b,\beta E}(\epsilon_{Eb}-i)}. \quad (4.86)$$

The value of the total integral I_3, then, becomes

$$\begin{aligned} I_3 &= -i\frac{\mathcal{O}_{b,\alpha}}{V_{b,\beta}}\frac{\mathcal{O}_{\alpha,g}}{\epsilon_{Eb}-i}+\frac{\Gamma_a}{2}\frac{q_{\tilde{a}g}-i}{\omega-\omega_{\tilde{a}g}}\frac{\mathcal{O}_{\alpha,g}}{\epsilon_{Eb}-i}\times \\ &\quad\times\left[\frac{\mathcal{O}_{b,\alpha}(q_{\tilde{a}b}-i)}{V_{b,\beta}}+\frac{\mathcal{O}_{\beta,a}(\epsilon_{Eb}+q_{\tilde{b}a})}{V_{\alpha,a}}-\frac{\mathcal{O}_{ba}/\pi}{V_{b,\beta}V_{\alpha,a}}\right]. \end{aligned} \quad (4.87)$$

In summary, the expression for the intermediate-continuum contribution to the two-photon resonant transition matrix element is

$$\begin{aligned}\mathcal{M}^{(c)}_{\beta E,g}(\omega) &= \frac{\epsilon_{Ea}+q_{\tilde{a}g}}{\epsilon_{Ea}+i}\frac{\epsilon_{Eb}+i}{\epsilon_{Eb}-i}\frac{\bar{\mathcal{O}}_{\beta\alpha}\mathcal{O}_{\alpha,g}}{E_g+\omega-E+i0^+} - \\ &- \frac{q_{\tilde{a}g}-i}{\epsilon_{Ea}+i}\frac{\epsilon_{Eb}+i}{\epsilon_{Eb}-i}\frac{\bar{\mathcal{O}}_{\beta\alpha}\mathcal{O}_{\alpha,g}}{\omega-\omega_{\tilde{a}g}} + \\ &+ (q_{\tilde{a}b}-i)\frac{q_{\tilde{a}g}-i}{\epsilon_{Eb}-i}\frac{\Gamma_a/2}{V_{b,\beta E}}\frac{\mathcal{O}_{b,\alpha}\mathcal{O}_{\alpha,g}}{\omega-\omega_{\tilde{a}g}} + \\ &+ \pi V_{a,\alpha}(\epsilon_{Eb}+q_{\tilde{b}a})\frac{q_{\tilde{a}g}-i}{\epsilon_{Eb}-i}\frac{\mathcal{O}_{\beta,a}\mathcal{O}_{\alpha,g}}{\omega-\omega_{\tilde{a}g}} - \\ &- \frac{q_{\tilde{a}g}-i}{\epsilon_{Eb}-i}\frac{V_{a,\alpha}}{V_{b,\beta}}\frac{\mathcal{O}_{ba}\mathcal{O}_{\alpha,g}}{\omega-\omega_{\tilde{a}g}} - \frac{i\mathcal{O}_{b,\alpha}\mathcal{O}_{\alpha,g}}{V_{b,\beta}(\epsilon_{Eb}-i)}.\end{aligned} \tag{4.88}$$

CASE OF NO FINAL RESONANCES. In the relevant special case in which there are no final resonances, Eq. (4.88) simplifies considerably since one can take its limit for vanishing radiative and non-radiative couplings involving the $|b\rangle$ state. The result is

$$\begin{aligned}\mathcal{M}^{(c)}_{\beta E,g}(\omega) &= \frac{\epsilon_{Ea}+q_{\tilde{a}g}}{\epsilon_{Ea}+i}\frac{\bar{\mathcal{O}}_{\beta\alpha}\mathcal{O}_{\alpha,g}}{E_g+\omega-E+i0^+} + \\ &+ \left(\beta_a-\frac{1}{\epsilon_{Ea}+i}\right)(q_{\tilde{a}g}-i)\frac{\bar{\mathcal{O}}_{\beta\alpha}\mathcal{O}_{\alpha,g}}{\omega-\omega_{\tilde{a}g}}\end{aligned} \tag{4.89}$$

where the parameter $\beta_a = \pi\mathcal{O}_{\beta,a}V_{a\alpha}/\bar{\mathcal{O}}_{\beta\alpha}$ is a pure number that depends solely on the properties of the atomic system. When considering resonant two-photon transitions with long overlapping pulses with frequencies ω_1 and ω_2 and duration larger than the lifetime of the intermediate resonance, Eq. (4.89) can be simplified further, since the conservation of energies applies, $E = E_g + \omega_1 + \omega_2$. With few algebraic passages, it is easy to show that the matrix element appropriate for the time-ordered diagram in which photon ω_1 is absorbed first becomes

$$\mathcal{M}^{(c,21)}_{\beta E,g}(\omega_1) = -\frac{\bar{\mathcal{O}}_{\beta\alpha}\mathcal{O}_{\alpha,g}}{\omega_2}\frac{\epsilon_{E_1a}+q_{\tilde{a}g}(1-\gamma_{a2})+i\gamma_{a2}}{\epsilon_{E_1a}+i}, \tag{4.90}$$

where we introduced the new real parameter

$$\gamma_{a2} = \frac{\omega_2\beta_a}{\Gamma_a/2} = \frac{\mathcal{O}_{\beta,a}}{\bar{\mathcal{O}}_{\beta\alpha}\frac{1}{\omega_2}V_{\alpha a}} \tag{4.91}$$

which measures the relative strength of two alternative paths for the dipole transition from the intermediate bound state $|a\rangle$ to the final continuum $|\beta E\rangle$: a direct one, $\mathcal{O}_{\beta,a}$, and an indirect one, $\bar{\mathcal{O}}_{\beta\alpha}V_{\alpha a}/\omega_2$ in which the transition is mediated by the non-radiative coupling of the bound state with the intermediate continuum $|\alpha E\rangle$ followed by the dipole coupling between the intermediate and final continuum. Notice that in the formulation (4.90), the reduced energy term ϵ is always relative to the energy of the intermediate state reached from the ground state by

the absorption of the first photon, exactly as in the one-photon formula (3.58). It is interesting, therefore, to analyze more in detail the similarities and differences between expression (4.90) and that for one-photon transitions. First of all, if we define an effective q parameter as

$$q_{\text{eff}}^{(21)} = q_{\tilde{a}g}(1-\gamma_{a2}) + i\gamma_{a2}, \tag{4.92}$$

the resonant factor is formally the same in either expressions,

$$\mathcal{R}^{(21)} = \frac{\epsilon_{E_1 a} + q_{\text{eff}}^{(21)}}{\epsilon_{E_1 a} + i}. \tag{4.93}$$

Only in the case in which the intermediate bound state $|a\rangle$ is not radiatively coupled to the final continuum ($\mathcal{O}_{\beta a} = 0 \implies q_{\text{eff}}^{(21)} = q_{\tilde{a}g}$), however, do the resonant factors in the one-photon and the two-photon transition amplitude actually coincide in value and not in form only (see green line in Fig. 20). In general, if $\gamma_{a2} \neq 0$, $q_{\text{eff}}^{(21)}$ is a complex number which depends on the frequency of the second exchanged photon. The resonant factor in the two-photon transition matrix element can also be written as

$$\mathcal{R}^{(21)} = \gamma_{a2} + (1-\gamma_{a2})\frac{\epsilon_{E_1 a} + q_{\tilde{a}g}}{\epsilon_{E_1 a} + i}, \tag{4.94}$$

which is the same factor as in the one-photon case, scaled by $(1-\gamma_{a2})$ and shifted along the real axis by γ_{a2}.

In particular, as the reduced detuning $\epsilon_{E_1 a}$ is increased from $-\infty$ to $+\infty$, $\mathcal{R}^{(21)}(\epsilon_{E_1 a})$ still describes counterclockwise a circle that starts and ends at 1. In contrast to the one-photon case, however, if $\gamma_{a2} \neq 0$, the circle does not intersect the origin. In particular, if $\gamma_{a2} < 0$, the circle, which is expanded with respect to the one-photon case, intersects the real axis at γ_{a2} and at 1, thus encircling the origin. This means that the phase of the two-photon transition matrix elements experiences a full 2π excursion. If, on the other hand, $\gamma_{a2} > 0$, the circle is contracted and it misses the origin. In this latter case, the phase of the two-photon transition matrix elements experiences a finite excursion but no overall variation (see blue line in Fig. 20). Furthermore, since γ_{a2} is proportional to ω_2, the sign of γ_{a2} for the emission of the second photon is the opposite of that for its absorption, the full 2π phase excursion and the no-net phase excursion case are both simultaneously present, one for the upper and one for the lower sidebands of the resonant two-photon transition. In the particular case in which $\gamma_{a2} = 1$, the circular complex trajectory contracts to a point, $\mathcal{R}^{(21)} = 1$, so that the two-photon amplitude does not bear any sign of the intermediate resonance (the amplitude for the opposite sideband, however, would still exhibit a pronounced 2π phase excursion).

So far, we have considered only the case in which the photon close to the resonance is absorbed first. In fact, the same final state is also reached by the path in which the photon ω_2 is exchanged first, and whose matrix element is $\mathcal{M}_{\beta E_i g}^{(c,12)}(\omega_2)$. In XUV-pump IR-probe experiment, where $\omega_{\text{IR}} \ll \omega_{\text{XUV}}$, and where the first excitation energy of the ground state is typically much larger than ω_{IR},

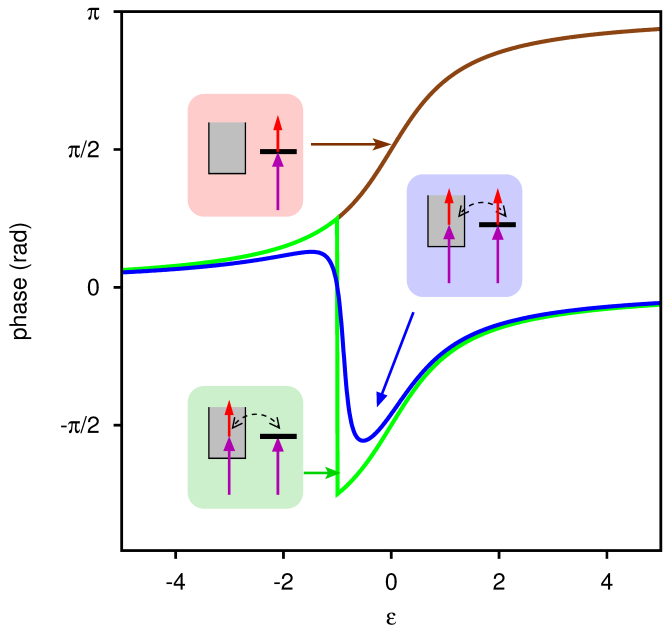

Figure 20: Argument of the resonant factor $\mathcal{R}^{21}$ (4.93) of the two-photon matrix element (4.90) as a function of the reduced detuning of the pump photon from the intermediate resonance. Brown line: the ground state is radiatively coupled to the discrete but not to the homogeneous component of the intermediate state, i.e., $q \to \infty$. Green line: the ground state is radiatively coupled to both the discrete and homogeneous components ($q = 1$), but the discrete component is not radiatively coupled to the final state, i.e., $\beta_{Ea} \to 0$. Blue line: both the discrete and continuum intermediate components are radiatively coupled with the initial and final states.

the contribution of the second path is generally small and it is often disregarded. Yet, the total transition matrix element should be computed as the sum of the two time-ordered contributions. If the path in which ω_2 is exchanged first is not resonant, then we can imagine that this term contributes with a small complex constant to the total transition. In principle, therefore, the inverted-order transition has an effect similar to that of γ_{a2}, as it shifts the transition amplitude trajectory towards or away from the origin.

The limit in which only the intermediate state $|a\rangle$ is radiatively coupled to the ground, while the intermediate continuum is not ($q_{\tilde{a}g} = \infty$), is also interesting, since it effectively reproduces the assumptions that have been made in [115] and [116], and which lead to a neat π excursion of the transition amplitude phase, as shown by the brown line in Fig. 20. In the general case, where the discrete-continuum dipole coupling is not negligible, the typical abrupt π discontinuity of (3.61) disappears (see blue line in Fig. 20).

CASE OF NO INTERMEDIATE RESONANCES. Two-photon excitation of a metastable state in the final continuum, with no intermediate resonances, which has been explored in the past by Cormier *et al.* [117], is a second relevant case. The frequency-dependent two-photon matrix element for this case is readily obtained from the general formula (4.88) by suppressing all the terms that involve the intermediate state $|a\rangle$,

$$\mathcal{M}^{(c)}_{\beta E,g}(\omega) = \frac{\epsilon_{Eb}+i}{\epsilon_{Eb}-i}\frac{\bar{\mathcal{O}}_{\beta\alpha}\mathcal{O}_{\alpha,g}}{E_g+\omega-E+i0^+} - \frac{i\mathcal{O}_{b,\alpha}\mathcal{O}_{\alpha,g}}{V_{b,\beta}(\epsilon_{Eb}-i)}.$$

If we specialise this formula to the long-pulse limit, and assume the conservation of energy $E = E_g + \omega_1 + \omega_2$, we obtain

$$\mathcal{M}^{(c,21)}_{\beta E,g}(\omega_1) = -\frac{\bar{\mathcal{O}}_{\beta\alpha}\mathcal{O}_{\alpha,g}}{\omega_2}\frac{\epsilon_{Eb}+i(1+\gamma_{b2})}{\epsilon_{Eb}-i}, \tag{4.95}$$

where we introduced the new real parameter

$$\gamma_{b2} = \frac{\omega_2\mathcal{O}_{b,\alpha}}{V_{b,\beta}\bar{\mathcal{O}}_{\beta\alpha}}. \tag{4.96}$$

A first surprising aspect of the resonant transition matrix element (4.95) in the present model is that it has a purely imaginary q parameter, $q = i(1+\gamma_{b2})$. As mentioned at the beginning of this section, however, when autoionizing final states are involved, the contribution of intermediate virtual bound states can be very large and, when added to (4.95), they give rise to an effective complex q parameter with comparable real and imaginary components, as predicted in [117]. Notice that, if the radiative coupling between the intermediate continuum and the final bound state is sufficiently large, it is in principle possible to select a value of ω_2 such that $1+\gamma_{b2}$ vanishes, thus making the transition amplitude disappear at one of the final resonances, as it happens at $\epsilon = -q$ for a traditional Fano profile.

4.4.2.2 *Time-resolved transition amplitudes*

From the expressions for the continuum (4.88) and discrete contribution (4.75) to the resonant two-photon transition matrix element, we can now proceed to compute the full transition amplitude associated to a pair of Gaussian pump and probe pulses. To do so, we will fold the transition matrix element $\mathcal{M}(\omega)$ with the FT of the field, as prescribed in Eq. (4.50). Except for the last term in (4.88), which does not depend on the integration frequency variable ω, all the other terms in either (4.88) or (4.75) depend on ω through elementary factors of the form $(\omega-\omega_0)^{-1}$. The folding in (4.50), therefore, can easily be carried out using Eq. (4.62). In the case of the absorption of photon 1 followed by that of photon 2, the expression for the transition amplitude reads

$$\begin{aligned}
\mathcal{A}^{21}_{\beta E,g} &= \mathcal{F}^{21}(\tau)\, e^{i\omega_2\tau}\bar{\mathcal{O}}_{\beta\alpha}\mathcal{O}_{\alpha E,g}\frac{\epsilon_{Eb}+i}{\epsilon_{Eb}-i}\times \\
&\times \left\{ \frac{\epsilon_{Ea}+q_{\tilde{a}g}}{\epsilon_{Ea}+i} w(z^{21}_E) + (q_{\tilde{a}g}-i)w(z^{21}_{\tilde{E}_a})\times \right. \\
&\times \left[\beta_a\frac{\epsilon_{Eb}+q_{\tilde{b}a}}{\epsilon_{Eb}+i} - \frac{1}{\epsilon_{Ea}+i} + \frac{\delta_{ba}(q_{\tilde{a}b}-i)-\zeta_{ba}}{\epsilon_{Eb}+i}\right] + \\
&+ \sqrt{\frac{2}{\pi}}\frac{1}{\sigma_t}\frac{\mathcal{O}_{b,\alpha}}{V_{b,\beta}\bar{\mathcal{O}}_{\beta\alpha}(\epsilon_{Eb}+i)} + \\
&+ \left. \sum_n \frac{\epsilon_{Eb}+q_{\tilde{b}n}}{\epsilon_{Eb}+i}\frac{\mathcal{O}_{\beta E,n}\mathcal{O}_{ng}}{\bar{\mathcal{O}}_{\beta\alpha}\mathcal{O}_{\alpha E,g}} w(z^{21}_{E_n}) \right\},
\end{aligned} \tag{4.97}$$

where we introduced the additional parameters

$$\delta_{ba} = \frac{\Gamma_a/2}{V_{b,\beta E}} \frac{\mathcal{O}_{b,\alpha}}{\bar{\mathcal{O}}_{\beta\alpha}}, \quad \zeta_{ba} = \frac{V_{a,\alpha}}{V_{b,\beta}} \frac{\mathcal{O}_{ba}}{\bar{\mathcal{O}}_{\beta\alpha}}. \tag{4.98}$$

Equation (4.97) depends on a minimal number of parameters for the radiative and non-radiative couplings between all the essential states involved in the dynamics, as well as the parameters of the pump and probe impinging pulses, including their time delay. Once the parameters of the model are established, therefore, this formula is able to provide, at a negligible computational cost, full energy and time-delay resolved attosecond pump-probe photoelectron spectra in the presence of both an intermediate and a final resonance for arbitrary pairs of (weak) pulses. Furthermore, this result is trivially extended to the case of an arbitrary number of Gaussian pulses, to represent, e.g., the effect of an attosecond pulse train, as well as to an arbitrary number of isolated resonances either in the intermediate or in the final states.

It is now interesting to consider more in detail the case of no final resonances, for which the transition amplitude (4.97) simplifies to

$$\begin{aligned} \mathcal{A}^{21}_{\beta E,g} = \mathcal{F}^{21}(\tau)\, e^{i\omega_2\tau} \bar{\mathcal{O}}_{\beta\alpha} \mathcal{O}_{\alpha E,g} \times \Bigg[& \frac{\epsilon_{Ea} + q_{\tilde{a}g}}{\epsilon_{Ea} + i} w(z^{21}_E) + \\ & + \left(\beta_a - \frac{1}{\epsilon_{Ea} + i} \right) (q_{\tilde{a}g} - i) w(z^{21}_{\tilde{E}_a}) + \sum_n \frac{\mathcal{O}_{\beta E,n} \mathcal{O}_{ng}}{\bar{\mathcal{O}}_{\beta\alpha}(E) \mathcal{O}_{\alpha E,g}} w(z^{21}_{E_n}) \Bigg], \end{aligned} \tag{4.99}$$

in relation to the simple two-photon transition matrix element (4.89) discussed earlier in this section. In particular, we want to examine the effect of using finite pulses on the complex trajectory of the two-photon transition amplitude as a function of the central energy of the pump pulse. Each of the upper panels in Fig. 21 shows the complex trajectories of the transition amplitude (4.99), with $\epsilon_{E_1 a} \in [-30, 30]$ and at four different pulse durations, $\sigma_t \Gamma_a = \infty$, 2, 1, 0.5, for a selected pair of resonance parameters: a) $q_{\tilde{a}g} = 20 \gg 1$, $\gamma_{a2} = 0$, b) $q_{\tilde{a}g} = 1$, $\gamma_{a2} = 0$, c) $q_{\tilde{a}g} = 1$, $\gamma_{a2} = 0.2$, d) $q_{\tilde{a}g} = 1$, $\gamma_{a2} = -0.2$. The amplitudes are normalised so to start at the same reference point on the real axis, which corresponds to the asymptotic background transition amplitude. The lower panels, Fig. 21.e-h, show the transition amplitude phase as a function of the reduced pump detuning ϵ_{Ea}. When the transition amplitude is dominated by the contribution of the intermediate autoionizing state ($q_{\tilde{a}g} \gg 1$, Figs. 21a,e), the observed phase excursion is always π. The shorter the pulse duration, the wider the step (Fig. 21e). If q is finite but the intermediate autoionizing state is not radiatively coupled to the final continuum, the trajectory intercepts the origin, but only in the limit of long pulses, while, for short pulses, folding with the pulse spectra contracts the circular trajectory towards the asymptotic background value (Fig. 21b). In particular, the phase loses its discontinuity, giving rise to a sigmoidal profile with no net phase change, with features that are progressively less pronounced as shorter pulses are employed (Fig. 21f). The effect of finite pulses, therefore, is similar to that of a direct dipolar coupling between the bound state and the final continuum or, as we will see later in this section, to that of multiple intermediate channels. A similar dependence on pulse duration is observed for $\gamma_{a2} > 0$ (Figs. 21c,g). The

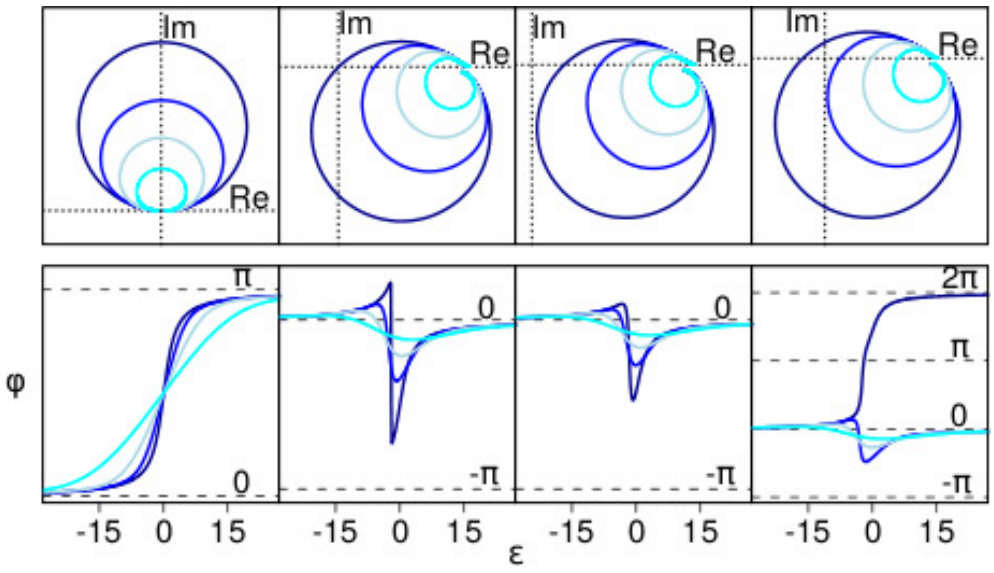

Figure 21: Complex trajectories of resonant finite-pulse two-photon two-colour absorption amplitudes (upper panels), and corresponding phase variation (lower panels) as the reduced intermediate energy detuning $\epsilon_{E_1 a}$ increases from large negative (-30) to large positive values ($+30$). In each of the upper panels, increasingly shorter pulses ($\sigma_t \Gamma_a = \infty$, 2, 1, 0.5) give rise to progressively more contracted trajectories (traced with lighter colour). Each column has a different set of q and γ parameters (see text for details).

complementary case of $\gamma_{a2} < 0$ (if $\gamma_{a2} > 0$ for probe absorption, $\gamma_{a2} < 0$ for probe emission, and viceversa) (Figs. 21c,g) is more interesting because, in the long-pulse limit, the phase experiences a full 2π jump, transitioning to the continuous excursion with no net phase through a point, for a definite finite pulse duration σ_t, at which the phase has a discontinuous jump or, stated otherwise, at which the resonant two-photon transition amplitude exactly vanishes.

If the energy of the second photon is much larger than the natural width of the intermediate resonance, $\omega_2 \gg \Gamma_a$, Eq. (4.99) can be further simplified. In fact, if the more stringent assumption $|\epsilon_{fa}| \gg q_a$ holds, we recover the expression given in Eq.(6) of [70],

$$\mathcal{A}^{21}_{\beta E,g} \simeq \mathcal{F}(\tau) e^{-i(\omega_2 \tau + \phi_1 + \phi_2)} \left[w(z^{21}_E) + (\beta_a - \epsilon^{-1}_{Ea})(q_{\tilde{a}g} - i) w(z^{21}_{\tilde{E}_a}) \right], \quad (4.100)$$

which was indeed justified in the context of helium photoionisation in the region of the doubly excited states converging to the $N = 2$ threshold.

CORRESPONDENCE BETWEEN INTERMEDIATE-ENERGY SCAN AND FINAL-ENERGY RESOLVED PHOTOELECTRON SPECTRUM. So far, when commenting the case of no final resonances, we have concentrated our attention on the phase of the resonant two-photon transition amplitude as a function of the central frequency ω_1 of the pump pulse scanning the resonance, for a given value of the final-energy detuning δ from the nominal value $E_g + \omega_1 + \omega_2$. Alternatively, one can keep ω_1 constant and study the dependence of the transition amplitude on the final energy instead. In either cases, the variation of the amplitude is essen-

tially dictated by the resonant argument $z^{21}_{\tilde{E}_a}$ of the Fadeeva function in (4.99),

$$z^{21}_{\tilde{E}_a} = \frac{\sigma_t}{\sqrt{2}}\left[(\omega_1 - \omega_{\tilde{a}g}) + \frac{\sigma_1^2}{\sigma^2}(E - E_g - \omega_1 - \omega_2) - i\frac{\tau}{\sigma_t^2}\right], \tag{4.101}$$

all the other terms in (4.99) having, in comparison, only a weak dependence on E and ω_1. From Eq. (4.101), the similarity between these two cases is evident: in the first case (scan over ω_1), the second term in parenthesis is constant while the first increases linearly with ω_1; in the second case (scan over E), the first term in parenthesis is constant while the second increases linearly with E. In attosecond pump-probe experiments, furthermore, the pump pulse is oftentimes much shorter than the probe, and hence $\sigma_1^2/\sigma^2 \simeq 1$. In these conditions, therefore, the two cases become essentially equivalent. It is important to notice, however, that computing the transition amplitude for a specific value of the final energy or integrating it over a range of final energies (which is the case in RABITT , for example), will not provide the same outcome due precisely to the final-energy dependence of $z^{21}_{\tilde{E}_a}$. This will be shown in § 5.3.1.

MONOCHROMATIC LIMIT. It is instructive to ascertain that the formula for the finite-pulse resonant two-photon transition amplitude (4.99) approaches the stationary expression (4.90) in the limit of long overlapping pulses, i.e., assuming pulse durations much longer than the resonance lifetime, $\sigma_t\Gamma_a \gg 1$, and time delays negligible if compared to the duration of the pulses, $\tau \ll \sigma_t$. For $\sigma_t \to \infty$, the argument of the Faddeeva function, z, tends to $(0, +\infty) \subset \mathbb{C}$, so one can use the first term in the asymptotic expansion of $w(z)$ restricted to the real axis, $w(x) \simeq i\pi^{-1/2}x^{-1}$, $x \in \mathbb{R}$ [109]. For $z^{21}_E \simeq \sigma_t/\sqrt{2}\,(E_i + \omega_1 - \delta\sigma_1^2/\sigma^2 - E)$, the Faddeeva function becomes $w(z^{21}_E) \simeq i\sqrt{2/\pi}\,\sigma_t^{-1}(E_i + \omega_1 - \delta\sigma_1^2/\sigma^2 - E)^{-1}$. If we neglect the effect of intermediate bound states, we obtain

$$\begin{aligned}\mathcal{A}^{21}_{\beta E,g} \;&\propto\; \frac{1}{E_g + \omega_1 - \delta\sigma_1^2/\sigma^2 - E}\frac{\epsilon_{Ea} + q_{\tilde{a}g}}{\epsilon_{Ea} + i} + \\ &+\; \frac{1}{E_g + \omega_1 - \delta\sigma_1^2/\sigma^2 - \tilde{E}_a}\left(\beta_a - \frac{1}{\epsilon_{Ea} + i}\right)(q_{\tilde{a}g} - i).\end{aligned}$$

At the nominal energy of the transition ($\delta = 0$), and using the energy-preserving condition $E = E_i + \omega_1 + \omega_2$, the transition amplitude finally becomes

$$\mathcal{A}^{21}_{\beta E,g} \propto \frac{\epsilon_{E_1 a} + q^{(21)}_{\text{eff}}}{\epsilon_{E_1 a} + i}, \tag{4.102}$$

as anticipated.

CASE OF NON-OVERLAPPING PULSES In the presence of an intermediate resonance $|a\rangle$, instead of plummeting as soon as $|\tau| \geq \sigma_t$, as it was the case for non-resonant transitions (see Fig. 18), the two-photon signal persists even for $\tau > \sigma_t$, decaying exponentially as $e^{-\tau/\tau_a}$ ($\tau_a = \Gamma_a^{-1}$). To see this, let us consider

the transition amplitude at zero final energy detuning, when $\tau \gg \sigma_t$, and the first photon absorption is right on resonance, $\omega_1 = \mathrm{Re}[\omega_{ag}]$,

$$z_a = \frac{i}{\sqrt{2}} \left(\frac{\sigma_t}{2\tau_a} - \frac{\tau}{\sigma_t} \right). \tag{4.103}$$

Then, the amplitude becomes proportional to

$$\mathcal{A}^{21}_{\beta E,g} \propto e^{-\tau^2/2\sigma_t^2}\, w(z_a) \simeq 2 \exp\left(-\tau/2\tau_a\right), \tag{4.104}$$

where we made the approximation $\mathrm{erfc}(-iz) \sim 2$ and we neglected the small term $\sigma_t^2/8\tau_a^2$. As expected, the transition amplitude decays exponentially with the time delay with half the lifetime of the resonant state.

Notice that for negative time delays the resonant signal still decays as the overlap of the pump and probe pulses (provided that the probe pulse is not itself in resonance with a transition from the ground state to a bound or autoionizing intermediate state). This latter circumstance illustrates how, in a time-resolved formulation, the time ordering of photon exchange in the transition matrix elements translates to an actual order in the two-photon transitions, when the two photons belong to non-overlapping pulses.

4.4.2.3 *Multichannel case*

In § 3.3.1 we showed that when a bound state is embedded in several continua, a unitary transformation permits to decouple it from all channels but one, which is then solution of the Fano problem. Furthermore, the residual decoupled continua $|\alpha' \varepsilon\rangle$ can be chosen so that only one of them, which we will call $|D\,\varepsilon\rangle$, is radiatively coupled to the ground state, $\mathcal{O}_{Dg} = \langle D\,\varepsilon|\mathcal{O}|g\rangle$, while the other continua are coupled neither to the resonance nor radiatively to the ground state, and can therefore be entirely ignored. As a consequence, the transition amplitude $\mathcal{A}_{\beta E,g}$ to a single final continuum β through a multichannel intermediate continuum can be reduced to the coherent sum of two amplitudes: one for a single resonant intermediate channel, $\mathcal{A}_{\beta E,R,g}$, and one for a single non-resonant intermediate channel, $\mathcal{A}_{\beta E,D,g}$,

$$\mathcal{A}_{\beta E,g} = \mathcal{A}_{\beta E,R,g} + \mathcal{A}_{\beta E,D,g}. \tag{4.105}$$

A similar reasoning applies to the final states, since even in that case it is possible to identify a single final resonant continuum. However, due to the presence of multiple intermediate states (two different continua, the bound states and the autoionizing state), more than two decoupled final continua can eventually be populated by means of a dipole transition. In any case, the final continua can be treated separately. If the final channel is not resolved, the individual contributions of all the final states to the total signal $P_{E,g}$ must be added incoherently,

$$P_{Eg} = \sum_{\beta} |\mathcal{A}_{\beta E,g}|^2. \tag{4.106}$$

In other terms, the problem of several final channels can be treated as several problems of a single final channel (being it resonant or not). In conclusion, if all

the relevant couplings with the intermediate and final resonant and decoupled unperturbed channels are available, the multichannel problem can be treated as a combination of the amplitudes given earlier in this section.

Let us examine the case of one intermediate resonance in a multichannel continuum and no final resonances. According to the above and to Eq. (4.99), we can write

$$\begin{aligned}\mathcal{A}^{21}_{\beta E,R,g} &= \mathcal{F}^{21}(\tau)\, e^{i\omega_2\tau}\bar{O}_{\beta R}\mathcal{O}_{Rg}\left[\frac{\epsilon_{Ea}+q_{\tilde{a}g}}{\epsilon_{Ea}+i}w(z^{21}_E)+\right.\\ &+ \left.\left(\beta_a-\frac{1}{\epsilon_{Ea}+i}\right)(q_{\tilde{a}g}-i)w(z^{21}_{\tilde{E}_a})\right]+ \qquad (4.107)\\ &+ \mathcal{F}^{21}(\tau)\, e^{i\omega_2\tau}\sum_n \mathcal{O}_{\beta E,n}\mathcal{O}_{ng}w(z^{21}_{E_n}),\\ \mathcal{A}^{21}_{\beta E,D,g} &= \mathcal{F}^{21}(\tau)\, e^{i\omega_2\tau}\bar{O}_{\beta D}\mathcal{O}_{Dg}\,w(z^{21}_E). \qquad (4.108)\end{aligned}$$

When taking the sum of the resonant and decoupled amplitudes, the latter can be integrated in the first term in parenthesis of the former, giving rise to an effective complex q parameter. The overall amplitude, however, cannot be assimilated to a single resonant transition amplitude by simply redefining the parameters involved. Thus, in principle, the presence of a decoupled channel qualitatively alters the finite-pulse resonant transition amplitude. In the long-pulse limit, however, the situation changes, as the total transition amplitude becomes proportional to [compare with Eq. (4.102)]

$$\mathcal{A}^{21}_{\beta E,g} \propto r_{DR}+\frac{\epsilon_{E_1a}+q^{(21)}_{\text{eff}}}{\epsilon_{E_1a}+i}, \quad r_{DR}=\frac{\bar{O}_{\beta D}\mathcal{O}_{Dg}}{\bar{O}_{\beta R}\mathcal{O}_{Rg}}. \qquad (4.109)$$

The constant term r_{DR} expresses the strength of the dipolar coupling to the final continuum through the decoupled intermediate continuum $|D\varepsilon\rangle$ relative to the one through the (unperturbed) resonant continuum $|R\varepsilon\rangle$. Equation (4.109) can be rewritten as

$$\mathcal{A}^{21}_{\beta E,g} \propto \frac{\epsilon_{E_1a}+q^{(21)}_{\text{eff}'}}{\epsilon_{E_1a}+i}, \quad q^{(21)}_{\text{eff}'}=\frac{1+ir_{DR}}{1+r_{DR}}\,q^{(21)}_{\text{eff}}. \qquad (4.110)$$

Therefore, in the long-pulse limit, the effect of multiple channels manifests itself as a simple modification of the effective complex q parameter, exactly as it happened in the case of a finite dipolar coupling between the intermediate metastable state $|a\rangle$ and the final continuum $|\beta E\rangle$, $\gamma_{a2}\neq 0$. While in the latter case the modification of the effective q was different for the absorption and for the emission of the second photon, however, in the multichannel case the variation of q is identical for the two paths. In principle, therefore, it is still possible to disentangle the two effects by comparing these two transition amplitudes.

4.4.2.4 *Multiple intermediate and final resonances*

The total transition amplitude (4.97) can be generalised to the case of several intermediate and final isolated resonances by adding to the common background

term the individual contribution from the intermediate and final states plus the residual contributions from all intermediate-final resonance pairs,

$$\begin{aligned}\mathcal{A}^{21}_{\beta E,g} &= \mathcal{F}^{21}(\tau)\, e^{i\omega_2\tau}\bar{\mathcal{O}}_{\beta\alpha}\mathcal{O}_{\alpha E,g}\,\mathcal{W}^{21}_{\beta E,g},\\ \mathcal{W}^{21}_{\beta E,g} &= \mathcal{W}^{21,\mathrm{bg}}_{\beta E,g} + \sum_a \mathcal{W}^{21,a}_{\beta E,g} + \sum_b \mathcal{W}^{21,b}_{\beta E,g} + \sum_{ba} \mathcal{W}^{21,ba}_{\beta E,g},\end{aligned}$$

where

$$\mathcal{W}^{21,\mathrm{bg}}_{\beta E,g} = w(z^{21}_E) + \sum_n \frac{\mathcal{O}_{\beta E,n}\mathcal{O}_{ng}}{\bar{\mathcal{O}}_{\beta\alpha}\mathcal{O}_{\alpha E,g}} w(z^{21}_{E_n}), \tag{4.111}$$

$$\mathcal{W}^{21,a}_{\beta E,g} = (q_{\tilde{a}g} - i)\left[\beta_a w(z^{21}_{\tilde{E}_a}) + \frac{w(z^{21}_E) - w(z^{21}_{\tilde{E}_a})}{\epsilon_{Ea} + i}\right] \tag{4.112}$$

$$\mathcal{W}^{21,b}_{\beta E,g} = \frac{2i\, w(z^{21}_E)}{\epsilon_{Eb} - i} + \sqrt{\frac{2}{\pi}}\frac{1}{\sigma_t}\frac{\mathcal{O}_{b\alpha}}{V_{b\beta}\bar{\mathcal{O}}_{\beta\alpha}}\frac{1}{\epsilon_{Eb} - i} + \sum_n \frac{q_{\tilde{b}n} + i}{\epsilon_{Eb} - i}\frac{\mathcal{O}_{\beta E,n}\mathcal{O}_{ng}}{\bar{\mathcal{O}}_{\beta\alpha}\mathcal{O}_{\alpha E,g}} w(z^{21}_{E_n})$$

$$\mathcal{W}^{21,ba}_{\beta E,g} = \frac{q_{\tilde{a}g} - i}{\epsilon_{Eb} - i}\left\{2i\frac{w(z^{21}_E) - w(z^{21}_{\tilde{E}_a})}{\epsilon_{Ea} + i} + w(z^{21}_{\tilde{E}_a})\left[2i\,\beta_a + q_{\tilde{b}a} - i + \delta_{ba}(q_{\tilde{a}b} - i) - \zeta_{ba}\right]\right\}.$$

This approach has been employed to compute the spectrum of a sideband comprising the $2p^2\ {}^1\mathrm{S}^e$ autoionising state in the RABITT ionisation of the helium atom from the ground state, when both the lower and the upper harmonics contributing to the resonant sideband were themselves in resonance with the sp_2^+ and the $sp_3^+\ {}^1\mathrm{P}^o$ states, respectively [70].

4.4.2.5 *Multiphoton transitions*

The $n-$th order finite-pulse transition amplitude (4.50) is

$$\begin{aligned}\mathcal{A}^{(n)}_{fg} &= \frac{-i}{(2\pi)^{\frac{n}{2}-1}}\int\cdots\int \delta(\omega_{fg} - \Omega'_n)\prod_{i=1}^{n}\left[\tilde{F}(\omega'_i)d\omega'_i\right]\times\\ &\times \langle f|\mathcal{O}\prod_{i=1}^{n-1}\left[G_0^+(E_g + \Omega'_i)\mathcal{O}\right]|g\rangle,\end{aligned} \tag{4.113}$$

where $\Omega'_i = \sum_{j=1}^{i}\omega'_j$ and the factors in the last operator product are assumed to be ordered from right to left. As long as the *on-shell* approximation is justified, the techniques employed in Sec. 4.4.2.1 for the two-photon transition matrix element can be used also to compute $n-$th order transition matrix element. Furthermore, if no more than one intermediate resonance contributes to the transition, the procedure followed in Sec. 4.4.2.2 can be subsequently applied to evaluate the folding with the field. A particularly relevant example that meets these conditions is the absorption of one pump photon ω_1 followed by that of two probe photons ω_2, when only the first intermediate continuum $|\psi_{\alpha\epsilon}\rangle$ is resonant while the second

intermediate continuum $|\beta\epsilon\rangle$ and the last continuum $|\gamma\epsilon\rangle$ are not. In this case, the three-photon transition matrix element $\mathcal{M}^{(221)}_{\gamma E,g}$ is

$$\begin{aligned}\mathcal{M}^{(221)}_{\gamma E,g} &= \langle \gamma E|\mathcal{O}G_0^+(E_g+\omega_1'+\omega_2')\mathcal{O}G_0^+(E_g+\omega_1')\mathcal{O}|g\rangle \simeq \\ &= \frac{\bar{\mathcal{O}}_{\gamma\beta}}{E_g+\omega_1'+\omega_2'-E+i0^+}\mathcal{M}^{(21)}_{\beta E,g}(\omega_1'). \end{aligned} \tag{4.114}$$

The transition amplitude then becomes

$$\begin{aligned}\mathcal{A}^{221}_{\gamma E,g} &= -\frac{i\bar{\mathcal{O}}_{\gamma\beta}}{\sqrt{2\pi}}\int d\omega_1'\mathcal{M}^{(21)}_{\beta E,g}(\omega_1')\tilde{F}_1(\omega_1')\int d\omega_2'\frac{\tilde{F}_2(\omega_{Eg}-\omega_1'-\omega_2')\tilde{F}_2(\omega_2')}{E_g+\omega_1'+\omega_2'-E+i0^+} \simeq \\ &\simeq \frac{i\bar{\mathcal{O}}_{\gamma\beta}}{\omega_2}\int d\omega\mathcal{M}^{(21)}_{\beta E,g}(\omega)\tilde{F}_1(\omega)\tilde{F}_2^2(\omega_{Eg}-\omega),\end{aligned}$$

where in the last passage we have assumed that the spectrum of the absorption component of the probe pulse is localized around ω_2 and we used the convolution theorem. This means that the three-photon amplitude $\mathcal{A}^{221}_{\gamma E,g}$ is equal, apart for a multiplicative factor, to the two-photon amplitude in which the frequency and spectral width of the probe field are larger by a factor of 2 and $\sqrt{2}$, respectively.

4.4.2.6 *Analytical expression of a metastable wave packet*

Let us derive an expression for the two-photon wave packet that results from a transition through an intermediate autoionizing state. The photoelectron wave packet created in the channel γ by a two-photon process from an initial atomic bound state $|g\rangle$ is

$$\Psi_\gamma(r,t) = \int d\varepsilon\, e^{-i\varepsilon t}\,\psi^-_{\gamma\varepsilon}(r)\mathcal{A}^{\pm}_{\gamma\varepsilon,g}, \tag{4.115}$$

where $\psi^-_{\gamma\varepsilon}$ is a scattering state fulfilling outgoing boundary conditions.

In the limit of a long IR pulse ($\sigma_t\Gamma_a \gg 1$), and for a time delay in which the center of the attosecond pulse train coincides with that of the IR pulse, i.e., $\tau = 0$, the two-photon amplitude in the presence of an intermediate metastable state $|a\rangle$ coupled via configuration interaction $V_{a,\alpha E}$ to the channel α, can be written as [see Equation (4.102)]

$$\mathcal{A}^{\pm}_{\gamma E,g} \propto \pm e^{i\Phi^{\pm}_{\gamma E}}\frac{\epsilon_{E\mp\omega_{\rm IR}}+q^{(21)}}{\epsilon_{E\mp\omega_{\rm IR}}+i}\,e^{-\frac{(E-E_0)^2}{2\sigma^2_{\rm APT}}} \tag{4.116}$$

In this expression, we have neglected the energy dependence of the strength of the dipole transition from the ground state to the non-resonant continuum, $|\mathcal{O}_{\alpha E,g}|^2$, assuming that the spectral width of the train, $\sigma_{\rm APT}$, is much smaller than the photoelectron energy, $\sigma_{\rm APT} \ll E - E_{\rm th}$. The term $\Phi^{\pm}_{\gamma E}$ incorporates all the phases associated to the Wigner and continuum-continuum delays, which here we do not treat explicitly. We point out that if $\gamma = 0$, (4.116) coincides with the

one-photon transition amplitude of Fano. For sufficiently large times, the wave packet has pure outgoing character, so that

$$\Psi_\gamma(r,t) \simeq \int d\varepsilon\, e^{-i\varepsilon t} \left[\psi^-_{\gamma\varepsilon}(r)\right]_{\text{out}} \mathcal{A}^\pm_{\gamma\varepsilon,g}. \tag{4.117}$$

The $\psi^-_{\gamma\varepsilon}$ states, discussed in § 2.3.1, are defined so that for $kr \gg 1$, their outgoing component can be written as

$$\left[\psi^-_{\gamma\varepsilon}\right]_{\text{out}} \propto e^{i\theta_k(kr)}, \quad \theta_k(kr) = kr + \frac{1}{k}\ln 2kr + \frac{i}{2}\ln k, \tag{4.118}$$

where the k-dependent normalization is taken into account in the last term, so the proportionality constant does not depend on either k or r.

When performing the integral in Eq. (4.117), we assume that the spectrum of the XUV harmonic is sufficiently narrow to justify the linearization of the phase $\theta_k(kr)$ with respect to k,

$$\begin{aligned}\theta_k(kr) &\simeq \theta_{k_0}(k_0 r) + \left[\partial_k \theta_k(kr)\right]_{k=k_0}(k-k_0) = \\ &= \theta_{k_0}(k_0 r) + (k-k_0) r_{\text{eff}}\end{aligned} \tag{4.119}$$

where we defined $r_{\text{eff}} \equiv \left[\partial_k \theta_k(kr)\right]_{k=k_0} = r - k_0^{-1}\ln 2k_0 r/e + i(2k_0)^{-1}$. Finally, we linearize the momentum deviation $k-k_0$ as a function of the corresponding energy deviation $\varepsilon - E_0$, where E_0 is the nominal central energy of the sideband, $E_0 \equiv E_g + \omega_{\text{XUV}} \pm \omega_{\text{IR}}$,

$$k - k_0 \simeq \frac{\varepsilon - E_0}{k_0}. \tag{4.120}$$

In conclusion, therefore, the outgoing part of a scattering state is approximately given by

$$\left[\psi^-_{\gamma E}(r)\right]_{\text{out}} \propto e^{i\theta_{k_0}(k_0 r)}\, e^{i(E-E_0)r_{\text{eff}}/k_0}. \tag{4.121}$$

Similarly, $\Phi^\pm_{\gamma\varepsilon} \simeq \Phi^\pm_{\gamma E_0} + (\varepsilon - E_0)\tau^\pm_\gamma$, $\tau^\pm_\gamma = \partial_E \Phi^\pm_{\gamma E}|_{E=E_0}$. We now insert (4.116) and (4.121) in (4.117),

$$\Psi_\gamma(r,t) \propto e^{i\left[\theta_{k_0}(k_0 r) - E_0 t + \Phi^\pm_{\gamma E_0}\right]} \int d\varepsilon\, e^{i\varepsilon(r_{\text{eff}}/k_0 - t + \tau^\pm_\gamma)} \frac{\varepsilon + \Delta^\pm + q^\pm}{\varepsilon + \Delta^\pm + i\Gamma/2}\, e^{-\frac{\varepsilon^2}{2\sigma^2_{\text{APT}}}}, \tag{4.122}$$

where now $\varepsilon = E - E_0$ and $\Delta^\pm = E_0 \mp \omega_{\text{IR}} - E_a$. The solution of the latter integral can be expressed analytically in terms of elementary functions and of the Faddeeva special function. After some algebra, we obtain the following expression for the photoelectron wavepacket,

$$\Psi_\gamma(r,t) \propto e^{i\left[\theta_{k_0}(k_0 r) - E_0 t\right]} e^{-\frac{\sigma^2_{\text{APT}}(r_{\text{eff}}/k_0 - t + \tau^\pm_\gamma)^2}{2}} \left[-i\pi(q^\pm - i)\frac{\Gamma}{2} w(z) + \sqrt{2\pi}\sigma_{\text{APT}}\right], \tag{4.123}$$

where the argument of the Faddeeva function is defined as

$$z = \frac{\Delta^\pm + i\left[\Gamma/2 + \sigma^2_{\text{APT}}(r_{\text{eff}}/k_0 - t + \tau^\pm_\gamma)\right]}{\sqrt{2}\sigma_{\text{APT}}}. \tag{4.124}$$

We will use this analytical expression to validate the reconstruction of the metastable photoelectron wave packet done in § 5.3.

Part III

RESULTS

5

RABITT SPECTROSCOPY

In this Chapter we present the study of electron dynamics in the helium and argon atoms by means of the RABITT technique. Particular attention is given to the correlated dynamics of autoionizing states. The Chapter is divided in three sections.

In § 5.1, we use the finite-pulse extension of the soft photon model introduced in § 4.3 to reproduce and interpret the background (non-resonant) features of angularly-resolved RABITT spectra in the energy region of the doubly-excited states of helium. We validate this approach by comparing the results of the SPA with the results of virtually exact *ab initio* simulations.

In § 5.2, we fully characterize the angularly-integrated RABITT spectrum using the analytical finite-pulse model derived in § 4.4 and validating it with the *ab initio* method. By doing so, we are able to study the effects of autoionizing states on continuum-continuum transitions, and explore their attosecond dynamics. In the first part of this section, we show that, when intermediate autoionizing states are involved, the RABITT photoelectron spectra does not follow the usual stationary picture. As a consequence of the finite pulse duration, the frequency of the sideband oscillation is no longer $2\omega_{\mathrm{IR}}$ and displays a pronounced resonant modulation, different from that discussed in § 4.4.1 in the context of non-resonant transitions with short pulse durations. As anticipated in § 4.4, we also show that the interplay between the resonant and the continuum contribution to the resonant quantum path of the RABITT scheme makes the apparent local phase offset not to undergo a π excursion anymore. Additionally, we explore the case in which the time delay is so large that the probe pulse does not overlap with the APT anymore. From the phase of the beating of the resonant sideband that persists, the coherent metastable wave packet created by the pump pulse can be reconstructed.

Experimental access to the resonant atomic phase came, recently and independently, from the groups of Pascal Salières and Anne L'Huillier, who performed state-of-the-art RABITT experiments in resonant regions of the helium and argon atoms, respectively. In § 5.3, we apply the model in the conditions of the experiments, and confirm that the observed dependence of the beating phase on the harmonic-resonance detuning in both experiments is compatible with our model. In the experiment of helium, the formidable experimental resolution permitted to extract the energy-resolved amplitude and phase of the resonantly-populated RABITT sidebands, thus allowing for the reconstruction of the unperturbed metastable wave packet. In the experiment of argon, we show that the

two-channel nature of the problem is responsible for the departure of the phase profile from a π shift.

In § 5.4, we study correlation effects on the angularly-resolved RABITT spectrum of helium, by means of *ab initio* simulations, in a region close to the first ionization threshold, where no resonances are present but where the effect of the Coulomb potential is more visible. In collaboration with the experimental group of Ursula Keller, we show that the laser-induced component of the photo-ejection time delay (τ_{CC}) has a significant dependence on the angle at which the photoelectron is emitted, with respect to the angle of polarization of the impinging light.

5.1 NON-RESONANT RABITT SPECTROSCOPY

In this section, we investigate the RABITT photoionization spectrum of the helium atom from the $1s^2$ ($^1S^e$) ground state to the energy region between 30 eV and 40 eV above the first ionization threshold, which features the series of metastable doubly excited states that converge to the $N = 2$ threshold. We choose this energy region since it will be the focus of our study also in § 5.2. For the moment, we will not aim to describe the DES.

Let us consider the case of a train of attosecond pulses comprising a sequence of Gaussian XUV pulses, with central energy $\omega_{\text{XUV}} = 60.29$ eV and fwhm=192 as, separated by half the period of the IR probe pulse and with alternating sign; the train envelope has a duration of 6 fs and a maximum intensity $I_{\text{XUV}} = 0.1$ TW/cm^2. We conduct the *ab initio* simulation with a short ($\text{fwhm}_{\text{IR}} = 5.36$ fs) moderately intense ($I_{\text{IR}} = 1$ TW/cm^2) IR pulse. On the one hand, the use of a short IR pulse significantly reduces the computational burden while at the same time reproducing most of the features observed in realistic experiments, in which the length of the IR pulse associated to XUV trains is often larger. On the other hand, since the duration of the XUV train and the IR pulse are now comparable, some effects due to the fact that the IR intensity is not uniform across the train are to be expected. For a meaningful comparison with the experiment, therefore, it is important to be able to identify and factor out such effects.

In Figure 22 we compare the photoelectron angular distribution for a fixed time delay $t_{\text{d}} = -T_{\text{IR}}/4 = -0.666$ fs computed with: (a) *ab initio* simulation, (b) SPA model with a monochromatic IR field, and (c) SPA model with a pulsed IR field. All three methods predict a minimum in the harmonic signal at $\sim 60^\circ$ from the polarization axis. This is an extreme example of the angular broadening observed experimentally and reproduced with single-active-electron simulations by Guyetand *et al.* [118]. In [119], the phenomenon was justified on the basis of the perturbative limit of the soft-photon approximation. Indeed, third-order corrections to the harmonic amplitude that come from the absorption or emission of two IR photons have an angular distribution proportional to $\cos^3\theta$. The interference term with the first-order amplitude, which is proportional to $\cos\theta$, therefore,

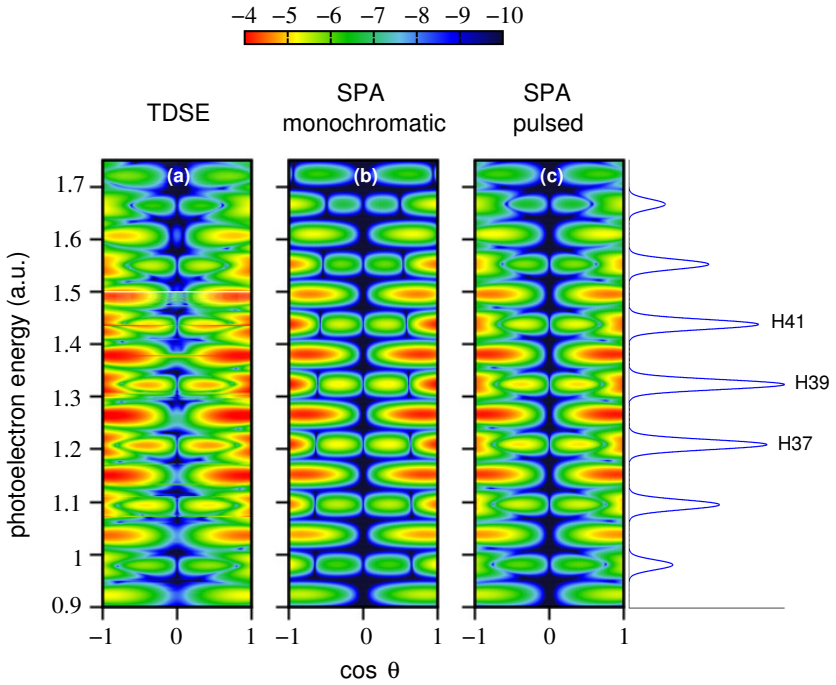

Figure 22: Calculated photoelectron spectra for the case where a helium atom is ionized by an attosecond pulse train with energy 61eV in the presence of an IR field ($\lambda_{IR} = 800nm$, $I_{IR} = 1$ TW/cm^2). Panel (a) represents the full calculation of the TDSE, using a cosine-square envelope for the IR probe pulse, while pannels (b) and (c) were calculated using the SPA for: (b) a monochromatic IR pulse and (c) a cosine-square modulated IR pulse. All panels are shown in logarithmic scale.

gives rise to a $\cos^4\theta$ term which alters the harmonic signal predominantly along the polarization axis.

The agreement of the monochromatic model (Figure 22b) with the simulation (Figure 22a), is not very impressive. In the simulation, the odd-harmonics signals next to the polarization axis are clearly split, a feature that the monochromatic model does not reproduce. That this feature is due to the finite duration of the probe pulse and not to the correlated electron dynamics in the atom is clearly demonstrated by the excellent agreement with the third panel, obtained with the pulsed SPA model. Indeed, apart from the missing narrow resonant lines associated to He doubly-excited states, the pulsed model is able to reproduce all the background features of the simulated spectrum. This splitting affects both the angular and the energy distribution of the harmonic signal. Therefore, it should be taken into account when assessing the effects of multi photon transitions and Coulomb corrections to the soft-photon model with short pulsed radiation.

Figure 23 compares the angularly-integrated photoelectron spectra computed with *ab initio* simulations and with the pulsed SPA model for five different time delays between the two pulses: −1.33 fs, −0.67 fs, 0 fs, 0.67 fs, and 1.33 fs (Figs. 23a-e, respectively). Again, apart from the resonant features, the agreement between model and simulation is very good across the whole IR period and energy range.

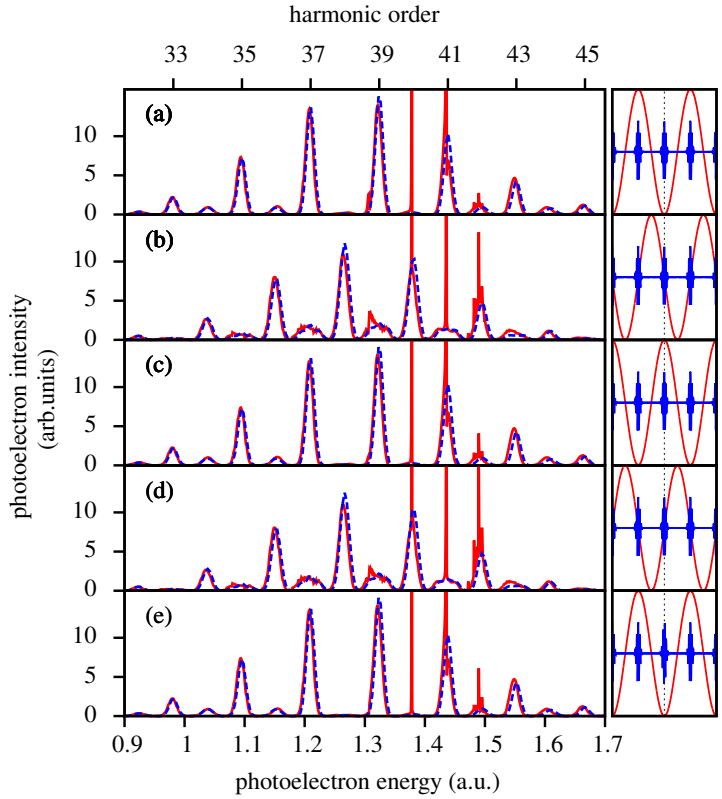

Figure 23: Total photoelectron distribution of an helium atom ionized by an attosecond XUV pulse train of central frequency 61eV in the presence of an IR dressing pulse ($\lambda_{IR} = 800nm$, $I_{IR} = 1$ TW/cm^2) for five different time stages: (a) XUV at the minimum of the vector potential; (b) XUV at inflection point; (c) XUV at maximum of vector potential; (d) XUV at inflection point (half an IR period later than case (b)); (e) XUV at minimum of vector potential (one IR period later than in case (a)). Red solid line: numerical solution of the TDSE. Blue dashed line: pulsed SPA model.

In conclusion, the pulsed version of the SPA model is able to reproduce the consequences of a finite duration of the IR dressing pulse on the fully differential photoelectron distribution. Possible application of such extended model include interpretation of photoelectron angular distributions in real experiments, refinements of the RABITT protocol, and assistance in the interpretation of photoelectron spectra containing features beyond the reach of a single-active-electron model, like autoionizing states and above-threshold multi-channel interactions. In fact, the validity of approximating the continuum wave functions to free spherical waves in the energy regions considered, will allow us, in the following section, to use such states as the unperturbed continuum states in the LOPT resonant model.

5.2 RESONANT RABITT SPECTROSCOPY. THEORETICAL PREDICTIONS

Let us now analyze the role of autoionizing states. While to describe the background features of the spectrum we were able to use a strong-field model, in presence of resonant structure a non-perturbative treatment in non-stationary conditions is not easily applicable. Here, therefore, we will follow a perturbative approach. As we did in the previous section, we will choose helium

as a target. Apart from being amenable to an accurate *ab initio* description in the presence of external light pulses, helium is an ideal candidate to investigate atomic transitions through autoionizing states because the ionization continuum of this atom has been the subject of intense study for more than fifty years [95]. In particular, the $N = 2$ $^1P^o$ and $^1S^e$ series of autoionizing states have been investigated both experimentally [10, 120, 121, 122, 123] and theoretically [124, 96, 125, 126, 127, 128, 129, 130, 131, 132, 133], and many of their properties, such as positions, width, and q parameter from the ground state, are well known. We note, nonetheless, that the results we obtain are general aspects of multi-photon resonant atomic transitions, as we show in § 5.3.2 for the argon atom.

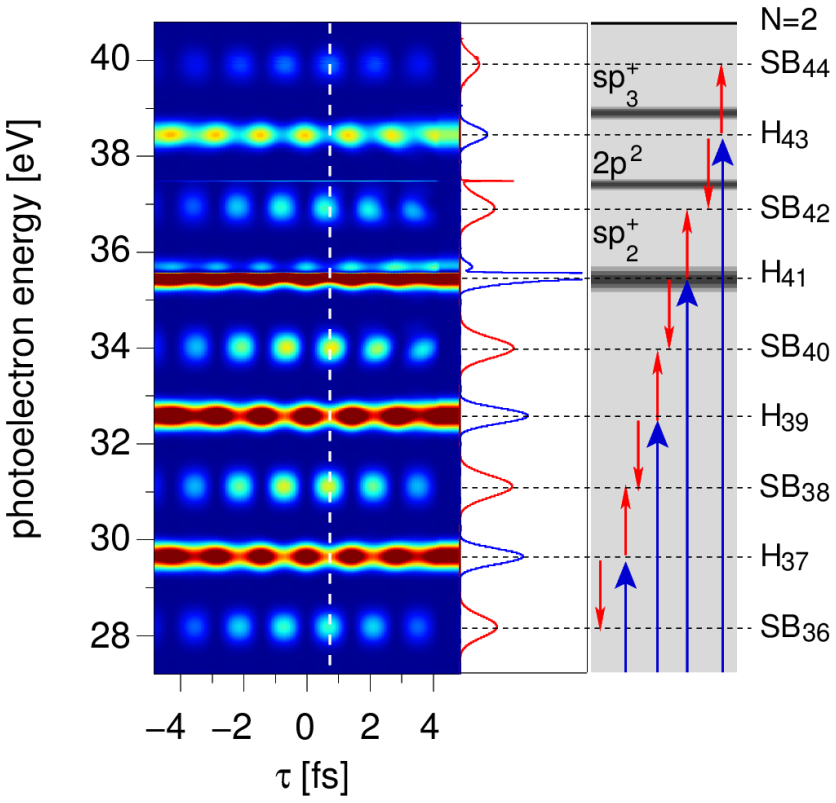

Figure 24: Left panel: *ab initio* photoelectron spectrum for the XUV-APT-pump weak-IR-probe ionization of He in the region of the $N = 2$ DESs as a function of pump-probe time delay. The APT is centered at $\hbar\omega_{\rm APT} = 57.21$ eV ($\rm IP_{He} = 24.6$ eV), with fundamental frequency $\hbar\omega_{\rm IR} = 1.466$ eV; both the pump and the probe have fwhm$\sim$7 fs. Central panel: signal at a fixed time delay (white dashed line). Right panel: outline of the relevant states in the process. Starting from the $1s^2$ ground state, the atom absorbs a XUV photon from the APT and exchanges an IR photon with the probe pulse, leading to strong $\rm H_{2n+1}$ harmonic signals, in the $^1P^o$ continuum, and to weak $\rm SB_{2n}$ sideband signals, in the $^1S^e$ and $^1D^e$ continua.

Fig. 24 shows a representative example of *ab-initio* results based on the solution of the TDSE for the helium atom ionized from the ground state with an XUV-APT in conjunction with a weak 845 nm IR pulse. We see that the sp_2^+ DES is resonantly excited by the $\rm H_{41}$ harmonic ($\hbar\omega_{\rm IR} = 1.466$ eV). The peak intensity and the FWHM of the APT are $I_{\rm APT} = 5\ \rm GW/cm^2$, $\rm fwhm_{APT} = 6.8$ fs, and those of the IR-probe pulse are $I_{\rm IR} = 10\ \rm GW/cm^2$, $\rm fwhm_{IR} = 7.2$ fs. Figure 25 shows the energy levels of helium in the region of interest and illustrates schematically the radiative couplings that must be plugged in the model to reproduce the RABITT spectrum

of the atom when the harmonics can be resonant with the first two $^1P^o$ bright autoionizing states, and sidebands can populate the final $2p^2\ ^1S^e$ state. The details of the obtention of these parameters are lengthy and are left for Appendix C.

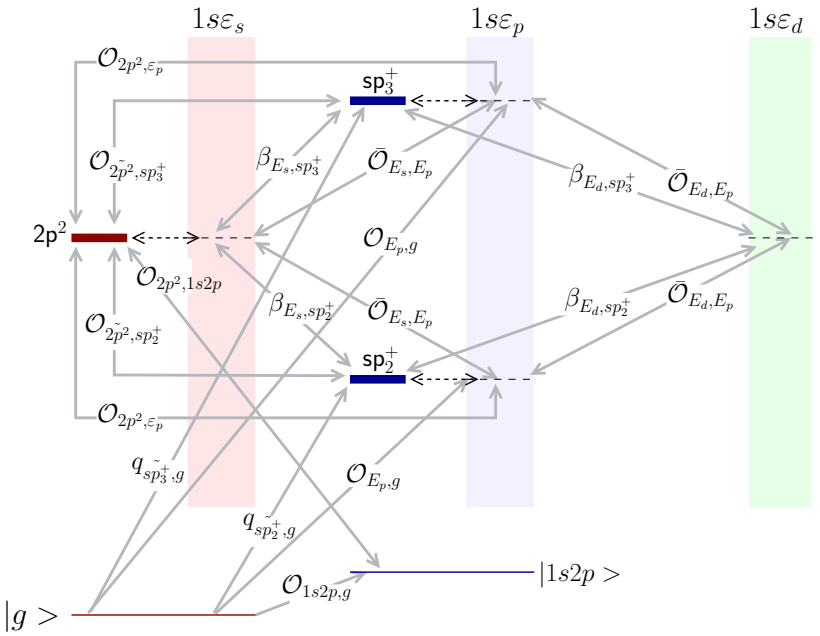

Figure 25: Scheme of the essential states involved in the RABITT ionisation of the helium atom in the region of the $N = 2$ auto ionizing states, together with the relevant radiative coupling between them that must be taken into account to reproduce the pump-probe photoelectron spectrum with the finite-pulse resonant two-photon model described in the text.

5.2.1 *Modulation of attosecond beating*

Fig. 26 shows both the *ab initio* (upper panel) and the model (central panel) prediction of the photoelectron spectrum as a function of the pump probe time delay for the sidebands SB_{38-42} at the fixed IR frequency of $\hbar\omega_{IR} = 1.466$eV (same as in Fig. 24). Positive time delays indicate the XUV pulse train comes first. The intermediate resonance sp_2^+ induces a local phase shift, in opposite directions, of the resonantly populated sidebands SB_{40} and SB_{42}, an effect that is not present when a sideband is populated via non-resonant paths only, as in the case of SB_{38}. Model and *ab intio* spectra look essentially the same. The vertical white lines in the two first panels denote the maximum of the sideband signal and show how the absolute value of the local phase shift $\delta\varphi(\omega_{IR}, \tau)$ of the two resonant sidebands increases with the time delay,

$$I_{SB}(\tau) \propto \cos\left\{2\omega_{IR}\tau + \delta\varphi(\omega_{IR}, \tau)\right\}. \tag{5.1}$$

This means that the resonance introduces a modulation of the RABITT beating frequency itself. In this scenario, the concept of a global RABITT phase loses its meaning. In the cases we examined, however, the phase deviation is well approximated by a linear interpolation in a wide time delay interval (bottom panel of Fig. 26), $\delta\varphi(\omega_{IR}, \tau) \approx \delta\varphi_0(\omega_{IR}) + \delta\omega(\omega_{IR})\tau$, so

$$I_{SB} \propto \cos\left\{\left[2\omega_{IR} + \delta\omega(\omega_{IR})\right]\tau + \delta\varphi_0\right\}. \tag{5.2}$$

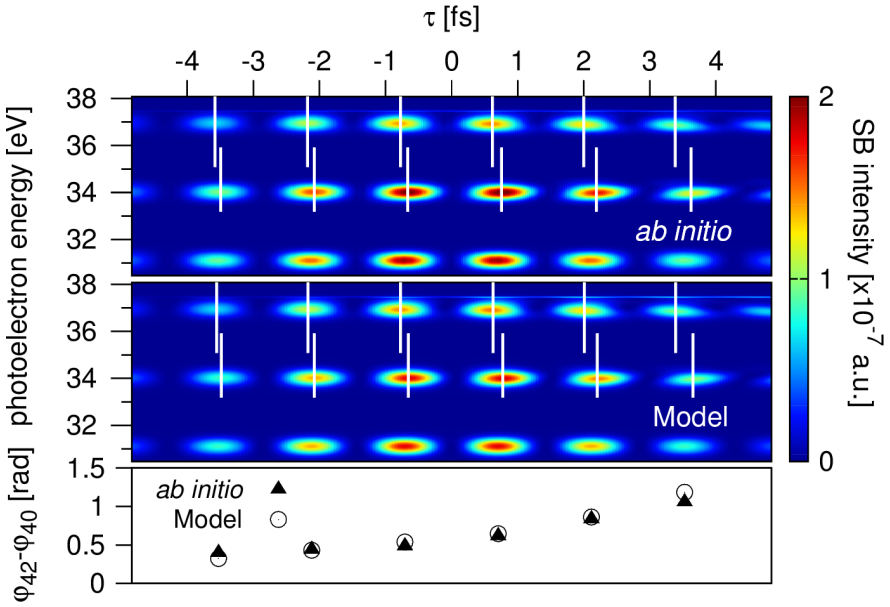

Figure 26: Left panel: photoelectron spectrum as a function of the pump-probe time delay for sidebands SB_{38}, SB_{40} and SB_{42} of the driving frequency $\omega_{IR} = 1.467$ eV. Right panel: energy-integrated photoelectron spectrum as a function of the pump-probe time delay for both model and *ab initio* simulations. The presence of the sp_2^+ DES (~ 35.5 eV), which is populated by the 41st harmonic (not shown) shifts sidebands SB_{40} and SB_{42} in opposite directions. Furthermore, due to the finiteness of the pulses used, the resonance induces a frequency modulation which can be seen by comparing the separation between the white lines that indicate the maxima of the sideband oscillations.

The local phase shift is affected by the apparent phase shift at $\tau = 0$ as well as by the modulation of the frequency, $\delta\omega(\omega_{IR})$. As discussed in § 4.4.1, the modulation of RABITT beating frequency appears even in absence of intermediate resonances, as a result of using finite pulses. The latter non-resonant effect, however, is always a shift towards the red, it does not depend much on the IR carrier frequency, and it rapidly disappears as longer pulses are employed. The resonant modulation of the sideband frequency, on the other hand, induces opposite shifts in the two resonant sidebands, it depends strongly on the detuning of the resonant harmonics from the intermediate autoionizing states, and it becomes sharper when longer pulses are used. The model prediction for the frequency modulation, obtained by Fourier analyzing the energy integrated sideband signal, is $\delta\omega = -0.073$ eV. The non-resonant redshift associated to the use of a 800 nm 6 fs probe pulse is comparatively large, $\delta\omega_{NR} = -0.038$ eV. Both the total and the non-resonant values are in agreement with those from the *ab initio* calculation (the latter being estimated from the non-resonant sideband SB_{38}). By taking the difference between the total and the non-resonant values, the resonant contribution to the sideband frequency modulation, due to the sp_2^+ doubly excited state, is estimated as $\delta\omega_{sp_2^+} = -0.035$ eV, which corresponds to a change in the RABITT period of 17 as.

Figure (27) shows the photoelectron spectrum of sidebands 40 and 42, as a function of the IR carrier frequency, for five different pump-probe time delays. The agreement between *ab initio* and model, again, is excellent. In particular, the sideband resonantly populated from below (SB_{42}) shows a maximum to the left and a minimum to the right of the central resonance frequency ($\hbar\omega \approx 1.466$ eV) for $\tau = T_{IR}$, while the opposite is true for the sideband that is populated from above. This feature is responsible for the apparent phase shifts for the two side-

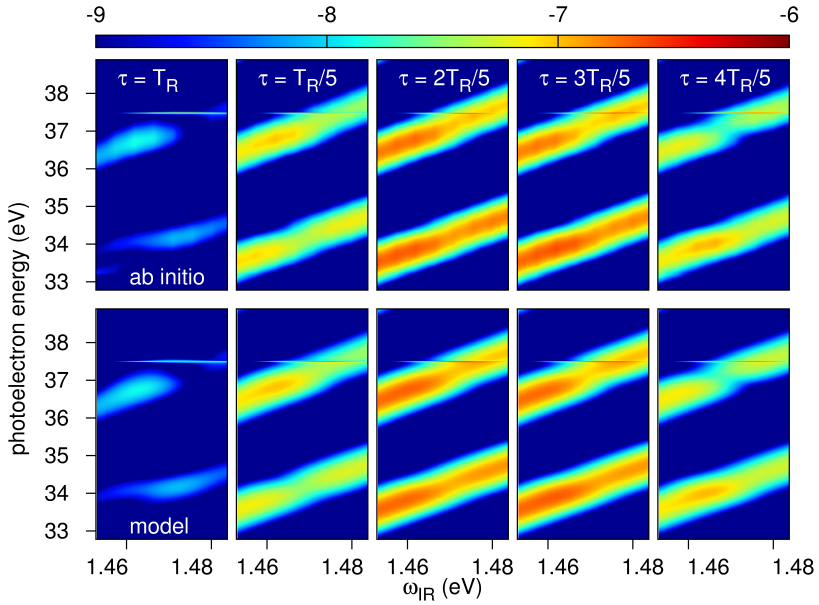

Figure 27: Photoelectron spectrum as a function of the driving laser frequency for SB_{40} and SB_{42} at five different stages of the sideband oscillation ($\tau = T_R$ corresponds to the minimum). Upper panels show the *ab initio* calculations and lower panels show the model results.

bands, which are shown in the first two panels of Fig. 28 and were obtained by Fourier analyzing the spectrum in the time-delay interval $\tau \in [0, T_{IR}/2]$. The sp_2^+ and sp_3^+, populated by H41 and H43, respectively, give rise to resonant structures in the apparent phase shift that are located at IR frequency close to the resonance condition of each DES with the corresponding harmonics. As noted in § 4.4.2, the overall phase excursion depends on the parameters of both the resonance and the pulses used. In the present case, the larger dipole matrix element of sp_2^+ with the ground state, compared with that of sp_3^+, makes the former dominate the shape of the profile, although the peak for the sp_3^+ DES can also be recognized. Finally, in the last panel of Fig. 28 we show the phase of the beating of the H_{39} integrated harmonic signal. In this case, the resonance profile arises from the interference between the direct one-photon ionization amplitude from the ground state and the *three-photon* amplitude for the resonant absorption, from the ground state, of one XUV photon of the H_{41} harmonic followed by the stimulated non-resonant emission of *two* IR photons. As we discussed at the end of § 4.4.2, this latter amplitude can be easily computed with a straightforward multi-photon extension of the finite-pulse resonant model discussed in § 4.4.2.5. The good agreement with the full-fledged *ab initio* simulation for this process certifies that such extended model works. The phase profile of the sideband is replicated in the non-resonant harmonic phase, which demonstrates both the small influence of the IR probe and the smooth phase variation of the background continuum. The interference between one and three photon paths could be used, for example, to extract the phase profiles of intermediate autoionizing states of even parity, which may be present in the second step of the three-photon process, and that would not be possible to obtain with typical pump-probe schemes due to the dipole selection rules.

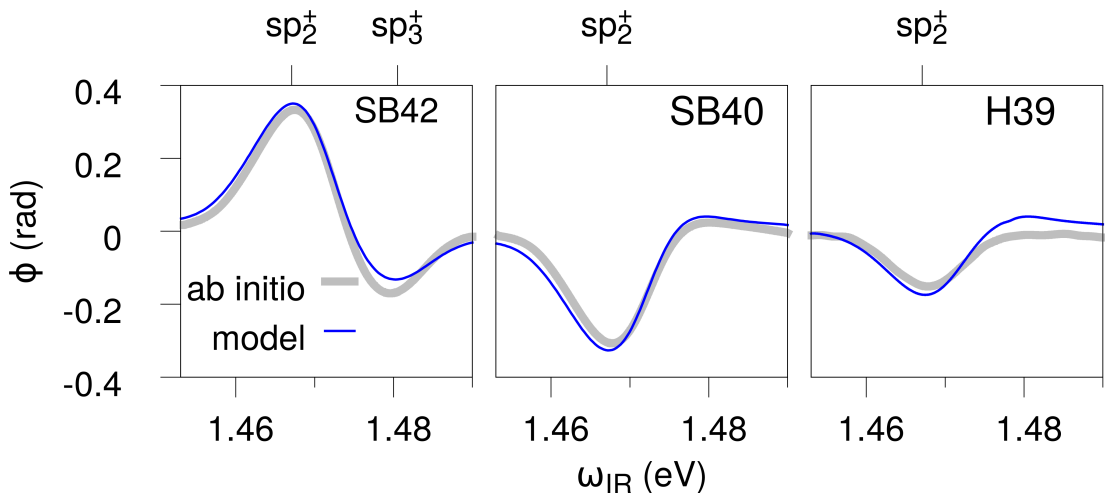

Figure 28: Apparent phase shift of the integrated-signal beating of sidebands SB_{42} (left panel), SB_{40} (central panel), and harmonic H_{41} (right panel), with respect to the non-resonant SB_{38} sideband phase, as a function of the fundamental IR carrier frequency. In all three cases, the largest phase excursion occurs when the intermediate harmonic H_{41} is resonant with the sp_2^+ DES. In SB_{42}, the effect of sp_3^+ through H_{43} is visible as well. The resonant profile of H_{41}, which is comparable to the one of SB_{40}, results from the interference between the direct one-photon excitation amplitude of the continuum from the ground state with the three-photon amplitude, in which the resonant absorption of one pump photon from H_{41} is followed by the stimulated emission of two IR probe photons.

5.2.2 *Separated pulses*

Let us now consider the case in which the pump and the probe pulse do not overlap. Fig. 29 shows the $SB_{40,42}$ sidebands in a wide range of time delays for $\omega_{IR} = 1.475$ eV. When the APT and the IR pulse do overlap ($|\tau| \lesssim 5$ fs), the sidebands are dominated by the non-resonant signal and are centered at $E = 2n\omega_{IR} - IP$, where IP is the ionization potential. Between 5 fs and 10 fs, when the pulses begin to separate, the non-resonant contributions disappear, while the sidebands narrow and shift to symmetric positions around the two resonances. In contrast with non-resonant two-photon transitions, the sideband signals persist even when pump and probe do not overlap. Furthermore, the SB_{42} sideband displays the characteristic interference fringes of the $sp_2^+ - sp_3^+$ beating, with a lifetime intermediate between those of the two resonances.

The strongest contribution to the sideband comes from the transition to the $2p^2$ state, which is permitted even at the level of the independent-particle approximation. The q parameters for the excitation of the $2p^2$ state from either the sp_2^+ or the sp_3^+ states differ, thus giving rise to an oscillating effective $q_{\text{eff}}(\tau)$ that manifests as a beating of the background continuum out of phase with respect to that of the final resonance. This beating could also be used to reconstruct the autoionizing wave packet, following concepts similar to those based on the holographic principle [134].

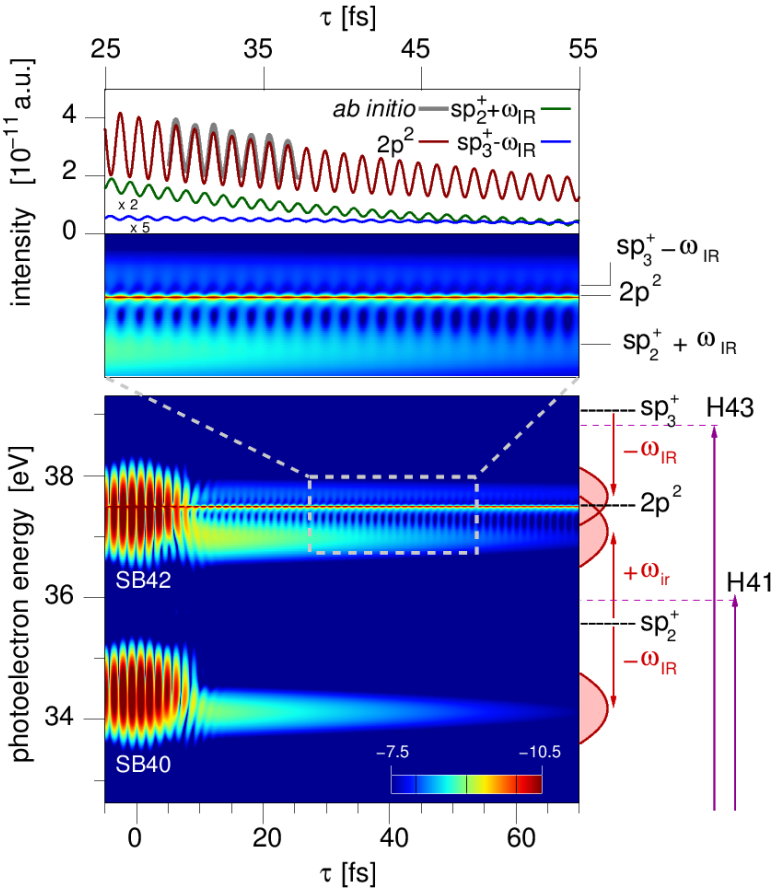

Figure 29: Bottom panel: spectrum of the $SB_{40,42}$ sidebands vs. τ computed with the model, for $\hbar\omega_{IR} = 1.475$ eV. The harmonics H_{41} and H_{43} (not shown) are detuned from the sp_2^+ and sp_3^+ $^1P^o$ DES by $\delta_{H_{41}-sp_2^+} = 0.37$ eV and $\delta_{H_{43}-sp_3^+} = -0.19$ eV, respectively. Top panel: the modeled final $2p^2$ resonant signal (red solid line), which dominates the spectrum, reproduces the *ab initio* prediction (gray thick solid line) with high accuracy.

5.3 RESONANT RABITT SPECTROSCOPY. EXPERIMENTAL OBSERVATIONS

Some of our theoretical predictions were recently confirmed by two independent RABITT experiments performed in the helium and argon atoms which we now discuss.

5.3.1 *Helium. Reconstruction of an unperturbed metastable wave packet*

Traditionally, RABITT was devised to measure the phase of the oscillations of the energy integrated sideband signal. This is very convenient since one does not need a very high spectral resolution. Nonetheless, obtaining high resolution energy-resolved spectra is certainly possible in some experimental facilities. Recently, RABITT experiments in helium in the energy region considered in the previous sections were carried out at CEA-Saclay in the laboratory of Pascal Salières with unprecedented precision. In these experiments, the IR pulses employed had

wavelengths of around 1300 nm and durations of 70 fs, which corresponds to a spectral width of $\Delta\nu = 26$ meV.

Fig. 30 (bottom panel) shows the experimentally observed RABITT photoelectron spectrum for an IR wavelength of 1295 nm ($\omega_{IR} \approx 0.958$ eV). At this IR frequency, the sp_2^+ state, which has an energy of $E_{sp_2^+} = 60.15$ eV and a width of $\Gamma_{sp_2^+} = 37$ meV, is populated by H63. The resonantly populated sidebands, SB62 and SB64, in contrast to the case with 845 nm light sources, are not affected by any other autoionizing states.

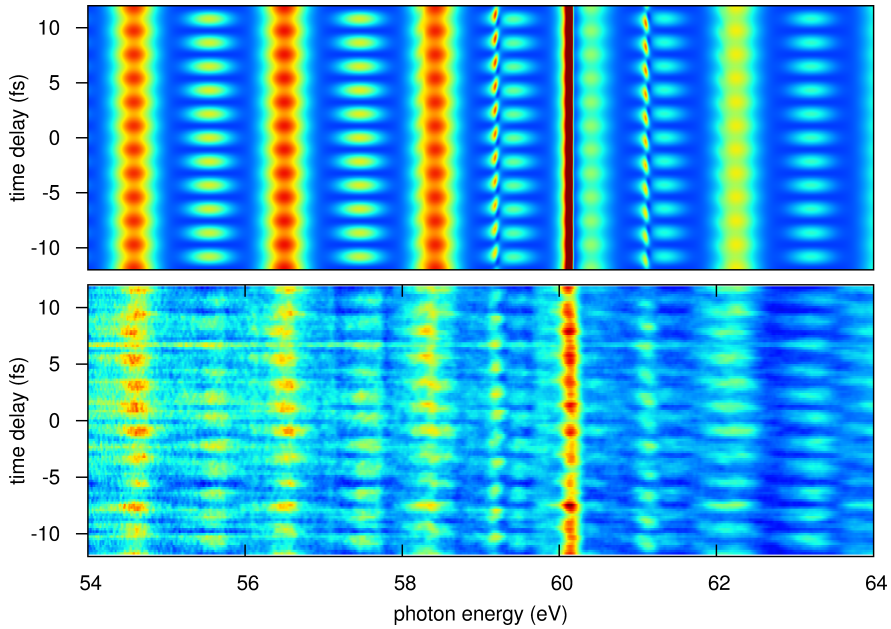

Figure 30: Experimental (bottom) and theoretical (top) spectrograms in the [54-64] eV region of helium for a laser wavelength of 1295 nm at which harmonic 63 lies on resonance the sp_2^+ doubly-excited state ($E_{sp_2^+}$ = 60.15 eV). The theoretical spectrum is convoluted with a Gaussian function of 190 meV fwhm to take into account the response of the apparatus function in the experiment.

We reproduced the experimental conditions with the model using the same value for the parameters as those obtained in the comparison with the *ab initio*. The top panel of Fig. 30 gives the model calculated spectrum up to third order. After the theoretical spectrum was calculated, we applied a convolution with a Gaussian function of 190 meV of full width at half maximum in order to take into account the response of the experimental apparatus function, which was estimated to be in this range. One can see that the main features are reproduced quite well, including the splitting of the resonant harmonic and of the resonantly populated sidebands. Indeed, Fig. 31 shows a magnification of the spectrum during one RABITT cycle in the energy region of SB62 (panel a, theory; panel c, experiment) and SB64 (panel b, theory; panel d, experiment). In it we see clearly that the sidebands are split into two components: a resonant component that is retarded for the lower sideband and advanced for the upper sideband, and a non-resonant component.

In § 4.4.2.2 we mentioned that the sideband dephasing depends on the electron kinetic energy in essentially the same way as it depends on the (resonant

harmonic) laser frequency. An alternative way to extract the phase imprinted by the autoionizing state is thus to spectrally resolve the sideband at a certain resonant frequency and fit the sideband's intensity signal, at each energy, to the RABITT interference equation:

$$I_{\mathrm{SB}}(E,\tau) = |S_{bg}(E)| + |A(E)|\cos[2\omega_{\mathrm{IR}}\tau + \varphi(E)] \tag{5.3}$$

where $S_{bg}(E) = |A^{+}(E)|^2 + |A^{-}(E)|^2$ is the time-averaged (or background) signal that corresponds to the sum of the square modules of the energy-resolved transition amplitude from below $A^{+}(E)$ and from above $A^{-}(E)$, $A(E) = 2|A^{-}(E)||A^{+}(E)|$ is the energy-resolved amplitude of the beating, and $\varphi(E) = \arg[A^{+}(E)] - \arg[A^{-}(E)]$ is the phase of the beating. Taking advantage of the exquisite experimental resolution, we compared the experimental and theoretical phases extracted with this procedure. The grey dots in Fig. 32 indicate the spectrally-resolved sideband phase retrieved experimentally while the blue solid line indicates the spectrally-resolved phase obtained with the model. The quantitative comparison between experiment and model is spectacular. Both phases are referenced with respect to the value of the phase of the non-resonantly populated sideband SB60.

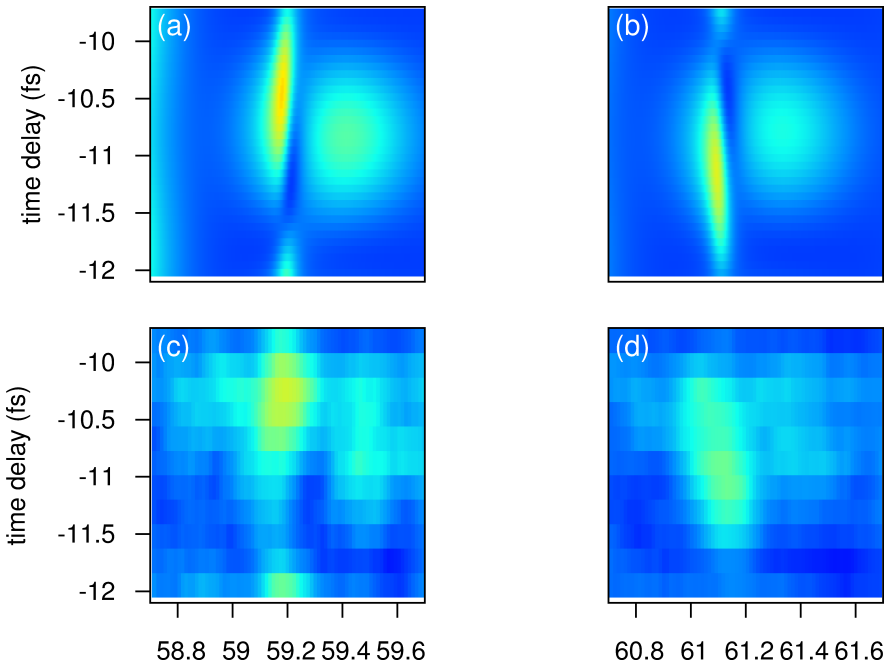

Figure 31: Close-up of the spectrum in Fig. 30 at the energy region of the two resonantly populated sidebands: (a) theory, (c) experiment for SB62, and (b) theory, (d) experiment for SB64.

To highlight the differences between the energy-resolved phase-extraction method and the frequency-resolved (energy-integrated) method applied in the traditional RABITT spectroscopy, additional experiments were carried out. Specifically, nine RABITT traces at different frequencies were measured. Each of the nine orange dots correspond to the sideband phase obtained at each of these frequencies. The red line, which is again in perfect agreement with the experiment, represents the results obtained with the model. The phase profiles obtained with the energy-resolved and frequency-resolved (energy-integrated) methods are clearly

different. This difference comes from the large spectral width of the XUV harmonics, which is estimated around 450 meV. In the energy-resolved method, the IR, which in this case may be regarded as monochromatic, replicates each chromatic component of the lower and upper harmonics in the sideband. The phase of the resonant harmonic is in this way transferred to the sideband without influence of the pulse durations, a situation which is not true when the sideband is integrated, as we commented in § 4.4.2.2. By looking at the energy-resolved spectrum of the nine frequencies, we observed that the phase profile did not change appreciably as long as the harmonic fully contained the resonance. This means that, in the energy-resolved method, knowing precisely the frequency of the exciting radiation is not needed, which experimentally is much more advantageous.

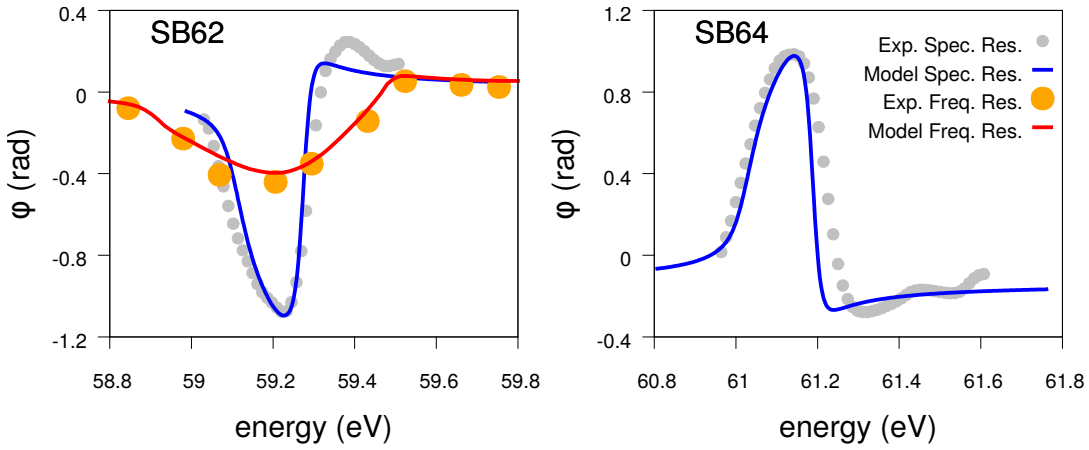

Figure 32: Spectral phase of the EWP corresponding to SB62 (left) and SB64 (right) for the resonant laser wavelength of 1295 nm, and phase of the energy-integrated SB62 obtained for nine different frequencies. For the energy-resolved case, experimental data are shown as grey points and the theory prediction as a blue solid line, while for the energy-integrated case, experimental data are shown as orange points and the theory prediction as a red solid line.

From the energy-resolved fitting procedure in Equation (5.3) applied to sideband SB62, using the non-resonant SB60 as a reference, and assuming that for the non-resonant sideband the upper and lower amplitudes are similar, one can obtain the amplitude of the resonant upper path $|A^+(E)|$. This, along with the resonant phase $\arg[A^+(E)]$ given in Fig. 32 (left panel), completely characterizes the two-photon metastable electron wave packet (EWP). Fig. 33 shows the comparison between the experimentally-reconstructed (grey solid line) and theoretically-reconstructed (black solid line) EWP at a fixed position.

We note that the experimental EWPs is distorted due to the spectral resolution of the detector. The theoretical EWP is as well, since, as we commented before, we convoluted the theoretical spectrum with a Gaussian function to account for this effect. The theoretical reconstructed EWP from the non-convoluted spectrum, i.e., without distortion from the experimental detector, is shown as the red solid line in Fig. 33, and we compare it to the EWP obtained analytically from Equation (4.123) (green-dashed line). The analytic two-photon EWP and the wave packet reconstructed from the non-convoluted sideband are very close, which validates the reconstruction method used. The minor difference in the decay tail at large times is due to the finite duration of the IR probe pulse (70 fs) which, although large, is sufficient to have visible effects on the time scale

of 40 fs of the figure. The first peak around 0 fs, is due for the most part to the direct photoelectron ejection to the continuum, while the long tail is the result of the autoionization of the resonance. The minimum (close to zero) between the two peaks is caused by the destructive interference between direct and resonant photoemission. Figure 33 is the temporal counterpart of the formation of a Fano profile in the continuum [54]. Notice that the wave packet, at a fixed position, as a function of time is not the same as a snapshot, at a given time, of the wave packet as a function of the position.

Moreover, in this case, the two-photon EWP essentially *coincides* with the one-photon EWP since i) the IR probe is, to all practical purposes, infinite and weak enough so that it does not affect the resonant line shape and does not deplete the doubly excited by multi-photon ionization, and ii) the radiative coupling between the localized component of the autoionizing state and the final continuum is negligible ($\gamma \approx 0.015$). Indeed, in the inset of Fig. 33 we compare the EWPs obtained analytically from Equation 4.123 for the value of $\gamma = 0$, which corresponds to a one-photon EWP (blue dotted line), and the analytical two-photon EWP (green dashed line) . Both essentially coincide, indicating that, leaving aside the effects due to the response of the apparatus function in the experiment, one can identify the experimentally reconstructed EWP with the single-photon EWP, i.e., the one obtained from Fano's formula.

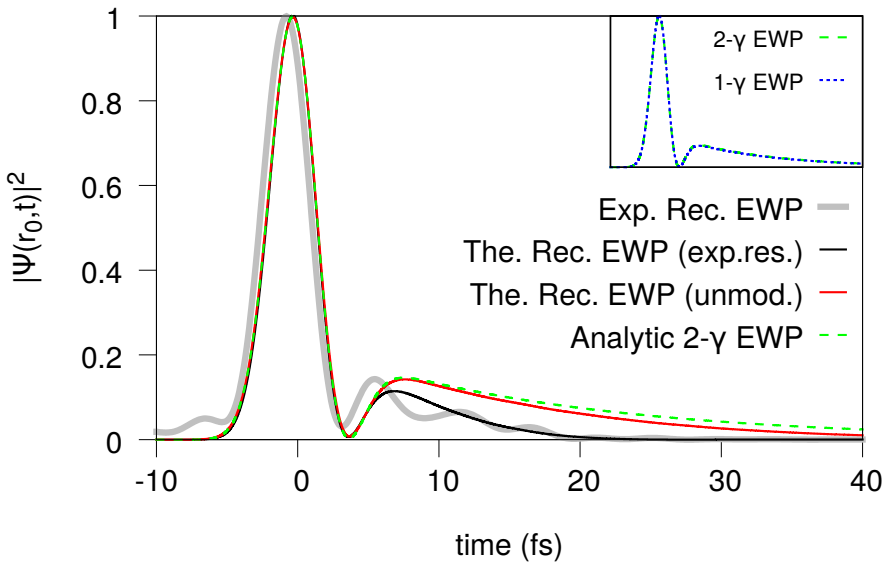

Figure 33: Reconstruction of the EWP of SB62 for a laser wavelength of 1295 nm. The position is set to $r_0 \approx 0$. Grey solid: experimental reconstruction. Black solid: theoretical reconstruction from the spectrum in Fig. 30 (top), i.e., taking into account the resolution of the experimental detector. Red solid: theoretical reconstruction from non-convoluted spectrum. Green dashed: two-photon EWP calculated analytically from Eq. 4.123. Top right inset of figure: comparison between the two-photon (green dashed) and one-photon (blue dotted) EWPs. The oscillations of the experimentally reconstructed EWP starting from 10 fs are ascribed to the truncation of the Fourier transform.

5.3.2 *Argon. Multichannel interferences*

So far we have illustrated the attosecond correlated dynamics unfolding in a single-channel continuum ($1s\varepsilon_p$ of helium). The results are, nonetheless, com-

pletely general. Indeed, the group of Anne L'Huillier performed the first resonant RABITT experiment in the argon atom using tunable attosecond pulses so that the frequency of the harmonics could be gradually varied (as it was done in § 5.2). In this experiment, photoelectron spectra were measured in the kinetic energy range between 4 eV and 20 eV, corresponding to photoionization with harmonics 13-23, as a function of the delay between the XUV and the IR pulses. In this energy region, the autoionizing singly-excited $3s3p^6np$ states, which are embedded in the multichannel $3s^23p^5\varepsilon_{s/d}$ continuum, appear. In particular, the experiment concentrated in populating, with harmonic 17, the first singly excited state of the series, namely, the $3s3p^64p$ configuration, which has an energy of $E_{3s4p} = 26.605$ eV, a width of $\Gamma_{3s4p} = 80.2$ meV and a Fano asymmetry parameter $q = -0.286$ [135, 136]. Fig. 34 shows the transitions involved in the measurement.

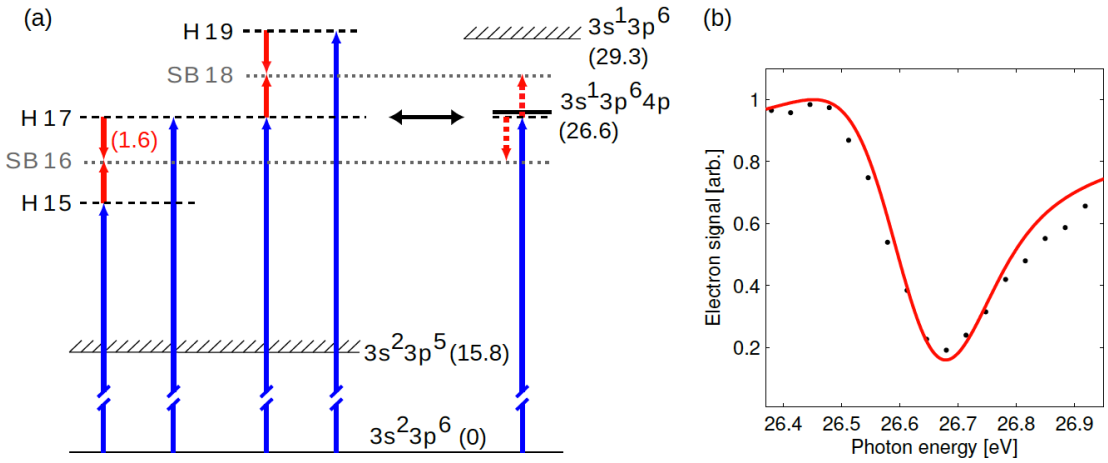

Figure 34: In the left, Ar energy diagram showing the states, channels and processes involved. The blue arrows represent ionization at different harmonic frequencies. The red arrows denote absorption or stimulated emission of IR photons. Energies (in eV) are indicated in parentheses. The energy harmonic 17 can be tuned across the $3s^{-1}4p$ resonance, which decays by autoionization (black arrow). The processes indicated by the red dashed arrows are found to be weak, as discussed below. In the right, photoionization signal as a function of harmonic 17 photon energy. The black symbols denote experimental results, and the res curve calculations.

When the laser wavelength is such that the 17th harmonic is far off the resonance, the pump-probe time delays at which the sidebands attain their peak value depend linearly on the sideband order. This dependence arises from the intrinsic chirp of the attosecond pulses [30], somewhat reduced by the anomalous dispersion of the aluminum foil [137]. The data presented in the following are corrected for the attosecond chirp, which is estimated, independently of the excitation wavelength, by linear interpolation between the maxima of sidebands 14 and 20. The intensity of the probe beam was kept well below 10^{12} W/cm^2, in order to suppress processes involving absorption or emission of more than one IR photon, thus allowing us to neglect the influence of the probe field on the resonance.

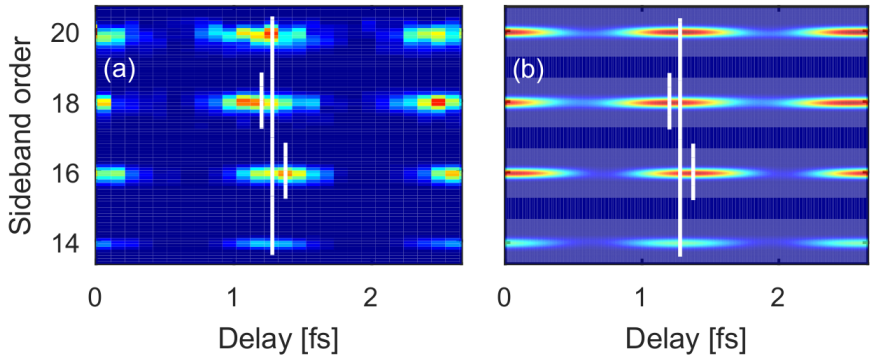

Figure 35: Photoelectron spectra as a function of delay, at an excitation energy of 26.63 eV; (a) Experimental data, corrected for the chirp of the attosecond pulses. (b) Theoretical calculations. Only the sidebands are shown. The short lines indicate the position of sidebands 16 and 18. The long lines join the maxima of sidebands 14 and 20.

Figure 35a shows the experimental photoelectron spectrum after correcting for the chirp of the attosecond pulses, at an energy of harmonic 17 slightly on the blue side of the autoionizing resonance. Clearly, the maxima of sidebands 16 and 18 are shifted in opposite directions. The photoelectron peaks are broadened due to the XUV and IR field bandwidths, the spectrometer resolution, and the spin-orbit splitting (0.17 eV), which is not resolved in the experiment. To reproduce the experimental conditions, we used the multi-channel extension of the model, discussed in § 4.4.2.3. To determine the unitary transformation needed to transform the channels into one that is resonant and one that is decoupled from the resonance, we used the ab initio complex one-photon partial transition amplitudes obtained from [138]. The strength of the transition amplitudes between the non-resonant components of the intermediate and final continuum channels were estimated in the plane-wave approximation. The only values which cannot be obtained from the literature are the γ_a parameters, which, in principle, may be different for the three final channels. Since the transition from the singly-excited configuration to the continuum, $3s3p^6 4p \rightarrow 3s^2 3p^6 \varepsilon_{p,f}$ is a double excitation, while that for the continuum-continuum $3s^2 3p^5 \varepsilon_{s,d} \rightarrow 3s^2 3p^5 \varepsilon_{p,f}$ is a single excitation, however, γ_a is expected to be small for all three final channels. For the moment, we will set it to zero and later we will study its possible influence.

Figure 35b shows theoretical results obtained by using the resonant model for a 12 fs APT, employing the duration estimated from the experiment. To extract the phase of the oscillation, the sideband signal was integrated and fitted to the RABITT interference equation. A Fourier analysis of the oscillation was also performed to verify that no component with frequency higher than 2ω, due to higher-order processes, was present.

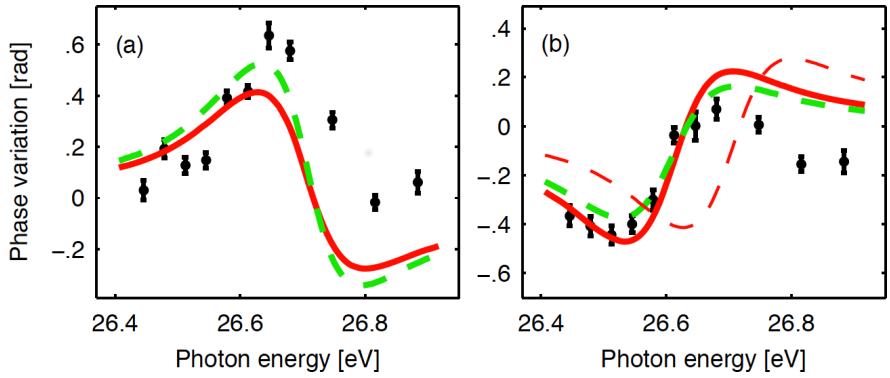

Figure 36: Phase variation of sideband 16 (a) and sideband 18 (b), as a function of the energy of harmonic 17. The theoretical results are indicated by the red solid line, while the experimental results are shown by the black symbols. The thin dashed red line in panel (b) is the opposite of the red line for sideband 16, which is close to the corresponding results for sideband 18, apart from an energy shift. The green dashed lines correspond to calculations including the processes indicated with dashed arrows in Fig. 34a.

Figure 36 presents the phase variations of sidebands 16 (a) and 18 (b) as a function of the photon energy of harmonic 17. The corresponding photoionization signal due to harmonic 17 shows the characteristic behavior of a window resonance (Fig. 34b). The black symbols are the experimental results, while the red solid and green dashed lines show theoretical calculations. The phase variation across the resonance, which is almost 0.6 radians, is asymmetric, with a bias towards positive values for sideband 16 and negative values for sideband 18. The agreement with the experimental data, both for the ionization signal due to harmonic 17 and for the phase variation of sidebands 16 and 18, is very good, especially on the low energy side of the resonance.

In principle, the phase variation of sidebands 16 and 18 should be one the mirror image of the other with respect to the energy axis, since the resonance affects the path corresponding to absorption of an IR photon for sideband 16, whereas it affects the path where an IR photon is emitted for sideband 18. The red dashed line in Fig. 36b is the mirror of the variation of sideband 16. Apart from an energy shift, the two curves are quite similar. This shift comes from the fact that the harmonic energies are slightly higher than a multiple of the probe photon energy, due to the ionization-induced blue shift of the fundamental field in the generation cell. Indeed, as we depict in Fig. 37, if the harmonics are blue-shifted, the sidebands will shift towards opposite directions. In this case, sideband SB_{q+2} will contain the information of the high-energy part of the harmonic H_{q+1}, while the lower sideband SB_q will contain the information of the lower-energy side of H_{q+1}. In absence of resonant structure, where the amplitude and phase in the higher and lower energy parts of the harmonic is approximately the same, such blue-shift cannot be determined. In presence of resonant features, however, the HHG induced blue-shift is clearly visible in the phase profiles.

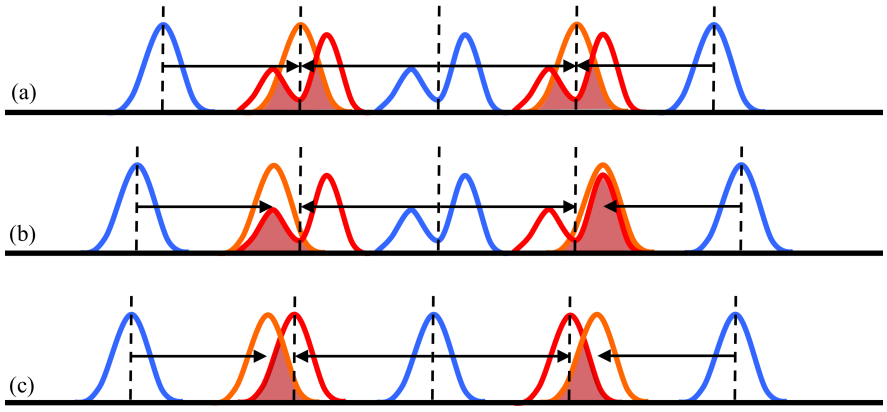

Figure 37: Effects of harmonic blue-shift in sideband position. (a) In absence of blue-shift of the harmonics, the form of the sidebands is symmetric with respect to the resonant harmonic (in the center). (b) For blue-shifted harmonics, the upper and lower sidebands map the higher and lower energy region of the resonant harmonic, respectively. (c) For blue-shifted harmonics but in absence of resonant structure, both sidebands are again symmetric.

Let us now explore the process induced by the interaction of the resonant state with the IR field, as represented by the dashed arrows in Fig. 34a. For this, we examine the effect of several values of the three parameters γ (one for each channel) in the sideband phase. Indeed, as we anticipated, the best agreement between the model's prediction and the experimental measurements is found when γ_a is small ($\gamma_a \approx 0.18$) as indicated by the green dashed curves in Fig. 36.

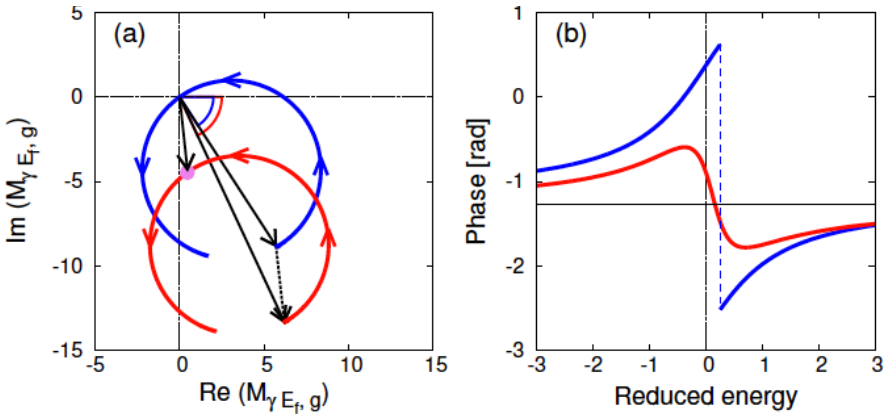

Figure 38: Complex plane representation of $M_{\gamma E_f,g}$ (red circle) and of its resonant $M^{(1)}_{\gamma E_f,g}(q+\epsilon)/(\epsilon+i)$,(blue circle) and non-resonant $M^{(2)}_{\gamma E_f,g}$ (magenta dot) components; (b) Phase variation of $M_{\gamma E_f,g}$ across the resonance ($q = -0.25$) in the absence of (blue line) and in the presence of (red line) a non-resonant component.

The measured phase profile across the autoionizing resonance can be interpreted by considering the multichannel nature of the problem. In the monochromatic limit, and taking $\gamma = 0$, we have that the two photon transition amplitude is split into a resonant and non-resonant component:

$$M_{\gamma E_f,g} = M^{(1)}_{\gamma E_f,g}\frac{q+\epsilon}{\epsilon+i} + M^{(2)}_{\gamma E_f,g}. \tag{5.4}$$

Fig. 38 shows the trajectory of $M_{\gamma E_f,g}$ in the complex plane, its resonant and non-resonant contributions, as the reduced energy varies from -3 to 3. The resonant contribution describes counterclockwise a circle that passes through the origin

for $\epsilon = -q$. In the absence of a contribution from the non-resonant channel, the phase of $M_{\gamma E_f,g}$ follows the phase of the Fano profile, $\arg[(q+\epsilon)/(\epsilon+i)]$. The phase increases first steadily with energy, then drops discontinuously by π when $\epsilon = -q$, to increase again thereafter, until it attains its original value [blue line in Fig. 38b]. For small values of q as it is the case in the present work, the π phase jump occurs close to $\epsilon = 0$ and the phase variation is almost symmetric. In the presence of a non-interacting channel, the phase variation across the resonance will in general differ from π. In the present case, the non-resonant complex amplitude moves the circular trajectory away from the origin, as indicated by the phase vectors (phasors) in Fig. 38a. As a result, the phase of the total amplitude varies smoothly across the resonance [red line in Fig. 38b], and by a total amount less than π.

5.4 ANGULARLY-RESOLVED RABITT

In this section we investigate the angle-dependent correlated dynamics that appear in RABITT experiments.

5.4.1 *Angular dependence in photoemission time delays*

Extremely small delays in electron emission induced by single photon absorption have been measured with the attosecond streaking [139] and RABITT methods [21]. Neither technique can give access to absolute photoemission time delays, but relative timing information between electrons originating from different states within the same atom [58, 32] or from different atoms [61, 35, 34] can be extracted.

An alternative perspective on the photoemission process can be obtained by studying the relative timing of electrons emitted from the same initial state within the same target system but at different emission angles θ, relative to the XUV-pump polarization (Fig. 39a). The possible dependence of time delays on the photoemission angle has not been considered, since all the measurements on photoionization time delays carried out so far have used either angle-integrating detection schemes, such as a magnetic bottle spectrometer [32], or directional detectors with time-of-flight spectrometers [58].

In atomic photoionization, the absorption of a single photon causes electrons to be excited from their initial state $n_i\ell_i$ into the final state $\varepsilon\ell$. The dipole selection rules impose that only final states of $\ell \pm 1$ symmetry become accessible. As shown in earlier works [140, 141] the interplay between two different angular components may give rise to anisotropic group delay τ_W of the photoelectron wave packet generated by the absorption of one XUV photon. So far, such an angular dependence was exclusively studied in the context of the ionization from a non-symmetric orbital, and assuming that the transition promoted by the IR did not induce any additional dependence on the emission angle [93].

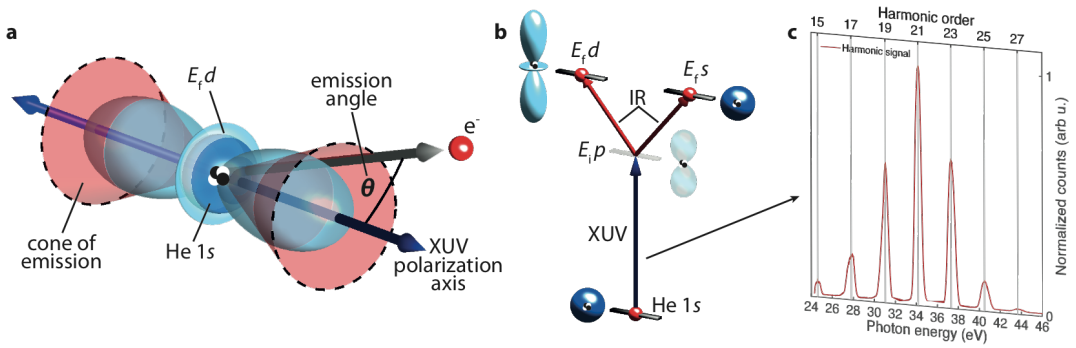

Figure 39: a, Schematic defining the emission angle θ as the electron emission direction relative to the XUV-pump polarization axis and illustrating the different photoelectron partial waves of the corresponding final quantum states, which arise from the exchange of two photons. b, Schematic illustrating the different quantum paths, which contribute to the final state of the liberated photoelectrons after the interaction with the XUV and IR fields. c, XUV spectrum, which has been used to carry out the experiments.

In the special case of ionization from a spherically symmetric orbital, however, only the photoionization transition $\ell \to \ell + 1$ (i.e., $ns \to \varepsilon_p$) is possible. If in addition the remaining ion is left in a spherically symmetric state, the orbital angular momentum of the photoelectron is conserved. In these conditions, the Wigner time delay is rigorously independent on the ejection angle, and so would be the time delay measured with an attosecond interferometric technique, provided the further exchange of an IR photon did not induce additional angular modulations. Yet, as soon as two photons are involved in the ionization process, two different final states $1s \to E_p \to E_{s/d}$ become accessible (Fig. 39). As a result, in principle, the group delay of the final photoelectron wave packet may still exhibit an angular dependence. This would be the case, for example, of the ionization of helium (He) from the ground state, which is spherically symmetric.

Indeed, while one expects an isotropic photoemission time delay associated to the XUV absorption, a perturbative analysis shows that the intrinsic two-photon nature of the interferometric measurement of the time-delay introduces by itself an inherent, universal anisotropy in the measurement. To which extent such anisotropy affects measurements of photoemission time delays along fixed directions, therefore, is a fundamental question of current attosecond spectroscopy, which has not been addressed before, due in part to the formidable challenges that angularly-resolved measurements of photoemission time delays entail.

In collaboration with the Ultrafast Laser Physics experimental group at ETH, in Zurich, led by Ursula Keller, we investigated the angle-dependent photo-ejection time delay of electrons removed from the spherically symmetric $1s^2$ ($^1S^e$) ground state of helium to produce the spherically symmetric ion $He^+(1s)$. Helium was chosen for two main reasons. First, because τ_W is rigorously isotropic in this atom and, second, because we have virtually exact *ab initio* solutions. Fig. 40 shows the principle of the angle-resolved RABITT measurements. Applying an angular filter on the detected electrons, i.e., choosing electrons emitted within the corresponding cone of emission (Fig. 39a), the Ultrafast Laser Physics group was able to obtain distinct RABITT traces representing only electrons out of particular hollow cones (Figs. 40a,c). For any angular sector, the SB signal is obtained by integrating the spectrogram in an energy window $\Delta E = 0.75$ eV wide centered around

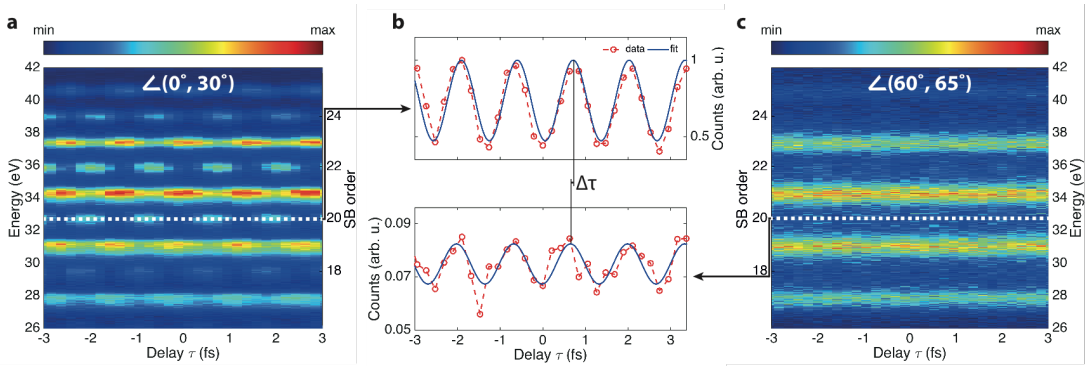

Figure 40: a-c, Examples of measured RABITT spectrograms and oscillations of sideband (SB) 20 (marked by white dashed lines) for different ranges in emission angle. Note that the energy scale corresponds to the sum of electron kinetic energy and the ionization potential of helium (ionization potential of He: 24.5874 eV). In (a) only the electrons detected within a 30° cone of emission (Fig. 39) are selected. Panel (c) comprises electrons emitted within a cone of emission between 60° and 65°. Panel (b) shows an example of the intensity oscillations of SB 20 (red data points) obtained by integrating the counts within an energy window of 0.75 eV centered at the peaks of the SB oscillations (white dashed lines) together with their corresponding fits (blue solid lines). The time delay $\Delta\tau$ is clearly visible as a temporal shift between the two different SB oscillations.

the peak of the SB position. Two curves showing the SB signal are presented in Fig. 40b for electrons emitted between 0° and 30° (top panel) and between 60° and 65° (lower panel).

While the SB beating at small angles is clearly visible even in the energy resolved spectrum (Fig. 40a), it is barely discernible at large angles (Fig. 40c). When the SB signals are integrated in energy, however, the characteristic oscillations with periodicity $2\omega_{\mathrm{IR}}$ appear for both angular ranges (Fig. 40b), and thus a clear phase angular-dependent delay $\Delta\tau$ can be extracted. This is the delay between electrons emitted at angles between 0° and 30° (reference) and electrons emitted into a specific hollow cone between θ and $\theta + \Delta\theta$ (Fig. 39a). The accuracy of the fit decreases at larger angles due to the smaller count rate thus resulting in larger error bars. Note that the angular range of the reference has been chosen to be as wide as 30° in order to improve the its signal-to-noise ratio and thus to minimize the error in the subsequent relative phase retrieval. The measured angularly resolved photoemission time delays relative to the zero emission angles are shown with error bars in Fig. 41 for four consecutive sidebands, SB18-SB24. For all sidebands, the measurements deviate significantly from zero for angles larger than 50°. The largest anisotropy is recorded for the lowest sideband, but it is statistically significant in all cases.

To validate and explain the experimental observations, we performed a series of *ab initio* simulations. Fig. 42 shows a comparison between the time-delay integrated photoelectron spectra measured in the experiment for a moderately weak (3×10^{11} W/cm^2) IR probe pulse with a center wavelength of 780 nm and the spectrum computed *ab initio* using pulse parameters that match the experimental ones. Fig. 41 shows the comparison of the time delays $\Delta\tau$ for the energy integrated SB signals. The results of the ab initio calculations are in quantitative agreement with the measurement. For SB18 the experimental data slightly deviate from the theoretical estimates as compared to the other SBs. We attribute these deviations to the low intensity of SB18 and consequently to a noisier signal, reflected also in larger error bars. Nevertheless, for the considered angular

range, the discrepancy between experimental data and the theory curves is not larger than 10-15 as, which we consider fairly acceptable given the complexity of experiment and theory.

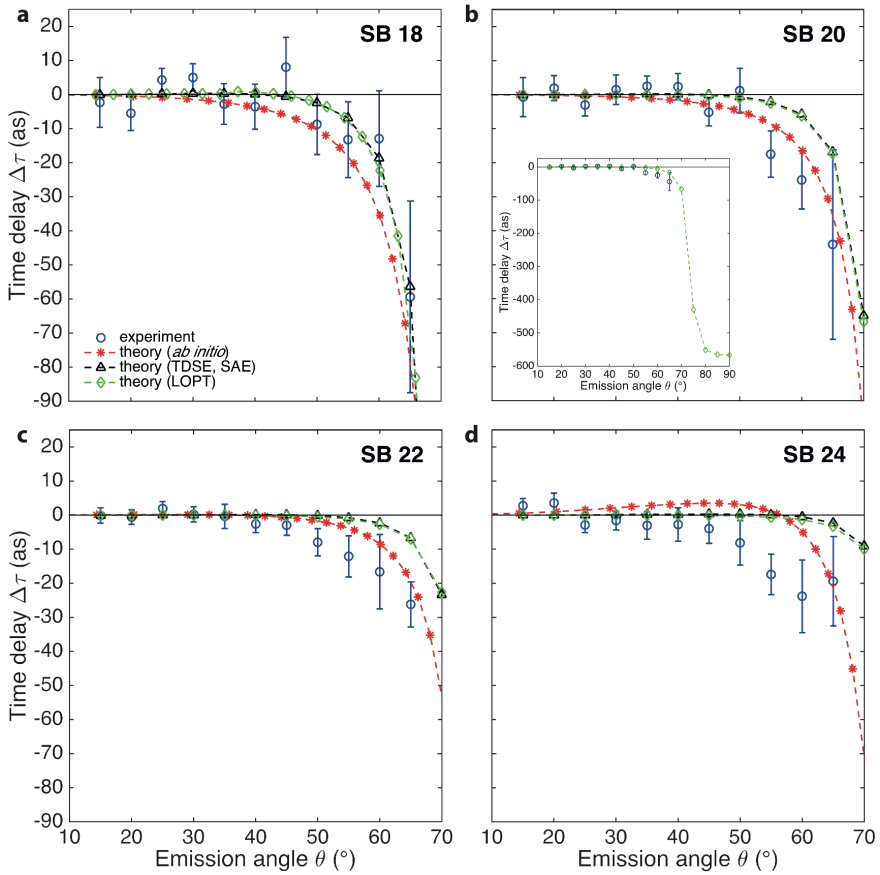

Figure 41: a-d, For all electron kinetic energies, referenced by the sidebands (SBs) of the harmonic spectrum of the attosecond XUV pulse train, the experimentally retrieved atomic delay (blue data points with error bars) is shown as a function of the emission angle θ, following the procedure described in Fig. 40. For example, a delay at 15° is understood as the delay between electrons emitted at angles between 0° and 30° (reference) and electrons emitted at angles between 10° and 15°. As a comparison the corresponding theoretical predictions are also included in the graphs comprising an ab inito simulation (red dashed line with asterisks), a calculation solving the time-dependent Schrödinger equation (TDSE) within the single active electron (SAE) approximation (black dashed line with triangles) and lowest-order perturbation-theory (LOPT) (green dashed line with diamonds). The different theories are in very good agreement and reproduce the experimental data well. The inset in (b) shows the typical behavior of the angle-dependent delay predicted by LOPT for an angular range up to 90°. As a consequence of the node in the d-wave, at large emission angles θ the delay changes significantly.

As it is known, the finite duration of the pulses gives rise to harmonics with a finite width, whose tail partly overlaps with the sidebands in the energy-resolved photoelectron spectrum. This effect, which is entirely negligible for angle-integrated measurements, is noticeable in angle-resolved measurements. To make sure that the observed anisotropy is still present in absence of any spectral overlap from the harmonics, we repeated the *ab initio* simulations with long laser pulses and compared the result with the prediction of an independent lowest-order perturbation-theory (LOPT) calculation that assumes infinitely long pulses.

Angle-resolved atomic delay LOPT calculations were performed by Marcus Dahlström using correlated two-photon (XUV+IR) matrix elements on an exterior complex scaled basis set [140]. This approach accounts for correlation effects

in the single-XUV-photon absorption with the screening of the remaining electron in the residual ion. The interaction with the IR field, however, is treated as an uncorrelated transition. Hence, if correlation effects in the final state become significant, LOPT may fail in explaining the observed experimental results. The two calculations are in excellent agreement and the prediction of the latter is shown in Fig. 41 (represented as a dashed green line with diamonds). Even if the time-delay anisotropy of this second set of calculations is smaller than before, the effect is still clearly visible, and in particular, the sharp drop around 50° is reproduced.

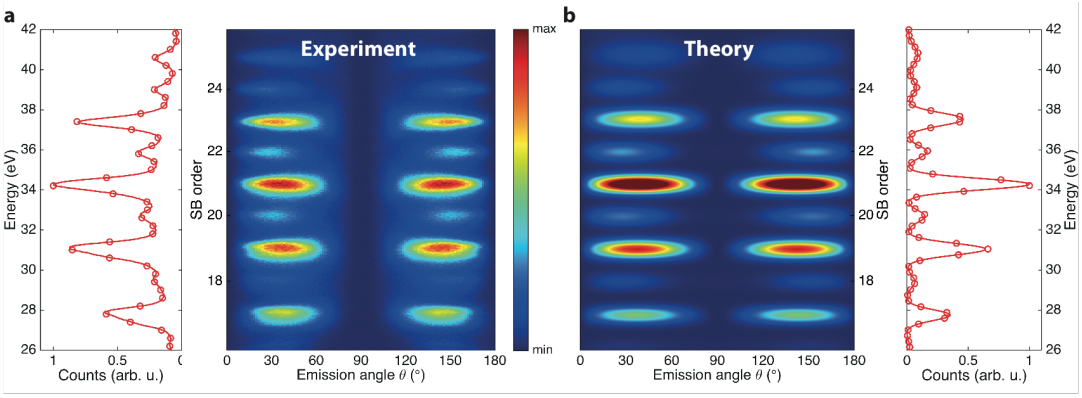

Figure 42: a, Experimental data. b, Results of the ab initio calculation. The 2D plots show the delay-integrated photoelectron spectrum as a function of the emission angle θ, defined in Fig. 39a. On the left and right hand side of (a) and (b), respectively, the angle-integrated projections for experiment and theory highlight the presence of four SBs comprising SB 18 to SB 24.

Within LOPT, the anisotropy of the time delay can be explained with an analytical description, which gives better physical insight into this anisotropy. As described in the introduction, if two linearly polarized photons are involved in the ionization of He, two different final states become accessible, represented by an s- or a d-wave. The angular shape of each final state can be described by a distinct spherical harmonic, Y_ℓ^m, with $\ell(m)$ representing the orbital angular momentum (magnetic) quantum number. While the Y_0^0 spherical harmonic representing the s- wave is isotropic, the Y_2^0 spherical harmonic associated to the d-wave exhibits a node at the magic angle of 54.7°. Therefore, the interference between the transitions in the continuum mediated by the IR pulse is expected to lead to an angular dependence of the atomic time delay. The variation of the delay is expected to become particularly pronounced when the emission direction of the photoelectrons with respect to the XUV and IR polarization axis approaches 60°. We can parametrize the observed angle-dependent delay in the special case of He as follows:

$$\Delta\tau = 1/2\omega_{\mathrm{IR}} \arg\left[(1+T^-)/(1+T^+)\right], \tag{5.5}$$

with $T^\pm = \sqrt{4\pi}\, c_\pm^{ds}\, e^{i\phi_\pm^{ds}}\, Y_2^0(\theta,0)$. Here, $c_\pm^{ds} = |A_\pm^d / A_{pm}^s|$ and $\phi_\pm^{ds} = \arg(A_\pm^d / A_\pm^s)$ are the absolute values and phases of the two-photon transition amplitudes representing the four quantum paths $s \to p \to s(+/-)$ and $s \to p \to d(+/-)$, respectively. The symbol (+) indicates the transition involving absorption of an IR photon, (-) the transition followed by the emission of an IR photon. The inset in Fig. 3b shows the behavior of the angle-dependent delay predicted by LOPT

up to 90°. As soon as the magic angle of approximately $\theta = 54.7°$ is reached, the d-wave changes sign and therefore exhibits a significant change in delay, which can be as large as 600 attoseconds outside the experimentally accessible angular range. The lack of experimental data for large angles prevents us from an accurate determination of the parameters $c_{\pm}^{ds}$, $\phi_{\pm}^{ds}$. Other targets may that have a smaller critical angle would then be more easily accessible with the current experimental setup.

In contrast to the other SBs, theory predicts a slight positive delay for SB 24 at angles smaller than about 55°, a trend that is not observed in the experimental data (Fig. 3). We attribute this effect to the spectral overlap of SB 24 with its two neighboring harmonics 23 and 25 for which the difference in intensity is the largest (Fig. 39c).

What is the physical origin of this angular modulation in the relative phase between the s- and the d waves? Is it due to correlation, is it essentially a multi-electron effect, or is it present also for hydrogenic systems? To answer these questions, two additional test calculations were conducted. In one, the group of Anatoli Kheifets solved the TDSE using a SAE model, following a strategy tested in previous studies [142]. This model is known to reproduce well both the ionization potential of He and the one-photon ionization cross section of the atom. However, by construction, it does not account for any correlation effects between the two electrons. The predictions of this model are shown in Fig. 41 as triangles following a black dashed line and are matching the values calculated with LOPT. We conclude, therefore, that correlation has only a minor influence on the observed anisotropy.

After revisiting the phase-shifts induced by the IR field in atomic hydrogen [93], we found evidence for small phase differences at low electron kinetic energies that depend on the final angular momentum of the electron. Surprisingly, these phases mostly cancel in angle-integrated experiments and have so far not been studied in greater detail. This opens up the question if the anisotropy, similar to that found in He, can be expected in atomic hydrogen where multi-electron effects are absent. To investigate this, we made additional simulations with atomic hydrogen. Fig. 43 shows a comparison of the results obtained from *ab initio* calculations for the angle-dependent time delay of He (red solid lines) and atomic hydrogen (blue and black solid lines) for a sideband centered in both cases at a photoelectron kinetic energy of 4 eV, which is close to the energy of SB 18 in Fig. 41.

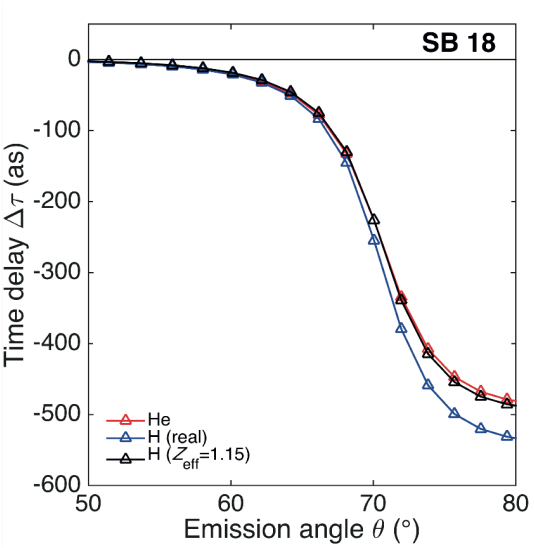

Figure 43: Comparison between the results obtained from *ab initio* calculations for the angle-dependent time delay (left panel) and their differences (right panel) of He (red solid lines), atomic hydrogen (blue solid lines) and artificial atomic hydrogen with an effective charge of $Z_{eff} = 1.15$ (black solid line). The last case should mimic a He atom in a simple single active electron (SAE) approximation in a screened potential. In order to reduce the effect of spectral overlap induced by the neighboring harmonics, the energy integration window has been chosen to be narrower than for the experimental data thus resulting in slightly smaller delays.

The trend of decreasing time delays with increasing emission angle is similar but not exactly the same for both He and atomic hydrogen (Fig. 43). The reason for this difference, which can be as large as 60 attoseconds, is due to the remaining electron in the He^+ ($1s$) parent ion, which modifies the effective potential seen by the departing photoelectron. Indeed, as can be seen in Fig. 43, this effect can be largely accounted for by using a fictitious hydrogen atom with an effective charge $Z_{eff} = 1.15$, which mimics the screening of the He nuclear charge by the 1s electron.

6

MODERATELY STRONG-FIELD REGIMES

In the previous chapter, we mainly focused on the *monitor* of electron correlation effects. For this, the IR field was kept weak so that it acted as an "unperturbing measuring tool". In this chapter, we explore the effects that arise when we vary the IR field's intensity to trigger, and thus *control*, higher-order processes.

This Chapter is organized as follows: in § 6.1 we apply the soft photon model for the description of the non-resonant features, demonstrating that it is a valid tool for high intensity experiments employing either SAPs, as it is done in the streaking technique, or APTs, such as RABITT , for which corrections to high intensity can be useful to improve it as a field reconstruction tool.

In the following two sections, we explore high-intensity effects on autoionizing states by means of *ab initio* simulations. In § 6.2, based on the experimental observation of the laser-induced inversion of the Fano profile in [56], we show that the Fano profile is *repeatedly* inverted as a function of the laser field intensity. Moreover, we demonstrate that the intensity-dependent phase of the DES exceeds the ponderomotive energy, indicating a genuine two-electron contribution to the polarization of the excited atom. Finally, in § 6.3 we explore the possibility of tunneling from the innermost orbital of a DES and observe that DES spectra display AC-Stark shifts which vary across series and final ionization channels.

6.1 THE SPA FOR INTENSE FIELDS

In this section we will apply the soft photon model to compute photoelectron energy and angularly resolved distribution for the photoionization of the helium atom from the ground state to the $1s$ channel of the He^+ parent ion in the energy region across the $N = 2$ excitation threshold, within the XUV-pump IR-probe schemes,

$$\mathrm{He}(1s^2) + \gamma_{\mathrm{XUV}} \pm n\gamma_{\mathrm{IR}} \rightarrow \mathrm{He}^+(1s) + e^-_{\vec{k}}. \tag{6.1}$$

We will consider two cases: that of an XUV single attosecond pulse (SAP) and that of an XUV APT.

6.1.1 *Single attosecond pulse*

A characteristic feature of experiments in which an isolated sub-femtosecond XUV pulse overlaps with an intense IR pulse is the streaking effect, i.e., an overall

shift $\Delta\vec{p} = -\alpha\vec{A}_{\rm IR}(t)$ of the momentum distribution of the photoelectron generated by an attosecond XUV pulse centred at time t. The streaking effect, which has a purely classical explanation, has been one of the first means to achieve control over the photoelectron ejection process [39]. For XUV pulses with duration larger than the period of the IR dressing field, a transition from the streaking picture to the sideband picture, characteristic of monochromatic XUV fields [143], is observed. Kazansky *et al* [144] examined in detail this transition within the strong-field approximation.

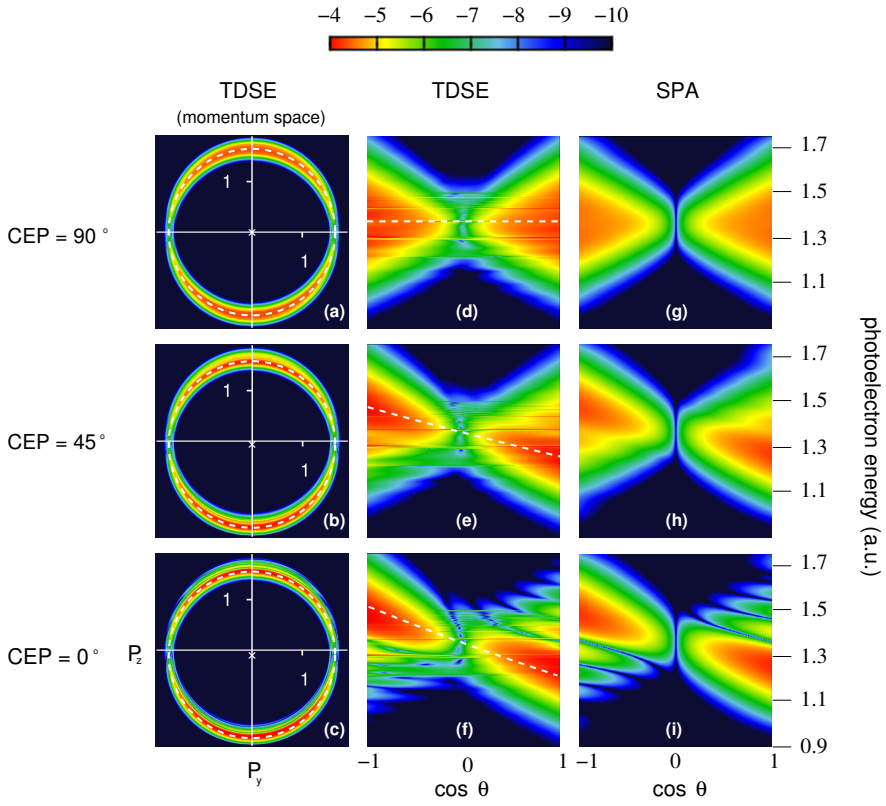

Figure 44: Comparison of photoelectron spectra in the 1s channel obtained by direct integration of the TDSE (a-f) with the prediction of the SPA (g-i) for the case where a helium atom is ionized by a SAP with central energy 61eV in the presence of an IR field ($\lambda_{\rm IR} = 800nm$, $I_{\rm IR}$=1 TW/cm^2) at zero time delay. The three panel rows correspond to three different value of the cosine-modulated IR CEP: 90°, 45°, 0°. First column: section of the photoelectron momentum distribution in the xz plane. Second column: same distribution as in the first column but in the representation photoelectron energy vs. cosine of the photoelectron ejection angle with respect to the laser polarization. Third column: prediction of the monochromatic SPA. The color code is on a $\log_{10}$ scale. The reported signal is a probability density per unit of cubic linear momentum (first column) or per unit of energy (second and third column), in atomic units.

Here, we employ an XUV pulse with $\text{fwhm}_{\rm XUV} = 709$ as, comparable to a quarter of the IR period,

$$\vec{A}_{\rm XUV}(t) = A_{\rm XUV,0}\,\hat{\epsilon}\,\frac{\exp\left[-\frac{(t-t_{\rm XUV})^2}{2\sigma_{\rm XUV}^2}\right]}{\sqrt{2\pi}\sigma_{\rm XUV}}\cos(\omega_{\rm XUV}t), \quad \sigma_{\rm XUV} = (8\ln 2)^{-1/2}\,\text{fwhm}_{\rm XUV}, \tag{6.2}$$

a choice situated at the boundary between the streaking and the side-band limits. The other pulse parameters used in the simulation are: $\omega_{\rm XUV} = 61.8$ eV,

I_{XUV}=0.1 TW/cm^2, $\omega_{IR} = 1.55$ eV, $I_{IR} = 1$ TW/cm^2, $fwhm_{IR}$=4.46 fs. Both pulses are linearly polarized along the $\hat{z}$ direction. We conducted simulations for three values of the carrier-envelope phase (CEP) of the IR pulse: 0°, 45°, and 90°. In the three cases, the centers of the XUV and the IR pulse coincide (zero time-delay). Since the duration of the XUV pulse is much shorter than the fwhm of the IR pulse, by changing the CEP we reproduce the case of a longer IR pulse where the time delay is changed instead. This approach is useful when conducting computationally-intensive simulations because it permits one to use short IR pulses thus keeping the overall propagation time to a minimum. The predictions of the SPA model were computed using the same set of parameters as in the simulation, with the exception of the fwhm of the IR field, which in this case is assumed to be monochromatic.

In Fig 44 we compare the photoelectron spectra resulting from the *ab initio* calculations (Figure 44a-f) with those from the SPA model (Figure 44g-i). The latter have been scaled by a common factor to closely match the absolute value obtained from the simulation. In all cases, the colour-code corresponds to a logarithmic scale. The three panels on the left column (Figure 44a-c) show the photoelectron distribution in the (p_x, p_z) plane as it would appear after reconstruction [145] from experimental data recorded with a velocity-map imaging detector [6]. A dashed circle on top of the data, centred on the white cross along the vertical axis, indicates the expected position of the signal predicted by the streaking formula. To better appreciate the distribution details, the panels in the middle column (Figure 44d-f) illustrate the same quantity as in the left column in a energy vs. $\cos\theta$ representation, where θ is the photoelectron ejection angle with respect to the laser polarization. We can recognize four characteristic features. (I) Two dominant lobes, centred at $\omega_{XUV} - IP$ in the case of CEP=0°, which (II) follow a clear streaking trajectory as the CEP of the dressing field is changed. In this representation and for the current IR intensity, the streaking effect appears as a tilt in the distribution. The prediction of the streaking formula is indicated with a dashed line. (III) For the case where the streaking is largest (Figure 44f), sidebands appear below the left and above the right lobe. Finally, (IV) narrow horizontal resonant features, due to the presence of doubly excited states, are visible. It is worth noting that, despite the opening of the $2s$ and $2p$ channels at $E_e = 1.5$ a.u., the $1s$ spectrum is remarkably smooth across threshold.

The three panels in the right column (Figure 44g-i) show the prediction of the SPA. The first three-dominant features of the *ab initio* angularly resolved spectra, (I-III), are accurately reproduced. In particular, the sidebands in Fig 44f are an interference effect of quantum streaking (Figure 44i is analogous to Figure 4a in [144]) instead of a consequence of the presence of intermediate doubly excited states. Such interference effect is due to the fact that, if the duration of the SAP used in the pump-probe ionization is comparable to half period of the IR, the streaking is not uniform across the pulse. When the center of the XUV pulse coincides with the zero of the vector potential (Figs. 44a,d,g), the IR accelerates the photoelectrons ejected in any given direction upward during the first half of the XUV pulse and downwards during the second half. As a consequence, the spectrum of the photoelectron is widened. Furthermore, the wave-packet in the upward direction acquires a negative chirp (not visible in the energy-resolved

signal) while the one heading downward acquires a positive chirp . In the case the centre of the XUV pulse coincides with the maximum of the vector potential (Figs. 44c,f,i), the energy bandwidth in either the lower or the upper lobe is smaller than in the previous case. The ionization amplitude generated at times $t_1 = t_{\rm XUV} - \Delta t/2$ and $t_2 = t_{\rm XUV} + \Delta t/2$ which are symmetric with respect to the XUV pulse centre are equally streaked by the IR, leading to the interference fringes above the upper and below the lower lobe.

This example illustrates how the SPA can be used to reproduce with remarkable accuracy all background features of photoelectron angular distributions in realistic systems, even in the presence of transiently bound states. Since the optical transition to these states from the ground state is forbidden at the level of the independent particle model, their influence on the spectrum is comparatively minor.

6.1.2 *Attosecond pulse train*

The variation of sideband intensity as a function of the time delay is a major observable in pump-probe experiments based on the use of attosecond pulse trains. In the following, we shall examine how such variation is affected by the intensity of the dressing field. To focus on this aspect without the interference of either finite-pulse or correlation effects, we will consider the monochromatic version of the SPA model only. As long as the IR pulse is longer than $3-4$ times the APT duration, this approximation is justified.

In Figure 45 we report the photoelectron spectrum computed with the monochromatic and pulsed version of the SPA model in the case of an APT with a duration of 6 fs and maximum intensity of $I_{APT} = 0.1\text{TW/cm}^2$, and an IR pulse of maximum intensity $I_{\rm IR} = 1\text{TW/cm}^2$ and duration $\text{fwhm}_{\rm IR} = 21.78$ fs. In these conditions, the consequences of a finite duration of the IR pulse are indeed sufficiently small to leave the most prominent features of the photoelectron spectrum dependence on laser intensity unaltered.

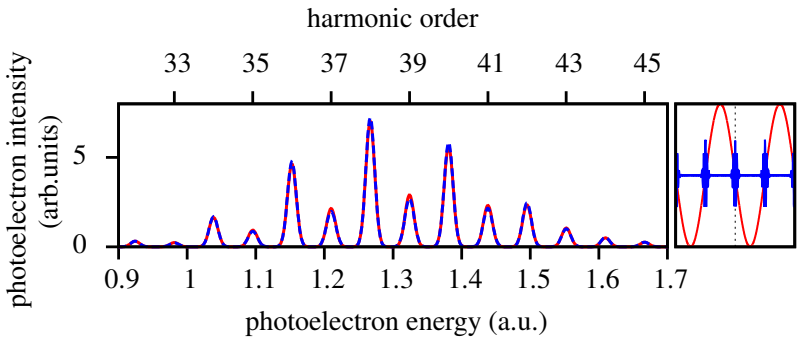

Figure 45: Photoelectron energy spectrum for the ionization of the helium atom from the ground state by means of a RABITT pump-probe scheme, computed with two different models: monochromatic SPA (red solid line) and pulsed SPA (blue dashed line). The pulse duration is 6 fs for the APT and 21.78 fs for the IR. In these conditions, the boundary effects associated to the finite duration of the dressing field (pulsed case) are negligible: the spectrum is well reproduced within the infinite-pulse approximation (monochromatic case).

In the perturbative limit, the sideband signal is known to oscillate at the fundamental RABITT angular frequency $2\omega_{IR}$. As discussed in Sec. 6.1, however, as the intensity of the dressing field is raised, overtone components with angular frequency $2n\omega_{IR}$ start to appear.

Figures 46a-e (left panels) show the integrated intensity of a central sideband as a function of the time delay across half a period of the IR for several values of the IR reduced field strengths ξ. For each intensity, three curves are plotted: one obtained with the analytical formulas in the frequency-comb limit, and two others computed with the monochromatic SPA model with parameters chosen either to approach the frequency-comb limit ($\text{fwhm}_{XUV} = 50$ as, $\text{fwhm}_{APT} = 24$ fs) or to reproduce ordinary experimental APT parameters ($\text{fwhm}_{XUV} = 263$ as, $\text{fwhm}_{APT} = 11$ fs).

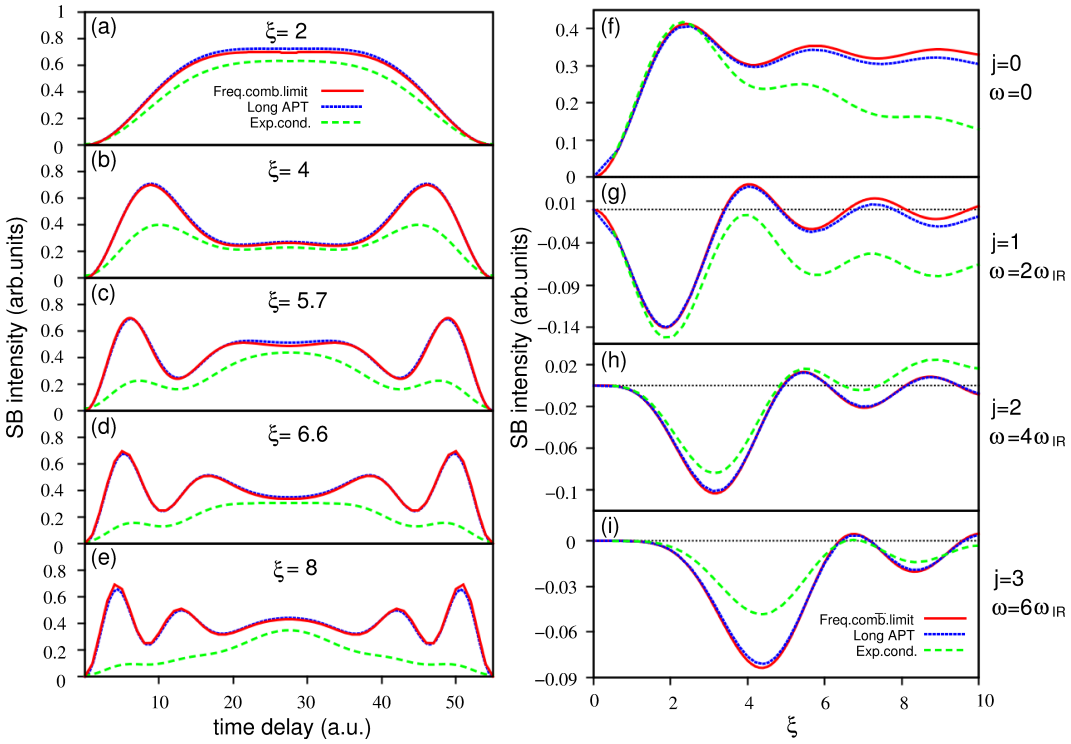

Figure 46: Left panels (a-e): energy integrated photoelectron signal of a central sideband as a function of the time delay between an XUV APT and a monochromatic IR probe for five different values of the reduced field strength ξ; from top to bottom: $\xi = 2$ a.u., 4 a.u., 5.7 a.u., 6.6 a.u., 8 a.u., corresponding to IR intensities, for a photoelectron with $E_e = 1$ a.u., of 4.08 TW/cm^2, 16.3 TW/cm^2, 33.1 TW/cm^2, 44.4 TW/cm^2, and 65.3 TW/cm^2, respectively. Frequency comb limit: solid red line; SPA for an XUV APT in close to the frequency comb limit (train duration=24fs, pulse duration=50as): dotted blue line; SPA for an XUV APT with common experimental parameters (train duration=11fs, pulse duration=263as). Right panels (f-i): coefficients $C_j(\xi)$, $j = 0, 1, 2, 3$ (top to bottom) of the harmonic components of the time-dependent integrated sideband signal (see text), as functions of the reduced field strength ξ, for the same three models as in the left panels.

Even for moderate field strengths, the time-delay dependence of the sideband signal deviates significantly from the characteristic sinusoidal modulation of the perturbative limit (2.48). For values of the reduced field strength of the order of 3 ($I_{IR} \sim 10$ TW/cm^2 at $E_e = 1$ a.u.), multiple maxima start to appear. In the case of a realistic APT, the sharp modulations predicted in the frequency-comb limit are somewhat washed out as a consequence of the finite energy span and duration of the APT. Yet, even with these realistic pulses, the qualitative change of the profile is still clearly visible.

The time dependence of the sidebands can be parametrized in terms of a discrete Fourier series which, for parity reasons, comprises only even multiples of the IR fundamental frequency (see Equation (4.48))

$$I_{\mathrm{SB}}(t;\xi) \propto \sum_{j=0} \cos(2j\omega_{\mathrm{IR}}t) C_j(\xi). \tag{6.3}$$

In Sec. 6.1 we derived an analytical expression for the amplitudes $C_j(\xi)$ of the harmonic components in the frequency comb limit. Figures 46.f-i (right panels) show the coefficients of the average sideband signal C_0, of the fundamental RABITT modulation C_1, and of the first two overtones C_2 and C_3, as a function of the reduced field strength for the same three models used in the left panels. The most striking feature of these plots is that all $C_j(\xi)$ amplitudes are predicted to oscillate periodically as the intensity of the laser increases. In particular, the fundamental modulation C_1 below $\xi = 10$ ($I_{\mathrm{IR}} \simeq 10^{14}$ W/cm^2 for $E_{\mathrm{e}} = 1$ a.u.) changes sign five times in the frequency comb limit, and even for the shortest APT it vanishes almost entirely for $\xi \simeq 4$ ($I_{\mathrm{IR}} \simeq 1.6 \cdot 10^{13}$ W/cm^2 for $E_{\mathrm{e}} = 1$ a.u.). Close to these intensities, overtones dominate. In [110], L'Huillier and co-workers reported measurements of the phase of the $4\omega_{\mathrm{IR}}$ and of the $6\omega_{\mathrm{IR}}$ overtones. Therefore, even if the authors did not report or comment on the dependence of the amplitude of the overtone components on the laser intensity, the determination of the oscillations shown in Figure 46.b should be well within the reach of current laser technology. In [110], the authors concluded that the appearance of overtones was to be associated to a loss of accuracy and a bias towards artificially compressed attosecond pulses in the RABITT reconstruction protocol. In fact, within the soft-photon approximation it is possible to keep track of all sideband frequency components even for large intensities, as soon as the experimental contrast and time-delay resolution is sufficiently high. The frequency-comb limit of the SPA can thus conceivably be the basis for an extension of the RABITT protocol to non-perturbative regimes.

6.2 LASER INTENSITY EFFECTS IN RESONANT ATAS SPECTRUM

Electronic wave packets can be controlled by altering the relative phase of their components, e.g., with a short light pulse that imparts a temporary intensity-dependent ac-Stark shift $\Delta E^{\mathrm{ac}}(I)$ on the states it is composed of. Recently, attosecond transient absorption spectroscopy (ATAS) experiments showed that the corresponding phase excursion, $\Delta\phi_i = \int dt \Delta E_i^{\mathrm{ac}}[I(t)]/\hbar$, maps onto the modulation of the asymmetry of the resonant profiles in the ATAS spectrum [56, 146, 147]. This principle has been recently applied to a metastable two-electron wave packet in the helium atom, formed by the $sp^+_{2,n}$ $^1\mathrm{P}^o$ doubly excited states (DES) [56, 51]. The experiment evidenced the inversion of the Fano profile in the higher terms of the $sp^+_{2,n}$ series as a function of both the time delay between the XUV and the VIS pulses, and the intensity of the VIS dressing field [56].

In this section we seek to obtain information on strongly correlated electrons dressed by a few-cycle moderately intense visible (VIS) pulse from the ATAS spectrum in the XUV around 60 eV, by means of *ab initio* calculations that repro-

duce the experimental results in [56, 51] for the helium atom. We will increase the VIS intensity beyond the values used in the experiment in order to explore the ac-Stark shift and the inversion of the Fano profiles of the doubly-excited states of helium.

Fig. 47 shows the principle of the method. In ATAS, the weak XUV pulse $\mathcal{E}(t)$ induces a time-dependent dipole moment $d(t;\mathcal{E})$ in the atom dressed by the VIS field. In turn, the dipole gives rise to an emission that interferes with the field and alters the spectrum of the XUV transmitted pulse.

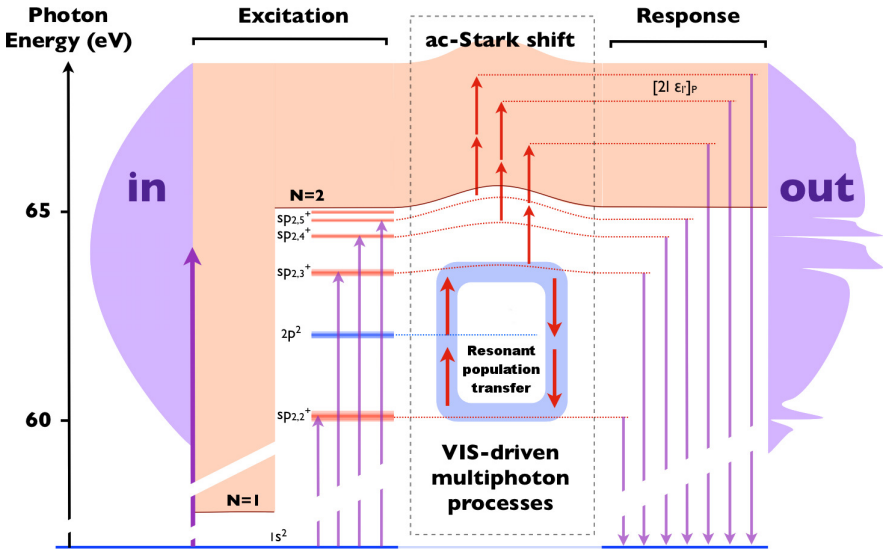

Figure 47: **Energy level scheme.** The ATAS of helium records the linear response in the XUV energy range of the atom dressed by an external VIS field. The attosecond XUV pulse excites a wide range of continuum and DES states (left) whose population and phase are altered by the dressing laser, due to multiphoton and non-perturbative transitions (center). The dipole response of the atom (right) reflects such change.

In Fig. 48a we show the ATAS spectrum $\sigma(\omega)$ as a function of the photon energy and the laser intensity at a fixed time delay $\tau = 200$ as. The $sp^+_{2,3-5}$ states show a clear tilt towards larger energies as the laser intensity is increased due to the ac-Stark shift.

In Fig. 48b we clearly observe an inversion of the Fano profile for all the higher terms in the $sp^+_{2,n}$ series as the intensity of the dressing field increases. In [56], this latter effect has been attributed to the ac-Stark shift $\Delta E_i^{\mathrm{ac}}(t)$ of the autoionizing states, which translates into an extra phase $\Delta\phi_i(I_0) = -\int_{-\tau}^{\infty} \Delta E_i^{\mathrm{ac}}[I(t)]dt$ between resonant and background amplitudes, a quantity approximately proportional to the peak intensity I_0 of the laser [113]. In principle, therefore, the inversion of the Fano profiles should take place multiple times as the laser intensity increases. Our calculations confirm such repeated inversion.

From the Fano profiles of the $sp^+_{2,3-6}$ and $sp^-_{2,5}$ states, $\sigma_i(\omega, I_0) \sim \sigma_{0,i}(I_0) + \frac{[\epsilon_i + q_i(I_0)]^2}{1+\epsilon_i^2}$, where $\epsilon_i = 2(\omega - \omega_{i,g})/\Gamma_i$ is the reduced energy with respect to each resonance, we extract the q parameters. The intensity-dependent phase of the states, $\varphi_i(I_0)$, is then obtained as $\varphi_i(I_0) = -2 \arctan q_i(I_0)$ [56]. The variation of such phase, $\Delta\varphi_i(I_0) = \varphi_i(I_0) - \varphi(0)$, is finally compared to the phase shift expected for a Rydberg singly-excited state: $\Delta\varphi_{\mathrm{free}} = \hbar^{-1} \int_{-\tau}^{\infty} U_{\mathrm{p}}[I(t)]dt$. Figure 48c

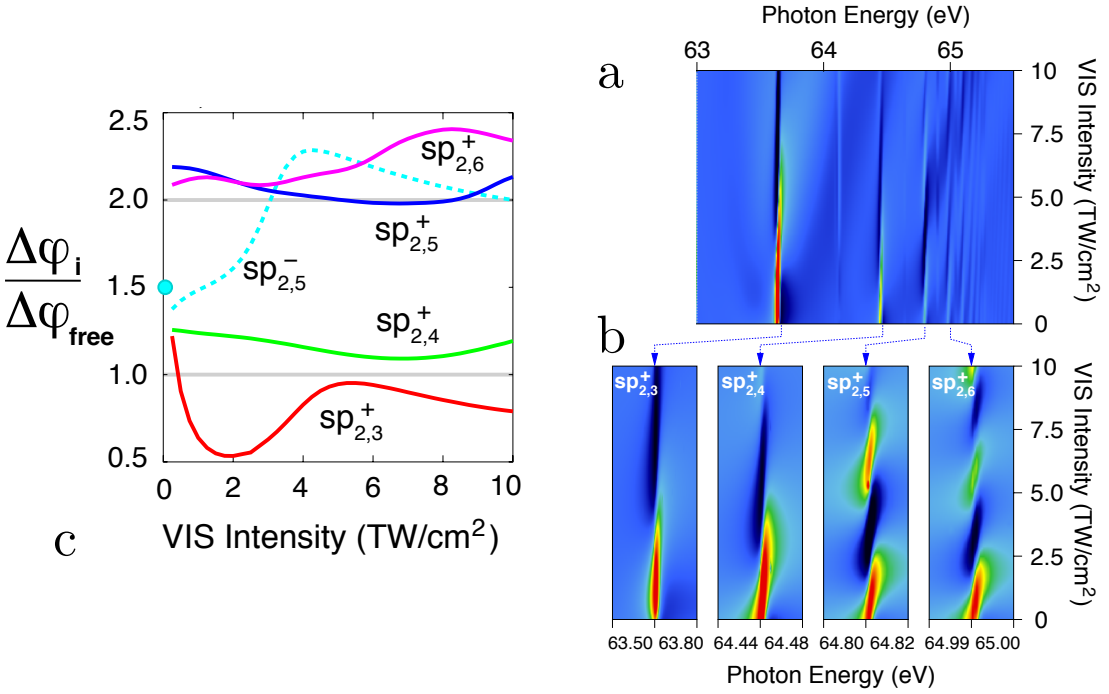

Figure 48: a) ATAS spectrum for overlapping XUV and VIS pulses as a function of the XUV photon energy (x-axis) and of the intensity of the VIS dressing field (y-axis). b) details of the spectrum near the $sp^+_{2,3-6}$ DES, whose Fano profiles undergo several inversions as the intensity of the dressing laser increases. c) DES phase compared to the SAE Rydberg limit.

shows that the ratio $\Delta\varphi_i(I_0)/\Delta\varphi_{\text{free}}(I_0)$ differs strikingly from unity, which is the limiting value expected for a Rydberg electron bound to an unpolarizable core [148]. Apart from the $sp^+_{2,3}$ state, the phase ratios lie well above unity, reaching values twice as large for $n \geq 5$. This finding indicates that the correlated Rydberg and core electrons give comparable contributions to the polarization of the state, which is a clear-cut confirmation of the multi-electron character of the atomic response to intense external fields evidenced in previous studies on tunneling suppression [149, 150]. Furthermore, even if the phase increases monotonically with the laser intensity, the phase ratio is clearly structured. In the case of the $sp^+_{2,3}$ state, the intensity dependence may be due to a detuned Rabi oscillation with the $[sp^+_{2,2} - 2p^2]$ pair. For the other states, the modulation arises from multiple concurrent coupling mechanisms, including coupling with other autoionizing states and states, as well as with states in the continuum above the N=2 threshold. For the narrow $sp^-_{2,5}$ state, we made a perturbative estimate of the polarizability, finding a value that is consistent with the change of phase observed for $I_0 \simeq 0$. The ac-Stark shift ΔE^{ac} of the $sp^-_{2,5}$ state was computed with the well-known second-order perturbative formula, adapted to autoionizing states,

$$\Delta E_i^{\text{ac}}(\omega_{\text{VIS}}) = -\frac{F_0^2}{2}\sum_j \frac{\langle\varphi_i^L|P|\varphi_j^R\rangle\,\langle\varphi_j^L|P|\varphi_i^R\rangle}{\omega_{ij}(\omega_{ij}^2 - \omega_{\text{VIS}}^2)} \tag{6.4}$$

where F_0 is the electric field amplitude, P is the total electronic canonical momentum operator, $\langle\varphi_i^L|H_0' = E_i\langle\varphi_i^L|$ and $H_0'|\varphi_i^R\rangle = |\varphi_i^R\rangle E_i$ are the left and right eigenvectors, respectively, of a non-hermitian reference Hamiltonian H_0', the E_i are the corresponding complex eigenvalues, and $\omega_{ij} = E_i - E_j$. The operator H_0' is defined as the field-free Hamiltonian of the atom plus a complex absorption

potential (CAP) $V = v(r_1) + v(r_2)$, $v(r) = -i\eta(r - R_0)^2\theta(r - R_0)$, which enforces outgoing boundary conditions. The real positive parameter η is varied until the expression for the ac-Stark shift approaches an almost stationary value [151]. In contrast to what is observed when the reference Hamiltonian is regularized using exterior complex scaling (ECS) [152, 153] instead of CAPs, due to the alteration of the wave functions in the complex-absorption region, the continuum-continuum matrix elements in Eq. (6.4) attain reasonably stationary values only for the narrowest resonances. We have ascertained that our estimates are reasonably converged by benchmarking them against selected ECS accurate calculations [154].

6.3 STRONG-FIELD IONIZATION OF DOUBLY-EXCITED STATES

The experiment of Ott *et al* mentioned at the beginning of the previous section, suggested that all the resonant features of the spectrum suddenly disappear when the intensity of the dressing field is higher than 4 TW/cm^2 [68]. It is unclear to date whether this effect has an instrumental or a genuine physical origin. Could it be that the common $N = 2$ innermost component of the DES is efficiently ionized by tunneling, in the conditions of the experiment? Our *ab initio* simulations, shown in Fig. 48a of the previous section, do not support the experimental findings. Indeed, clear traces of the Fano profiles are observable at intensities up to 10 W/cm^2. To clarify this issue further and investigate if tunneling plays a role at this intensities, we performed additional channel-resolved *ab initio* calculations for the photoionization of selected doubly-excited states of helium, upon exposure to moderately intense few-cycle 720 nm laser pulses. Additionally, we contrasted the results with spectra obtained using representative single-active electron models to highlight the role of electron-electron correlation in the ionization of doubly-excited states.

Initial State	5 TW/cm^2		10 TW/cm^2		15 TW/cm^2		20 TW/cm^2	
	IP	BP	IP	BP	IP	BP	IP	BP
$2s$	2.24[−7]	1.22[−6]	1.44[−5]	3.35[−5]	1.48[−4]	1.84[−4]	6.65[−4]	5.73[−4]
$2p_z$	2.54[−7]	1.28[−6]	1.89[−5]	3.71[−5]	1.94[−4]	2.29[−4]	8.66[−4]	6.95[−4]
$2sp^{+\dagger}$	2.40[−7]	1.25[−6]	1.66[−5]	3.54[−5]	1.69[−4]	2.08[−4]	7.70[−4]	6.29[−4]
$3s$	0.185	0.113	0.362	0.237	0.466	0.388	0.556	0.420
$3p$	0.254	0.269	0.502	0.307	0.624	0.315	0.668	0.315
$3d$	0.163	0.506	0.377	0.603	0.432	0.460	0.485	0.460

† $(2s + 2p_z)/\sqrt{2}$.

Table 2: Probability of ionization (IP) and excitation to higher bound states (BP), from $N = 2$ and $N = 3$ bound states of He^+ ion, as a result of the exposure to a 7 fs VIS Gaussian pulse ($\lambda = 730$ nm) with peak intensities ranging from 5 TW/cm^2 to 20 TW/cm^2. The results are obtained solving the TDSE in a Gaussian B-spline (GABS) basis (see [113]). The notation $a[b]$ stands for $a \times 10^b$.

To test the hypothesis of tunneling from the innermost orbital, we computed the probabilities for the ionization and the excitation to higher bound states of the $2s$, $2p$, $2sp^+ \equiv (2s + 2p_z)/\sqrt{2}$, $3s$, $3p$, and $3d$ states of the He^+ parent ion as a result of the interaction with VIS pulses with peak intensities of 5 TW/cm^2,

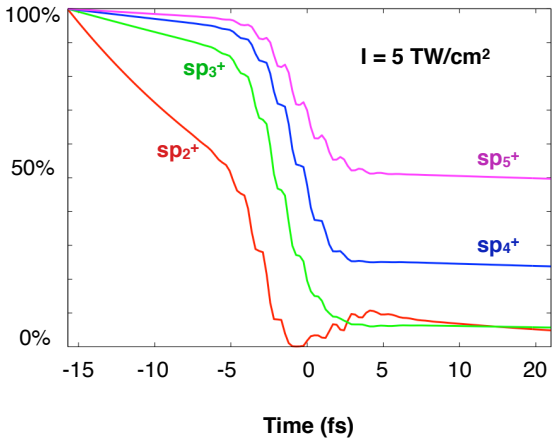

Figure 49: Evolution of the percentage of population in each corresponding state as a function of time when in presence of a VIS pulse of 5 TW/cm^2 of intensity and 7 fs duration centered at $t = 0$.

Pop. (%)	I (TW/cm^2)			
	5	10	15	20
sp_2^+	6.9	1.4	1.0	2.6
sp_3^+	6.2	0.2	2.1	3.4
sp_4^+	24.6	3.7	0.03	0.3
sp_5^+	50.6	15.9	5.4	1.8
sp_3^-	44.1	19.3	6.2	4.2
sp_4^-	8.0	15.1	5.9	0.1
sp_5^-	12.6	15.5	6.7	2.3

Table 3: Residual population of each corresponding DES after the interaction with a VIS pulse of 5, 10, 15 and 20 TW/cm^2 of intensity and 7 fs duration.

10 TW/cm^2, 15 TW/cm^2, and 20 TW/cm^2, which are all larger than the value at which the resonant features disappear from the experimental spectrum. Our results, listed in Table 2, clearly show that the effect of the external pulse on the $N = 2$ innermost electron is entirely negligible, even at intensities that are well beyond those realised in the experiment. Furthermore, in the present conditions, the preparation of the parent ion in a polarized state, what could conceivably affect the tunneling probability, gives rise instead to an excitation/ionization probability that sits in between that for the $2s$ and the $2p$ states. The picture changes dramatically when we consider an initial $N = 3$ state. In this case, irrespective of the orbital momentum, the population of the initial state is indeed significantly if not almost entirely depleted as a result of the interaction of the external pulses. These results strongly support the view that ionization or excitation of the inner electron are not viable explanations for the effect seen in the experiment. However, this effect would play a determinant role were the attention moved to higher photoelectron energies, where the series of the doubly excited states which converge to the $N = 3$ threshold are located.

The diagonalization of the Hamiltonian in the box in the presence of a complex absorber (the quenched Hamiltonian, H_Q) returns a quite accurate value for the position of the autoionizing states j as isolated poles $\tilde{E}_j = E_j - i\Gamma_j/2$ in the complex plane. The wave functions corresponding to these eigenstates fulfill outgoing boundary conditions, and can be thus regarded as Siegert states [155]. To tell whether the population of DES is depleted as a result of the interaction with the external pulse, we conducted simulations starting from selected Siegert states and monitored their time evolution. In particular, we considered the first four and first three states of the sp_n^+ and sp_n^- autoionizing series that converge to the $N = 2$ threshold, respectively. In Fig. 49 and Table 3 we present the results. The residual population of the DESs at the end of the VIS pulse at 5 TW/cm^2 is never negligible nor is it comparable for different terms across the series. This excludes the sudden depletion of DES all at once.

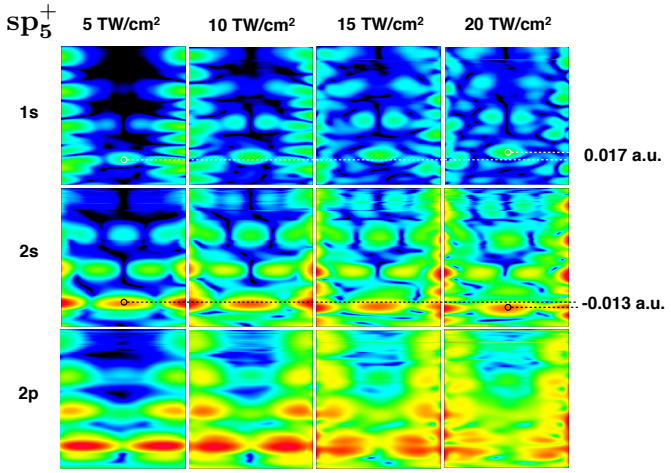

Figure 50: Photoelectron angular distributions of the three possible final ionization channels from the sp_5^- state for four different VIS intensities: 5, 10, 15 and 20 TW/cm^2. In the vertical axis we plot the energy, while in the horizontal axis we plot the cosine of the photoelectron ejection angle with respect to the laser polarization. The black and white dotted lines indicate the shift in the energy position of recognizable features in the spectrum.

In Fig. 50 we report the angularly-resolved spectra for the photoionization from the sp_5^+ state to each possible final channel. The most favored photoionization process from the DES converging to the $N = 2$ threshold is to the $2s$ and $2p$ channels, which are accessible already when dynamic correlation is not taken into account,

$$\mathrm{He}^{**} + n\gamma \rightarrow \mathrm{He}^+(N = 2) + e^-. \tag{6.5}$$

Table 4 gives the probability of excitation from all the considered DES to a given final N=2 channel.

	I (TW/cm^2)			
	5		10	
	$2s$	$2p$	$2s$	$2p$
sp_2^+	3	3	6	7
sp_3^+	6	13	11	20
sp_4^+	15	44	22	55
sp_5^+	7	19	12	30
sp_3^-	14	10	21	20
sp_4^-	14	21	24	23
sp_5^-	9	9	15	18

Table 4: Probability of exciting a DES to a given final N=2 channel (in %).

Not only does the position of the DES change across each final channel, but across each term of the series as well. As Fig. 51 shows, the energy shift of recognizable features in the photoelectron spectrum, as a function of the intensity of the probe laser, differs from term to term, $\Delta E_{tot} = \Delta E_f^{\mathrm{ac}} - \Delta E_i^{\mathrm{ac}}$. This suggests

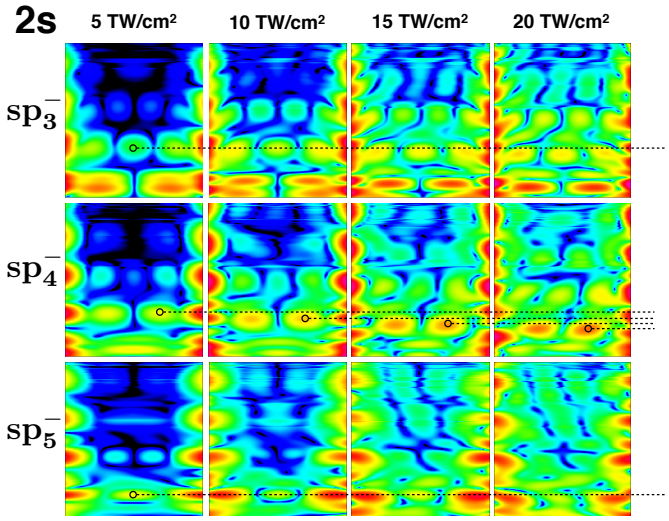

Figure 51: Photoelectron angular distributions for ionization to the 2*s* final channel from selected DES, at four intensities. In the vertical axis we plot the energy, while in the horizontal axis we plot the cosine of the photoelectron ejection angle with respect to the laser polarization.The black dotted line indicates the energy shift of recognizable features in the spectrum as a function of the intensity.

that the ac-Stark shift of individual DES is strongly affected by the contribution of states close to the ionization threshold and does not identify with the ponderomotive energy. The circumstance that for the sp_5^+ state the shift in the 1*s* channel is positive while that in the 2*s* channel is negative (see Fig. 50) suggests that, for this state, the ac-Stark shift is intermediate between the ponderomotive energy and a the higher value of the shift for the $N = 2$ continua, where the polarizable parent ion may contribute significantly.

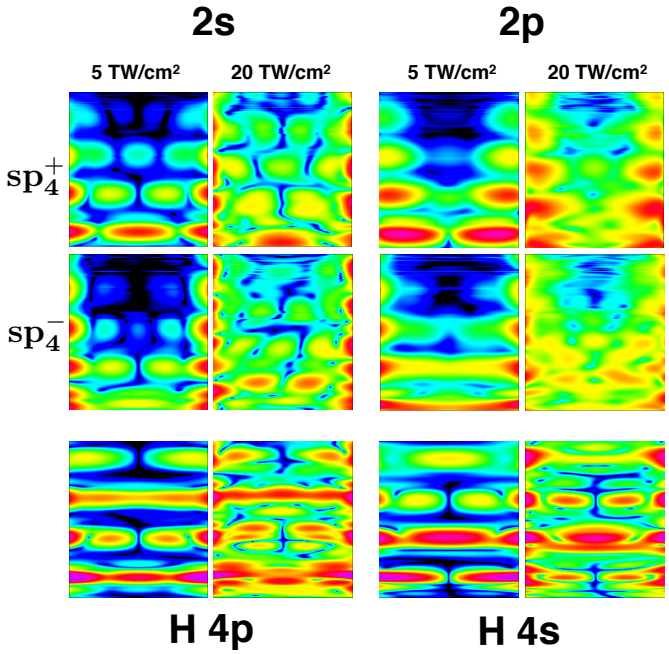

Figure 52: Photoelectron angular distributions for photoionization from the sp_4^+ and sp_4^- DES of helium to the 2*s* and 2*p* ionization channels, and from the 4*p* and 4*s* Rydberg states of hydrogen. Two intensities, 5 and 10 TW/cm^2, are shown.

To elucidate the role of electron correlation, in Fig. 52 we compare the photoelectron angular distributions from helium DES to those from hydrogen Rydberg states. We can see that DES are: i) shifted at lower energies (the ac-Stark shift of the initial and final states do not compensate with each other), ii) more aligned to the laser polarization axis, iii) decaying more rapidly with increasing electron energy, iv) more asymmetric at high intensity of the laser. When we compare, in the same figure, different autoionizing $^1P^o$ series, we observe that the spectra are similar across series in the $2s$ channel, but differ from the $2p$ channel. Also, the spectra in the $2s$ channel are more similar to those from the homologous p Rydberg state in hydrogen; conversely, the spectra in the $2p$ channel are more similar to those from s hydrogen states.

Part IV

CONCLUSIONS & PERSPECTIVES

7

CONCLUSIONS & PERSPECTIVES

This thesis has detailed the radiative transitions that occur in the atomic ionization continuum by means of novel attosecond pump-probe techniques. Its results are provide a theoretical framework for future attosecond experiments. In particular, we have: i) extended the soft photon approximation to finite dressing pulses and specialized it to the laser assisted ionization by means of XUV APT, ii) developed a model that permits us to study autoionization with state-of-the-art time-resolved interferometric spectroscopies, iii) analyzed the time-resolved dynamics of autoionizing states in two-photon experiments, iv) demonstrated a universal time delay anisotropy in photoemission delays, and v) detailed the effects of the field intensity on the positions and phases of doubly-excited states in helium.

In the extension of the soft-photon approximation, we considered two typical attosecond pump-probe schemes, streaking and RABITT , applied to the single ionization of helium. The results obtained within the SPA, compared to those of *ab initio* simulations, showed that SPA accounts quantitatively for all single-particle effects both in strong field or perturbative regimes for either pump-probe scheme [69]. Moreover, we developed a SPA model for excitation with APT in the long-pulse limit that may be the basis for the extension of the RABITT technique beyond the perturbative limit for which it was initially devised.

We have elaborated a new finite-pulse model for resonant two-photon transitions, which can be applied to simulate, at a negligible computational cost, attosecond pump-probe photoionization processes in the presence of autoionizing states [156]. The model, which is based on Fano's theory of configuration interaction in the continuum, accounts for multiple intermediate and final channels, as well as the possible presence of multiple isolated resonances. Further generalization to higher order transitions has been outlined. When used as a phenomenological tool, the model can be employed to extrapolate, from time-resolved experiments with table-top laser apparatuses, the radiative-coupling strength between short-lived excited states, such as autoionizing states in heavier rare gases, which can be hard to obtain otherwise, either theoretically, due to the challenging role of electronic correlation, or experimentally, due to the need of coupling lasers to a synchrotron x-ray beamline [157]. Conversely, once the model is parametrized, it can be used as a computationally inexpensive alternative to the numerical integration of the TDSE.

Using this model, and corroborated by full numerical solution of the TDSE in helium, we explained the physical origin of resonant phase profiles in two-photon ionization spectra as a function of the pump-resonance detuning. In particular,

we demonstrated that intermediate resonances manifest themselves in RABITT experiments with variations in the sideband phase shift and beating frequency as a function of the fundamental carrier frequency. More specifically, if the intermediate states comprise a single continuum and a resonance not radiatively coupled to the final continuum states, the phase of the two-photon amplitude coincides with that of Fano one-photon transition, while in presence of multiple intermediate continua or of a finite radiative coupling between the intermediate resonance and the final continuum states, the phase experiences a continuous excursion with a net variation that can be either 0 or 2π [70].

This latter prediction was confirmed in the argon atom by the experimental group of Anne L'Huillier, in the first measurement of the distortion of the phase of the continuum induced by the coupling with an autoionizing state, which made use of the RABITT technique. By reproducing the experimental conditions with the model, we showed that the observed phase profile was due to the multichannel nature of the problem.

At the same time and independently, the group of Pascal Salières managed to spectrally-resolve the structure of the resonantly populated sidebands of helium in the region of the doubly-excited states of the atom. This made possible to access the amplitude and phase across a Fano resonance in order to reconstruct the temporal shape of the structured resonant electron wave packet as it is born in the continuum. The comparison between the experimentally-reconstructed wave packet and the theoretical prediction obtained with the model yielded excellent agreement. Furthermore, we showed that owing to the long duration of the IR field and to the negligible influence of the radiative parameter γ between the localized part of the autoionizing state and the final continuum, the measured metastable wave packet corresponds essentially that of the one-photon process.

Alternative to the method described above or to those based on the holographic principle [134], we proposed a new means for the reconstruction of the autoionizing wave packet from the beating of two long-lived resonances excited by consecutive resonant harmonics in the region where the pump and probe pulses do not overlap. Additionally, we showed that when a resonance is present in the final state, it appears in the photoelectron spectrum as Fano-like profiles, strongly modulated with respect to the pump-probe time delay, and out of phase with respect to the background signal.

In collaboration with the experimental group lead by Ursula Keller, we provided the first evidence of an angular dependence in the measurement of photoemission time delays with the RABITT technique. We did so in a spherically symmetric system: helium, where the single-photon emission delay is rigorously isotropic. This photoemission angular dependence results from the interference between two different final quantum states accessible in two-photon processes, and the values can be as high as 60 as for $\sim 65^{o}$. By solving the TDSE with a virtually exact *ab initio* method for the helium atom, we showed that the observed time delay anisotropy in He is due to the effect of the spherical ionic potential on the outgoing photoelectron during the probe stage. In particular, at variance with atomic hydrogen, where anisotropies are also expected, the remaining electron in

the He+ (1s) parent ion has a noticeable effect on the observed anisotropy, thus pointing out the potential of this technique to investigate multi-electron effects from angularly resolved time delays. This results may shed new light on previous experiments [58, 32], where the angular dependence of the measured time delays was not always taken into account and where in most cases SAE approximations have been used.

In the moderately-high intensity regime, we have shown that ATAS allows one to measure the non-perturbative response of autoionizing states to external dressing fields. In particular, the inversion of asymmetric resonant features in the spectrum is found to repeat almost periodically as the intensity of the driving laser is increased. The ac-Stark shift of the doubly-excited states, which are important parameters for the implementation of quantum-control protocols, are shown to increase non-linearly with the intensity of the dressing field and, for the higher states of the autoionizing $sp^+_{2,n}$ series, to exceed by more than twice the theoretical SAE limit. These results demonstrate that ionization models based on the SAE approximation are inapplicable to strongly correlated multi-electron states and, conversely, that attosecond spectroscopy provides insight to the correlated optical response of excited electronic states.

Finally, we have studied the role of electron correlation in the photo-ionization from the doubly-excited states of helium. Motivated by the experimental observation of the depletion of the DES population at intensities above 4 TW/cm^2 and its possible explanation in terms of tunneling from the innermost orbital of the DES, we conducted *ab initio* simulations that confirmed that He^+ (N=2) parent ions are largely unaffected by short VIS laser pulses with intensities up to 20 TW/cm2. Tunneling of the inner electron, therefore, does not explain the sudden simultaneous depletion of $N = 2$ resonant features. However, the opposite is true for He^+ ($N = 3$) states, which are almost quantitatively depleted at the higher end of the intensity scale. We found the survival probability of the DES is strongly affected by their coupling to other DES, which gives rise to Rabi oscillations. Comparison with calculations in the hydrogen atom, show that the photoelectron spectra of DES bear little resemblance to those from homologous states in hydrogen. In particular, DES spectra often display energy shifts which change across series as well as final channels.

The line of research initiated during this work of thesis can be developed along manifold directions. A natural extension of the work will be to relate the argument of the resonant two-photon transition matrix element with a resonant two-photon photo-ejection time delay. Even if, at a first inspection, the argument of the resonant two-photon transition amplitude cannot be separated into a non-resonant ($\tau_W + \tau_{CC}$) and a resonant contribution when the autoionizing state is radiatively coupled to the final state, one can still explore those cases in which this separation can be done, or look for alternative partitioning schemes. Still in the context of photoemission delays, another possibility is to consider the case of several open channels, where the time delay is expressed in terms of a matrix and the simple correspondence with the energy derivative of a single phase-shift is consequently lost. In a similar way, it is interesting to consider whether the

autoionization branching ratio of metastable states embedded in a multichannel continuum can be controlled.

The resonant model proposed in this thesis can also be extended in numerous ways. It is in principle possible to apply it to the study of time-resolved multiphoton resonant transitions in more complex atoms, molecules or solids susceptible of a description in terms of a finite number of free-particle channels and metastable states. Think, for example, to the radiative excitation of image-potential states on metal surfaces, which, on the one side, can decay tunnel to the conduction-band, and on the other side, can exchange a further photon and be liberated to either the metal or to the vacuum (photoemission channel) [158, 159]. A second readily made extension of the model is to make it resolved in angle since angularly-resolved two-photon ionization involving autoionizing states is still unexplored and now within experimental reach. Another possibility is to include higher-orders terms in the perturbative expansion. In most common case only one or two resonances are relevant. Hence, the number of parameters will remain tractable even at higher order. With these extensions, the model could be applicable to explain experiments with moderately-high IR intense lasers such as resonant streaking. Finally, if one were able to incorporate autoionizing states in the strong field approximation, one could extend the recollision process on which HHG is based to the case of excited parent ions. Indeed, resonant HHG is an active field of research where theoretical support is largely missing.

8

CONCLUSIONES

Esta tesis ha detallado las transiciones radiativas que se producen en el continuo de ionización atómica por medio de técnicas *pump-probe* de attosegundos. Los resultados aquí expuestos proporcionan un marco teórico para futuros experimentos de attosegundos. En particular, hemos: i) extiendido la aproximación de *soft-photon* (SPA) a pulsos finitos y la hemos especializado a la ionización láser asistida por trenes de attosegundos (APT), ii) desarrollado un modelo que nos permite estudiar la autoionización con técnicas espectroscópicas interferométricass resueltas temporalmente , iii) analizado la dinámica, resuelta en el tiempo, de los estados autoionizantes en experimentos de dos fotones, iv) demostrado una anisotropía en los tiempos de foto-emisión, y v) detallado los efectos de la intensidad del campo láser en las posiciones y fases de los estados doblemente excitados del helio.

En la extensión de la aproximación *soft-photon*, hemos considerado dos técnicas *pump-probe* de attosegundos bien conocidas, *streaking* y RABITT , aplicadas a la ionización simple del helio. Los resultados obtenidos con la SPA, comparados a los obtenidos con las simulaciones *ab initio*, demuestran que la SPA reproduce cuantitativamente todos los efectos de partícula simple tanto en el régimen perturbativo como de campo intenso, para cualquiera de las dos técnicas pump-probe consideradas [69]. Por otra parte, hemos desarrollado un modelo en la SPA para la excitación con trenes de attosegundos en el límite de pulsos largos, que puede sentar las bases para la extensión de la técnica de RABITT más allá del límite perturbativo para el que inicialmente fue diseñada.

Hemos elaborado un modelo para tratar las transiciones resonantes a dos fotones con pulsos finitos, que puede aplicarse para simular, con un ínfimo coste computacional, procesos de fotoionización *pump-probe* de attosegundos en presencia de estados autoionizantes [156]. El modelo, que está basado en la teoría de Fano de interacción de configuraciones en el contínuo, tiene en cuenta múltiples canales intermedios y finales, así como la posible presencia de múltiples resonancias aisladas. Una generalización a órdenes perturbativos más altos ha sido comentada. Usado como herramienta fenomenológica, el modelo puede ser empleado para extrapolar, de experimentos temporalmente resueltos, el acoplamiento radiativo entre estados excitados de corta vida, tales como estados autoionizantes en gases nobles pesados, que son dificíles de obtener de otra manera, tanto teóricamente debido a la fuerte correlación electrónica, como experimentalmente debido a la necesidad del uso combinado de láseres y líneas de luz de sincrotrón. De manera inversa, una vez que los parámetros del modelo sean conocidos, el mismo puede ser usado como una alternativa computacional, de coste cero, de la integración numérica de la TDSE.

Usando este modelo, y corroborado por la solución numérica virtualmente exacta de la TDSE en helio, hemos explicado el orígen físico de los perfiles de fase resonantes en el espectro de ionización de dos fotones. En particular, hemos demostrado que la presencia de resonancias en los pasos intermedios, se manifiesta en experimentos de RABITT como variaciones en el desfase de la *sideband* y la frecuencia de oscilación de la frecuencia fundamental. Específicamente, si el estado intermedio comprende un sólo canal de contínuo y una resonancia no acoplada radiativamente a los estados finales del contínuo, la fase de la amplitud de dos fotones coincide con la dada por Fano para la transición a un fotón, mientras que en presencia de múltiples canales del contínuo o de un acoplamiento finito entre la resonancia intermedia y los estados finales del contínuo, la fase experimenta una excursión finita con una variación neta que puede ser o bien 0 o 2π [70].

Esta última predicción ha sido confirmada en el átomo de argon por el grupo experimental de Anne L'Huillier, en la primera medida de la distorsión de la fase en el contínuo inducida por el acoplamiento con un estado autoionizante, que hizo uso de la técnica de RABITT . Reproduciendo las condiciones del experimento con el modelo, demostramos que el perfil de la fase que se observaba era debido a la naturaleza multi-canal del problema.

Al mismo tiempo y de manera independiente, el grupo de Pascal Salières consiguió resolver espectralmente la estructura de una *sideband* resonante en la región de los estados doblemente excitados del átomo de helio. Esto hizo posible acceder a la amplitud y fase a través de una resonancia de Fano para reconstruir el perfil temporal del paquete de ondas electrónico resonante. La comparación entre el paquete de ondas reconstruido experimentalmente y la predicción teórica obtenida con el modelo dio un acuerdo excelente. Además, hemos demostrado que debido a la larga duración del pulso IR y a la poca influencia del parámetro radiativo γ entre la parte localizada del estado autoionizante y el contínuo final, el paquete de ondas metaestable medido corresponde, esencialmente, con el paquete de ondas del proceso de un fotón.

Alternativamente al método descrito o a aquellos métodos basados en el principio holográfico [134], hemos propuesto una nueva manera para la reconstrucción del paquete de ondas autoionizante a partir de la interferencia de dos resonancias de larga vida excitadas por dos armónicos consecutivos en la región de tiempos donde el pulso *pump* y el pulso *probe* no solapan. Adicionalmente, hemos demostrado que cuando una resonancia está presente en un estado final, aparece en el espectro fotoelectrónico como un cuasi-perfíl de Fano, fuertemente modulado con respecto a la separación temporal entre el *pump* y el *probe* y fuera de fase con respecto a la señal de fondo.

En colaboración con el grupo experimental liderado por Ursula Keller, hemos proporcionado la primera evidencia de una dependencia angular en la medida de los retrasos del tiempo de fotoemsión mediante la técnica de RABITT . Este estudio fue realizado en helio, un sistema esféricamente simétrico donde el retraso del tiempo de fotoemisión de un fotón es rigurosamente isotrópico. Esta dependencia angular de la fotoemisión resuelta de la interferencia entre dos estados cuánticos

finales accesibles en procesos de dos fotones y los valores pueden ser tan altos como 60 as para $\sim 65^{o}$.

Resolviendo la TDSE con un método *ab initio* prácticamente exacto para el átomo de helio, se demostró que la observada anisotropía en el tiempo de retardo en helio es debida al efecto del potencial iónico esférico en el fotoelectrón saliente durante la etapa de *probe*. En particular, a diferencia del átomo de hidrógeno, en donde también se espera anisotropía, el electrón que permanece en el ión padre He+ (1s) tiene un efecto notable en la anisotropía observada, lo que pone de manifiesto el potencial de esta técnica para investigar los efectos multielectrónicos con mediciones de retardos de tiempo resueltas angularmente. Estos resultados pueden arrojar nueva luz sobre los experimentos anteriores [58, 32], donde la dependencia angular de los retrasos de tiempo de medición no siempre se tuvo en cuenta y donde en la mayoría de los casos se han utilizado aproximaciones de partícula simple.

En el régimen de alta intensidad, hemos demostrado que la técnica de ATAS permite medir la respuesta no perturbativa de los estados autoionizantes a los campos exteriores. En particular, hemos encontrado que la inversión de los perfiles de Fano en el espectro se repite cuasi-periódicamente a medida que se incrementa la intensidad del láser. El desplazamiento ac-Stark de los estados doblemente excitados, que son parámetros importantes para la aplicación de los protocolos de control cuántico, se demuestra que crece de manera no lineal con la intensidad del campo y, para estados autoionizantes de energías más altas, que excede el doble del valor esperado para un estado Rydberg ligado a un ión padre no polarizable. Estos resultados demuestran que los modelos de ionización basados ??en la aproximación de partícula simple son inaplicables en estados multielectrónicos fuertemente correlacionados y, de manera inversa, que la espectroscopía de attosegundos proporciona información acerca de la respuesta óptica correlacionada de estados electrónicos excitados.

Por último, se ha estudiado el papel de la correlación electrónica en la fotoionización desde los estados doblemente excitados de helio. Motivados por la observación experimental de la disminución de la población de estos estados a intensidades superiores a 4 TW/cm^2 y su posible explicación en términos de efecto túnel desde el orbital más interno del estado doblemente excitado, se realizaron simulaciones *ab inito* que demostraron que los iones padre He+ (N=2) no son afectados por pulsos VIS con intensidades de hasta 20 TW/cm^2. De este modo, el efecto túnel desde el orbital interno es, no explica la repentina y simultánea disminución de población de las señales resonantes. Sin embargo, para estados doblemente excitados con ión padre He^+ ($N = 3$), prácticamente la población de todos los estados desaparece para las intensidades altas consideradas. Encontramos que la probabilidad de supervivencia de los estados doblemente excitados está fuertemente afectada por su acoplamiento a otros estados doblemente excitados, lo que da lugar a oscilaciones de Rabi. La comparación con cálculos en el átomo de hidrógeno, muestran que los espectros de fotoelectrones de los estados doblemente excitados tienen poca semejanza con sus estados homólogos en el átomo de hidrógeno. En particular, los espectros de los primeros a menudo

muestran desplazamientos de energía que cambian tanto a través de la serie autoionizante, como a través de los canales de ionización finales.

Part V

APPENDICES

A

THEORETICAL CHARACTERIZATION OF LIGHT PULSES

The vector potential of a plane wave can be written as

$$A(t) = A_0 \cos(\omega t + \phi), \tag{A.1}$$

where A_0 is the amplitude of the field, ω is the frequency of the pulse, and ϕ is the phase of the pulse. In the Coulomb gauge, the vector potential is related to the electric field by

$$E(t) = -\frac{1}{c}\frac{\partial}{\partial t}A(t) = E_0 \sin(\omega t + \phi), \quad E_0 = A_0\frac{\omega}{c}, \tag{A.2}$$

where c is the speed of light. We define the intensity as the time-averaged magnitude of the Poynting vector (or energy flux),

$$I = \langle S \rangle, \quad S = E \times H = \frac{c^2}{4\pi} E \times B. \tag{A.3}$$

Since the magnetic field is perpendicular to the electric field and $|B| = |E|/c$, this expression can be written as

$$S = \frac{1}{4\pi}|E|^2 c, \tag{A.4}$$

and, since $\langle |E|^2 \rangle = E_0^2/2$, the intensity is

$$I = I_0\, E_0^2 = I_0\, \frac{\omega^2}{c^2} A_0^2, \tag{A.5}$$

where $I_0 = c/(8\pi) = 3.51 \cdot 10^{16}$ W/cm^2, is the atomic unit of intensity.

The pulses used in common pump-probe experiments, however, do not exhibit the monochromatic character represented by the plane waves of Eq. (A.1). Mathematically, experimental (non-chirped) pulses can be well described by inserting an envelope $f(t)$ in Eq. (A.1),

$$A(t) = A_0\, f(t - t_0) \cos(\omega(t - t_0) + \phi), \tag{A.6}$$

where t_0 is the center of the pulse.

In the majority of cases studied in this thesis, we made use of attosecond pulse trains. An APT can be expressed as a modulated infinite sequence of identical pulses, with alternating signs,

$$A_{\mathrm{XUV}}(t) = A_0\; g(t) \sum_{n=-\infty}^{+\infty} (-1)^n f\left(t - n\,\pi/\omega_{\mathrm{IR}}\right), \tag{A.7}$$

where $g(t)$ is the envelope of the train, $f(t)$ is the envelope of each single pulse in the train and ω_{IR} is the frequency of the IR field that generated the train. Alternatively, the same train can also be expressed as a combination of in-phase harmonics of the fundamental IR frequency (see Figure 3 in Chapter 1),

$$A_{\text{XUV}}(t) = \sqrt{\frac{8}{\pi}}\,\omega_{\text{IR}} A_0\, g(t) \sum_{k=0}^{\infty} |\tilde{f}_{2k+1}| \cos\left[(2k+1)\omega_{\text{IR}} t + \phi_{2k+1}\right], \tag{A.8}$$

where the index k runs now over the harmonics, and we introduced the notation $\tilde{f}_n = \tilde{f}(n\omega_{\text{IR}})$, $\phi_n = \arg f_n$. The spectrum of this field reads,

$$\tilde{A}_{\text{XUV}}(\omega) = \sqrt{\frac{2}{\pi}}\, A_0\, \omega_{\text{IR}} \sum_{k=-\infty}^{+\infty} \tilde{f}_{2k+1}\, \tilde{g}\left[\omega - (2k+1)\omega_{\text{IR}}\right]. \tag{A.9}$$

In this latter formulation, the individual harmonic phases ϕ_{2k+1} can be freely changed.

Two commonly used envelopes are the gaussian and cosine-squared envelopes. For Gaussian envelopes, the vector potential reads

$$A(t) = A_0 \exp\left(-2\ln 2\,\frac{(t - n\pi/\omega_{\text{IR}})^2}{\tau^2}\right) \cos\left[\omega(t - n\pi/\omega_{\text{IR}}) + \phi)\right], \tag{A.10}$$

while the electric field is

$$\begin{aligned} E(t) = -\frac{1}{c}\frac{\partial}{\partial t}A(t) = \frac{1}{c}A_0\omega \exp\left(-2\ln 2\,\frac{(t - n\pi/\omega_{\text{IR}})^2}{\tau^2}\right) \times \\ \left[\frac{4\ln 2}{\omega\tau^2}(t - nT/2)\cos\left[\omega(t - n\pi/\omega_{\text{IR}}) + \phi\right] + \sin\left[\omega(t - n\pi/\omega_{\text{IR}}) + \phi\right]\right], \end{aligned} \tag{A.11}$$

where we used τ to symbolize the full width at half maximum relative to the intensity. For cosine-squared envelopes, the vector potential is given by

$$A(t) = A_0 \cos^2\left[\frac{\pi(t - n\pi/\omega_{\text{IR}})}{2\sqrt{2}\,\tau}\right] \cos\left[\omega(t - n\pi/\omega_{\text{IR}}) + \phi\right], \tag{A.12}$$

and the electric field by

$$\begin{aligned} E(t) = \frac{1}{c}A\omega \Bigg\{ \cos\left[\frac{\pi(t - n\pi/\omega_{\text{IR}})}{2\sqrt{2}\,\tau}\right] \sin\left[\frac{\pi(t - n\pi/\omega_{\text{IR}})}{2\sqrt{2}\,\tau}\right] \times \\ \times \cos\left[\omega(t - n\pi/\omega_{\text{IR}}) + \phi\right] \frac{\pi}{\sqrt{2}\tau\omega} + \cos^2\left[\frac{\pi(t - n\pi/\omega_{\text{IR}})}{2\sqrt{2}\,\tau}\right] \sin\left[\omega(t - n\pi/\omega_{\text{IR}}) + \phi\right] \Bigg\}. \end{aligned} \tag{A.13}$$

Figure 53 shows an individual pulse and an APT with a gaussian envelope in the temporal and spectral domain.

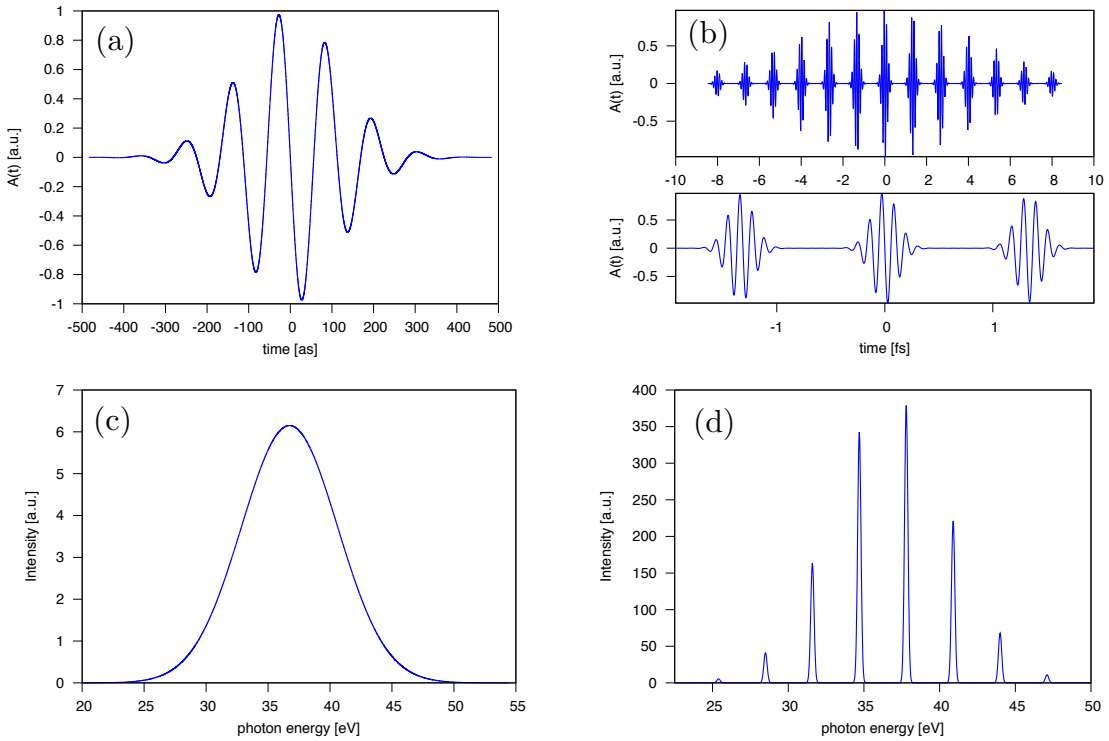

Figure 53: (a) XUV pulse centered at $t_0 = 0$ with a τ = 282 as and a carrier-envelope phase of $\phi = \pi/2$. (b) Top panel: train of XUV pulses. Bottom panel: close-up of the three central pulses. The individual XUV pulses are of the form of panel a, while the APT has τ_{APT} = 10 fs. (c,d) Fourier transform of panels a and b, respectively.

In this thesis, we have used both envelopes. For the *ab initio* simulations, the attosecond pulses (either isolated or inside a train) were represented with a gaussian envelope [Equation (A.10)], as was the envelope of the APTs. The IR, on the contrary, was represented by a cosine-square envelope [Equation (A.12)], mostly because it vanishes faster than a gaussian, thus permitting a faster convergence. For the soft photon and resonant models, we only used gaussian envelopes.

B

FADDEEVA FUNCTION

In this appendix we derive the general analytical expression for the two-photon transition amplitude between an initial state $|g\rangle$, with energy E_g, and a final state $|\beta E\rangle$, with energy E, due to the absorption/emission of a photon from a first Gaussian pulse F_1, centered in $t_1 = 0$, followed by the absorption/emission of a photon from a second Gaussian pulse F_2, centered in $t_2 = t_1 + \tau = \tau$,

$$\mathcal{A}^{21}_{\beta E,g} = -i \int d\omega \, \tilde{F}_2(\omega_{Eg} - \omega; \tau) \tilde{F}_1(\omega) \mathcal{M}_{\beta E,g}(\omega), \tag{B.1}$$

under the hypothesis, recurrent in the derivation of the model illustrated in Sec. 4.4.2, that the two-photon matrix element $\mathcal{M}_{\beta E,g}(\omega)$ has an isolated simple pole at $\omega = E_a - E_g$, where $E_a \in \mathbb{C}$, $\mathrm{Im} E_a < 0$, and that, to a very good approximation, $(\omega + E_g - E_a)\mathcal{M}_{\beta E,g}(\omega)$ is constant in the region where the product $\tilde{F}_2(\omega_{Eg} - \omega; \tau)\tilde{F}_1(\omega)$ does not vanish,

$$\mathcal{M}_{\beta E,g}(\omega) \simeq \frac{T_{\beta E,g}}{\omega - \omega_{ag}}. \tag{B.2}$$

In the following, to consider all the possible cases at once, we will indicate both the absorption and the emission spectral components 4.61 of the n-th Gaussian wavepacket (4.60) with the single expression

$$\tilde{A}_n(\omega) = \frac{A_n}{2\sigma_n} \mathrm{e}^{-i\varphi \, \mathrm{sgn}(\omega_n)} \mathrm{e}^{i\omega t_n} \mathrm{e}^{-\frac{(\omega-\omega_n)^2}{2\sigma_n^2}}, \tag{B.3}$$

where the absorption/emission components are differentiated by attributing to ω_0 a positive or negative sign, respectively. The two-photon transition amplitude (B.1), thus, becomes

$$\begin{aligned} \mathcal{A}^{21}_{\beta E,g} &= -i \frac{A_2}{2\sigma_2} \mathrm{e}^{-i\varphi_2 \, \mathrm{sgn}(\omega_2)} \frac{A_1}{2\sigma_1} \mathrm{e}^{-i\varphi_1 \, \mathrm{sgn}(\omega_1)} \times \\ &\times T_{\beta E,g} \int_{-\infty}^{\infty} d\omega \, \frac{e^{i(\omega_{Eg}-\omega)\tau}}{\omega - \omega_{ag}} e^{-\frac{(\omega_{Eg}-\omega-\omega_2)^2}{2\sigma_2^2}} e^{-\frac{(\omega-\omega_1)^2}{2\sigma_1^2}}. \end{aligned} \tag{B.4}$$

After some lengthy but straightforward algebraic passages, it is possible to cast the previous result in the following form

$$\begin{aligned} \mathcal{A}^{21}_{\beta E,g} &= -i \frac{A_2}{2\sigma_2} \mathrm{e}^{-i\varphi_2 \, \mathrm{sgn}(\omega_2)} \frac{A_1}{2\sigma_1} \mathrm{e}^{-i\varphi_1 \, \mathrm{sgn}(\omega_1)} \times \\ &\times \exp\left(-\frac{\delta^2}{2\sigma^2} - \frac{\tau^2}{2\sigma_t^2} - i \frac{\sigma_2}{\sigma_1} \frac{\tau}{\sigma_t} \frac{\delta}{\sigma} + i\omega_2 \tau \right) \times \\ &\times T_{\beta E,g} \int_{-\infty}^{\infty} d\omega \, \frac{\exp\left[-\frac{1}{2} \left(\sigma_t \omega + \frac{\sigma_1}{\sigma_2} \frac{\delta}{\sigma} + i \frac{\tau}{\sigma_t} \right)^2 \right]}{\omega_1 + \omega - \omega_{ag}}, \end{aligned} \tag{B.5}$$

where we have introduced a convoluted spectral width $\sigma = \sqrt{\sigma_1^2 + \sigma_2^2}$ and temporal width $\sigma_t = \sqrt{\sigma_1^{-2} + \sigma_2^{-2}}$ (notice that $\sigma = \sigma_1\sigma_2\sigma_t$), as well as the nominal detuning $\delta = E_g + \omega_1 + \omega_2 - E$. By performing the change of variable $x = -\frac{1}{\sqrt{2}}(\sigma_t\omega + \frac{\sigma_1}{\sigma_2}\frac{\delta}{\sigma} + i\frac{\tau}{\sigma_t})$, the integral in Eq. (B.5) can be expressed in terms of the Faddeeva special function $w(z) = e^{-z^2}\mathrm{erfc}(-iz)$, which, in the upper half of the complex plane, admits the following integral representation (see §7.1.3-4 in [109]),

$$w(z) = \frac{i}{\pi}\int_{-\infty}^{+\infty}\frac{\mathrm{e}^{-t^2}}{z-t}dt, \qquad \mathrm{Im}[z] > 0. \tag{B.6}$$

Indeed, by introducing the dimensionless complex variable z_a^{21},

$$z_a^{21} = \frac{\sigma_t}{\sqrt{2}}\left[\left(\omega_1 - \frac{\sigma_1^2}{\sigma^2}\delta - i\frac{\tau}{\sigma_t^2}\right) - \omega_{ai}\right], \tag{B.7}$$

the integral in Eq. (B.5) can be expressed as

$$\int_{-\infty}^{\infty} d\omega \frac{\exp\left[-\frac{1}{2}\left(\sigma_t\omega + \frac{\sigma_1}{\sigma_2}\frac{\delta}{\sigma} + i\frac{\tau}{\sigma_t}\right)^2\right]}{\omega_1 + \omega - \omega_{ai}} = -i\pi w(z_a). \tag{B.8}$$

Notice that to establish the correspondence between the integral in Eq. (B.5) and the r.h.s. of (B.6), one must continuously deform the integration path from the initial real axis to a final re-defined real axis without crossing the pole, which requires $\tau < \sigma_t^2\,\mathrm{Im}E_a$. Once the integral is written in terms of the Faddeeva function, however, the expression is valid for any value of the time delay, since the Faddeeva function is defined on the whole complex plane by analytic continuation. The time-ordered two-photon transition amplitude finally becomes

$$\begin{aligned}\mathcal{A}^{21}_{\beta E_i g} &= -\pi\frac{A_1A_2}{4\sigma_1\sigma_2}\,\mathrm{e}^{-i\varphi_2\,\mathrm{sgn}(\omega_2)}\mathrm{e}^{-i\varphi_1\,\mathrm{sgn}(\omega_1)}\,T_{\beta E_i g}\,e^{i\omega_2\tau}\times \\ &\times \exp\left[-\frac{1}{2}\left(\frac{\delta^2}{\sigma^2} + \frac{\tau^2}{\sigma_t^2} + 2i\frac{\sigma_2}{\sigma_1}\frac{\delta}{\sigma}\frac{\tau}{\sigma_t}\right)\right] w(z_a^{21}).\end{aligned}$$

C

OBTENTION OF MODEL PARAMETERS

In this Appendix we describe how we estimated the model parameters. For clarity in what follows, we repeat Figure 25 here again.

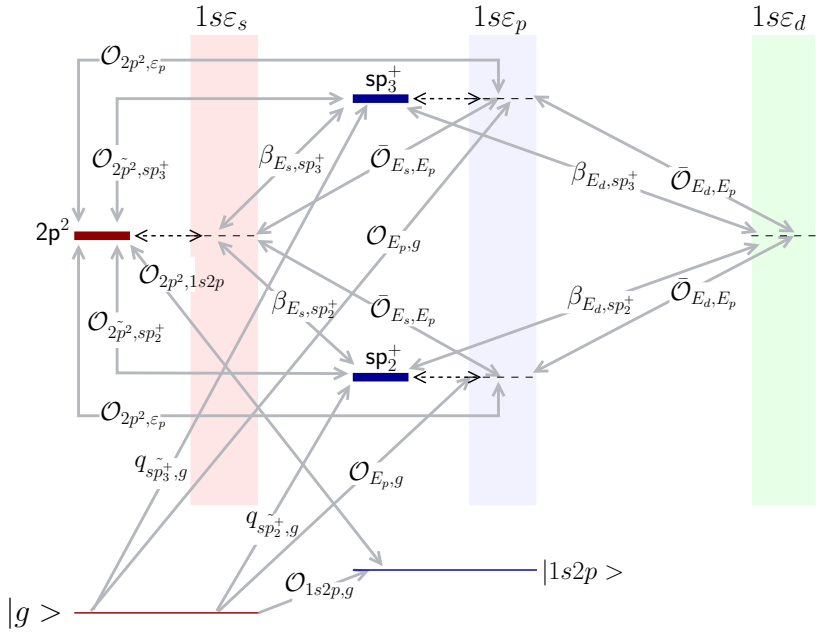

Figure 54: Scheme of the essential states involved in the RABITT ionisation of the helium atom in the region of the $N = 2$ auto ionising states, together with the relevant radiative coupling between them that must be taken into account to reproduce the pump-probe photoelectron spectrum with the finite-pulse resonant two-photon model described in the text.

In the intermediate states of the model we included one $^1\mathrm{P}^o$ intermediate continuum, $1sE_p$, with the two isolated resonances sp_2^+ and sp_3^+ [**?**], and one intermediate bound state, $1s2p$, which contributes significantly to the excitation amplitude of the final $2p^2\ ^1\mathrm{S}^e$ state, owing to the strong dipolar coupling between the $1s$ and $2p$ orbitals. In the final states of the model we included the $1sE_s\ ^1\mathrm{S}^e$ continuum, featuring the $2p^2$ metastable state, and the $1sE_d\ ^1\mathrm{D}^e$ continuum. For the latter, we did not include any resonance, as the most relevant one, also with dominant configuration $2p^2$, lies very close in energy to the sp_2^+ state and hence it is not reached by any sideband within the chosen range of IR frequencies. The sp_n^- and $2pnd$ states, as well as higher terms in the sp_n^+ series, which are all narrow and have a small dipole coupling with the ground state if compared with the $sp_{2/3}^+$ states, are not expected to affect significantly the sideband spectrum near or below the $2p^2\ ^1\mathrm{S}^e$ state and were therefore not included in the model.

The position, width and q parameter from the ground state of the two intermediate resonances, as well as the background photoionisation cross section, can be taken from the literature, where one can find also the position and width of the final $^1S^e$ state and the energy of the bound $1s2p$ state. Even with these data, there are still 14 independent parameters not reported in the literature that are in principle needed to apply the model: the two continuum-continuum couplings, $\bar{\mathcal{O}}_{1sE_\ell,1sE_p}$; the relative strength of the direct dipole coupling of the two intermediate autoionizing states with the two final continua, β_{1sE_ℓ,sp_2^+}, β_{1sE_ℓ,sp_3^+} (4 parameters); the dipolar coupling to the two final continua through the intermediate $1s2p$ bound state, $\mathcal{O}_{1s\varepsilon_\ell,1s2p}\mathcal{O}_{1s2p,1s^2}$; the q parameter for the excitation of the final resonance from the intermediate bound and the two intermediate autoionizing states, $q_{\tilde{2p^2},1s2p}$, $q_{\tilde{2p^2},sp_2^+}$, $q_{\tilde{2p^2},sp_3^+}$, and, conversely, for the excitation of the $sp_{2/3}^+$ intermediate resonances from the $2p^2$ final metastable state, $q_{s\tilde{p}_2^+,2p^2}$, $q_{s\tilde{p}_3^+,2p^2}$; the dipole coupling between the final metastable state and the intermediate continuum, $\mathcal{O}_{2p^2,1s\varepsilon_p}$. The value of the residual parameters δ_{2p^2,sp_2^+}, δ_{2p^2,sp_3^+}, $\zeta_{2p^2,sp_{2,2}^+}$, and ζ_{2p^2,sp_3^+}, can be determined from the previous ones with the additional assumption $\mathcal{O}_{2p^2,sp_{2/3}^+} \simeq \mathcal{O}_{\tilde{2p^2},sp_{2/3}^+}$, which is justified by the strong dipole coupling between doubly excited states compared to that between an $N = 2$ doubly excited state and a $1sE_\ell$ continuum (the latter optical transition, being itself a double excitation, is prohibited within the quasi-particle approximation). In the same spirit, we can assume $\mathcal{O}_{s\tilde{p}_{2/3}^+,2p^2} = \mathcal{O}_{sp_{2/3}^+,2p^2}$, with which $q_{s\tilde{p}_{2/3}^+,2p^2}$ become derived quantities, thus reducing to 12 the total number of independent parameters. Finally, we assume $q_{\tilde{2p^2},1s2p} \gg 1$, so that the product $\mathcal{O}_{1s\varepsilon_\ell,1s2p}\mathcal{O}_{1s2p,1s^2}q_{\tilde{2p^2},1s2p}$ comes as a single parameter $\gamma_{\tilde{2p^2}\leftarrow 1s2p\leftarrow 1s^2}$, thus reducing the total number of parameters to 11.

In § 5.1 we showed the validity of the soft-photon model in treating the the non-resonant ionization of helium. In this approximation, the continuum singlet states of the atom were given by the product of the $1s$ ground state of the He^+ parent-ion with free spherical waves,

$$\phi_{1s,E\ell m} = \frac{\alpha\beta - \beta\alpha}{\sqrt{2}}\frac{1+\mathcal{P}_{12}}{\sqrt{2}}\phi_{1s}^{\text{ion}}(\vec{r}_1)\sqrt{\frac{2k}{\pi}}j_\ell(kr_2)Y_{\ell m}(\hat{r_2}), \tag{C.1}$$

where j_ℓ are spherical bessel functions, $Y_{\ell m}$ are spherical harmonics, and $E = k^2/2$, while the ground state was approximated by the $1s^2$ configuration, where, following Slater's prescription, the $1s$ orbital was an hydrogenic wavefunction with effective charge $Z = 1.7$,

$$\phi_{1s}^{\text{He}}(k) = \frac{2\sqrt{2}Z^{5/2}}{\pi[k^2+Z^2]^2}. \tag{C.2}$$

With this model we were able to predict, with quantitative accuracy, the background distribution of the photoelectrons generated by the interaction of the atom with sequences of XUV-pump and IR-probe pulses, even in the presence of autoionizing resonances and for large IR intensities, provided that the whole spectrum (which occupied a limited energy region approximately 1 a.u. above the $1s$ threshold) was scaled by a constant factor $\mathcal{C}$, of the order of unity, which accounts for the known difference between the hydrogenic ionization cross section

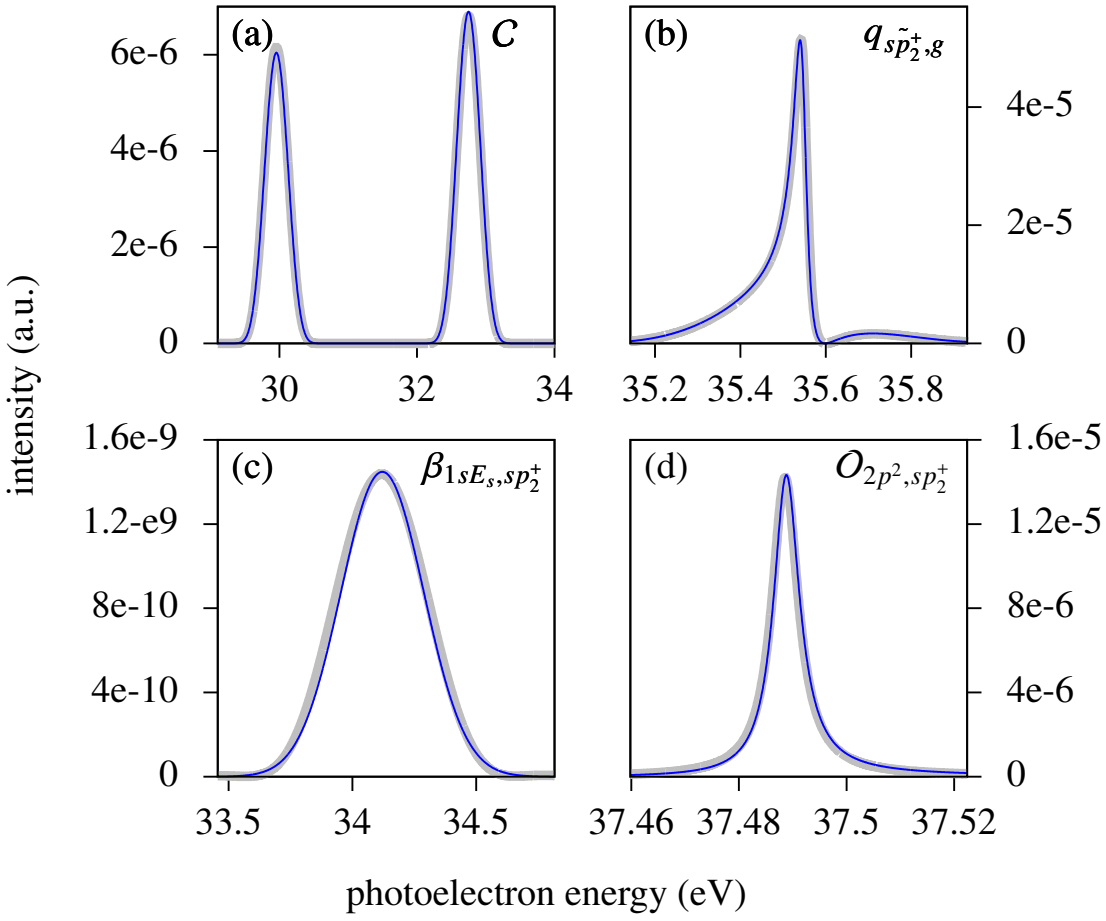

Figure 55: Photoelectron spectra obtained *ab initio* (thick gray solid line in the background) and with the model (thin black line in the foreground) for four different pulse sequences useful to calibrate the model parameters. a) non-resonant and b) resonant one-photon photoelectron spectrum obtained with using the XUV APT alone. The first spectrum (a) was used to determine the global scaling factor $\mathcal{C}$, while spectra like the one in (b) were used to confirm the parameters of the two $^1\mathrm{P}^o$ autoionizing state. c) from the lower sideband of the sp_2^+ resonance generated with disjoint pump and probe pulses, we could estimate the resonance-continuum β radiative couplings. d) from the resonant shape of the sp_2^+ state upper sideband, which strikes the $2p^2\ ^1\mathrm{S}^e$ state, we could determine the resonance-resonance dipolar coupling.

and the one predicted by the first Born approximation. Since we are currently considering the same region of the photoelectron spectrum, it is justified to estimate the continuum-continuum couplings $\bar{\mathcal{O}}_{1sE_\ell,1sE_p}$ within the soft-photon approximation, further reducing the total number of free parameters to 9.

To determine the values of these parameters, and to subsequently verify the prediction of the model against reliable benchmarks, we carried out accurate *ab initio* simulations. In the simulations, both the XUV APT and the IR probe have a duration (fwhm) of 6 fs, while their peak intensity is $I_{\mathrm{XUV}} = 5$ GW/cm^2 and $I_{\mathrm{IR}} = 10$ GW/cm^2, respectively. The individual attosecond pulses in the train have central energy $\omega_{\mathrm{XUV}} = 57$ eV and a duration of 250 as; consecutive pulses are separated by half the nominal IR period, $T_{\mathrm{IR}} = 2\pi/\omega_{\mathrm{IR}}$. As we are particularly interested in the transition that, through the sp_2^+ and sp_3^+ ($^1P^o$) DESs, populates the optically forbidden $2p^2$ ($^1S^e$) DES, we performed simulations for IR frequencies ranging from $\omega_{\mathrm{IR}} = 1.455$ eV to $\omega_{\mathrm{IR}} = 1.485$ eV.

Using the XUV APT alone, we could determine the value of the scaling constant $\mathcal{C}$ to match the non-resonant background of the model to that of the *ab initio* prediction (which agrees with the absolute value of the background photoionization cross section reported in the literature). With $\mathcal{C} = 1.2$, the model and *ab initio* backgrounds are in excellent agreement across an energy domain of $\sim 4\omega_{IR}$ (see Fig. 55a). From the one-photon spectrum in the energy region where the sp_2^+ and sp_3^+ resonances are present, we determined position, width and q parameter for the two autoionizing states: $\bar{E}_{sp_2^+} = -18.86$ eV, $\Gamma_{sp_2^+} = 0.037$ eV, $q_{\tilde{sp_2^+ g}} = -2.77$, $\bar{E}_{sp_3^+} = -15.34$ eV, $\Gamma_{sp_3^+} = 0.0082$ eV, $q_{\tilde{sp_3^+ g}} = -2.58$ (see Fig. 55b), in agreement with the values reported in the literature [133].

We obtain the parameters $\beta_{1sE_\ell, sp_{2/3}^+}$ from the *ab initio* background spectrum, resolved with respect to the orbital angular momentum ℓ, of the two intermediate resonances for a time delay at which the pump and the probe pulses do not overlap since, as we already saw in the Sec. 4.4.2.2, in this way the homogeneous contribution of the intermediate state vanishes. Notice that one could retrieve the same parameters also from the experiment by measuring the photoelectron spectrum at two different ejection angles. We determine both $\beta_{1sE_p, 2p^2}$ and $\gamma_{\tilde{2p^2} \leftarrow 1s2p \leftarrow 1s^2}$ by matching the parameters of the asymmetric resonant profile in the two-photon excitation of $2p^2$ with a pair of overlapping pump and probe pulses in which the harmonics are tuned out of resonance with respect to the intermediate autoionizing states. Finally, to determine $q_{sp_{2/3}^+, 2p^2}$, we look at the $2p^2$ resonant profile in the sideband of the *ab initio* spectrum for non-overlapping APT and IR probe pulses, where alternatively the lower and the upper harmonics are in resonance with the sp_2^+ and the sp_3^+ state, respectively.

In Table 5 we report the full list of the parameters that gave the best match with the *ab initio* spectra discussed above.

	$\bar{E}_a$	Γ_a	$q_{\tilde{a}}$	$\beta_{1sE_s, a}$	$\beta_{1sE_d, a}$
a=sp_2^+	-0.693	1.37[-3]	-2.77	-0.0003	-0.0003
a=sp_3^+	-0.564	3.01[-4]	-2.58	-0.003	-0.01

Table 5: Radiative parameters for the two-photon resonant transitions model in helium. Atomics units are used.

	$\bar{E}_b$	Γ_b	q_{b, sp_2^+}	q_{b, sp_3^+}	$\beta_{b, 1sE_p}$	$\gamma_{\tilde{b} \leftarrow 1s2p \leftarrow 1s^2}$
b=$2p^2$	-0.622	2.16[-4]	153	20	-0.003	4255

Notice that almost all the parameters of the model were determined independently of each other by comparison with a minimal number of well defined selected numerical experiments. Once these values are determined, the model can reproduce the photoelectron spectrum for several values of the IR frequency and pump-probe delay in the general case of partly overlapping pulses with multiple intermediate and one final resonant states, with no residual freedom to adjust the outcome.

D

THIRD ORDER CORRECTION FOR RESONANT MODEL

To reproduce the beating of harmonic signals in RABITT spectroscopy, it is necessary to extend the perturbative expansion to third order. The contribution from the Feynman diagram for the exchange of photons 1, 2, and 3 is

$$\mathcal{A}^{(3)}_{\gamma E,g} = \frac{-i}{\sqrt{2\pi}} \iint \tilde{F}_3(\omega_{fg} - \omega'_1 - \omega'_2)\tilde{F}_2(\omega'_2)\tilde{F}_1(\omega'_1)d\omega'_1 d\omega'_2 \mathcal{M}^{(3)}_{\gamma E,g}(\omega'_1, \omega'_2).$$

We will consider only the paths in which the XUV photon is exchanged first, and the exchange of the sidebands are non resonant.

$$\begin{aligned}\mathcal{M}^{(3)}_{\gamma E,g} &= \langle \psi_{\gamma E}|\mathcal{O}G_0^+(E_g + \omega'_1 + \omega'_2)\mathcal{O}G_0^+(E_g + \omega'_1)\mathcal{O}|g\rangle = \\ &= \int d\varepsilon \frac{\langle \psi_{\gamma E}|\mathcal{O}|\beta\varepsilon\rangle\langle\beta\varepsilon|\mathcal{O}G_0^+(E_g + \omega'_1)\mathcal{O}|g\rangle}{E_g + \omega'_1 + \omega'_2 - \varepsilon + i0^+}.\end{aligned}$$

This first factor in the integrand numerator is a continuum-continuum dipole transition between a resonant and a non-resonant continuum,

$$\begin{aligned}\langle \psi_{\gamma E}|\mathcal{O}|\beta\varepsilon\rangle &= \bar{\mathcal{O}}_{\gamma\beta}\delta(E-\varepsilon) + \\ &+ \frac{1}{\pi}\left(\frac{\mathcal{O}_{c,\beta\varepsilon}}{V_{c,\gamma E}} - \frac{\bar{\mathcal{O}}_{\gamma\beta}}{\varepsilon - E + i0^+}\right)\frac{1}{\epsilon_{Ec} - i'},\end{aligned} \tag{D.1}$$

while the second factor is a two-photon transition matrix element from the ground to a flat continuum, with an intermediate resonance [compare with Eq. (4.89)],

$$\begin{aligned}\mathcal{M}^{(c)}_{\beta\varepsilon,g}(\omega'_1) &= \frac{\epsilon_{\varepsilon a} + q_{\tilde{a}g}}{\epsilon_{\varepsilon a} + i}\frac{\bar{\mathcal{O}}_{\beta\alpha}\mathcal{O}_{\alpha,g}}{E_g + \omega'_1 - \varepsilon + i0^+} + \\ &+ \left(\beta_a - \frac{1}{\epsilon_{\varepsilon a} + i}\right)(q_{\tilde{a}g} - i)\frac{\bar{\mathcal{O}}_{\beta\alpha}\mathcal{O}_{\alpha,g}}{\omega'_1 - \omega_{\tilde{a}g}}\end{aligned} \tag{D.2}$$

$$
\begin{aligned}
\mathcal{M}^{(3)}_{\gamma E,g} = &\left[\frac{\epsilon_{Ea}+q_{\tilde{a}g}}{\epsilon_{Ea}+i}\frac{\bar{\mathcal{O}}_{\beta\alpha}\mathcal{O}_{\alpha,g}}{E_g+\omega_1'-E+i0^+}+\left(\beta_a-\frac{1}{\epsilon_{Ea}+i}\right)(q_{\tilde{a}g}-i)\frac{\bar{\mathcal{O}}_{\beta\alpha}\mathcal{O}_{\alpha,g}}{\omega_1'-\omega_{\tilde{a}g}}\right]\times\\
&\times\frac{\bar{\mathcal{O}}_{\gamma\beta}}{E_g+\omega_1'+\omega_2'-\varepsilon+i0^+}+\\
&+\frac{1}{\pi}\frac{1}{\epsilon_{Ec}-i}\frac{\mathcal{O}_{c,\beta E}}{V_{c,\gamma E}}\bar{\mathcal{O}}_{\beta\alpha}\mathcal{O}_{\alpha,g}\int d\varepsilon\frac{1}{E_g+\omega_1'-\varepsilon+i0^+}\frac{1}{E_g+\omega_1'+\omega_2'-\varepsilon+i0^+}+\\
&+\frac{1}{\pi}\frac{q_{\tilde{a}g}-i}{\epsilon_{Ec}-i}\frac{\mathcal{O}_{c,\beta E}}{V_{c,\gamma E}}\bar{\mathcal{O}}_{\beta\alpha}\mathcal{O}_{\alpha,g}\int d\varepsilon\frac{1}{\epsilon_{\varepsilon a}+i}\frac{1}{E_g+\omega_1'-\varepsilon+i0^+}\frac{1}{E_g+\omega_1'+\omega_2'-\varepsilon+i0^+}+\\
&+\frac{1}{\pi}\frac{q_{\tilde{a}g}-i}{\epsilon_{Ec}-i}\frac{\mathcal{O}_{c,\beta E}}{V_{c,\gamma E}}\frac{\bar{\mathcal{O}}_{\beta\alpha}\mathcal{O}_{\alpha,g}}{\omega_1'-\omega_{\tilde{a}g}}\beta_a\int d\varepsilon\frac{1}{E_g+\omega_1'+\omega_2'-\varepsilon+i0^+}-\\
&-\frac{1}{\pi}\frac{q_{\tilde{a}g}-i}{\epsilon_{Ec}-i}\frac{\mathcal{O}_{c,\beta E}}{V_{c,\gamma E}}\frac{\bar{\mathcal{O}}_{\beta\alpha}\mathcal{O}_{\alpha,g}}{\omega_1'-\omega_{\tilde{a}g}}\int d\varepsilon\frac{1}{\epsilon_{\varepsilon a}+i}\frac{1}{E_g+\omega_1'+\omega_2'-\varepsilon+i0^+}-\\
&-\frac{1}{\pi}\frac{\bar{\mathcal{O}}_{\gamma\beta}\bar{\mathcal{O}}_{\beta\alpha}\mathcal{O}_{\alpha,g}}{\epsilon_{Ec}-i}\int d\varepsilon\frac{1}{\varepsilon-E+i0^+}\frac{1}{E_g+\omega_1'-\varepsilon+i0^+}\frac{1}{E_g+\omega_1'+\omega_2'-\varepsilon+i0^+}-\\
&-\frac{1}{\pi}\frac{\bar{\mathcal{O}}_{\gamma\beta}\bar{\mathcal{O}}_{\beta\alpha}\mathcal{O}_{\alpha,g}}{\epsilon_{Ec}-i}(q_{\tilde{a}g}-i)\int d\varepsilon\frac{1}{\varepsilon-E+i0^+}\frac{1}{\epsilon_{\varepsilon a}+i}\frac{1}{E_g+\omega_1'-\varepsilon+i0^+}\frac{1}{E_g+\omega_1'+\omega_2'-\varepsilon+i0^+}-\\
&-\frac{1}{\pi}\frac{\bar{\mathcal{O}}_{\gamma\beta}\bar{\mathcal{O}}_{\beta\alpha}\mathcal{O}_{\alpha,g}}{\epsilon_{Ec}-i}\frac{q_{\tilde{a}g}-i}{\omega_1'-\omega_{\tilde{a}g}}\beta_a\int d\varepsilon\frac{1}{\varepsilon-E+i0^+}\frac{1}{E_g+\omega_1'+\omega_2'-\varepsilon+i0^+}+\\
&+\frac{1}{\pi}\frac{\bar{\mathcal{O}}_{\gamma\beta}\bar{\mathcal{O}}_{\beta\alpha}\mathcal{O}_{\alpha,g}}{\epsilon_{Ec}-i}\frac{q_{\tilde{a}g}-i}{\omega_1'-\omega_{\tilde{a}g}}\int d\varepsilon\frac{1}{\varepsilon-E+i0^+}\frac{1}{\epsilon_{\varepsilon a}+i}\frac{1}{E_g+\omega_1'+\omega_2'-\varepsilon+i0^+}.
\end{aligned}
$$

$$
\begin{aligned}
\mathcal{M}^{(3)}_{\gamma E,g} &= \frac{\epsilon_{Ec}+i}{\epsilon_{Ec}-i}\frac{\epsilon_{Ea}+q_{\tilde{a}g}}{\epsilon_{Ea}+i}\frac{1}{E_g+\omega_1'-E+i0^+}\frac{\bar{\mathcal{O}}_{\gamma\beta}\bar{\mathcal{O}}_{\beta\alpha}\mathcal{O}_{\alpha,g}}{E_g+\omega_1'+\omega_2'-E+i0^+}+\\
&+\frac{\epsilon_{Ec}+i}{\epsilon_{Ec}-i}\left(\beta_a-\frac{1}{\epsilon_{Ea}+i}\right)\frac{q_{\tilde{a}g}-i}{\omega_1'-\omega_{\tilde{a}g}}\frac{\bar{\mathcal{O}}_{\gamma\beta}\bar{\mathcal{O}}_{\beta\alpha}\mathcal{O}_{\alpha,g}}{E_g+\omega_1'+\omega_2'-E+i0^+}-\\
&-i\frac{q_{\tilde{a}g}-i}{\epsilon_{Ec}-i}\frac{\mathcal{O}_{c,\beta E}}{V_{c,\gamma E}}\frac{\bar{\mathcal{O}}_{\beta\alpha}\mathcal{O}_{\alpha,g}}{\omega_1'-\omega_{\tilde{a}g}}\beta_a.
\end{aligned}
$$

$$
\begin{aligned}
\mathcal{M}^{(3)}_{\gamma E,g}(\omega_1',\omega_2') &= \frac{\epsilon_{Ec}+i}{\epsilon_{Ec}-i}\frac{\epsilon_{Ea}+q_{\tilde{a}g}}{\epsilon_{Ea}+i}\frac{\bar{\mathcal{O}}_{\gamma\beta}\bar{\mathcal{O}}_{\beta\alpha}\mathcal{O}_{\alpha,g}}{\omega_2'}\frac{1}{E_g+\omega_1'-E+i0^+}-\\
&-\frac{\epsilon_{Ec}+i}{\epsilon_{Ec}-i}\frac{\epsilon_{Ea}+q_{\tilde{a}g}}{\epsilon_{Ea}+i}\frac{\bar{\mathcal{O}}_{\gamma\beta}\bar{\mathcal{O}}_{\beta\alpha}\mathcal{O}_{\alpha,g}}{\omega_2'}\frac{1}{E_g+\omega_1'+\omega_2'-E+i0^+}+\\
&+\frac{\epsilon_{Ec}+i}{\epsilon_{Ec}-i}\left(\beta_a-\frac{1}{\epsilon_{Ea}+i}\right)(q_{\tilde{a}g}-i)\frac{1}{\tilde{E}_a+\omega_2'-E}\frac{\bar{\mathcal{O}}_{\gamma\beta}\bar{\mathcal{O}}_{\beta\alpha}\mathcal{O}_{\alpha,g}}{\omega_1'-\omega_{\tilde{a}g}}-\\
&-\frac{\epsilon_{Ec}+i}{\epsilon_{Ec}-i}\left(\beta_a-\frac{1}{\epsilon_{Ea}+i}\right)(q_{\tilde{a}g}-i)\frac{1}{\tilde{E}_a+\omega_2'-E}\frac{\bar{\mathcal{O}}_{\gamma\beta}\bar{\mathcal{O}}_{\beta\alpha}\mathcal{O}_{\alpha,g}}{E_g+\omega_1'+\omega_2'-E+i0^+}-\\
&-i\frac{q_{\tilde{a}g}-i}{\epsilon_{Ec}-i}\frac{\mathcal{O}_{c,\beta E}}{V_{c,\gamma E}}\frac{\bar{\mathcal{O}}_{\beta\alpha}\mathcal{O}_{\alpha,g}}{\omega_1'-\omega_{\tilde{a}g}}\beta_a.
\end{aligned}
$$

We can considerably simplify this expression if we replace the non-resonant denominators with their nominal values,

$$\begin{aligned}\mathcal{M}^{(3)}_{\gamma E,g}(\omega_1';\omega_2,\omega_3) &\simeq \frac{\epsilon_{Ec}+i}{\epsilon_{Ec}-i}\frac{\bar{\mathcal{O}}_{\gamma\beta}\bar{\mathcal{O}}_{\beta\alpha}\mathcal{O}_{\alpha,g}}{\omega_2\omega_3}\left[\frac{\epsilon_{Ea}+q_{\tilde{a}g}}{\epsilon_{Ea}+i}\left(\frac{\omega_3}{E_g+\omega_1'-E+i0^+}+1\right)-\right.\\ &- \left(\beta_a-\frac{1}{\epsilon_{Ea}+i}\right)(q_{\tilde{a}g}-i)\frac{\omega_2}{\omega_1-\omega_{\tilde{a}g}+\omega_3}\left(\frac{\omega_3}{\omega_1'-\omega_{\tilde{a}g}}+1\right)-\\ &- \left.\frac{q_{\tilde{a}g}-i}{\epsilon_{Ec}+i}i\phi_{ca}\frac{\omega_3}{\omega_1'-\omega_{\tilde{a}g}}\right],\end{aligned}$$

where we defined

$$\phi_{ca}=\frac{\omega_2\beta_a\mathcal{O}_{c,\beta E}}{V_{c,\gamma E}\bar{\mathcal{O}}_{\gamma\beta}}. \tag{D.3}$$

Now the frequency integral can be done exactly.

In particular, the integrand does not depend on ω_2' anymore, as one could expect on the basis that the exchange of the two last photons is consecutive and does not involve intermediate resonances.

$$\begin{aligned}\mathcal{A}^{(3)}_{\gamma E,g} &\approx \frac{-i}{\sqrt{2\pi}}\int\tilde{F}_1(\omega_1')\mathcal{M}^{(3)}_{\gamma E,g}(\omega_1';\omega_2,\omega_3)d\omega_1'\times\\ &\times \int\tilde{F}_3(\omega_{fg}-\omega_1'-\omega_2')\tilde{F}_2(\omega_2')d\omega_2'=\\ &= -i\int\tilde{F}_1(\omega_1')\widetilde{F_2F_3}(\omega_{fg}-\omega_1')\mathcal{M}^{(3)}_{\gamma E,g}(\omega_1';\omega_2,\omega_3)d\omega_1'.\end{aligned} \tag{D.4}$$

where in the last passage we made use of the convolution theorem.

The product of the two pulses $F_2F_3(t)$ is written as

$$\begin{aligned}&F_2F_3(t)=\frac{F_{02}F_{03}}{2}e^{-\frac{\sigma_2^2+\sigma_3^2}{2}(t-t_0)^2}\times\\ &\times\left\{\cos\left[(\omega_2+\omega_3)(t-t_0)+(\varphi_2+\varphi_3)\right]+\right.\\ &\left.+\cos\left[(\omega_2-\omega_3)(t-t_0)+(\varphi_2-\varphi_3)\right]\right\},\end{aligned} \tag{D.5}$$

and its Fourier transform is

$$\begin{aligned}&\widetilde{F_2F_3}(\omega)=\frac{F_{02}F_{03}}{4\sqrt{\sigma_2^2+\sigma_3^2}}\times\\ &\left\{e^{i[\omega t_0-\varphi_2\mathrm{sgn}(\omega_2)-\varphi_3\mathrm{sgn}(\omega_3)]}e^{-\frac{(\omega-\omega_2-\omega_3)^2}{2(\sigma_2^2+\sigma_3^2)}}\right\},\end{aligned} \tag{D.6}$$

where the frequencies ω_2 and ω_3 can be positive or negative, corresponding to photon absorption or emission, respectively. The third order amplitude (D.4) can now be readily computed, and it reads

$$\begin{aligned}\mathcal{A}^{(3)}_{\gamma E_g} \approx & \frac{\epsilon_{Ec}+i}{\epsilon_{Ec}-i}\frac{\bar{\mathcal{O}}_{\gamma\beta}\bar{\mathcal{O}}_{\beta\alpha}\mathcal{O}_{\alpha,g}}{\omega_2\omega_3}\mathcal{F}^{321}(\tau)e^{i(\omega_2+\omega_3)\tau}\left[\frac{\epsilon_{Ea}+q_{\tilde{a}g}}{\epsilon_{Ea}+i}\left(\omega_3\, w(z_E^{321})+\sqrt{\frac{2}{\pi}}\frac{i}{\sigma_{t(3)}}\right)-\right.\\ & -\left(\beta_a-\frac{1}{\epsilon_{Ea}+i}\right)(q_{\tilde{a}g}-i)\frac{\omega_2}{\omega_1-\omega_{\tilde{a}g}+\omega_3}\left(\omega_3\, w(z^{321}_{\tilde{E}_a})+\sqrt{\frac{2}{\pi}}\frac{i}{\sigma_{t(3)}}\right)+\\ & \left.-\ i\frac{q_{\tilde{a}g}-i}{\epsilon_{Ec}+i}\phi_{ca}\omega_3\, w(z^{321}_{\tilde{E}_a})\right],\end{aligned}$$

where we defined the form factor for the three-photon sequence [compare with (4.63)]

$$\begin{aligned}\mathcal{F}^{321} = & -\pi\frac{A_1A_2A_3}{8\sigma_1\sqrt{\sigma_2^2+\sigma_3^2}}e^{-[\varphi_1\mathrm{sgn}(\omega_1)+\varphi_2\mathrm{sgn}(\omega_2)+\varphi_3\mathrm{sgn}(\omega_3)]}\times\\ & \times\exp\left[-\frac{1}{2}\left(\frac{\delta^2_{(3)}}{\sigma^2_{(3)}}+\frac{\tau^2}{\sigma^2_{t(3)}}+2i\frac{\sqrt{\sigma_2^2+\sigma_3^2}}{\sigma_1}\frac{\delta_{(3)}}{\sigma_{(3)}}\frac{\tau}{\sigma_{t(3)}}\right)\right],\end{aligned}\tag{D.7}$$

with $\sigma_{(3)}=\sqrt{\sigma_1^2+\sigma_2^2+\sigma_3^2}$, $\sigma_{t(3)}=\sqrt{\sigma_1^{-2}+(\sigma_2^2+\sigma_3^2)^{-1}}$ and $\delta_{(3)}=E_g+\omega_1+\omega_2+\omega_3-E$, and the complex parameter z_E^{321} as

$$z_E^{321}=\frac{\sigma_{t(3)}}{\sqrt{2}}\left[\left(\omega_1-\frac{\sigma_1^2}{\sigma^2_{(3)}}\delta_{(3)}-i\frac{\tau}{\sigma^2_{t(3)}}\right)-E+E_g\right].\tag{D.8}$$

BIBLIOGRAPHY

[1] J. Seres, E. Seres, A. J. Verhoef, G. Tempea, C. Streli, P. Wobrauschek, V. Yakovlev, A. Scrinzi, C. Spielmann, and F. Krausz. Laser technology: Source of coherent kiloelectronvolt x-rays. *Nature*, 433(7026):596–596, 02 2005. URL http://dx.doi.org/10.1038/433596a.

[2] A. H. Zewail. 4d ultrafast electron diffraction, crystallography, and microscopy. *Annual Review of Physical Chemistry*, 57(1):65–103, 2006. doi: 10.1146/annurev.physchem.57.032905.104748. URL http://dx.doi.org/10.1146/annurev.physchem.57.032905.104748. PMID: 16599805.

[3] F. Krausz and M. Ivanov. Attosecond physics. *Rev. Mod. Phys.*, 81(1):163–234, February 2009. ISSN 0034-6861. doi: 10.1103/RevModPhys.81.163. URL http://link.aps.org/doi/10.1103/RevModPhys.81.163.

[4] A. Einstein. On a heuristic point of view about the creation and conversion of light. *Annalen der Physik*, 17:132–148, 1905.

[5] Synchrotron Soleil. URL http://www.synchrotron-soleil.fr/portal/page/portal/SourceAccelerateur.

[6] A. T. J. B. Eppink and D. H. Parker. Velocity map imaging of ions and electrons using electrostatic lenses: Application in photoelectron and photofragment ion imaging of molecular oxygen. *Rev. Sci. Instrum.*, 68:3477–3484, 1997.

[7] J. Ullrich, R. Moshammer, A. Dorn, R. Dörner, L. Ph. H. Schmidt, and H. Schmidt-Böcking. Recoil-ion and electron momentum spectroscopy: reaction-microscopes. *Rep. Prog. Phys.*, 66(9):1463–1545, September 2003. ISSN 0034-4885. doi: 10.1088/0034-4885/66/9/203. URL http://stacks.iop.org/0034-4885/66/i=9/a=203?key=crossref.4f0ed0c11253bbad6096727290d95871.

[8] P. O'Keeffe, V. Feyer, P. Bolognesi, M. Coreno, C. Callegari, G. Cautero, a. Moise, K. C. Prince, R. Richter, R. Sergo, M. Alagia, M. de Simone, a. Kivimäki, M. Devetta, T. Mazza, P. Piseri, V. Lyamayev, R. Katzy, F. Stienkemeier, Y. Ovcharenko, T. Möller, and L. Avaldi. A velocity map imaging apparatus for gas phase studies at FERMI@Elettra. *Nuclear Instruments and Methods in Physics Research Section B: Beam Interactions with Materials and Atoms*, 284:69–73, August 2012. ISSN 0168583X. doi: 10.1016/j.nimb.2011.07.020. URL http://linkinghub.elsevier.com/retrieve/pii/S0168583X11006641.

[9] A. Matsuda, M. Fushitani, C. Tseng, Y. Hikosaka, J. Eland, and A. Hishikawa. A magnetic-bottle multi-electron-ion coincidence spectrometer. *Rev.Sci.Instrum.*, 82(10):103–105, 2011.

[10] R. Madden and K. Codling. New autoionizing atomic energy levels in He, Ne, and Ar. *Phys. Rev. Lett.*, 10(12):516–518, June 1963. ISSN 0031-9007. doi: 10.1103/PhysRevLett.10.516. URL http://link.aps.org/doi/10.1103/PhysRevLett.10.516.

[11] J. J. Wynne and J. P. Hermann. Spectroscopy of even-parity autoionizing levels in ba. *Opt. Lett.*, 4(4):106–108, Apr 1979. doi: 10.1364/OL.4.000106. URL http://ol.osa.org/abstract.cfm?URI=ol-4-4-106.

[12] W. E. Cooke, T. F. Gallagher, S. A. Edelstein, and R. M. Hill. Doubly excited autoionizing rydberg states of sr. *Phys. Rev. Lett.*, 40:178–181, Jan 1978. doi: 10.1103/PhysRevLett.40.178. URL http://link.aps.org/doi/10.1103/PhysRevLett.40.178.

[13] P. Lambropoulos and P. Zöller. Autoionizing states in strong laser fields. *Phys. Rev. A*, 24(1), 1981.

[14] P. F. Moulton. Spectroscopic and laser characteristics of Ti:Al_2 O_3. *J.Opt.Soc.Am.B*, 3(1):125–133, 1986.

[15] P.A. Franken, A.E. Hill, C.W. Peters, and G. Weinreich. Generation of optical harmonics. *Phys.Rev.Lett.*, 7(1):118–120, 1961.

[16] P. B. Corkum. Plasma perspective on strong-field multiphoton ionization. *Phys. Rev. Lett.*, 71(13):1994–1997, 1993.

[17] R. Kienberger, E. Goulielmakis, M. Uiberacker, A. Baltuska, V. Yakovlev, F. Bammer, A. Scrinzi, Th. Westerwalbesloh, U. Kleineberg, U Heinzmann, M Drescher, and F. Krausz. Atomic transient recorder. *Nature*, 427:817–821, 2004.

[18] E. Goulielmakis, M. Schultze, M. Hofstetter, V. S. Yakovlev, J. Gagnon, M. Uiberacker, A. L. Aquila, E. M. Gullikson, D. T. Attwood, R. Kienberger, F. Krausz, and U. Kleineberg. Single-cycle nonlinear optics. *Science*, 320 (5883):1614–7, June 2008. ISSN 1095-9203. doi: 10.1126/science.1157846. URL http://www.ncbi.nlm.nih.gov/pubmed/18566281.

[19] G. Sansone, E. Benedetti, F. Calegari, C. Vozzi, L. Avaldi, R. Flammini, L. Poletto, P. Villoresi, C. Altucci, R. Velotta, S. Stagira, S. De Silvestri, and M. Nisoli. Isolated single-cycle attosecond pulses. *Science*, 314(5798): 443–6, October 2006. ISSN 1095-9203. doi: 10.1126/science.1132838. URL http://www.ncbi.nlm.nih.gov/pubmed/17053142.

[20] R. Trebino, K. W. DeLong, D. N. Fittinghoff, J. N. Sweetser, M. A. Krumbügel, B. A. Richman, and D. J. Kane. Measuring ultrashort laser pulses in the time-frequency domain using frequency-resolved optical gating. *Rev.Sci.Instrum.*, 68(9):3277–3295, 1997.

[21] P. M. Paul, E. S. Toma, P. Breger, G. Mullot, F. Auge, P. Balcou, H. G Muller, and P. Agostini. doi: 10.1126/science.1059413.

[22] P. Agostini and L. F. DiMauro. The physics of attosecond light pulses. *Rep. Prog. Phys.*, 67(6):813–855, June 2004. ISSN 0034-4885. doi: 10.1088/0034-4885/67/6/R01. URL http://stacks.iop.org/0034-4885/67/i=6/a=R01?key=crossref.387405b965aa7674e3634f3ed96f47ba.

[23] A. H. Zewail. Four-dimensional electron microscopy. *Science*, 328(5975): 187–93, April 2010. ISSN 1095-9203. doi: 10.1126/science.1166135. URL http://www.ncbi.nlm.nih.gov/pubmed/20378810.

[24] A. Vredenborg, C.S. Lehmann, D. Irimia, W.G. Roeterdink, and M.H.M. Janssen. The reaction microscope: imaging and pulse shaping control in photodynamics. *Chem.Phys.Chem.*, 12, 2011.

[25] R. Saha and V. S Batista. Tunneling under coherent control by sequences of unitary pulses. *J. Phys. Chem. B*, 115(18):5234–42, May 2011. ISSN 1520-5207. doi: 10.1021/jp108331x. URL http://www.ncbi.nlm.nih.gov/pubmed/21384933.

[26] V. Véniard, R. Taïeb, and A. Maquet. Phase dependence of $(N+1)$-color $(N>1)$ ir-uv photoionization of atoms with higher harmonics. *Phys. Rev. A*, 54(1):721–728, July 1996. ISSN 1050-2947. URL http://www.ncbi.nlm.nih.gov/pubmed/9913529.

[27] A. L'Huillier and P. Balcou. High-order harmonic generation in rare gases with a 1-ps 1053-nm laser. *Phys. Rev. Lett.*, 70(6):774–777, 1993.

[28] J. M. Dahlström, A. L'Huillier, and J. Mauritsson. Quantum mechanical approach to probing the birth of attosecond pulses using a two-color field. *J. Phys. B: At. Mol. Opt. Phys.*, 44(9):1291v1, May 2011. ISSN 0953-4075. doi: 10.1088/0953-4075/44/9/095602. URL http://stacks.iop.org/0953-4075/44/i=9/a=095602?key=crossref.334e5b77a3af5bc95badfb6e83446f89.

[29] K. Varjú, P. Johnsson, Rodrigo López-Martens, T. Remetter, E. Gustafsson, Johan Mauritsson, Mette B. Gaarde, Kenneth J. Schafer, Ch Erny, I. J. Sola, A. Zaïr, Eric Constant, Eric Cormier, E. Mével, and Anne L'Huillier. Experimental Studies of Attosecond Pulse Trains. *Laser Physics*, 15(6):888–898, 2005.

[30] Y. Mairesse, A. de Bohan, L. J. Frasinski, H. Merdji, L. C. Dinu, P. Monchicourt, P. Breger, M. Kovacev, R. Taïeb, B. Carré, H. G. Muller, P. Agostini, and P. Salières. Attosecond synchronization of high-harmonic soft x-rays. *Science (New York, N.Y.)*, 302(5650):1540–3, November 2003. ISSN 1095-9203. doi: 10.1126/science.1090277. URL http://www.ncbi.nlm.nih.gov/pubmed/14645841.

[31] J. Mauritsson, M. Gaarde, and K. Schafer. Accessing properties of electron wave packets generated by attosecond pulse trains through time-dependent calculations. *Physical Review A*, 72(1):013401, July 2005. ISSN 1050-2947. doi: 10.1103/PhysRevA.72.013401. URL http://link.aps.org/doi/10.1103/PhysRevA.72.013401.

[32] K. Klünder, J. M. Dahlström, M. Gisselbrecht, T. Fordell, M. Swoboda, D. Guénot, P. Johnsson, J. Caillat, J. Mauritsson, A. Maquet, R. Taïeb, and A. L'Huillier. Probing single-photon ionization on the attosecond time scale. *Phys. Rev. Lett.*, 106(14):143002, April 2011. ISSN 0031-9007. doi: 10.1103/PhysRevLett.106.143002. URL http://link.aps.org/doi/10.1103/PhysRevLett.106.143002.

[33] D. Guénot, K. Klünder, C. Arnold, D. Kroon, J. Dahlström, M. Miranda, T. Fordell, M. Gisselbrecht, P. Johnsson, J. Mauritsson, E. Lindroth, A. Maquet, R. Taïeb, A. L'Huillier, and A. Kheifets. Photoemission-time-delay measurements and calculations close to the 3s-ionization-cross-section minimum in Ar. *Phys. Rev. A*, 85(5):1–8, May 2012. ISSN 1050-2947. doi: 10.1103/PhysRevA.85.053424. URL http://link.aps.org/doi/10.1103/PhysRevA.85.053424.

[34] D. Guénot, D. Kroon, E. Balogh, E. W. Larsen, M. Kotur, M. Miranda, T. Fordell, P. Johnsson, J. Mauritsson, M. Gisselbrecht, K. Varjú, C. L. Arnold, T. Carette, A. S. Kheifets, E. Lindroth, A. L'Huillier, and J. M. Dahlström. Measurements of relative photoemission time delays in noble gas atoms. *J. Phys. B: At. Mol. Opt. Phys.*, 47(24):245602, December 2014. ISSN 0953-4075. doi: 10.1088/0953-4075/47/24/245602. URL http://stacks.iop.org/0953-4075/47/i=24/a=245602?key=crossref.e923488b0a9225bad269cddd1cc67c36.

[35] C. Palatchi, J. M. Dahlström, A. S. Kheifets, I. A. Ivanov, D. M. Canaday, P. Agostini, and L. F. DiMauro. Atomic delay in helium, neon, argon and krypton. *J. Phys. B: At. Mol. Opt. Phys.*, 47(24):245003, December 2014. ISSN 0953-4075. doi: 10.1088/0953-4075/47/24/245003. URL http://stacks.iop.org/0953-4075/47/i=24/a=245003?key=crossref.1d49b6738fcebde75585285d88cc03b2.

[36] E. P. Mansson, D. Guénot, C. L. Arnold, D. Kroon, S. Kasper, J. M. Dahlström, E. Lindroth, A. S. Kheifets, A. L'Huillier, S. L Sorensen, and M. Gisselbrecht. Double ionization probed on the attosecond timescale. *Nature Physics*, 10(3):207–211, January 2014. ISSN 1745-2473. doi: 10.1038/nphys2880. URL http://www.nature.com/doifinder/10.1038/nphys2880.

[37] F. Kelkensberg, W. Siu, J. F. Pérez-Torres, Felipe Morales, G. Gademann, Arnaud Rouzée, Per Johnsson, M. Lucchini, F. Calegari, José Luis Sanz-Vicario, Fernando Martín, and Marc J. J. Vrakking. Attosecond control in photoionization of hydrogen molecules. *Phys. Rev. Lett.*, 107(4):043002, July 2011. ISSN 0031-9007. doi: 10.1103/PhysRevLett.107.043002. URL http://link.aps.org/doi/10.1103/PhysRevLett.107.043002.

[38] X. Feng, S. Gilbertson, H. Mashiko, S. Khan, H. Wang, M. Chini, Y. Wu, and Z. Chang. Single Isolated Attosecond Pulses Generation with Double Optical Gating. *Chemical Physics*, 99:89–111, 2010.

[39] T. Remetter, P. Johnsson, J. Mauritsson, K. Varjú, Y. Ni, F. Lépine, E. Gustafsson, M. Kling, J. Khan, R. López-Martens, K. J. Schafer, M. J. J. Vrakking, and A. L'Huillier. Attosecond electron wave packet interferometry. *Nat.*

Phys., 2(5):323–326, April 2006. ISSN 1745-2473. doi: 10.1038/nphys290. URL http://www.nature.com/doifinder/10.1038/nphys290.

[40] S. Gilbertson, M. Chini, X. Feng, S. Khan, Y. Wu, and Z. Chang. Monitoring and controlling the electron dynamics in helium with isolated attosecond pulses. *Phys. Rev. Lett.*, 105:263003, Dec 2010. doi: 10.1103/PhysRevLett.105.263003. URL http://link.aps.org/doi/10.1103/PhysRevLett.105.263003.

[41] A. Palacios, A. GonzÃ¡lez-Castrillo, and F. Martín. Molecular interferometer to decode attosecond electron-nuclear dynamics. *PNAS*, 111(11):3973–3978, 2014. doi: 10.1073/pnas.1316762111. URL http://www.pnas.org/content/111/11/3973.abstract.

[42] M. Lein. Attosecond probing of vibrational dynamics with high-harmonic generation. *Phys. Rev. Lett.*, 94:053004, Feb 2005. doi: 10.1103/PhysRevLett.94.053004. URL http://link.aps.org/doi/10.1103/PhysRevLett.94.053004.

[43] S. Baker, J. S. Robinson, C. A. Haworth, H. Teng, R. A. Smith, C. C. Chirila, M. Lein, J. W. G. Tisch, and J. P. Marangos. Probing proton dynamics in molecules on an attosecond time scale. *Science*, 312(5772):424–427, 2006. doi: 10.1126/science.1123904. URL http://www.sciencemag.org/content/312/5772/424.abstract.

[44] O. Smirnova, Y. Mairesse, S. Patchkovskii, N. Dudovich, D. Villeneuve, P. Corkum, and M. Yu. Ivanov. High harmonic interferometry of multi-electron dynamics in molecules. *Nature*, 460(7258):972–977, 08 2009. URL http://dx.doi.org/10.1038/nature08253.

[45] S. Haessler, J. Caillat, W. Boutu, C. Giovanetti-Teixeira, T. Ruchon, T. Auguste, Z. Diveki, P. Breger, a. Maquet, B. Carré, R. Taïeb, and P. Salières. Attosecond imaging of molecular electronic wavepackets. *Nature Physics*, 6(3):200–206, January 2010. ISSN 1745-2473. doi: 10.1038/nphys1511. URL http://www.nature.com/doifinder/10.1038/nphys1511.

[46] Y. Mairesse, J. Higuet, N. Dudovich, D. Shafir, B. Fabre, E. Mével, E. Constant, S. Patchkovskii, Z. Walters, M. Yu. Ivanov, and O. Smirnova. High harmonic spectroscopy of multichannel dynamics in strong-field ionization. *Phys. Rev. Lett.*, 104:213601, May 2010. doi: 10.1103/PhysRevLett.104.213601. URL http://link.aps.org/doi/10.1103/PhysRevLett.104.213601.

[47] *Multielectron High Harmonic Generation: Simple Man on a Complex Plane*, pages 201–256. Wiley-VCH Verlag GmbH & Co. KGaA, 2014. ISBN 9783527677689. doi: 10.1002/9783527677689.ch7. URL http://dx.doi.org/10.1002/9783527677689.ch7.

[48] V. Sundstrom, P. M. Rentzepis, and M. L. Applebury. Kinetics of rhodospin at room temperature measured by picosecond spectroscopy. *Nature*, 267:645–646, 1977.

[49] M. Dantus, M. J. Rosker, and A. H. Zewail. Real-time femtosecond probing of transition states in chemical reactions. *J. Chem. Phys.*, 87(4), 1987.

[50] E. Goulielmakis, Z-H Loh, A. Wirth, R. Santra, N. Rohringer, V. S. Yakovlev, S. Zherebtsov, T. Pfeifer, A. M. Azzeer, M. F. Kling, S. R. Leone, and F. Krausz. Real-time observation of valence electron motion. *Nature*, 466 (7307):739–743, August 2010. ISSN 0028-0836. doi: 10.1038/nature09212. URL http://www.nature.com/doifinder/10.1038/nature09212.

[51] C. Ott, A. Kaldun, L. Argenti, P. Raith, K. Meyer, M. Laux, Y. Zhang, A. Blättermann, S. Hagstotz, T. Ding, R. Heck, J. Madroñero, F. Martín, and T. Pfeifer. Reconstruction and control of a time-dependent two-electron wave packet. *Nature*, 516(7531):374–378, December 2014. ISSN 0028-0836. doi: 10.1038/nature14026. URL http://www.nature.com/doifinder/10.1038/nature14026.

[52] U. Fano. Effects of configuration interaction on intensities and phase shifts. *Phys. Rev.*, 124:1866, 1961.

[53] M. Garnica, D. Stradi, S. Barja, F. Calleja, C. Diaz, M. Alcami, N. Martin, A. L. Vazquez de Parga, F. Martín, and R. Miranda. Long-range magnetic order in a purely organic 2d layer adsorbed on epitaxial graphene. *Nat Phys*, 9(6):368–374, 06 2013. URL http://dx.doi.org/10.1038/nphys2610.

[54] M. Wickenhauser, J. Burgdörfer, F. Krausz, and M. Drescher. Time resolved Fano resonances. *Phys. Rev. Lett.*, 94(2):023002, January 2005. ISSN 0031-9007. doi: 10.1103/PhysRevLett.94.023002. URL http://link.aps.org/doi/10.1103/PhysRevLett.94.023002.

[55] Z. Zhao and C. D. Lin. Theory of laser-assisted autoionization by attosecond light pulses. *Phys. Rev. A*, 71(6):060702, June 2005. ISSN 1050-2947. doi: 10.1103/PhysRevA.71.060702. URL http://link.aps.org/doi/10.1103/PhysRevA.71.060702.

[56] C. Ott, A. Kaldun, P. Raith, K. Meyer, M. Laux, J. Evers, C.H. Keitel, C.H. Greene, and T. Pfeifer. Lorentz meets Fano in spectral line shapes: a universal phase and its laser control. *Science*, 340:716–720, 2013.

[57] E. Wigner. Lower limit for the energy derivative of the scattering phase shift. *Phys. Rev.*, 98(1):145–147, April 1955. ISSN 0031-899X. doi: 10.1103/PhysRev.98.145. URL http://link.aps.org/doi/10.1103/PhysRev.98.145.

[58] M. Schultze, M. Fiess, N. Karpowicz, J. Gagnon, M. Korbman, M. Hofstetter, S. Neppl, a. L. Cavalieri, Y. Komninos, T. Mercouris, C. a. Nicolaides, R. Pazourek, S. Nagele, J. Feist, J. Burgdorfer, a. M. Azzeer, R. Ernstorfer, R. Kienberger, U. Kleineberg, E. Goulielmakis, F. Krausz, and V. S. Yakovlev. Delay in photoemission. *Science*, 328(5986):1658–1662, June 2010. ISSN 0036-8075. doi: 10.1126/science.1189401. URL http://www.sciencemag.org/cgi/doi/10.1126/science.1189401.

[59] J. Breidbach and L. Cederbaum. Universal attosecond response to the removal of an electron. *Phys. Rev. Lett.*, 94(3):033901, January 2005. ISSN 0031-9007. doi: 10.1103/PhysRevLett.94.033901. URL http://link.aps.org/doi/10.1103/PhysRevLett.94.033901.

[60] L. R. Moore, M. a. Lysaght, J. S. Parker, H. W. van der Hart, and K. T. Taylor. Time delay between photoemission from the 2p and 2s subshells of neon. *Phys. Rev. A*, 84(6):061404, December 2011. ISSN 1050-2947. doi: 10.1103/PhysRevA.84.061404. URL http://link.aps.org/doi/10.1103/PhysRevA.84.061404.

[61] M. Sabbar, S. Heuser, R. Boge, M. Lucchini, T. Carette, E. Lindroth, L. Gallmann, C. Cirelli, and U. Keller. Resonance effects in photoemission time delays. *Phys. Rev. Lett.*, 115:133001, Sep 2015. doi: 10.1103/PhysRevLett.115.133001. URL http://link.aps.org/doi/10.1103/PhysRevLett.115.133001.

[62] S. Sukiasyan, K. L. Ishikawa, and M. Ivanov. Attosecond cascades and time delays in one-electron photoionization. *Phys. Rev. A*, 86(3):033423, September 2012. ISSN 1050-2947. doi: 10.1103/PhysRevA.86.033423. URL http://link.aps.org/doi/10.1103/PhysRevA.86.033423.

[63] R. Pazourek, J. Feist, S. Nagele, and J. Burgdörfer. Attosecond streaking of correlated two-electron transitions in helium. *Phys. Rev. Lett.*, 108(16):163001, April 2012. ISSN 0031-9007. doi: 10.1103/PhysRevLett.108.163001. URL http://link.aps.org/doi/10.1103/PhysRevLett.108.163001.

[64] S. Nagele, R. Pazourek, J. Feist, K. Doblhoff-Dier, C. Lemell, K. Tőkési, and J. Burgdörfer. Time-resolved photoemission by attosecond streaking: extraction of time information. *Journal of Physics B: Atomic, Molecular and Optical Physics*, 44(8):081001, April 2011. ISSN 0953-4075. doi: 10.1088/0953-4075/44/8/081001. URL http://stacks.iop.org/0953-4075/44/i=8/a=081001?key=crossref.c56d1467cb7f685278df1f53ffd231b7.

[65] A. Zielinski, V. P. Majety, S. Nagele, R. Pazourek, J. Burgdörfer, and A. Scrinzi. Anomalous Fano Profiles in strong fields. *arXiv [physics.atom-ph]*, 14(05):4279, 2014.

[66] L. Argenti and E. Lindroth. Ionization branching ratio control with a resonance attosecond clock. *Phys. Rev. Lett.*, 105(5):053002, July 2010. ISSN 0031-9007. doi: 10.1103/PhysRevLett.105.053002. URL http://link.aps.org/doi/10.1103/PhysRevLett.105.053002.

[67] A. Maquet and R. TaÏeb. Two-colour IR + XUV spectroscopies: the soft-photon approximation. *J. Mod. Opt.*, 54(13-15):1847–1857, September 2007. ISSN 0950-0340. doi: 10.1080/09500340701306751. URL http://www.tandfonline.com/doi/abs/10.1080/09500340701306751.

[68] Christian Ott, Andreas Kaldun, Philipp Raith, Kristina Meyer, Martin Laux, Yizhu Zhang, Steffen Hagstotz, Thomas Ding, Robert Heck, and Thomas Pfeifer. Quantum Interferometry and Correlated Two-Electron Wave-Packet Observation in Helium. *arXiv:1205.0519v1 [physics.atom-ph]*, 2012. URL http://arxiv.org/abs/1211.2566.

[69] Á. Jiménez Galán, L. Argenti, and F. Martín. The soft-photon approximation in infrared-laser-assisted atomic ionization by extreme-ultraviolet attosecond-pulse trains. *New J. Phys.*, 15(11):113009,

November 2013. ISSN 1367-2630. doi: 10.1088/1367-2630/15/11/113009. URL http://stacks.iop.org/1367-2630/15/i=11/a=113009?key=crossref.902ef5dc3421f8715465c1e75e104dd1.

[70] Á. Jiménez Galán, L. Argenti, and F. Martín. Modulation of Attosecond Beating in Resonant Two-Photon Ionization. *Phys. Rev. Lett.*, 113(26):263001, December 2014. ISSN 0031-9007. doi: 10.1103/PhysRevLett.113.263001. URL http://link.aps.org/doi/10.1103/PhysRevLett.113.263001.

[71] J. D. Jackson. *Classical Electrodynamics*. John Wiley & Sons, 1962. ISBN 978-0471309321.

[72] B.H. Bransden and C.J. Joachain. *Physics of Atoms and Molecules*. Prentice Hall, 1983. ISBN 978-0582356924.

[73] A. Messiah. *Quantum mechanics*. 1958. ISBN 9780486409245.

[74] H. Bachau, P. Lambropoulos, and R. Shakeshaft. Theory of laser-induced transitions between autoionizing states of He. *Phys. Rev. A*, 34(6):4785–4792, December 1986. ISSN 0556-2791. doi: 10.1103/PhysRevA.34.4785. URL http://link.aps.org/doi/10.1103/PhysRevA.34.4785.

[75] O. Smirnova, V. S. Yakovlev, and A. Scrinzi. Quantum coherence in the time-resolved Auger measurement. *Phys. Rev. Lett.*, 91:253001, 2003. doi: 10.1103/PhysRevLett.91.253001.

[76] X-M. Tong and C. D. Lin. Double photoexcitation of He atoms by attosecond xuv pulses in the presence of intense few-cycle infrared lasers. *Phys. Rev. A*, 71(3):033406, March 2005. ISSN 1050-2947. doi: 10.1103/PhysRevA.71.033406. URL http://link.aps.org/doi/10.1103/PhysRevA.71.033406.

[77] L. Argenti, Á. Jiménez Galán, C. Marante, C. Ott, T. Pfeifer, and F. Martín. Dressing effects in the attosecond transient absorption spectra of doubly excited states in helium. *Phys. Rev. A*, 91(6):061403(R), June 2015. ISSN 1050-2947. doi: 10.1103/PhysRevA.91.061403. URL http://link.aps.org/doi/10.1103/PhysRevA.91.061403.

[78] D. A. Varshalovich. *Quantum theory of angular momentum*. World Scientific, 1988. ISBN 978-9971501075.

[79] F. Faisal. *Theory of multiphoton processes*. Springer, 1987. ISBN 978-0306423178.

[80] R. G. Newton. *Scattering theory of waves and particles*. Dover Publications, 1982. ISBN 978-0486425351.

[81] P. Ehrenfest. Bemerkung über die angenäherte gültigkeit der klassischen mechanik innerhalb der quantenmechanik. *Zeitschrift für Physik*, 45(7-8):455–457, 1927. ISSN 0044-3328. doi: 10.1007/BF01329203. URL http://dx.doi.org/10.1007/BF01329203.

[82] *Springer Handbook of Atomic, Molecular and Optical Physics*. 2006. ISBN 978-0-387-33634-3.

[83] J. Taylor. *Scattering theory: the quantum theory on nonrelativistic collisions*. John Wiley & Sons, Inc., New York, 1972.

[84] W. Pauli. *Handbuch der Physik*. Springer, 1926.

[85] W. Pauli. *Handbuch der Physik*. Springer, 1933.

[86] M. H. Stone. Linear transformations in hilbert space. iii. operational methods and group theory. *Proceedings of the National Academy of Sciences of the United States of America*, 16(2):172–175, 1930. ISSN 00278424. URL http://www.jstor.org/stable/85485.

[87] J. von Neumann. Über einen satz von herrn mh stone. *Ann. Math.*, 33: 567–573, 1932.

[88] Felix T. Smith. Lifetime matrix in collision theory. *Phys. Rev.*, 118(1), 1960.

[89] R. Pazourek, S. Nagele, and J. Burgdörfer. Attosecond chronoscopy of photoemission. *Rev. Mod. Phys.*, 87:765–802, Aug 2015. doi: 10.1103/RevModPhys.87.765. URL http://link.aps.org/doi/10.1103/RevModPhys.87.765.

[90] A. Maquet, J. Caillat, and R. Taïeb. Attosecond delays in photoionization: time and quantum mechanics. *J. Phys. B: At., Mol. Opt. Phys.*, 47(20):204004, 2014. URL http://stacks.iop.org/0953-4075/47/i=20/a=204004.

[91] Misha Ivanov and Olga Smirnova. How accurate is the attosecond streak camera? *Phys. Rev. Lett.*, 107:213605, Nov 2011. doi: 10.1103/PhysRevLett.107.213605. URL http://link.aps.org/doi/10.1103/PhysRevLett.107.213605.

[92] S. Nagele, R. Pazourek, J. Feist, and J. Burgdörfer. Time shifts in photoemission from a fully correlated two-electron model system. *Phys. Rev. A*, 85:033401, Mar 2012. doi: 10.1103/PhysRevA.85.033401. URL http://link.aps.org/doi/10.1103/PhysRevA.85.033401.

[93] J. M. Dahlström, D. Guénot, K. Klünder, M. Gisselbrecht, J. Mauritsson, A. L'Huillier, A. Maquet, R. Taïeb, and A. L'Huillier. Theory of attosecond delays in laser-assisted photoionization. *Chem. Phys.*, 414:53, February 2013. ISSN 03010104. doi: 10.1016/j.chemphys.2012.01.017. URL http://linkinghub.elsevier.com/retrieve/pii/S0301010412000298.

[94] H. Feshbach. Unified theory of nuclear reactions. *Annals of Physics*, 5(4):357 – 390, 1958. ISSN 0003-4916. doi: http://dx.doi.org/10.1016/0003-4916(58)90007-1. URL http://www.sciencedirect.com/science/article/pii/0003491658900071.

[95] G. Tanner, K. Richter, and J. M. Rost. The theory of two-electron atoms: between ground state and complete fragmentation. *Rev. Mod. Phys.*, 72(2): 497–544, April 2000. ISSN 0034-6861. doi: 10.1103/RevModPhys.72.497. URL http://link.aps.org/doi/10.1103/RevModPhys.72.497.

[96] J. W. Cooper, U. Fano, and F. Prats. Classification of two-electron excitation levels of helium. *Phys. Rev. Lett.*, 10(12):10–13, 1963.

[97] C.D. Lin. Classification of doubly excited states of two-electron atoms. *Phys. Rev. Lett.*, 51, 1983.

[98] H. Bachau, E. Cormier, P. Decleva, J.E. Hansen, and F. Martín. Applications of B-splines in atomic and molecular physics. *Rep. Prog. Phys.*, 1815, 2001.

[99] F. Ferrari, F. Calegari, M. Lucchini, C. Vozzi, S. Stagira, G. Sansone, and M. Nisoli. High-energy isolated attosecond pulses generated by above-saturation few-cycle fields. *Nat. Phot.*, (AOL):1–5, 2010. doi: 10.1038/NPHOTON.2010.250. URL http://dx.doi.org/10.1038/nphoton.2010.250.

[100] M. Lewenstein, P. Balcou, M. Yu. Ivanov, A. L'Huillier, and P. B. Corkum. Theory of high-harmonic generation by low-frequency laser fields. *Phys. Rev. A*, 49(3):2117, 1994.

[101] G. Sansone, F. Kelkensberg, J. F. Pérez-Torres, F. Morales, M. F. Kling, W. Siu, O. Ghafur, P. Johnsson, M. Swoboda, E. Benedetti, F. Ferrari, F. Lépine, J. L. Sanz-Vicario, S. Zherebtsov, I. Znakovskaya, A. L'Huillier, M. Yu. Ivanov, M. Nisoli, F. Martín, and M. J. J. Vrakking. Electron localization following attosecond molecular photoionization. *Nature*, 465(7299):763, June 2010. ISSN 0028-0836. doi: 10.1038/nature09084. URL http://www.nature.com/doifinder/10.1038/nature09084http://www.ncbi.nlm.nih.gov/pubmed/20535207.

[102] L. V. Keldysh. Ionization in the field of a strong electromagnetic wave. *JETP*, 20(5):1307–1314, 1965.

[103] F. Faisal. Multiple absorption of laser photons by atoms. *J. Phys. B: At. Mol. Opt. Phys.*, 6:L89, 1973.

[104] H. R. Reiss. Effect of an intense electromagnetic field on a weakly bound system. *Phys. Rev. A*, 22(5):1786–1813, November 1980. ISSN 0556-2791. doi: 10.1103/PhysRevA.22.1786. URL http://link.aps.org/doi/10.1103/PhysRevA.22.1786.

[105] M. Lewenstein, P. Salieres, and A. L'Huillier. Phase of the atomic polarization in high-order harmonic generation. *Phys. Rev. A*, 52(6):4747–4754, 1995.

[106] L. B. Madsen. Strong-field approximation in laser-assisted dynamics. *Am. J. Phys.*, 73(1):57, 2005. ISSN 00029505. doi: 10.1119/1.1796791. URL http://link.aip.org/link/AJPIAS/v73/i1/p57/s1&Agg=doi.

[107] A. Cionga, V. Florescu, A. Maquet, and R. Taïeb. Target dressing effects in laser-assisted x-ray photoionization. *Phys. Rev. A*, 47(3):1830, 1993.

[108] C-H. Zhang and U. Thumm. Electron-ion interaction effects in attosecond time-resolved photoelectron spectra. *Phys. Rev. A*, 82:043405, 2010. doi: 10.1103/PhysRevA.82.043405.

[109] M. Abramowitz and I. A. Stegun. *Handbook of Mathematical Functions with Formulas, Graphs, and Mathematical Tables*. Dover Publications, Inc., New York, 1965. doi: 10.1119/1.15378. URL http://link.aip.org/link/?AJP/56/958/4&Agg=doi.

[110] M. Swoboda, J.M. Dahlström, T. Ruchon, J. Mauritsson, A. L'Huillier, and K. J. Schafer. Intensity dependence of two-color laser-assisted photoionization spectra. *Laser Physics*, 19:1591–1599, 2009.

[111] K. Varjú, P. Johnsson, J. Mauritsson, T. Remetter, T. Ruchon, Y. Ni, F. Lépine, M. F. Kling, J. I. Khan, K. J. Schafer, M. J. J. Vrakking, and A. L'Huillier. Angularly resolved electron wave packet interferences. *J. Phys. B: At. Mol. Opt. Phys.*, 39:3983, 2006. doi: 10.1088/0953-4075/39/18/026.

[112] A. Scrinzi. Infinite-range exterior complex scaling as a perfect absorber in time-dependent problems. *Phys. Rev. A*, 81:053845, May 2010. doi: 10.1103/PhysRevA.81.053845. URL http://link.aps.org/doi/10.1103/PhysRevA.81.053845.

[113] C. Marante, L. Argenti, and F. Martín. Hybrid Gaussian-B-spline basis for the electronic continuum: Photoionization of atomic hydrogen. *Phys. Rev. A*, 90(1):012506, July 2014. ISSN 1050-2947. doi: 10.1103/PhysRevA.90.012506. URL http://link.aps.org/doi/10.1103/PhysRevA.90.012506.

[114] K. L. Ishikawa and K. Ueda. Competition of resonant and nonresonant paths in resonance-enhanced two-photon single ionization of He by an ultrashort extreme-ultraviolet pulse. *Phys. Rev. Lett.*, 108(3):033003, January 2012. ISSN 0031-9007. doi: 10.1103/PhysRevLett.108.033003. URL http://link.aps.org/doi/10.1103/PhysRevLett.108.033003.

[115] M. Swoboda, T. Fordell, K. Klünder, J. M. Dahlström, M. Miranda, C. Buth, K. J. Schafer, J. Mauritsson, a. L'Huillier, and M. Gisselbrecht. Phase measurement of resonant two-photon ionization in helium. *Phys. Rev. Lett.*, 104(10):12–15, March 2010. ISSN 0031-9007. doi: 10.1103/PhysRevLett.104.103003. URL http://link.aps.org/doi/10.1103/PhysRevLett.104.103003.

[116] J. Caillat, A. Maquet, S. Haessler, B. Fabre, T. Ruchon, P. Salières, Y. Mairesse, and R. Taïeb. Attosecond resolved electron release in two-color near-threshold photoionization of N$_2$. *Phys. Rev. Lett.*, 106:093002, 2011. doi: 10.1103/PhysRevLett.106.093002.

[117] E. Cormier, H. Bachau, and J. Zhang. Discretization techniques applied to the study of multiphoton excitation of resonances in helium. *J. Phys. B: At. Mol. Opt. Phys.*, 26(23):4449–4463, December 1993. ISSN 0953-4075. doi: 10.1088/0953-4075/26/23/016. URL http://stacks.iop.org/0953-4075/26/i=23/a=016?key=crossref.c15f36f5237959bb63d5f0d0c897c4a8.

[118] O Guyétand, M Gisselbrecht, a Huetz, P Agostini, R Taïeb, V Véniard, a Maquet, L Antonucci, O Boyko, C Valentin, and D Douillet. Multicolour above-threshold ionization of helium: quantum interference effects in angular distributions. *J. Phys. B: At. Mol. Opt. Phys.*, 38(22):

L357–L363, November 2005. ISSN 0953-4075. doi: 10.1088/0953-4075/38/22/L01. URL http://stacks.iop.org/0953-4075/38/i=22/a=L01?key=crossref.0735ab958087e900a7134ada62354623.

[119] O. Guyétand, M. Gisselbrecht, A. Huetz, P. Agostini, R. Taïeb, A. Maquet, B. Carré, P. Breger, O. Gobert, D. Garzella, J. F. Hergott, O. Tcherbakoff, H. Merdji, M. Bougeard, H. Rottke, M. Böttcher, Z. Ansari, and P. Antoine. Evolution of angular distributions in two-colour, few-photon ionization of helium. *J. Phys. B: At. Mol. Opt. Phys.*, 41(5):051002, March 2008. ISSN 0953-4075. doi: 10.1088/0953-4075/41/5/051002. URL http://stacks.iop.org/0953-4075/41/i=5/a=051002?key=crossref.c23adee4c160f24bedb8bbaa248cee5f.

[120] M. Domke, K. Schulz, G. Remmers, G. Kaindl, and D. Wintgen. High-resolution study of $^1P^o$ double-excitation states in helium. *Phys. Rev. A*, 53 (3):1424–1438, 1996. ISSN 1050-2947. doi: 10.1103/PhysRevA.53.1424. URL http://journals.aps.org/pra/abstract/10.1103/PhysRevA.53.1424.

[121] K. Schulz, G. Kaindl, M. Domke, J. D. Bozek, P. A. Heimann, A. S. Schlachter, and J. M. Rost. Observation of new Rydberg series and resonances in doubly excited Helium at ultrahigh resolution. *Phys. Rev. Lett.*, 77(15):3086–3089, October 1996. ISSN 0031-9007. doi: 10.1103/PhysRevLett.77.3086. URL http://link.aps.org/doi/10.1103/PhysRevLett.77.3086.

[122] M. Domke, C. Xue, A. Puschmann, T. Mandel, E. Hudson, D. A. Shirley, G. Kaindl, C. H. Greene, H. R. Sadeghpour, and H. Petersen. Extensive double-excitation states in atomic helium. *Phys. Rev. Lett.*, 66(10):1306–1309, March 1991. ISSN 0031-9007. doi: 10.1103/PhysRevLett.66.1306. URL http://link.aps.org/doi/10.1103/PhysRevLett.66.1306.

[123] M. Nagasono, E. Suljoti, A. Pietzsch, F. Hennies, M. Wellhöfer, J. T. Hoeft, M. Martins, W. Wurth, R. Treusch, J. Feldhaus, J. R. Schneider, and A. Föhlisch. Resonant two-photon absorption of extreme-ultraviolet free-electron-laser radiation in helium. *Phys. Rev. A*, 75:051406(R), 2007. doi: 10.1103/PhysRevA.75.051406.

[124] P. G. Burke, D. D. McVicar, and K. Smith. Calculation of autoionizing levels in He. *Phys. Rev. Lett.*, 11(1):559, July 1963. doi: 10.1103/PhysRevLett.11.559. URL http://journals.aps.org/prl/abstract/10.1103/PhysRevLett.11.559.

[125] A. K. Bhatia, P. G. Burke, and A. Temkin. Calculation of the $^1P(2s2p)$ autoionization state of He with a pseudostate nonresonant continuum. *Phys. Rev. A*, 8(1):21–26, July 1973. ISSN 0556-2791. doi: 10.1103/PhysRevA.8.21. URL http://link.aps.org/doi/10.1103/PhysRevA.8.21.

[126] R. Moccia and P. Spizzo. An L^2 calculation of the $^{1,3}P^o$ resonances of atomic helium. *J. Phys. B: At. Mol. Opt. Phys.*, 20:1423, 1987. doi: 10.1088/0022-3700/20/7/011. URL http://iopscience.iop.org/article/10.1088/0022-3700/20/7/011.

[127] A. Macías, F. Martín, A. Riera, and M. Yañez. Simple discretization method for autoionization widths. I. Theory. *Phys. Rev. A*, 36(9):4179–4186, November 1987. ISSN 0556-2791. doi: 10.1103/PhysRevA.36.4179. URL http://link.aps.org/doi/10.1103/PhysRevA.36.4179.

[128] A. Macías, F. Martín, A Riera, and M. Yañez. Simple discretization method for autoionization widths. II. Atoms. *Phys. Rev. A*, 36(9):4187–4202, November 1987. ISSN 0556-2791. doi: 10.1103/PhysRevA.36.4187. URL http://link.aps.org/doi/10.1103/PhysRevA.36.4187.

[129] R. Moccia and P. Spizzo. Helium photoionization between the N=2 and N=3 thresholds including angular distribution and resonance properties: A K-matrix L2 basis-set calculation. *Phys. Rev. A*, 43(5):2199–2214, 1991. ISSN 10502947. doi: 10.1103/PhysRevA.43.2199. URL http://journals.aps.org/pra/abstract/10.1103/PhysRevA.43.2199.

[130] I. Sánchez and F. Martín. Photoionization of He above the n =2 threshold. *Phys. Rev. A*, 44(11):7318–7334, December 1991. ISSN 1050-2947. doi: 10.1103/PhysRevA.44.7318. URL http://link.aps.org/doi/10.1103/PhysRevA.44.7318.

[131] E. Lindroth. Calculation of doubly excited states of helium with a finite discrete spectrum. *Physical Review A*, 49(6), 1994.

[132] A. Bürgers, D. Wintgen, and J. M. Rost. Highly doubly excited S states of the helium atom. *J. Phys. B: At. Mol. Opt. Phys.*, 28(15): 3163–3183, August 1995. ISSN 0953-4075. doi: 10.1088/0953-4075/28/15/010. URL http://stacks.iop.org/0953-4075/28/i=15/a=010?key=crossref.e51138cf94300551417b0032ddd1c63e.

[133] J.M. Rost, K. Schultz, M. Domke, and G. Kaindl. Resonance parameters of photo doubly excited helium. *J. Phys. B: At. Mol. Opt. Phys.*, 4663, 1997.

[134] J. Mauritsson, T. Remetter, M. Swoboda, K. Klünder, A. L'Huillier, K. J. Schafer, O. Ghafur, F. Kelkensberg, W. Siu, P. Johnsson, M. J. J. Vrakking, I. Znakovskaya, Th. Uphues, S. Zherebtsov, M. F. Kling, F. Lépine, E. Benedetti, F. Ferrari, G. Sansone, and M. Nisoli. Attosecond electron spectroscopy using a novel Interferometric pump-probe technique. *Phys. Rev. Lett.*, 105(5):053001, July 2010. ISSN 0031-9007. doi: 10.1103/PhysRevLett.105.053001. URL http://link.aps.org/doi/10.1103/PhysRevLett.105.053001.

[135] S. L. Sorensen, T. Aberg, J. Tulkki, E. Rachlew-Källne, G. Sundström, and M. Kirm. Argon 3 *s* autoionization resonances. *Phys. Rev. A*, 50:1218–1230, Aug 1994. doi: 10.1103/PhysRevA.50.1218. URL http://link.aps.org/doi/10.1103/PhysRevA.50.1218.

[136] N. Berrah, B. Langer, J. Bozek, T. W. Gorczyca, O. Hemmers, D. W. Lindle, and O. Toader. Angular-distribution parameters and r -matrix calculations of ar $3s^{-1} \rightarrow$ np resonances. *Journal of Physics B: Atomic, Molecular and Optical Physics*, 29(22):5351, 1996. URL http://stacks.iop.org/0953-4075/29/i=22/a=013.

[137] R. López-Martens, K. Varjú, P. Johnsson, J. Mauritsson, Y. Mairesse, P. Salières, M. B. Gaarde, K. J. Schafer, A. Persson, S. Svanberg, C.-G Wahlström, and A. L'Huillier. Amplitude and phase control of attosecond light pulses. *Phys. Rev. Lett.*, 94:033001, 2005. doi: 10.1103/PhysRevLett.94.033001.

[138] T. Carette, J. M. Dahlström, L. Argenti, and E. Lindroth. Multiconfigurational hartree-fock close-coupling ansatz: Application to the argon photoionization cross section and delays. *Phys. Rev. A*, 87:023420, Feb 2013. doi: 10.1103/PhysRevA.87.023420. URL http://link.aps.org/doi/10.1103/PhysRevA.87.023420.

[139] J. Itatani, F. Quéré, G. L. Yudin, M. Yu. Ivanov, F. Krausz, and P. B. Corkum. Attosecond streak camera. *Phys. Rev. Lett.*, 88:173903, 2002. doi: 10.1103/PhysRevLett.88.173903.

[140] J. M. Dahlström and E. Lindroth. Study of attosecond delays using perturbation diagrams and exterior complex scaling. pages 1–36, April 2014. URL http://arxiv.org/abs/1404.3895v1.

[141] J. Wätzel, A. S. Moskalenko, Y. Pavlyukh, and J. Berakdar. Angular resolved time delay in photoemission. *J. Phys. B: At., Mol. Opt. Phys.*, 48(2):025602, 2015. URL http://stacks.iop.org/0953-4075/48/i=2/a=025602.

[142] I. A. Ivanov and A. S. Kheifets. Time delay in atomic photoionization with circularly polarized light. *Phys. Rev. A*, 87:033407, Mar 2013. doi: 10.1103/PhysRevA.87.033407. URL http://link.aps.org/doi/10.1103/PhysRevA.87.033407.

[143] P. Radcliffe, M. Arbeiter, W. B. Li, S. Düsterer, H. Redlin, P. Hayden, P. Hough, V. Richardson, J. T. Costello, T. Fennel, and M. Meyer. Atomic photoionization in combined intense XUV free-electron and infrared laser fields. *New J. Phys.*, 14(4):043008, April 2012. ISSN 1367-2630. doi: 10.1088/1367-2630/14/4/043008. URL http://stacks.iop.org/1367-2630/14/i=4/a=043008?key=crossref.8018ae46abb817a2319ab327fb94e8e1.

[144] A. Kazansky, I. Sazhina, and N. Kabachnik. Angle-resolved electron spectra in short-pulse two-color XUV+IR photoionization of atoms. *Phys. Rev. A*, 82 (3):1–8, September 2010. ISSN 1050-2947. doi: 10.1103/PhysRevA.82.033420. URL http://link.aps.org/doi/10.1103/PhysRevA.82.033420.

[145] Marc J. J. Vrakking. An iterative procedure for the inversion of two-dimensional ion/photoelectron imaging experiments. *Rev. Sci. Instrum.*, 72: 4084, 2001.

[146] A. Blättermann, C. Ott, A. Kaldun, T. Ding, and T. Pfeifer. Two-dimensional spectral interpretation of time-dependent absorption near laser-coupled resonances. *J. Phys. B: At. Mol. Opt. Phys.*, 47(12): 124008, June 2014. ISSN 0953-4075. doi: 10.1088/0953-4075/47/12/124008. URL http://stacks.iop.org/0953-4075/47/i=12/a=124008?key=crossref.bef80279ed14e96db5fbae8b6681a903.

[147] A. Kaldun, C. Ott, A. Blättermann, M. Laux, K. Meyer, T. Ding, A. Fischer, and T. Pfeifer. Extracting phase and amplitude modifications of laser-coupled Fano resonances. *Phys. Rev. Lett.*, 112(10):103001, March 2014. ISSN 0031-9007. doi: 10.1103/PhysRevLett.112.103001. URL http://link.aps.org/doi/10.1103/PhysRevLett.112.103001.

[148] M. Davidson, J. Wals, H. G. Muller, and H. van Linden van den Heuvell. Observation of full ponderomotive shift for the photodetachment threshold in a strong laser field. *Phys. Rev. Lett.*, 71(14):2192–2195, October 1993. ISSN 0031-9007. doi: 10.1103/PhysRevLett.71.2192. URL http://link.aps.org/doi/10.1103/PhysRevLett.71.2192.

[149] M. Smits, C. de Lange, A. Stolow, and D. Rayner. Dynamic polarization in the strong-field ionization of small metal clusters. *Phys. Rev. Lett.*, 93 (20):203402, November 2004. ISSN 0031-9007. doi: 10.1103/PhysRevLett.93.203402. URL http://link.aps.org/doi/10.1103/PhysRevLett.93.203402.

[150] A. N. Pfeiffer, C. Cirelli, M. Smolarski, D. Dimitrovski, M. Abu-samha, L. B. Madsen, and U. Keller. Attoclock reveals natural coordinates of the laser-induced tunnelling current flow in atoms. *Nat. Phys.*, 8(1):76–80, October 2011. ISSN 1745-2473. doi: 10.1038/nphys2125. URL http://www.nature.com/doifinder/10.1038/nphys2125.

[151] R. Santra. Why complex absorbing potentials work: A discrete-variable-representation perspective. *Physical Review A*, 74(3):034701, September 2006. ISSN 1050-2947. doi: 10.1103/PhysRevA.74.034701. URL http://link.aps.org/doi/10.1103/PhysRevA.74.034701.

[152] A. Mihelič and M. Žitnik. *Ab Initio* calculation of photoionization and inelastic photon scattering spectra of He below the $N = 2$ threshold in a dc electric field. *Phys. Rev. Lett.*, 98(24):243002, June 2007. ISSN 0031-9007. doi: 10.1103/PhysRevLett.98.243002. URL http://link.aps.org/doi/10.1103/PhysRevLett.98.243002.

[153] M. Žitnik, A. Mihelič, K. Bučar, M. Kavčič, J-E. Rubensson, M. Svanquist, J. Söderström, R. Feifel, C. Saathe, Y. Ovcharenko, V. Lyamayev, T. Mazza, M. Meyer, M. Simon, L. Journel, J. Lüning, O. Plekan, M. Coreno, M. Devetta, M. Di Fraia, P. Finetti, R. Richter, C. Grazioli, K. C. Prince, and C. Callegari. High resolution multiphoton spectroscopy by a tunable Free-Electron-Laser light. *Phys. Rev. Lett.*, 113(19):193201, November 2014. ISSN 0031-9007. doi: 10.1103/PhysRevLett.113.193201. URL http://link.aps.org/doi/10.1103/PhysRevLett.113.193201.

[154] Andrej Mihelič. private communication, 2014.

[155] A. J. F. Siegert. On the derivation of the dispersion formula for nuclear reactions. *Phys. Rev.*, 56:750–752, Oct 1939. doi: 10.1103/PhysRev.56.750. URL http://link.aps.org/doi/10.1103/PhysRev.56.750.

[156] A. Jiménez-Galán, F. Martín, and L. Argenti. Two-photon finite-pulse model for resonant transitions in attosecond experiments. 2015.

[157] F. J. Wuilleumier and M. Meyer. Pump-probe experiments in atoms involving laser and synchrotron radiation: an overview. *J. Phys. B: At. Mol. Opt. Phys.*, 39(23):R425–R477, 2006. ISSN 0953-4075. doi: 10.1088/0953-4075/39/23/R01.

[158] U. Höfer, I. L. Schumay, Ch. Reuß, U. Thomann, W. Wallauer, and Th. Fauster. Time-Resolved Coherent Photoelectron Spectroscopy of Quantized Electronic States on Metal Surfaces. *Science*, 277(5331):1480–1482, September 1997. ISSN 00368075. doi: 10.1126/science.277.5331.1480. URL http://www.sciencemag.org/cgi/doi/10.1126/science.277.5331.1480.

[159] R. D. Muino, D. Sanchez-Portal, V. M. Silkin, E. V. Chulkov, and P. M. Echenique. Time-dependent electron phenomena at surfaces. *PNAS*, 108 (3):971–976, January 2011. ISSN 0027-8424. doi: 10.1073/pnas.1008517107. URL http://www.pnas.org/cgi/doi/10.1073/pnas.1008517107.